Mass, Momentum and Energy Transfer in Aggregated Particulate Media

A DISSERTATION
SUBMITTED TO THE FACULTY OF
UNIVERSITY OF MINNESOTA
BY

Thaseem Thajudeen

IN PARTIAL FULFILLMENT OF THE REQUIREMENTS
FOR THE DEGREE OF
DOCTOR OF PHILOSOPHY

Professor Christopher J Hogan Jr.

December 2013

Acknowledgements

The journey started four years back. On a typical snow clad Minnesotan day in December 2009, Chris welcomed me to the new group with an Alpaca cap as a Christmas gift. It was more or less a smooth ride from then on; mainly because of my mentor/advisor. It was by far one of the best decisions in my life, to be part to 'Hogan's Heroes'. Chris's passion for science and determination to do better was always an inspiration for me. You do not have to look for inspirations elsewhere when you see your advisor working so hard. This would not have been possible but for his vision, pep talks and above all his love for research. I specifically thank him for letting me work with the flame generator even after watching me almost setting the lab on fire and above all for being an awesome advisor!!

It was fun being part of Hogan's Heroes. Starting as a lab room with hardly any instruments four years ago, ME 4136 has grown into one of the busiest lab rooms in the department. I had the opportunity to work with some really awesome people during my doctoral studies here. It was a smaller group then. I thank my "Ph D bros" (a term which was used by Ranga and I do not think I can suggest an authentic reference to that here!!) Ranga and Derek for all the fruitful discussions and the debugging sessions. After four years of sharing lab space with Derek, I am more confident as a mechanical engineer now. Instruments are no longer black boxes and it was fun and educational watching him fix the broken instruments; including the ones that I managed to break. Ranga was a lot more than a coworker; never shy of giving his opinions. He was always there as a senior lab mate and a friend willing to help. Vinay and Daniel were my first officemates and it was fun doing all the assignments and course projects with them. It was not easy adjusting to a new routine where you actually start doing the assignments well before the due date. Chris then introduced a new member to the group." This is Carlos and he is joining as a post doc in our group. He knows everything about everything." The second-in-command not only proved those words true, but also showed that you can have all the fun in the world and still get a lot of work done in the lab. Thanks for all that and for being such an awesome friend. Special thanks to Hui and Seongho who helped me a lot in conducting the experimental studies in the lab. Working with Ben on the filtration study was a nice experience. (Special thanks for the Seinfeld Original DVDs too!!) I thank the newer members of the group SK, Vivek, Gus, Hallie, Jikku, David for keeping me on my toes and obviously for the fun times outside lab too. I thank the Minnesota Super Computing Institute (MSI) for providing high performance computing hardware for most of the numerical work in this dissertation.

Life would have been miserable but for the awesome friends I made here during the last four years. Worst part of doing a Ph D is that you have to bid adieu to a number of friends during your stay at the U. I am really thankful for the wonderful set of friends I

made here and hope I do not forget to mention anyone here, who made this such an awesome experience for me. I am truly indebted to my brother and sister here, Jikku and Jyothy. Thanks for taking care of me and for all the help. It was a big difference to know you are going back after work to a place you could call home. Roopa is my worst critic and one of my closest friends. Thanks for all the wonderful moments and for still listening me out. Special thanks to Bala, my classmate for eight years and then my apartment mate here for three years. Ram, Vineeth and Ganesh were very gracious hosts during my first few months in Minneapolis and been good friends ever since. 516 boys (Sarath, Vivek, Dilip and Rohit), (310-621 group) (Neetha, Govind, Raghu, Pavani , (special thanks for the daal ☺), Koshy, Anand, GV, Sreekanth, Palak,Aruna, Karthik,Sreejith),Anwar and rest of the 3M group, It was equally important to have a group of friends in the department to meet once in a while and sulk about the travails of a grad student. Thanks to Rohini, Meenakshi,Venkat(s), Savio, Praggi, Ashwin and Smita. Muchas Gracias to Carlos and SK for the late night chats, happy hour sessions and for being such awesome friends.

None of this would have been possible but for the constant support and encouragement from my parents and my sister, who supported my decision to come to a place thousands of miles away.

To
My Parents

Table of Contents

List of Tables

List of Figures

Chapter 1: Introduction

The synthesis of nanoparticles (particles with feature sizes below 100 nm) in the gas phase typically occurs via nucleation and condensation (gas-to-particle conversion), followed by the subsequent collision and adherence of the collided particles (aggregation). For this reason, gas-phase nanoparticles can rarely be treated as isolated spheres; instead the entities formed are better described as clusters of many individual spheres, normally called aggregates. Aggregates are not limited to gas-phase synthesized particles, but are also found very commonly in colloidal systems, either from liquid-phase synthesis, or from the resuspension of gas-phase synthesized particles in solvent. Given the ubiquity of these particles (e.g. Carbon black in tire rubber, titania in photo catalysis/sunblock, silica in biomedical application), it is important to study both (1) how the exact morphology of aggregates arises and affects the aggregate formation, such that their shape can be predicted in a given synthesis system, and (2) how the morphology of the aggregates will influence the physicochemical properties of any material or system in which they are incorporated. The purpose of the studies in this dissertation are therefore to use computational, theoretical, and experimental approaches to better understand momentum, mass, and energy transfer processes which lead to aggregate formation, aggregation transport, and the influence aggregates have on energy transfer through a system. Particular emphasis is given to aggregate formation and transport in aerosols; as noted such aggregates often manifest in industrially scalable gas phase synthesis processes. In the subsequent sections of Chapter 1, the theoretical framework commonly used to describe aggregates (as statistical/quasifractals) is reviewed. Subsequently, a brief introduction to each of the topics focused on in this dissertation is provided, which includes: the drag force on aggregates at low speeds, which governs their motion, the collision rate between to aggregated particles in a gaseous medium, the deposition of aggregates on a fibrous filter, aggregate formation in a gaseous medium, conduction through a solid medium embedded with aggregates, and convective heat transfer in an aggregate laden liquid

suspension. While this dissertation is intended to be a fairly complete work describing aggregation, aggregate transport, and thermal transport in aggregated media, each chapter is written as a stand-alone work with its own introduction section, as each has been prepared for publication in a peer-reviewed scientific journal. Therefore, readers only concerned with specific topic areas may read only the necessary sections; an effort has been made to minimize the self-referential nature of this work.

1.1 Morphological Description of Aggregates

While the geometry of the aggregates is certainly complex with a considerable degree of randomness, numerous experimental and theoretical studies suggest that nearly all aggregate shapes can be accurately described as statistical fractals. This description dates back to Mandelbrot's use of fractal descriptors to link mechanical properties to tortuosity, the fractal framework has been used to describe the self-similar nature of aggregates (Given and Mandelbrot 1984; Havlin and Benavraham 1987). For statistical fractals (also termed quasifractals), the number of primary spheres in an aggregate is related to the aggregate radius of gyration by a power law given by:

$$N = k_f \left(\frac{R_g}{a_p}\right)^{D_f} \tag{1}$$

where N is the number of primary spheres with radius a_p , R_g is the radius of gyration and k_f and D_f are the pre exponential factor and the fractal dimension respectively. A fractal dimension of 3.0 suggests a spherical particle while a fractal dimension of 1.0 represents a linear structure (Given and Mandelbrot 1984). Most prior investigations have reported the value range of pre exponential factor to be between 1.0 and 5.0 (Sorensen and Roberts 1997). For computational studies it is necessary to have algorithms that can generate aggregates based on preset values of the morphological parameters. Figure 1.1 shows the image of a computationally generated fractal aggregate (using the noted CCA algorithm) and a TEM (Transmission Electron Microscopy) image of titanium dioxide particles synthesized in a flame synthesis reactor. Prior investigations have used primarily two algorithms to generate computer

aggregates that resemble realistic aggregates closely. Both algorithms are used extensively in this work, hence they are noted here. First, the Sequential Algorithm (SA) is a computationally efficient way for generating tailor made fractal aggregates of different morphological parameters (Filippov, Zurita et al. 2000), in which aggregates are generated by adding monomers sequentially, satisfying equation (1) for a prescribed fractal dimension and pre-exponential factor with each addition. However, for large numbers of primary particles, while equation (1) is satisfied, SA generated aggregates do not match experimentally observed aggregates in other properties, e.g. the structure factor inferred from static light scattering. Conversely, Cluster-Cluster Aggregation (CCA) algorithm, in which aggregates are generated satisfying equation (1) from smaller aggregate building blocks, is more complex to implement, but does lead to aggregates with properties better mimicking those in experimentally observed aggregates (Jullien 1986; Jullien, Botet et al. 1987; R Jullien 1987; Filippov, Zurita et al. 2000).

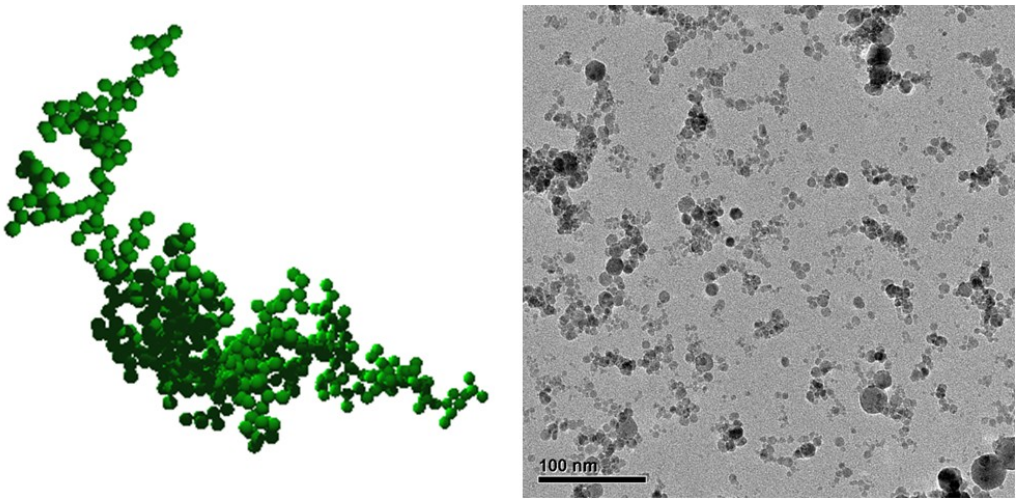

Figure 1.1: A computationally generated fractal with D_f=1.80, k_f=1.30 and 500 primary particles (left). On the right is the TEM image of Titania particles produced in a flame, showing the fractal nature.

1.2 Drag on Non-spherical Particles

The friction factor of particles, which is a representation of the drag force on the particles (Drag force (D)= friction factor (f) x relative fluid velocity (V) , at low Reynolds number (Re) and low Mach number (Ma)), is an important parameter as low speed drag forces control the motion of small particles in virtually all gas phase environments. Therefore, the focus of Chapter 2 of this work is to examine theoretically and experimentally the drag force, quantified by the scalar friction factor (and its inverse, termed the mobility) on aggregates. The first part of Chapter 2 describes two size descriptors that can be used to calculate the friction factor of non-spherical entities under all the regimes of momentum transfer. There are regression equations to calculate the size descriptors for convex non-spherical particles, such as cylinders (Hansen 2004), which are useful in calculating the friction factor of particles whose 2-Dimensional images are available (Transmission Electron Microscopy, TEM and Scanning Electron Microscopy, SEM images). However, such an understanding is lacking in the case of convex shaped aggregates and it is very important and interesting to calculate 3-Dimensional aggregate properties from the 2-Dimensional images of aggregates collected and obtained through high resolution microscopy. With that consideration, the experimental aspect of this study deals with synthesis of non-spherical aggregates using a flame reactor followed by particle coagulation and subsequent collection and analysis to aim at predict the size descriptors in order to calculate the friction factor and thereby the drag on these particles. Flame synthesis is a commonly used method to synthesize nanoparticles and this study uses Titanium (IV) Isopropoxide as a liquid pre cursor to produce Titania nanoparticles. Titania particles which are mobility classified using a Differential Mobility Analyzer (DMA) (Knutson and Whitby 1975) are collected on a TEM Grid and imaged using TEM. With an in house code developed to calculate some length scales from 2-Dimensional image, these length scales are further compared to a database with exhaustive set of quasi fractal aggregates spanning a wide range of D_f, k_f and N values. The output is used to predict

the size descriptors of the aggregate, to calculate the aggregate's mobility and compare with the theoretical value (set by the DMA).

1.3 Collision Rate between Non-spherical Particles

Even with complete understanding of the drag acting on particles, it is still important to know how particles interact with each other resulting in collision and subsequent coagulation. Despite previous attempts at studying the aggregate growth rate (Rogak and Flagan 1992), experimentally and computationally, a rigorous method to determine aggregate growth rate via collisions in the gas phase and the subsequent morphology of the formed aggregates remains elusive. The focus of Chapter 3 is hence the theoretical development of a collision rate expression for arbitrary shaped particles (aggregates) in the gas phase, under arbitrary background gas conditions. Analogous to momentum transfer, the difficulty in studying mass transfer processes also arise from the existence of different regimes. The approach used in the study is based on the dimensional analysis approach implemented successfully in understanding the mass transfer phenomenon of vapor uptake by non-spherical and also collision between spherical particles (Gopalakrishnan and Hogan 2011; Gopalakrishnan, Thajudeen et al. 2011). The influences of the transition regime momentum transfer process, i.e. the results of Chapter 2, are also incorporated into this work. Algorithms are also developed to calculate the appropriate length scales in the mass transfer continuum and free molecular regimes named the combined Smoluchowski radius (Northrup, Allison et al. 1984; Gopalakrishnan and Hogan 2011; Gopalakrishnan, Thajudeen et al. 2011) and the combined projected area respectively, which can calculate the collision rate between non-spherical particles accurately. The algorithms suggested are based on the same concepts used for calculating the length scales in the case of gas molecules to particle momentum transfer with the extra complexity introduced by the effect of sizes of both the colliding entities.

1.4 Fibrous Filtration of Non-Spherical Particles

An important application of the calculation of collision rate between non-spherical entities is in the fibrous filtration of particles, as filtration is an often used particle control technology. There have thus been number of attempts, experimental and theoretical, aimed at studying the filtration of nanoparticles by filter fibers (Stechkina and Fuchs 1966; Kirsch, Stechkina et al. 1974; Lee and Liu 1982; Balazy and Podgorski 2007; Seto, Furukawa et al. 2010). Prior studies have primarily looked at different mechanisms of filtration through particle deposition mainly diffusion, inertia and interception, and determined the filtration efficiency by considering the different mechanisms independently. Further, little work has been done to look at the filtration efficiency for non-spherical particles in a theoretically rigorous manner. The purpose of Chapter 4 is to build upon the methods of Chapter 3, and develop a method to determine the filtration efficiency for non-spherical, aggregate particles. Like particle-particle collisions, filtration can be thought of as a collision process where particles are collected subsequent to collisions with filter fibers. With the knowledge of collision rate between the particles and fibers, the filtration efficiency of fibrous filters can be calculated which depends on the morphological properties of the particles. Like Chapter 3, a non-dimensional theoretical approach is used to calculate the collision rate of non-spherical aggregates, and the collision rate is directly linked to the filtration efficiency. The main difference in the modeling from Chapter 3 is that filtration collision process is essentially a two dimensional one with the length of cylindrical fibers being very large compared to the particle dimensions and hence the particles can be assumed to be undergoing collisions with a circular disk of infinite length. This brings a difference in the definitions of the size descriptors required for the calculations, compared to the collisions between particles of similar sizes. A recent study has come up with an expression to calculate the collision rate of spherical particles with a cylindrical fiber as a function of different parameters(Hunt, Thajudeen et al. 2013). The study discussed in Chapter 4 on non-spherical filtration uses this expression and makes necessary modifications to account for the effect of particle morphology.

1.5 Aggregation / Aerosol Growth in the Mass and Momentum Transfer Transition Regime

As is the case with most aerosol processes, most prior investigations on aerosol aggregation have been performed assuming particle motion occurs in the continuum regime or the free molecular regime, without acknowledging the fact that aerosol aggregation process predominantly occurs in the mass and momentum transfer transition regimes (Mountain, Mulholland et al. 1986; Chakrabarty, Garro et al. 2011). For particles undergoing aggregation in the continuum regime, the motion of particles is modeled using Brownian Dynamics simulation (Ball, Nauenberg et al. 1984; Carpineti and Giglio 1993; Keblinski, Maritan et al. 1994) with random motion, while in the free molecular regime, particles are assumed to move in straight trajectories before colliding and aggregating (Puri, Richardson et al. 1993; Feldermann, Jander et al. 1994; Oh and Sorensen 1997). In the case of aggregation happening predominantly in the continuum regime, the phenomenon is termed as Diffusion Limited Cluster Aggregation (DLCA) while it is named Ballistic Limited Cluster Aggregation (BLCA) when the process happens in the mass transfer free molecular regime. In actuality, particle motion is not described well by either algorithm and further evolves as particles aggregate; as particles grow, their motion between collisions is effectively more diffusive. The purpose of Chapter 5 is to introduce a new numerical algorithm to correctly model aerosol aggregation, accounting for the change in particle ballistic/diffusive motion as aggregation proceeds. This algorithm is used to model aggregate formation directly under different background gas conditions and for the formed aggregates, parameters necessary to calculate the scalar friction factor and collision rate are inferred.

1.6 Dependence of Bulk Transport Properties on Particle Morphology

It is clearly important to understand the growth kinetics and the growth rate of aggregates in a synthesis system. It is equally vital to have insight into how these particles can change the physicochemical properties of the system they are incorporated into. Of considerable recent interest is the effect aggregates have on conduction and

convection in a liquid suspension (i.e. in a nanofluid). Numerous studies have shown that the rate of conductive transport in such nanofluid suspensions, as well as in aggregate-laden composite materials, in which the solid particles are embedded within a host medium, can be substantially different from the rate of conductive transport in the host medium alone (Das, Choi et al. 2006; Putnam, Cahill et al. 2006; Buongiorno, Venerus et al. 2009). Thermal conductivities of particle laden suspensions are noticeably enhanced even at low volume fractions of the embedded particles (Wang, Xu et al. 1999; Xie, Wang et al. 2002; Yu, France et al. 2008). In the case of convective transport, several experimental and numerical studies have come up with contrasting results for the enhancement in the net convective heat transfer coefficient (Putra, Roetzel et al. 2003; Anoop, Sundararajan et al. 2009). The enhancements are often very high compared to predictions based on effective medium approximation which assumes that the particles are well dispersed as individual spherical particles. As is true for aggregate dynamics in the gas phase, the influence of morphology on thermal transport through aggregate laden suspension and composition should be strongly dependent on aggregate morphology (number of primary particles, fractal dimension, and pre-exponential factor), which by definition the effective medium approximation neglects. Along with aggregation, the degree of coalescence between primary particles is also expected to play a critical role in changing the properties of the host media.

The relationship between particle morphology with heat transfer via conduction and convection are dealt in detail in Chapters 6 and 7 respectively. Continuum models of heat transfer are used throughout these chapters, however, the influence of aggregate morphology on both the thermal conductivity of a suspension, and the dynamic viscosity are considered with detailed models of aggregates and precise Monte-Carlo algorithms. The results of these studies can explain a variety of observed experimental results, including how contradictory results can be explained.

1.7 Publications Resulting from This Dissertation

Aspects of the dissertation has already been published/ submitted for review. Reference to be the publications are given below:

Chapter 2: *The Mobility of Flame Synthesized Aggregates/Agglomerates in the Transition Regime.* Thajudeen T, Jeon S.H & Hogan C. J (2013. To be submitted)

Chapter 3: *The collision rate of NonSpherical Particles and Aggregates for all Diffusive Knudsen Numbers.* Thajudeen T, Gopalakrishnan R, & Hogan C. J Aerosol Science and Technology. 46(11). 1174-1186.

Chapter 4: *The Single Fiber Collision Rate & Filtration Efficiency for Nanoparticles II. Extension to Arbitrary Shaped Particles*. Thajudeen T, Hunt B, & Hogan C. J (Under Review: Aerosol Science and Technology).

Chapter 5: *Aggregation in the Transition Regime*. Thajudeen T, Deshmukh H & Hogan C. J (2013, To be submitted)

Chapter 6: *First-Passage Calculation of the Conductivity of Particle Aggregate-Laden Suspensions and Composites*. Thajudeen T. & Hogan C. J. Powder Technology 218:31-39.

Chapter 7: *Forced and Natural Convection in Aggregate-Laden Nanofluids.* Thajudeen T. & Hogan C. J. J. Nanoparticle Research. 13: 7099-7113.

Chapter 2: The Scalar Friction Factor/Mobility of Non-Spherical Particles in the Transition Regime

Abstract: This chapter discusses in detail the proposed theory for calculating size descriptors that quantifies the drag on non-spherical particles. The theory is then validated by experiments in which flame synthesized titanium dioxide aggregates are mobility classified and the experimental values of mobility are compared with predicted mobility values.

2.1 Introduction

The friction factor, and thereby the drag on aerosol particles, depends on the regime in which momentum transfer occurs between the background gas molecules and the aerosol particle. Hence, friction factor depends on the momentum Knudsen number (Kn) which is the ratio of the background gas mean free path to a relevant length scale (λ) which is the radius in the case of a sphere (a). In the continuum regime, when the radius is very large compared to the gas mean free path, the friction factor for a spherical particle can be expressed by Stokes' law:

$$f_C = 6\pi\mu a \tag{1a}$$

where the subscript C denotes the continuum limit and μ is the gas dynamic viscosity. In the opposite limit, the free molecular regime, where the gas mean free path is very large compared to the particle radius, the friction factor is expressed as(Epstein 1924):

$$f_{FM} = 2.67\frac{\mu}{\lambda}\xi a^2 \tag{1b}$$

where the subscript FM denoted free molecular limit and a number of experimental studies suggesting that $\xi \approx 1.356$ (Hogan and de la Mora 2011; Larriba and Hogan 2013). Between these limiting cases, the friction factor has direct Knudsen number dependence and can be calculated using the semi-empirical Cunningham Slip Correction factor:

$$f = \frac{6\pi\mu a}{C_C(Kn)} \tag{1c}$$

C_C is the Cunningham Correction factor given by:

$$C_C(Kn) = 1 + Kn\left[A_1 + A_2 \exp\left(-{}^{A_3}/_{Kn}\right)\right] \tag{1d}$$

A_1,A_2 and A_3 are empirically obtained values and equation 1c correctly converges to 1a when $Kn \rightarrow 0$ and 1b when $Kn \rightarrow \infty$. Many experimental studies (Eglin 1923; Rader 1990) have concluded that Stokes Millikan expression works for spheres in the momentum transfer transition regime (intermediate *Kn* numbers) and found that the values for A_1,A_2 and A_3 to be 1.257, 0.4 and 1.1 respectively as given by Davies (Davies 1945) to be in very good agreement.

A well-founded theory is not yet in place to define the scalar friction factor and thereby the drag on non-spherical particles. In addition to their unique structures, a key challenge in determining the friction factor of aggregates is appropriate consideration of the "transition regime" nature of gas molecule-particle momentum transfer (i.e. non-continuum effects), which has a considerable influence on aggregate mobility. To address this issue theoretically for non-spherical particles, Dahneke (Dahneke 1973) proposed the "adjusted sphere" model, which remains to-date the most tractable approach to non-spherical particle mobility calculations. However, recent investigations do not make use of Dahneke's method and clearly there is need for further investigation to study the scalar friction factor of non-spherical particles in the continuum, free molecular and transition regimes. The first part of this chapter explains the theory for calculating the length scales involved, and provides an expression for calculating the scalar friction factor of non-spherical aggregates. Although the method is universal, this numerical investigation focuses on quasi-fractal aggregates which are found ubiquitously during gas phase synthesis of aerosol particles.

The second part of this chapter focuses on experimental measurements of the morphologies of flame synthesized aggregates, inference of their friction factors

(though discussed in terms of mobilities) and comparison to friction factors predicted for these aggregates using the theoretical expression developed in the first part. Flame synthesis with gas phase precursors is a scalable route to the production of a variety of nanoparticles, and is well suited to produce test aggregates to examine theoretical expressions for the drag force on non-spherical particles. In the final stages of the flame synthesis process, particle-particle collisions are typically the dominant particle growth mechanism. While particles may restructure/rearrange themselves subsequent to colliding, they typically do not fully coalesce; the time scales for viscous flow and grain boundary diffusion-driven sintering are slow relative to the characteristic time-scale for collisions, even in elevated temperature environments. For this reason, flame synthesis leads to the production of aggregates/agglomerates, i.e. ensembles of point-contacting (in the case of agglomerates) or overlapping (aggregates, used henceforth to refer to both types of ensembles in this work) near-spherical primary particles which can also be generated computationally for comparison.

2.2 Theoretical Methods

2.2.1 Continuum Regime

As in the case of spheres, the orientationally averaged friction factor for non-spherical particles (neglecting rotation) can be written similar to equation (1a) as:

$$f_C = 6\pi\mu R_H \tag{2}$$

where R_H is the non-spherical particle hydrodynamic radius. R_H is not dependent on gas properties and depends only on the geometry of the particles. Many prior studies have been devoted to R_H calculation for quasifractal aggregates (Chen, Deutch et al. 1984; Chen, Weakliem et al. 1988) applying the theories of Kirkwood & Riseman (Kirkwood and Riseman 1948) for the calculation of Hydrodynamic radius. Previous investigations have modeled aggregates as porous spheres and uses permeability to relate mobility to particle geometry with the theory applicable for only a group of spherical subunits. It is

necessary to have an easier approach to calculate the size descriptor in the continuum which is the hydrodynamic radius for non-spherical particles.

The relationship between hydrostatics and reaction kinetics have been dealt with before, similarity being the governing equation in the form of Poisson Equation. R_H can be thought of as the hydrodynamic equivalent of the reaction kinetic size descriptor in the continuum regime, called in this study as the Smoluchowski radius, R_S; which can be defined as the radius of the sphere having the same reaction rate of particles as the non-spherical particle under consideration. Like R_H, R_S depends solely on the geometry of the particle; hence, can be thought of as the mass transfer analog of R_H. There is precedence in the field of biophysics in the calculation of R_S (Kirkwood and Riseman 1948; Chen, Weakliem et al. 1988; Zhou, Szabo et al. 1994; Given, Hubbard et al. 1997) and this study borrows the algorithm from previously published work. Prior studies have found that if both orientationally averaged R_S and R_H are considered, the assumption is accurate within certain point percentage. Isella and Drossinos (Zhou, Szabo et al. 1994; Isella and Drossinos 2011) have also found that R_S and R_H are within 5% of one another (without orientational averaging) for linear aggregates of up to 8 primary particles. Therefore, it is a reasonable assumption that R_S can be used in place of R_H for calculating the orientationally averaged friction factor. In this study, a combination of the method used by Hubbard and coworkers is used in tandem with the first passage simulation to come up with a computationally efficient and fast algorithm to calculate R_S of non-spherical particles, as described in the next paragraphs.

To calculate R_S, a particle of interest with a well described geometry is placed within a sphere of specified radius R_{outer} whose center is the origin of the simulation domain, as shown in Figure 2.1. An inertialess, Brownian walker is next placed randomly (uniformly distributed) on the surface of the outer sphere, and moved in a random direction, where the distance walker moves is determined as described in the first passage simulations of Torquato and coworkers. If, after moving, the random walker is a distance greater than R_{outer} from the center of the simulation domain, the probability that the walker will not collide with the particle, P_{exc}, i.e. the probability that

it will travel an infinite distance from the particle surface, is calculated(Given, Hubbard et al. 1997). For hard sphere potentials P_{esc} is given by the equation:

$$P_{esc} = 1 - \frac{R_{outer}}{R_{walker}} \tag{3}$$

where R_{walker} is the distance from the present walker location to the center of the simulation domain, and $R_{walker} > R_{outer.}$ To determine whether the walker will travel an infinite distance from the particle, a uniformly distributed random variable between zero and one is calculated. If this number is less than P_{esc}, the walker leaves the simulation domain, it is counted as a non-colliding walker, and a new walker is placed randomly on the outer sphere surface. However, if it is determined that the walker will not escape, it is again placed on the outer sphere surface, at a location determined from the surface location probability distribution, given for hard sphere interactions by:

$$w(\theta) = \frac{2P_{esc} - P_{esc}^2}{4\pi\left[2(1-P_{esc})(1-\cos(\theta)) + P_{esc}^2\right]^{3/2}} \tag{4}$$

where θ is defined in Figure 2.1, and w is the probability distribution density for the location at which the walker returns to the surface. Obtaining a θ value defines a circle on the outer sphere surface to which the walker returns. To identify the precise point to which the walker returns, the angle ϕ is sampled randomly from a uniform distribution, as once a θ value is identified all points on the circle are equally probable.

After returning to the surface of the outer sphere or if the walker is less than a distance R_{outer} from the simulation domain center, the walker moves a first passage specified distance in a subsequent random direction. Provided that the walker remains a distance less than R_{outer} from the simulation domain center, the walker continues to move randomly via first passage steps. If the walker reaches a distance less than a small critical value δ from any point on the particle surface (taken for the aggregate spherical ensembles examined here as 0.1% of the radius of the primary spheres within the aggregate), it is assumed that a walker-particle collision will occur and the walker is counted as a colliding walker. Each random walker is either a non-colliding walker or a

colliding walker, and after N_{NC} non-colliding walkers and N_C colliding walkers have been counted (where $N = N_{NC} + N_C$ is sufficiently large), the Smoluchowski radius of the particle is calculated as:

$$R_S = \frac{N_C}{N_C + N_{NC}} R_{outer} \tag{5}$$

Note that the results of this approach are independent of R_{outer} provided that a sufficient number of walkers are examined and that the outer sphere completely encapsulates the particle. All R_s calculations are performed dimensionlessly here, with the primary particle radius with examined aggregates taken as 1.0 and R_{outer} scaled accordingly.

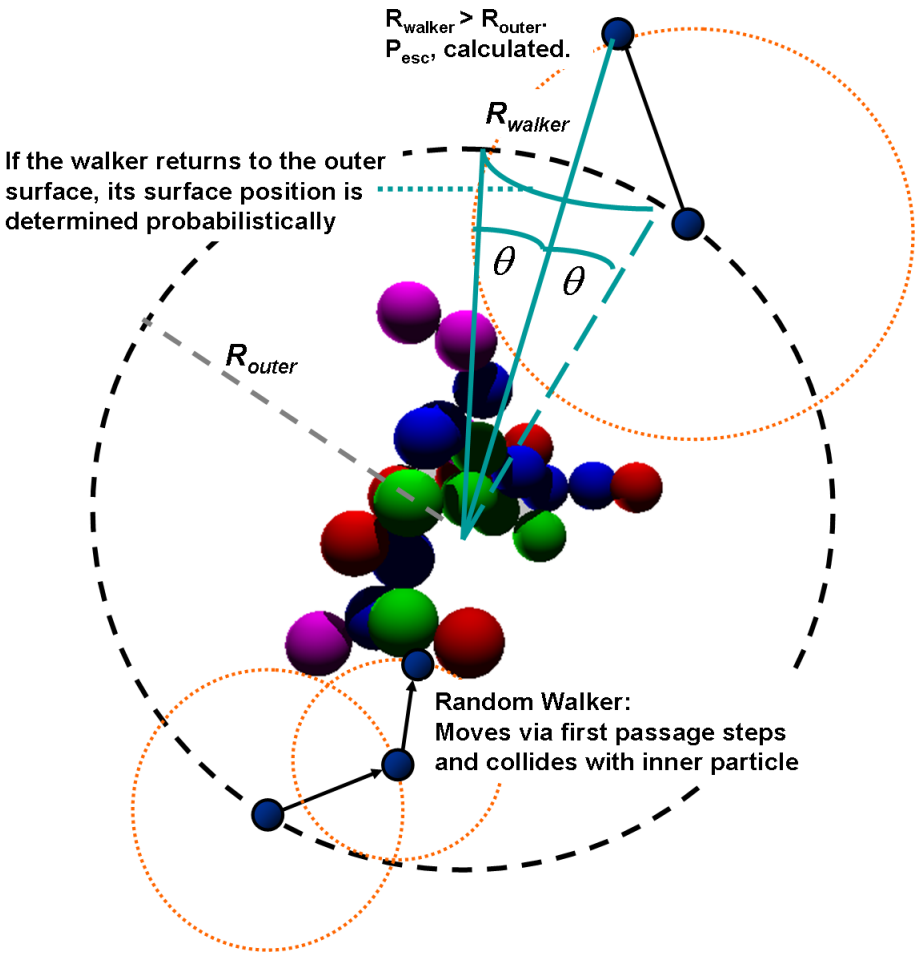

Figure 2.1. Visual representation of the algorithm used in calculation of the Smoluchowski radius for arbitrarily shaped particles.

2.2.2 Free Molecular Regime

In the free Molecular regime the collisions between gas molecules and the particle can be assumed to be ballistic and the relevant size descriptor for the orientationally averaged friction factor will be a function of the projected area of the particle. For a non-spherical particle in the momentum transfer free molecular regime (also referred as 'Epstein's Regime') can be given by the equation (Mason and McDaniel 1988; Li and Wang 2003):

$$f_{FM} = 2.67\frac{\mu}{\lambda}\Omega \tag{6}$$

where Ω is the collision cross section/momentum scattering cross section for the particle. Collision cross section is a function of the background gas as well and numerous studies have found a link between Ω and the orientationally averaged projected area (PA) of the particle given as $\Omega \approx \xi PA$, and ξ was approximately found to be 1.356(Hogan and de la Mora 2011) . Monte Carlo simulation is used to calculate the orientationally averaged projected area similar to the algorithm used to calculate the value of π using the area of a circle inscribed inside a square. The aggregate is first projected on to a plane and is enclosed completely in a rectangle. N_{tot} points are randomly chosen inside the rectangle and N_{in} is the number of points that falls inside the projection of the aggregate. The projected area of the aggregate is the product of the area of the rectangle and the probability that a point is inside the projection of the aggregate (N_{in}/N_{tot}). A visual representation is the algorithm is provided in figure 2.2.The aggregate is randomly orientated and the projected are is calculated for each orientation and thereby its orientationally averaged projected area (PA) is calculated and thereby the friction factor in the free molecular regime.

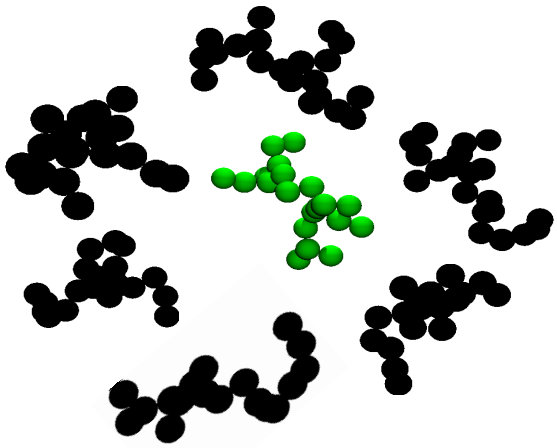

Figure 2.2: The aggregate is rotated randomly and the projected area (black) is calculated for each orientation and the average gives the orientationally averaged projected area.

2.2.3 Transition Regime

Building on the success made in the mass transfer analysis of non-spherical particles in the transition regime in calculating the collision rate of vapor molecules with arbitrary shaped particles, by using non dimensionalization and Buckingham pi theorem, the Knudsen number for an arbitrarily shaped particle can be defined as:

$$Kn=(\lambda\pi R_H/PA) \tag{7a}$$

The orientationally averaged friction factor can be calculated using modified form of equation 1c with the Cunningham correction factor being a function of *Kn* as described in equation 1d.

$$f = \frac{6\pi\mu R_H}{C_C(Kn)} \tag{7b}$$

2.2.4 Mobility of Non-Spherical Aggregates

From equation (7a-b) it follows that the mobility of a non-spherical particle, defined as the proportionality constant between a particle's velocity and an external force acting on the particle, can be written as:

$$B = \frac{1}{f} = \frac{1+\frac{\lambda\pi R_H}{PA}\left(1.257+0.4exp\left(\frac{-1.1PA}{\lambda\pi R_H}\right)\right)}{6\pi\mu R_H} \quad (8)$$

For measurements made at room temperature and atmospheric pressure in air, $\lambda \approx 67$ nm, and for most aggregates produced in flame synthesis reactors, *Kn* is of order 0.1 to 10. Equation (8) predictions are in good agreement with direct simulation Monte Carlo (DSMC) (Zhang, Thajudeen et al. 2012) model inferred mobilities for selected aggregate particles in this *Kn* range, as well measurements on small aggregates (2-5 primary particles) (Cheng, Allen et al. 1988; Cho, Hogan et al. 2007), larger straight chain aggregates (lower *Kn*, but with appreciably high aspect ratios) (Kasper 1982), and most recently, gold nanorods with aspect ratios in the 1 to 14 and *Kn* in the 1 to 6 range (in both air and carbon dioxide) (Gopalakrishnan, McMurry et al. 2013).

Comparison of equation (8) predictions to measurements for flame synthesized aggregates remains unreported, and has been hindered because as inputs equation (8) requires knowledge of the hydrodynamic radii and projected areas of measured aggregates, which are difficult to determine by direct means. To date, the most successful study linking aggregate mobility to structure is that of Rogak et al(Rogak, Flagan et al. 1993), who made measurements of the electron micrograph observed projected areas of mobility selected (via a differential mobility analyzer, DMA) flame synthesized TiO_2 aggregates at intermediate *Kn* (*0.2-2.0*), and showed good agreement between the projected area equivalent diameter and the mobility diameter, d_m, inferred from an aggregate's mobility via the relationship:

$$B = \frac{1+\frac{2\lambda}{d_m}\left(1.257+0.4exp\left(\frac{-0.55d_m}{\lambda}\right)\right)}{3\pi\mu d_m} \quad (9)$$

The equivalence of d_m and the projected area based diameter has also been assumed in recent analysis of flame synthesized aggregates (Eggersdorfer, Grohn et al. 2012). However, while a one-to-one correspondence of d_m and the projected area based diameter has been observed in numerical simulations(Zhang, Thajudeen et al. 2012) as $Kn \rightarrow \infty$ (the free molecular limit), equation (1) suggests that this correspondence should

break down at intermediate Kn, unless $\pi R_H^2 \approx PA$ for the aggregates in question. Along with examination of the validity of equation (8), the link between the projected area based diameter and the mobility diameter therefore requires further scrutiny. Alternative to equating d_m to the projected area diameter, aggregates have been assumed to be straight chains with their mobilities equivalent to the free molecular limit mobility(Lall and Friedlander 2006; Wang, Shin et al. 2010), i.e. their mobilities are assumed inversely proportional to the number of primary particles per aggregate(Lall and Friedlander 2006). Again, use of this approach could only apply as $Kn \rightarrow \infty$, and further invokes the unproven (and contradicted by computations(Larriba and Hogan 2013)) claim that the mobility of aggregates does not depend on actual aggregate structure. Finally, there is strong theoretical and experimental support for describing most flame synthesized aggregates as quasifractal entities(Cai, Lu et al. 1995; Koylu, Xing et al. 1995; Huang, Oh et al. 1998; Filippov, Zurita et al. 2000; Wang and Sorensen 2002), approximately obeying the fractal law:

$$N_p = k_f \left(\frac{R_g}{a_p}\right)^{D_f} \tag{10}$$

where N_p is the number of primary particles in an aggregate, k_f is the pre-exponential factor, R_g is the radius of gyration, a_p is the primary particle radius, and D_f is the fractal dimension. Based on this scaling, McMurry & coworkers have attempted to scale the mass of mobility selected particles with their mobility diameters (Scheckman, McMurry et al. 2009; Shapiro, Vainshtein et al. 2012), i.e. the power D_{mob} in the relationship $m \sim d_m^{D_{mob}}$, where m is an aggregates mass, has been inferred from measurements. However, as noted by Sorensen (Wang and Sorensen 1999; Sorensen 2011) and in accordance with equation (1), the parameter D_{mob}, even for quasifractal aggregates, should vary with Kn, and is hence a function not only of particle structure, but also measurement conditions.

The purpose of the experimental portion of this study is to provide a more direct comparison of equation (1) predictions to mobility measurements of flame synthesized

TiO_2 aggregates than has been performed previously, as well as to re-examine the validity of prior approaches used in interpreting mobility measurements of flame synthesized particles. Specifically, a methane diffusion flame is used with titanium tetraisopropoxide (TTIP) injected as a vapor to produce TiO_2 aggregates, sample a narrow mobility window of these aggregates via a DMA onto a TEM (transmission electron micrograph) grid, and infer aggregate two-dimensional properties from TEM images. These efforts are similar to those of Rogak & Flagan (Rogak, Flagan et al. 1993), but in addition attempt is made to reconstruct 3-dimensional structures of the observed aggregates(Brasil, Farias et al. 1999; Latin, Ferry et al. 2013), facilitating calculating of aggregate hydrodynamic radii and projected areas, and hence their expected mobilities via equation (1). The proceeding sections describe the synthesis and measurement system, the TEM image analysis approach, the determination of aggregate three-dimensional properties, and finally the comparison between measurements and image-processing facilitated predictions.

2.3 Experimental methods

2.3.1 Flame Synthesis of TiO2 Aggregates

TiO_2 aggregates were synthesized using a laminar diffusion flame reactor similar in dimensions to that described by Jiang et al (Jiang, Chen et al. 2007). The diffusion flame reactor, depicted on the left side of Figure 2.3, consisted of three concentric copper tubes with a common outlet and was housed within a class I fume hood. All gases used in the reactor were of high purity and were purchased from Matheson Gas. For particle synthesis, nitrogen carrier gas at a flowrate of 0.72 l min^{-1} was passed through a glass bubbler (ACE Glass) filled with liquid titanium tetraisopropoxide (TTIP, Sigma-Aldrich). The bubbler was wrapped with heating tape and heated to 150^o C to increase the vapor pressure of TTIP, though the temperature was maintained below TTIP's boiling point (232^o C). Upon exiting the bubbler, the N_2 gas was further heated (again by heating tape surrounding the copper tubing) to ~215^o C to prevent condensation of TTIP vapor molecules onto tubing walls and then sent

through the central tube of the diffusion flame reactor. To maintain a stable flame, methane at a flowrate of 0.9 l min^{-1} was passed through the middle tube and oxygen at a flowrate of 8.6 l min^{-1} was passed through the outermost tube. The flame reactor was initiated by first sending only methane into the reactor, igniting the methane in air via a spark ignition, subsequently adding oxygen to create a stable, soot free flame, and finally adding the TTIP laden N_2. As the goal of this study was to examine the validity of an expression for aggregate mobility which should apply universally, minimal effort was placed on control the flame temperature profile and residence time, rather, the flame reactor was operated to produce aggregates in a manner analogous to a scalable production system.

Flame synthesized aerosol particles were sampled into a conical tube placed ~10 cm above the flame reactor outlet and operated with > 20 l min^{-1} suction to ensure collection of all flame synthesized particles. Particles were then passed through a ~ 1 m long stainless steel tube (3/8" outer diameter) surrounded by a water jacket heat exchanger, which was operated with a continuous countercurrent flow of room temperature water. At the outlet of the water-jacketed tubing, 0.5 l min^{-1} of the aerosol flow was sampled and diluted with 4.5 l min^{-1} of particle free air (using an ejector, Air Vac AVR093H) with the remainder pulled via sunction to through a HEPA filter. The sampled and diluted aerosol flow passed through an in house-built silica bead diffusion dryer to remove combustion generated water vapor. Finally, the diluted aerosol flow was again split, with 3.0-3.5 l min^{-1} going to a HEPA filter, and 1.0 – 1.5 l min^{-1} passing through a ~ 3 L vessel prior to the aerosol flow entering a differential mobility analyzer (DMA).

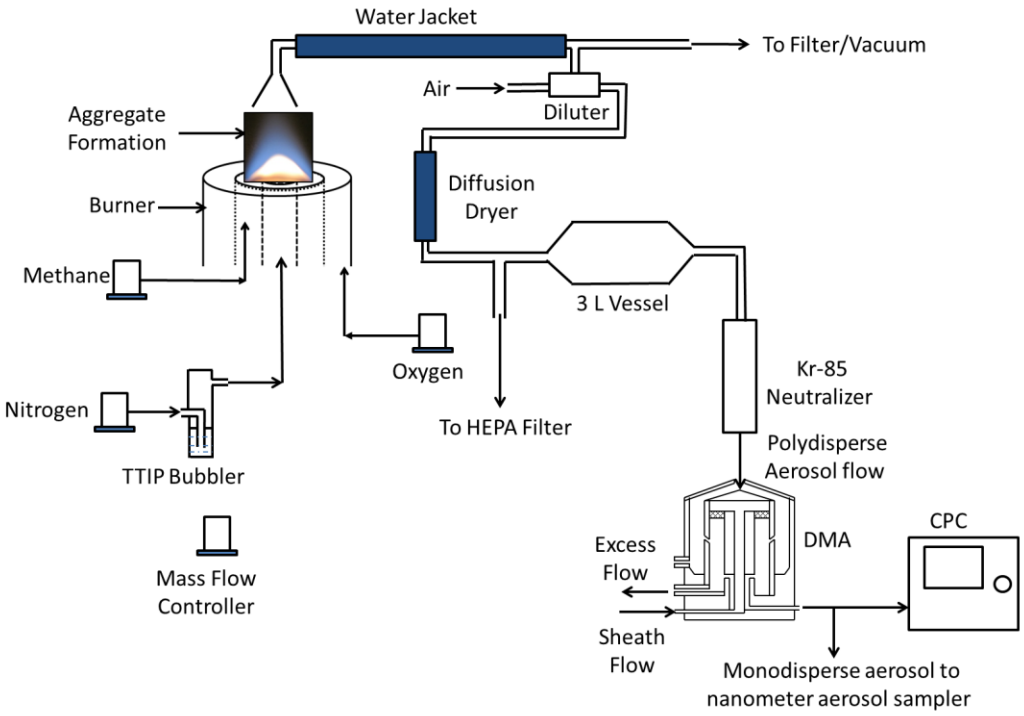

Figure 2.3. A schematic of the flame synthesis system used to produce titanium dioxide (TiO_2) aggregates, measure aggregate size distribution functions (mobility based), and collect mobility classified aggregates.

2.3.2 Nanoparticle Mobility Classification, Collection, and Electron Microscopy

The polydisperse, aggregate TiO_2 particles were sampled into a Kr-85 bipolar ion source, imparting particles with a near-steady state bipolar charge distribution (Gopalakrishnan, Meredith et al. 2013) and then into a TSI Inc. Nano-DMA (model 3085) (Chen, Pui et al. 1998) operated with electrostatic classifier model 3080 to control the DMA sheath flowrate (maintained at 8 l min^{-1}) and applied voltage. The DMA was operated in two modes for particle analysis, selecting positively charged particles in both instances. In the first mode, the DMA was coupled with a butanol-based condensation particle counter (CPC, TSI model 3776) (Stolzenburg and Mcmurry 1991), with which the aerosol flowrate into the DMA and to the CPC was 1.5 l min^{-1}.

The DMA-CPC combination was operated in tandem as an SMPS (Scanning mobility particle spectrometer)(Wang and Flagan 1990) system for measurements of the mobility diameter based size distribution functions for the sampled particles, in which the mobility diameter is inferred from the electrical mobility, Z_p, maximally transmitted by the DMA at a given time during an SMPS scan:

$$Z_p = zeB = \frac{ze\left[1+\frac{2\lambda}{d_m}\left(1.257+0.4exp\left(\frac{-0.55d_m}{\lambda}\right)\right)\right]}{3\pi\mu d_m} \quad (11)$$

where e is the unit electron charge, z is the net number of charges on a particle, which was inferred using the standard Weidensohler approximation(Wiedensohler 1988) for particle populations attaining their bipolar steady-state charge distributions in air/N_2 at atmospheric pressure near room temperature, but without the multiple charge correction (i.e. $z = 1$ or $z = 0$). Size distribution functions, expressed as the number concentration of particles per unit log mobility diameter as a function of mobility diameter, were measured for all experiments after the flame reactor and sampling system was allowed to run continuously for at least 15 minutes.

Following size distribution measurements, the DMA was interfaced with a TSI nanometer aerosol sampler (model 3089), designed to electrostatically deposit DMA transmitted particles onto a transmission electron microscope (TEM) grid (Ted Pella, Inc., Carbon Type B, 15-25 nm, with Formvar). When operated with the nanometer aerosol sampler, the DMA aerosol flowrate was 1.0 l min^{-1}, and it was operated with a constant applied voltage to maximally transmit singly charged particles with room temperature, atmospheric pressure mobility diameters of 45 nm, 50 nm, 60 nm, 70 nm, 75 nm, and 80 nm. For each constant voltage, the DMA and nanometer aerosol sampler were operated for 15-30 minutes to ensure collection of a sufficient number of aggregates on each TEM grid while at the same time minimizing the deposition of multiple aggregates onto one another. TEM images for individual aggregates (15 or more at each mobility diameter) transmitted through the DMA were collected using a FEI Tecnai T12 transmission electron microscope with Digital Micrograph software

(Gatan, Inc.), available in the University of Minnesota Characterization Facility (CharFac). For selected aggregates, energy-dispersive X-ray spectrometry was used to confirm the presence of titanium and oxygen. No other elements (other than those found in the TEM grids themselves, carbon and copper) were detected in particles .

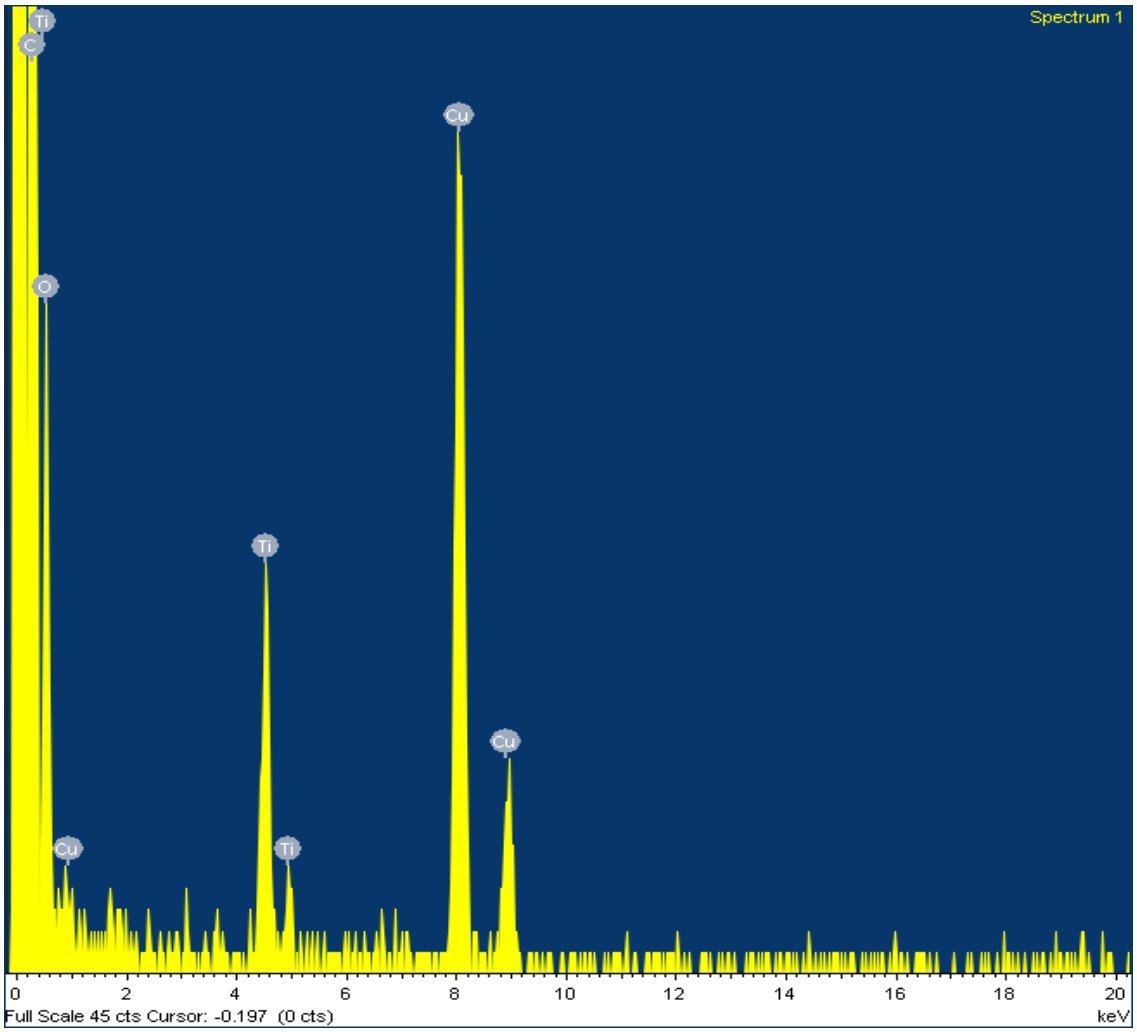

Figure 2.4 EDS spectrum showing the presence of Titania particles

As shown in figure 2.4, a spectrum was obtained using Energy Dissipative X-Ray Spectrometry (EDS), which asserted the presence of Titania particles in the grid.

2.3.3 Aggregate Image Analysis

(The detailed code for optimization and prediction of the most probable aggregate morphology and average properties was developed by Seongho Jeon, ME Department, University of Minnesota and only excerpts are given here on how the calculation is being done).

As is depicted in Figure 2.5 for a selected aggregate image, probable 3-dimensional structures for each aggregate projection were inferred as follows: First, an image (Figure 2.5 a) was loaded into Photoshop (Adobe), and the aggregate projection was manually cropped from the entire TEM image and placed on a white background (Figure 2.5 b). The aggregate image was then loaded into ImageJ (U.S. National Institute of Health) and by setting a grayscale threshold at 250 (note each grayscale pixel has a value from 0 to 255, where 255 is white and 0 is black) each pixel in the image was assigned a value of 0 if its grayscale value was above 250 and assigned a value of 1 if its grayscale value was less than or equal to 250. In this manner, three-dimensional arrays (x, y, α), where x and y are the spatial coordinates in an image and α is either 0 or 1, were generated and used to calculate specific parameters describing each observed aggregate. In conjunction array calculations, the average primary particle radius in each aggregate was determined via manual measurements with ImageJ. 20-30 visible primary particles were measured in each aggregate, and the projected area weighted mean primary particle radius ($a_{p,mean}$) was determined as:

$$a_{p,mean} = \frac{\sum_{i=1}^{N_{ob}} a_{p,i}^3}{\sum_{i=1}^{N_{ob}} a_{p,i}^2} \tag{12}$$

where N_{ob} is the number of observed and measured primary particles in an aggregate, and $a_{p,i}$ is the primary particle radius of observed primary particle i. The parameters subsequently determined for each image were the two dimensional radius of gyration ($R_{g,2D}$), the visible projected area (A_{vis}), the perimeter (P_L), and the longest pixel to pixel distance in the aggregate (L_{max}). $R_{g,2D}$ and A_{vis} were calculated using the equations:

$$R_{g,2D} = \left(\frac{\sum_{j=1}^{N_{\alpha=1}} (x_j - x_{cm})^2 + (y_j - y_{cm})^2}{N_{\alpha=1}} \right)^{1/2} \quad (13a)$$

$$A_{vis} = N_{\alpha=1} s_p^2 \quad (13b)$$

where j is an index over all pixels (x,y locations, Figure 2.5c) for which $\alpha = 1$, $N_{a=1}$ is the number of pixels where $\alpha = 1$, s_p is the side length of each pixel, and x_{cm} and y_{cm} are the x and y coordinates of the image's center of mass:

$$x_{cm} = \frac{\sum_{j=1}^{N_{\alpha=1}} x_j}{N_{\alpha=1}} \quad (13c)$$

$$y_{cm} = \frac{\sum_{j=1}^{N_{\alpha=1}} y_j}{N_{\alpha=1}} \quad (13d)$$

P_L was determined (Figure 2.5d) as the product of s_p and N_b, the number of pixels in an aggregate found to be on the aggregate's boundary, identified by having $\alpha = 1$ and with at least one neighboring pixel with $\alpha = 0$. L_{max} for each aggregate was determined (Figure 2.5e) by calculation of the scalar distance between all pixels in a given aggregate and was equated with the maximum scalar distance obtained.

$R_{g,2D}$, A_{vis}, P_L, and L_{max} were each non-dimensionalized to give four parameters describing an aggregate: $C_1 = R_{g,2D}/a_{p,mean}$, $C_2 = A_{vis}/\pi a_{p,mean}^2$, $C_3 = P_L/a_{p,mean}$, & $C_4 = L_{max}/a_{p,mean}$. In determining each parameter it was critical to mitigate the influence of non-infinitesimal pixel length on calculation; pixel lengths of approximately 1/15 the primary particle radius were found in most images, which we found to minimally influence C_1 - C_4.

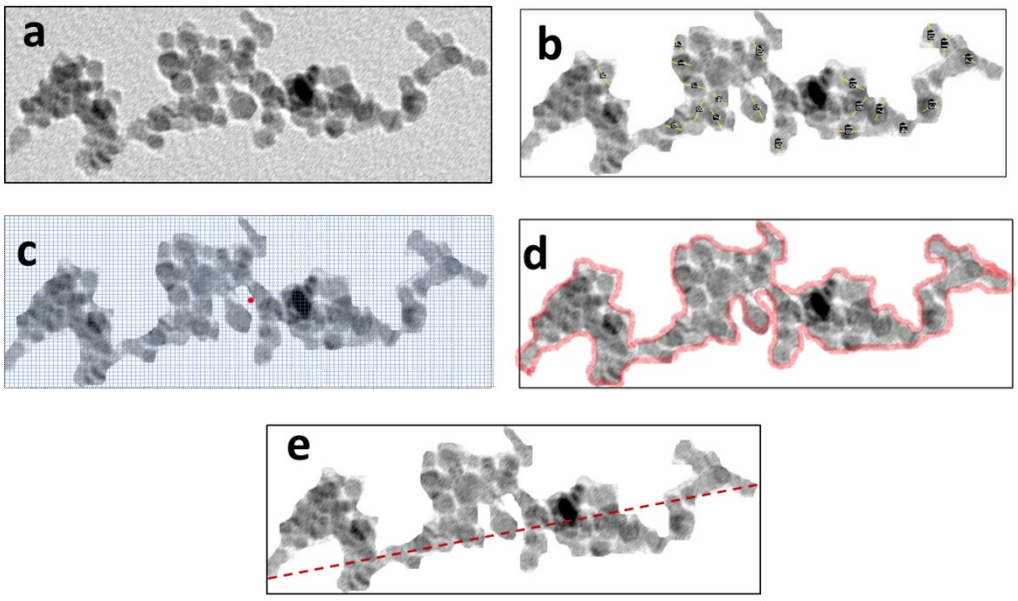

Figure 2.5. (a.) A TEM image of an aggregate transmitted through the DMA with the mobility equivalent diameter set to 80 nm. (b.) A depiction of the same aggregate on a white background, with marks denoting the primary particles measured. (c.) A depiction of a pixelated image of the aggregate (though with coarser pixels than actually employed), and a red dot denoting the aggregate projection's center of mass. (d.) A depiction of the perimeter of the aggregate projection. (e.) A depiction of the longest end-to-end distance in the aggregate projection.

2.3.4 Aggregate Mobility and Mobility Diameter Prediction

The database (*put together by Seongho Ieon*) reconstructed probable structures for aggregates by comparing C_1-C_4 values for computationally generated aggregates to those found with TEM images. Candidate aggregate geometries were constructed by assuming that aggregates were composed of primary particles with identical radii, in point-contact with one another and with morphologies obeying equation (3). In the N_p = 10-1000, D_f = 1.5-2.5, and k_f = 1.2 – 2.0 ranges, aggregates were generated using the cluster-cluster algorithm described by Filippov et al(Filippov, Zurita et al. 2000). In the same N_p and k_f ranges but with D_f = 1.3 and 2.7, candidate aggregates were similarly generated with the sequential algorithm, also described by Filippov et al. In total, >16,000 aggregates with varying N_p, D_f, and k_f were generated, with ~10 replicates for

each prescribed N_p, D_f, k_f, as the aggregate generation algorithms both produce random structures.

Equation (8) suggests that the mobility of an aggregate (and hence its electrical mobility and mobility diameter) is dependent on the background gas conditions (μ and λ), a particle's hydrodynamic radius (R_H), and its orientationally averaged projected area (PA). Mobility classification was performed in air near room temperature and atmospheric pressure, for which μ = 1.98 x 10^{-5} Pa*s, and λ = 66.5 nm. For all computationally generated aggregates, a primary particle normalized R_H was determined by invoking the Hubbard-Douglas approximation (Hubbard and Douglas 1993; Zhou, Szabo et al. 1994) and equating it with each aggregate's Smoluchowski radius/capacity. Primary particle normalized orientationally averaged projected areas for aggregates were also calculated using algorithms described previously(Hubbard and Douglas 1993; Larriba and Hogan 2013). R_H and PA were calculated using the precise geometry of each aggregate; formulae linking these parameters to quasifractal descriptors(Lattuada, Wu et al. 2003) were not employed. Moreover, the constraint of quasifractal morphologies for computationally generated aggregates was only used to aid in producing aggregates with a wide range of morphologies, i.e. the examination of the validity of equation (1) does not only apply to quasifractal aggregates.

Three orthogonal projections of each aggregate were then examined (i.e. computationally deposited) to determine C_1-C_4 with a similar pixel side length to primary particle radius ratio as was observed in images. To compare to TEM images, for each projection the square error (E_k) was calculated as:

$$E_k = \sum_{i=1}^{4} \left(\frac{C_{i,image} - C_{ik}}{C_{i,image}} \right)^2 \tag{14a}$$

where the subscript "*image*" denotes the parameters calculated from a TEM image. Two candidate aggregate morphologies were subsequently examined for each image. First, the "most probable" aggregate morphology was inferred as that which had a projection leading to the minimum value of E_k for all aggregates. Second,

dimensionless $R_{H,ave}$, and PA_{ave}, were determined for an "average aggregate" with the equations:

$$R_{H,ave} = \frac{\sum_{k=1}^{n_{proj}} R_{H,k} exp(-bE_k)}{\sum_{k=1}^{n_{proj}} exp(-bE_k)} \quad (14b)$$

$$PA_{ave} = \frac{\sum_{k=1}^{n_{proj}} PA_k exp(-bE_k)}{\sum_{k=1}^{n_{proj}} exp(-bE_k)} \quad (14c)$$

where b is a bias factor empirically set to 300, though values between 100-500 change results by ~2%. The properties of both the most probable and average aggregate were used for mobility calculations with equation (8) and comparison to the DMA settings under which each aggregate was transmitted.

2.4 Results and Discussion

2.4.1 TiO_2 Mobility Based Size Distribution Functions

Mobility classified particle collection was performed on two separate days, both on which size distribution functions were highly polydisperse with peak mobility diameters slightly above 60 nm. SMPS inferred size distribution functions without correction for multiply charged particles are shown in Figure 2.6. Multiple charge correction was not employed to these results because (1) when the DMA was operated to transmit particles in a narrow mobility range, it transmitted both singly and multiply charged particles, (2) multiple charge correction requires measurement of larger mobility diameters (lower mobilities) than were accessible with the DMA operated as noted, and (3) recent computations suggest that the multiple charge correction necessary for not only aggregates(Gopalakrishnan, Meredith et al. 2013), but also spheres(López-Yglesias and Flagan 2013), may differ slightly from what is conventionally used(Wiedensohler 1988). Also displayed in Figure 2.6 are the approximate classification windows of the DMA, assuming a near triangular mobility DMA transfer function(López-Yglesias and Flagan 2013) when set to maximally transmit particles of mean mobility diameters 45 nm, 70 nm, and 80 nm with the first size distribution, and

50 nm, 60 nm, and 75 nm with the second size distribution. Clearly apparent is that the widths of the DMA classification windows are not negligible; a collected and imaged aggregate's electrical mobility may fall within +/- 12% of the maximally transmitted electrical mobility.

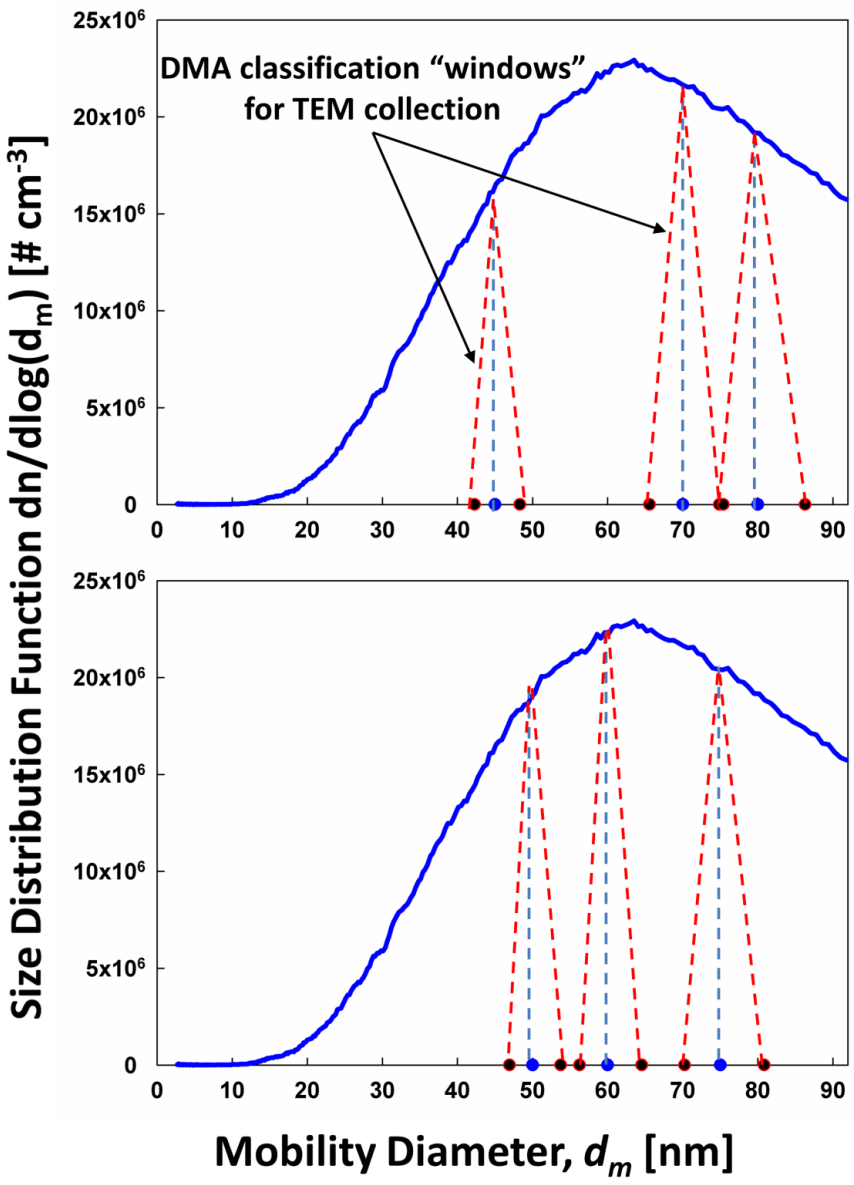

Figure 2.6. Size distribution functions of the produced TiO_2 aggregates. The singly charged mobility diameter transmission windows employed are also depicted.

2.4.2 Comparison between DMA-Selected and Image Inferred Electrical Mobilities

Results of the analysis of four TEM images are provided in Figure 2.7. Specifically, for each TEM image, the average primary particle radius from equation (12) is listed, and a depiction and the quasifractal descriptors of the most probable (minimum E_k) aggregate as well as the average aggregate are displayed. The properties of the latter were determined via the equations:

$$D_{f,ave} = \frac{\sum_{k=1}^{n_{proj}} D_{f,k} exp(-bE_k)}{\sum_{k=1}^{n_{proj}} exp(-bE_k)} \quad (15a)$$

$$k_{f,ave} = \frac{\sum_{k=1}^{n_{proj}} k_f exp(-bE_k)}{\sum_{k=1}^{n_{proj}} exp(-bE_k)} \quad (15b)$$

$$N_{p,ave} = \frac{\sum_{k=1}^{n_{proj}} N_p exp(-bE_k)}{\sum_{k=1}^{n_{proj}} exp(-bE_k)} \quad (15c)$$

Equation (15c) results were rounded to the nearest multiple of 5 primary particles for construction of the average aggregate via the cluster-cluster algorithm. The quasifractal descriptors of the most probable aggregate and the average aggregate are similar to one another, and qualitatively, their projections are similar to those observed in TEM images. These similarities are not unique to the Figure 2.7 depicted images; they found for all analyzed aggregates. Tables A.1 & A.2 of the Appendix information list for each examined TEM image the prescribed singly charged mobility diameter at which the DMA was set during collection, the average primary particle radius for the aggregate, and the quasifractal descriptors of the aggregates for the most probable and average aggregates, respectively.

Also displayed in Tables A.1 and A.2 are the hydrodynamic radii (nm), the projected areas (nm^2), and the Knudsen numbers for the most probable aggregates and average aggregates. These values enable calculation of the expected mobilities for these aggregates, via equation (8). Unfortunately, for comparison to DMA measurements, as noted by Rogak et al(Rogak, Flagan et al. 1993), it is necessary to

"fit" a charge state value, z, for each aggregate, such that its electrical mobility can be calculated. First assuming that $z = 1$ for all imaged aggregates, direct comparison is made with the mobilities of DMA transmitted particles to those calculated from TEM images. Using the properties of the most probable aggregates, this comparison is shown in Figure 2.8a, which is a plot of $1/B$ from equation (1) as a function of $1/zB$ at the point of maximum transmission (the midpoint) in the DMA classification window. Also shown on this plot are a 1:1 guideline (black), 0.9:1 & 1.1:1 guidelines (dark gray), and 0.8:1 & 1.2:1 guidelines (light gray).

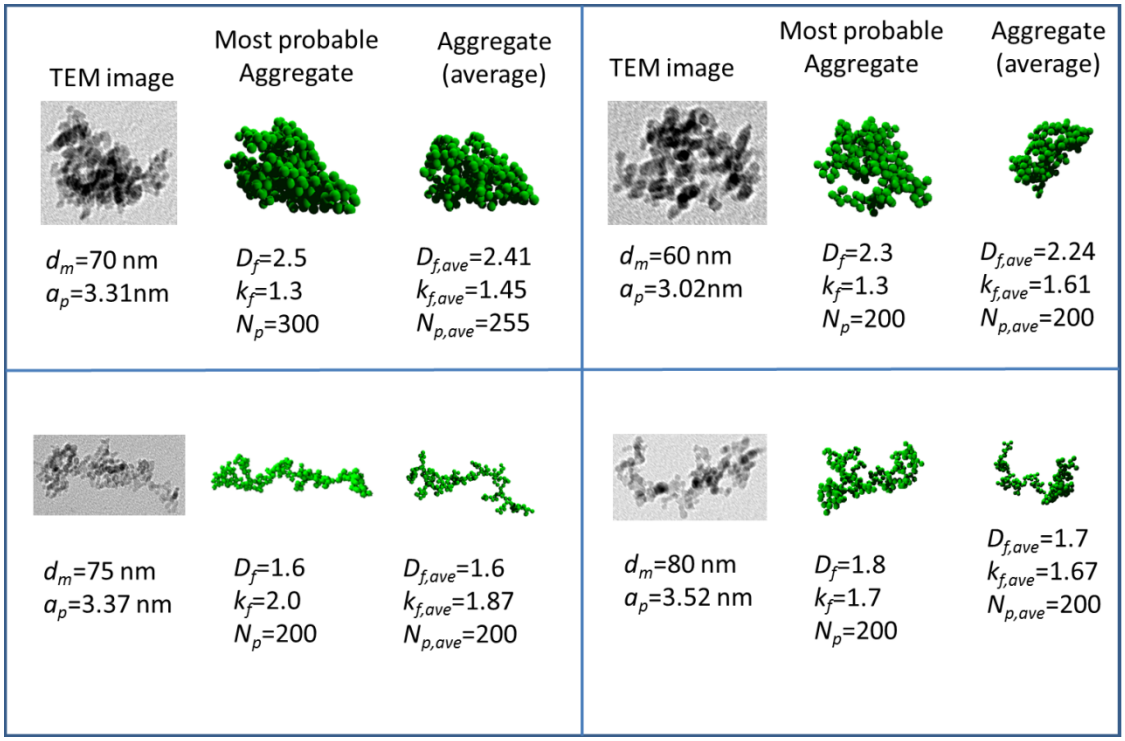

Figure 2.7. Examples of image analysis results, with the quasifractal descriptors of the most probable and average aggregates provided.

While many results are close to the 1:1 guideline or bounded by the other guidelines, at the smallest $1/zB$ values plotted (lower mobility diameters), disagreement is evident. This suggests that many collected and imaged aggregates were multiply charged, which must be considered in comparison. A priori, it is expected that many of the aggregates imaged at the smaller DMA selected mobility diameters (higher

electrical mobilities) would carry multiple charges. The peak mobility diameters in the SMPS size distribution functions were larger than 60 nm; thus, the number of multiply charged particles may be comparable in concentration to the singly charged particle concentration at higher electrical mobilities.

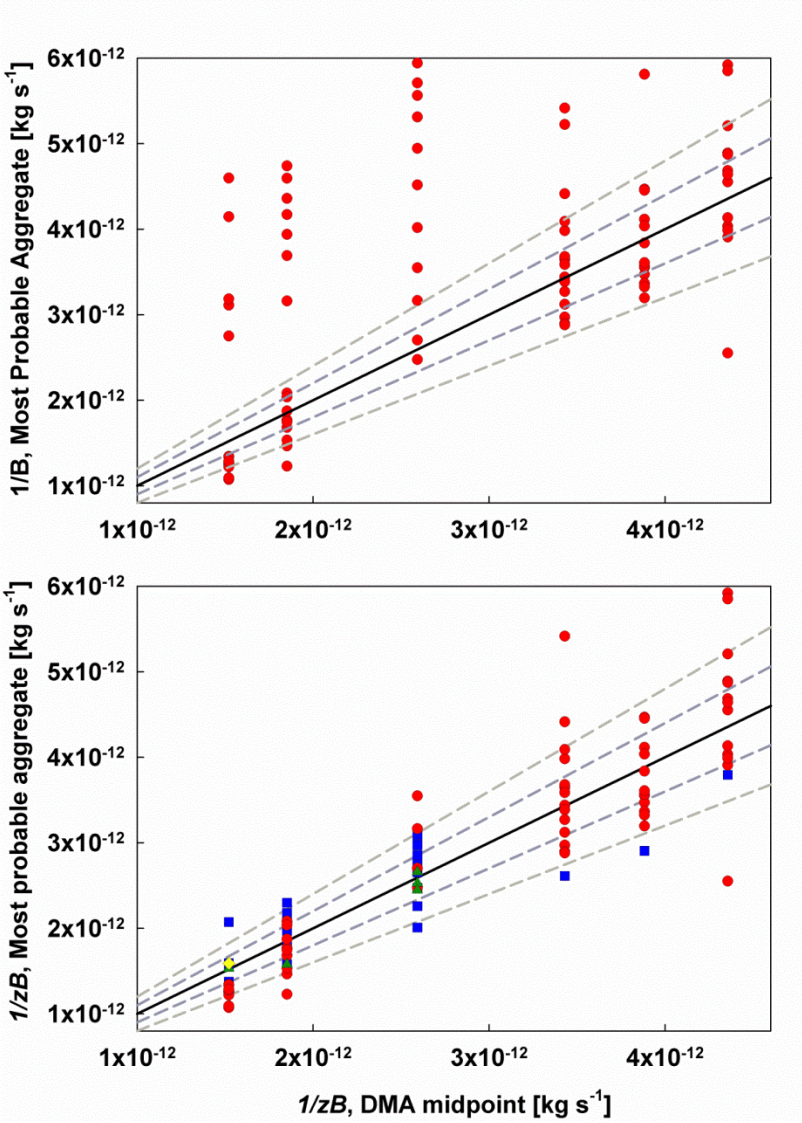

Figure 2.8. A comparison of the *1/zB* values to *1/zB* inferred for the most probable aggregate structures with (a.) $z = 1$ assumed and (b.) best fit z values. Circles: $z = 1$; Squares: $z = 2$; Triangles: $z = 3$; Diamonds: $z = 4$.

Rather than assume $z = 1$ for all aggregates, by fitting a z value for each TEM examined aggregate, $1/zB$ for the most probable aggregates as a function of the DMA midpoint $1/zB$ values is replotted in Figure 2.8b. With this fitting, the correction to the data is modest; most aggregates appear singly charged, the majority of multiply charged aggregates appear doubly charged, and only one aggregate of the 92 examined has a fit value of $z = 4$. Fitting additionally brings the $1/zB$ values for the most probable aggregate structures in remarkably good agreement with expectations for the DMA settings employed. Results are centered upon the DMA midpoint $1/zB$ value, and most of the scatter observed can be attributed to the width of the DMA transfer function. This finding is in good agreement with those of Gopalakrishnan et al(Gopalakrishnan, McMurry et al. 2013), who made similar comparisons of the equation (1) mobilities/friction factors of gold nanorods of clearly defined dimensions to those expected to be transmitted by a DMA, and were able to nearly reproduce DMA transfer functions from histograms of equation (1) predictions. Overall, it is found that results support both the use of equation (1) for aggregate mobility calculation and for the use of noted image analysis approach to reconstruct probable three-dimensional aggregate structures.

2.4.3 Comparison to Alternative Aggregate Analysis Approaches

It can be safely assumed that equation (8) is reasonably valid in describing the mobility of flame synthesized aggregates, as its use is supported well by the performed measurements. What remains is to compare the mobilities of the most probable aggregates to those for the average aggregates, as well as the expected mobilities using previously employed analysis techniques. Prior to making such comparison, it is noted that for many of the most probable and average aggregates inferred from images, $PA < \pi R_S^2$, such that these aggregates' mobility diameters are expected to depend on background gas conditions (μ and λ). The examined aggregates also had average primary particle radii below 5 nm, and defining a Kn based solely on the primary particle radius, as has been incorrectly performed in the past(Lall and Friedlander

2006), would suggest (erroneously) that equation (1) could be replaced by a free molecular mobility expression. Finally, while in image analysis comparison is to quasifractal aggregates structures, a range of k_f (1.21-2.00) and D_f (1.44-2.55) values were obtained for the most probable and average aggregates, suggesting that models assuming constant quasifractal descriptors for all aggregates may satisfactorily describe flame synthesized aggregates under all circumstances.

To compare the mobilities of the most probable aggregates to the average aggregates, all equation (8) determined mobilities are converted to mobility diameters via equation (9), which are listed in Tables A.1 and A.2. This also facilitates comparison to several proposed aggregate mobility diameter expressions. First, the expression advocated by Lall & Friedlander(Lall and Friedlander 2006) as well as by Wang et al(Wang, Shin et al. 2010), and based upon Chan & Dahneke's(Lall and Friedlander 2006) analysis of straight chain aggregates in the free molecular regime is given as:

$$\frac{d_{m,LF}}{1+\frac{2\lambda}{d_{m,LF}}\left(1.257+0.4exp\left(\frac{-0.55d_{m,LF}}{\lambda}\right)\right)} = \frac{c^* N_p a_{p,mean}^2}{3\pi\lambda} \tag{16a}$$

where c^* is a constant dependent upon the extent of diffuse versus specular gas molecule scattering upon collision with an aggregate's surface, and equal to 9.17 to align with the results of the Millikan oil drop experiments(Millikan 1923). Second, Eggersdorfer et al(Eggersdorfer, Grohn et al. 2012), also assuming that the mobility of an aggregate is well described by free molecular expressions, proposed use of the relationship:

$$d_{m,E} = 2a_{p,mean}\left(\frac{N_p}{k_\alpha}\right)^{\frac{1}{2D_\alpha}} \tag{16b}$$

where k_α = 1.1 and D_α = 1.08, both of which are based on results of diffusion limited cluster aggregation (DLCA) simulations. While Eggersdorfer et al find good agreement between equation (16b) and the mobility diameters of flame made zirconia aggregates, algebraic manipulations with (16b) lead to a relationship between the mobility diameter,

primary particle radius, and aggregate volume (equation (A8) of Eggersdorfer et al(Eggersdorfer, Grohn et al. 2012)), wherein for all possible values of D_α, considering two aggregates of equivalent volume, the aggregate of larger mobility diameter must be composed of smaller primary particles (note D_α is bounded by $1.0 < D_\alpha < 1.5$, with the lower limit a straight chain and the upper limit near spherical). This conclusion is reasonable for aggregates of similar morphology; it is not necessarily valid for two aggregates that are structurally distinct. Third, there is comparison to the TEM image projected area diameter d_A, as was used by Rogak et al(Rogak, Flagan et al. 1993) and is calculated with the equation:

$$d_A = 2\left(\frac{A_{vis}}{\pi}\right)^{\frac{1}{2}} \tag{16c}$$

A_{vis} values for all aggregates are provided in Table A.1. The mobility diameter based on average aggregate properties in image analysis, the equation (16a) mobility diameter, the equation (16b) mobility diameter, and d_A are plotted for all analyzed aggregates in Figure 2.9. For equation (16a) & (16b), results are shown using both the parameters for the most probable aggregates. A 1:1 guideline is also provided.

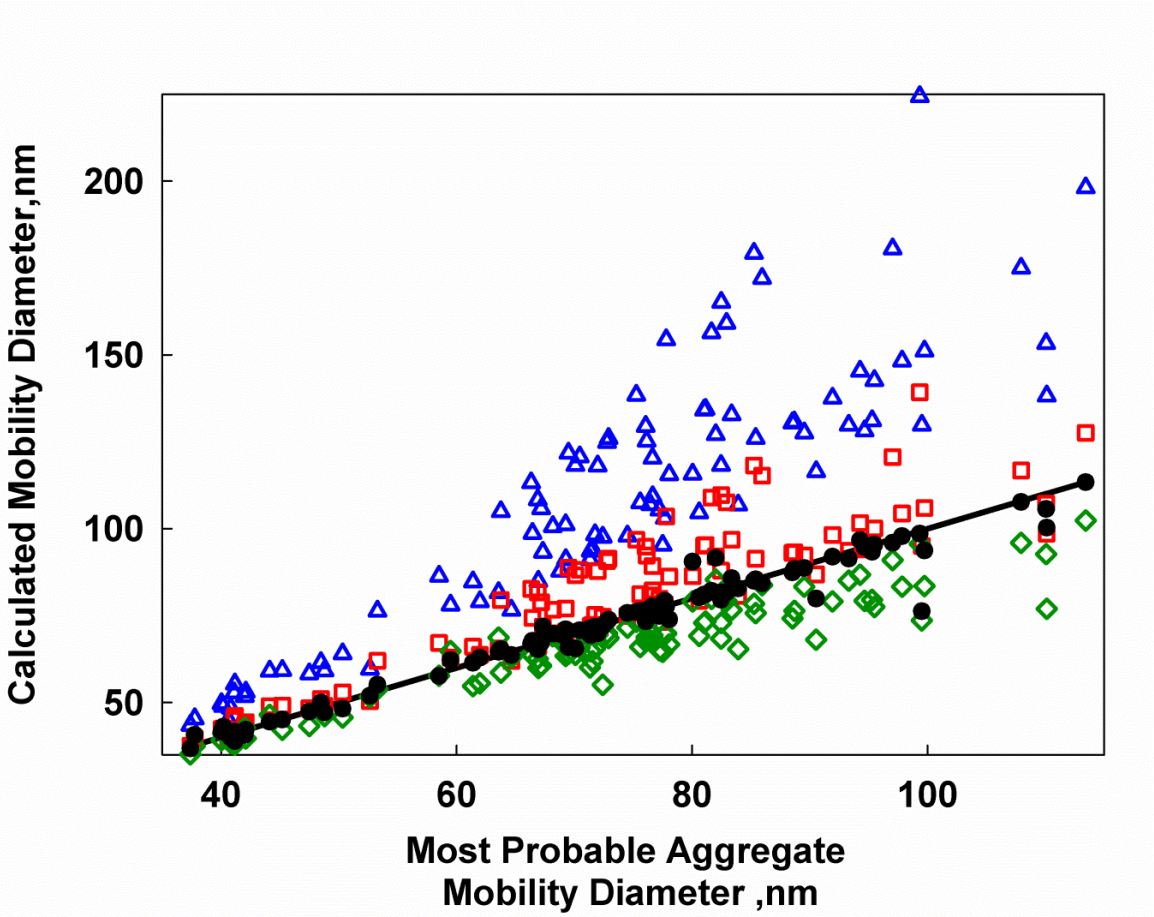

Figure 2.9. A comparison of the mobility diameter calculated by various methods to the mobility diameter calculated for the most probable aggregates. Closed circles: the average aggregate mobility diameters; triangles: equation (16a); squares: equation (16b); diamonds: equation (16c).

With few exceptions, the mobility diameter inferred for the average aggregate is in excellent agreement with the mobility diameter of the most probable aggregate, indicating that the use of either in TEM image analysis enables estimation of an aggregate's hydrodynamic radius and projected area. Reasonable agreement is also found with equation (16b) & (16c) determined mobility diameters at the smallest mobility diameter particles. At larger mobility diameters, equation (16b) predictions are slightly higher than the mobility diameter of the most probable aggregate, while equation (16c) predictions are slightly lower. The former result presumably arises

because equation (16b) applies only to DLCA-like aggregates in the free molecular regime, while the aggregates analyzed here (and likely many flame synthesized aggregates) are found to be slightly denser (higher in k_f and D_f) than DLCA-like aggregates ($k_f = 1.3$, $D_f = 1.8$). Conversely, the latter clearly arises because for all aggregates $\pi R_H^2 > PA$, leading to a monotonic increase in the mobility diameter in the transition regime, an influence which is not captured when equating the mobility diameter and the observed projected area equivalent diameter. However, the disagreement between the projected area equivalent diameter and the mobility diameter is slight in most circumstances, hence the results are not in stark disagreement with those of Rogak et al(Rogak, Flagan et al. 1993).

Unlike the slight disparities found between image inferred mobility diameters and those from equations (16b) & (16c), above 50 nm, equation (16a) calculations differ drastically from these results. This difference arises from the fact that except in rare circumstances, it is a poor assumption to model aggregates as straight chains with mobilities equivalent to their free molecular values. In fact, near straight chains are only observed in systems where particles aggregation in an aligned fashion, e.g. when particles are magnetized (Kasper 1982; Kasper and Shaw 1982; Zimmer and Biswas 2001). This finding is particularly noteworthy in light of recently commercialized instruments designed to infer aggregate primary particle size where equation (16a) is embedded into the data analysis procedure (Wang, Shin et al. 2010; Liu, Kim et al. 2012).

As a final comparison between these results and prior analysis approaches, using the most probable aggregates, the inferred aggregate volume (the product of the number of primary particles determined and the mean primary particle volume) is plotted as a function of the aggregate mobility diameter in Figure 2.10.

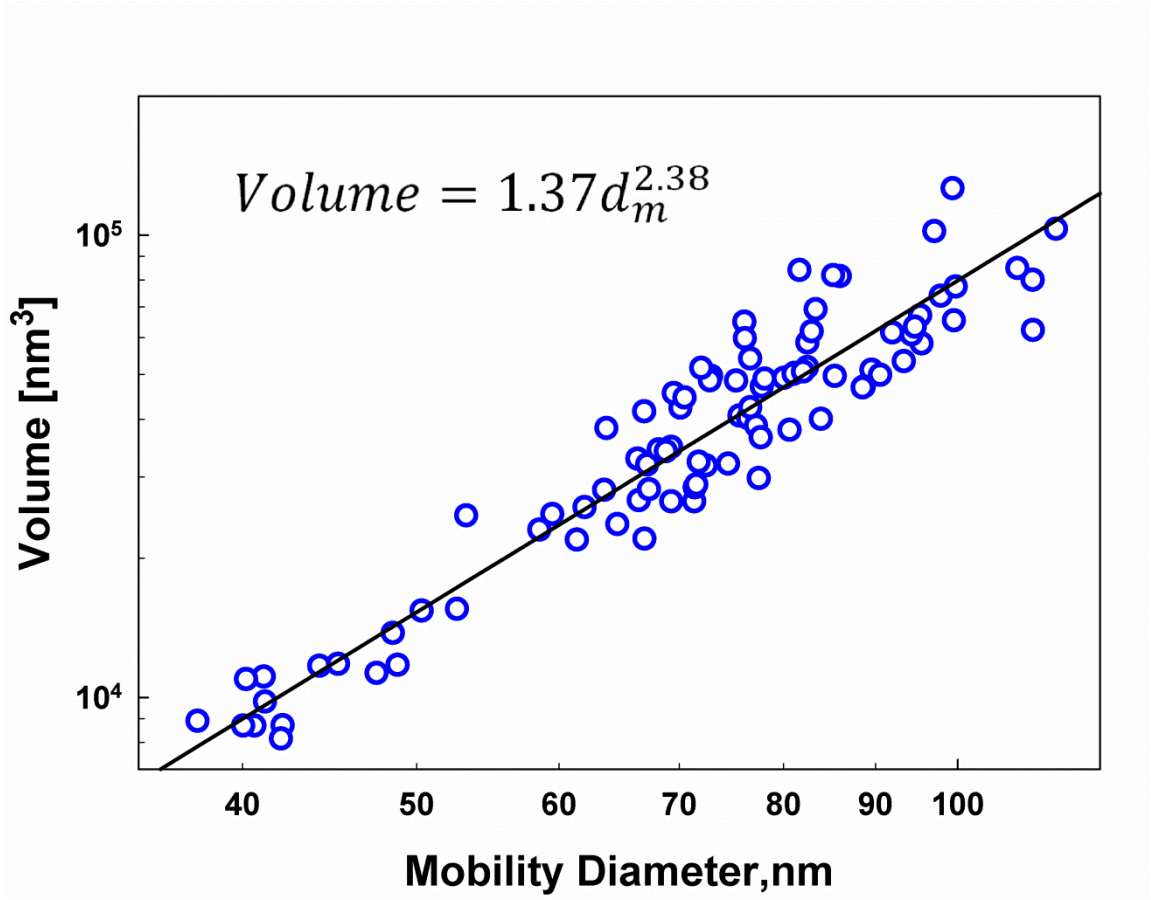

Figure 2.10. The inferred volumes of the most probable aggregates as functions of their mobility diameters. A power-law regression equation to results is also provided.

A power law scaling between aggregate mass/volume and the mobility diameter has been observed(Weber, Baltensperger et al. 1996; Scheckman, McMurry et al. 2009; Eggersdorfer, Grohn et al. 2012; Shapiro, Vainshtein et al. 2012) and used to suggest that aggregates of near constant fractal dimension are produced in most flame synthesis processes. However, image analysis reveals aggregates with a wide range of fractal dimensions and pre-exponential factors, yet their inferred volumes scale well their mobility diameters, yielding $volume = 1.37d_m^{2.38}$ (plotted black line). Such a scaling relationship can exist (at least in a particular mobility diameter range) without all aggregates having the same quasifractal descriptors. Presumably, this scaling

relationship arises statistically simply because (1) volume and mobility diameter show a positive correlation almost without exception, and (2) most measurements of the aggregate volume-mobility diameter relationship are taken only over an order of magnitude in mobility diameter, which is likely insufficient to detect any deviation from a power law dependency. As noted by Sorensen(Sorensen 2011), when the volume-mobility diameter relationship is known it enables estimation of one of these parameters from measurement of the other, but aside from this, the results extracting detailed structural information from the values of both the pre-exponential and power law terms does not appear tractable.

2.5 Conclusions

Results support the validity of equation (8) to determine the mobilities of aggregates in the transition regime at intermediate *Kn*, as the equation (8) calculated mobilities for the obtained three dimensional structures are in good agreement with mobilites inferred from DMA operating conditions. Unlike prior examinations by flame synthesized aggregate structures, image analysis suggests that aggregates with a wide range of quasifractal descriptors can be generated in a single flame synthesis reactor, and for most of these aggregates, the assumptions invoked in Lall & Friedlander's(Lall and Friedlander 2006) approach to aggregate mobility analysis are not valid. In spite of the range of morphologies observed, reconstructed aggregate volumes are found to scale with their mobility diameters. In total, this study provides a clearer examination of theoretical mobility expressions applicable in the transition regime to measurements than has been performed previously. While image analysis, as performed here, may be employed in future studies of aggregates to infer their mobilities, it is not an online measurement. It is recommended that online aggregate measurement methods continue to be developed, but with the transition regime nature of gas molecule aggregate interactions considered, as opposed to the use of expressions only valid in a limited number of circumstances.

Chapter 3: Determination of Collision Kernel for Arbitrarily Shaped Particles across the Entire Diffusive Knudsen Number Regime

Abstract: This chapter deals with the calculation of collision kernel to calculate the collision rate between arbitrarily shaped particles across, the entire Diffusive Knudsen number regime. Two different geometric length scales are defined that can be used to predict the collision rate between a pair of colliding entities taking into account the shape and size of both the colliding entities. Attempt is made at developing regression equations to calculate these size descriptors as well.

3.1 Introduction

The growth of non-spherical aerosol particles via particle-particle collisions is difficult to examine theoretically, as collision dynamics are governed by both gas molecule to particle momentum transfer, and particle to particle mass transfer. For particles in the sub micrometer and nanometer size ranges in atmospheric pressure environments, or for micrometer sized particles in reduced pressure environments, both momentum and mass transfer processes occur in the transition regime, with the rates of transition regime momentum transfer and mass transfer functions of the Knudsen number (*Kn*, the ratio of the gas molecule mean free path to particle length scale) and diffusive Knudsen number (Kn_D, the ratio of the particle-particle mean persistence distance to the collision length scale) (Dahneke 1983), respectively. Knudsen number calculations require a priori knowledge of the appropriate length scales for gas molecule-particle collisions and particle-particle collisions. However, neither of these length scales have been clearly identified for non-spherical particles (Schmidt-Ott, Baltensperger et al. 1990), nor are they necessarily identical for *Kn* and Kn_D (Zurita-Gotor and Rosner 2002).

Despite this complexity, collisional growth of non-spherical particles plays an important role in many aerosol systems, particularly those in which aggregates form and

evolve (Maricq 2007; Chakrabarty, Moosmuller et al. 2009; Sorensen and Chakrabarti 2011), and for this reason analysis of non-spherical particle collision dynamics is often necessary. Colliding entities are sufficiently dilute and well-mixed in most aerosol systems, such that the collision rate for two non-spherical particles of type i and type j can be expressed as:

$$R_{ij} = \beta_{ij} n_i n_j \quad (1)$$

where R_{ij} is the number of collisions per unit volume of space per unit time, n_i and n_j are the number concentrations of type i and type j particles, respectively, and β_{ij} is the collision kernel. The complications of non-spherical particle momentum and mass transfer are locked within the collision kernel function, and there have thus been several prior efforts to develop an expression for this function for non-spherical particles, with a specific focus on aggregates composed of a number of point contacting primary spheres. In examining such aggregates, Sorensen and coworkers have assumed that the collision kernel is a homogenous function, and attempted to determine the collision kernel homogeneity factor both experimentally (Wang and Sorensen 2001) and theoretically (Pierce, Sorensen et al. 2006). Their analyses, however, do not account for the non-continuum nature of the collision process, i.e. they neglect Kn_D dependencies. To account for non-continuum mass transfer, Rogak & Flagan (Rogak and Flagan 1992) used Dahneke's transition regime collision kernel expression (Dahneke 1983) as a basis for an expression for aggregates. Required in their proposed expression are appropriate length scales for the Knudsen number and the diffusive Knudsen number. While some theoretical justification is provided for the length scales selected, further examination is necessary to determine validity of the choices made. More recently, Cho et al (Cho, Chung et al. 2011) examined the collision kernel for aggregates in a manner similar to Rogak and Flagan (1992), only differing in their use of Fuchs's transition regime collision kernel (Fuchs 1964) and of simpler expressions for the length scales used in Knudsen number definition. Using Brownian Dynamics simulations, Gutsch et al (Gutsch, Pratsinis et al. 1995) attempted to determine the collision kernel for monomer spheres with aggregates across the entire Kn_D range. Unfortunately, their inferred

collision kernels for spherical particles are substantially below the $\beta_{ij}(Kn_D)$ found both theoretically and experimentally elsewhere (Fuchs 1964; Wagner and Kerker 1977; Veshchunov 2010), drawing the conclusions of this work into question. To this date, the most theoretically rigorous examination of non-spherical aerosol particle collisions seems to be the work of Zurita-Gotor & Rosner (2002), who determined the appropriate collision area for the collision kernel in the mass transfer free molecular regime ($Kn_D \rightarrow \infty$), accounting for the rotational energy of both particles. Outside the mass transfer free molecular regime, however, the equation they develop cannot be accurately applied.

In addition to the aforementioned limitations of prior work, non-spherical particle collisional growth in the transition regime and the important concept of the diffusive Knudsen number are both disregarded in several widely used introductory texts on aerosol science (e.g. (Hinds 1999; Friedlander 2000)). This study is thus motivated by the need to further examine collisional growth in aerosol systems with non-spherical particles in both the mass and momentum transfer transition regimes. In subsequent sections, collisional growth in the mass transfer continuum regime ($Kn_D \rightarrow 0$), free molecule regime ($Kn_D \rightarrow \infty$), and transition regime ($0<Kn_D<\infty$) is discussed theoretically for non-spherical particles, as is a combined dimensional analysis- mean first passage time simulation approach to infer the collision kernel in all regimes. This approach has been used successfully to analyze mass transfer transition regime sphere-sphere collisions (Hinds 1999), vapor molecule uptake by non-spherical particles (Friedlander 2000), and charged particle-ion collisions (Gopalakrishnan and Hogan 2012). The influence of transition regime momentum transfer on the collision process is incorporated into this analysis through the relationship examined in Chapter 2 for the orientationally averaged scalar friction factor of an arbitrarily shaped particle moving at low Reynolds number and low Mach number. This result of the analysis performed is a dimensionless expression for the collision kernel, which is applicable to non-spherical particles across the entire Kn and Kn_D ranges, and receives as inputs clearly defined and calculable length scales for the particles. While the developed

expression is applicable for particles of any morphology, detailed analysis is given for collisions specifically between quasifractal (statistically fractal) aggregates.

3.2 Theory and Numerical Methods

3.2.1. Mass Transfer Continuum Regime

In the mass transfer continuum regime, the Smoluchowski equation is commonly used to express the collision kernel between two spherical entities *i* and *j*, given as (Friedlander 2000):

$$\beta_{ij} = 4\pi kT\left(\frac{1}{f_i}+\frac{1}{f_j}\right)(a_i + a_j) \qquad \text{as } Kn_D \rightarrow 0 \tag{2}$$

where k is Boltzmann's constant, T is the background gas temperature, f_i and f_j are the scalar friction factors, and a_i and a_j are the radii of particle's i and j, respectively. Additionally, f_{ij} is defined as the reduced friction factor (Gopalakrishnan and Hogan 2012), calculated from the equation $1/f_{ij} = 1/f_i + 1/f_j$. To adapt equation (2) for collisions between two non-spherical entities, it is clear that the friction factors must be appropriately defined, as must an appropriate length for the collision in lieu of a_i+a_j (Ziff, McGrady et al. 1985). Described in Chapter 2, the orientationally averaged scalar friction factor of an arbitrarily shaped particle i can be expressed by the equation:

$$f_i = \frac{6\pi\mu R_{S,i}}{1+Kn_i\left[1.257+0.4exp\left(^{-1.1}/_{Kn_i}\right)\right]} \tag{3a}$$

$$Kn_i = \frac{\lambda\pi R_{S,i}}{PA_i} \tag{3b}$$

where μ is the dynamic viscosity of the background gas, λ is the (hard sphere) gas mean free path, Kn is the Knudsen number for momentum transfer, $R_{S,i}$ is the Smoluchowski radius for particle i, and PA_i is particle i's orientationally averaged projected area. Both $R_{S,i}$ and PA_i are purely geometric properties of an object (Gopalakrishnan, Thajudeen et al. 2011), and there are algorithms available to calculate both $R_{S,i}$ (referred to also as the Capacity) (Douglas, Zhou et al. 1994; Zhou, Szabo et al. 1994; Given, Hubbard et al. 1997) and PA_i accurately for arbitrarily shaped entities and are explained in detail in Chapter 2. Use of equations (3a-b) to describe particle motion accounts entirely for

non-continuum effects on particle drag; thus, it is valid across the entire *Kn* range. However, any hydrodynamic interaction between entities as they collide (Alam 1987; Gopinath and Koch 1999; Chun and Koch 2006) is neglected in these equations.

To then account for the influence of non-spherical particle geometry on the collision length scale, equation (2) is rewritten as:

$$\beta_{ij} = 4\pi \frac{kT}{f_{ij}} R_{S,ij} \tag{4}$$

where $R_{S,ij}$ is the combined Smoluchowski radius for the collision of particles *i* and *j*. Like the Smoluchowski radius for a single entity, the combined Smoluchowski radius for the collision two particles can be calculated using Brownian Dynamics approaches which derive from procedures used in biophysics to study bimolecular reaction rates in solution (Northrup, Allison et al. 1984; Gopinath and Koch 1999; Chun and Koch 2006). A schematic describing the Brownian Dynamics procedure adopted here is shown in Figure 3.1a, in which particle rotation during collision is neglected. To use this algorithm, the boundaries of the two non-spherical particles under examination must be clearly described mathematically. One of the particles (henceforth referred as particle *i*) is placed at a random orientation with its center of mass at the center of a sphere of radius R_{outer}, which is large enough to completely enclose both particles (though it does not completely enclose both entities throughout the entire simulation). The second particle, particle *j*, is oriented randomly with its center of mass at a random location on the surface of the outer sphere. Particle *j* is then moved via diffusive first passage motion (Kim and Torquato 1991; Given, Hubbard et al. 1997; Thajudeen and Hogan 2012), which is accomplished in two steps. First, another sphere is formed, with its center at particle *j*'s center of mass and its radius defined by the minimum distance particle *j* needs to move to reach point contact with particle *i*. Second, particle *j* is moved to a random location on the surface of this formed sphere. If, after the first passage step, the center of mass of particle *j* is a distance less than R_{outer} from the center of particle *i* but the distance between the edges of both particles is greater than a prescribed distance Λ (0.1% of the local radius of curvature, i.e. the primary particle radius in the case of aggregates), particle *j* is again moved via first passage motion and

procedure continues until the edge to edge distance between the two particles is less than Λ. At this point the two particles are considered to have collided, particle i and particle j are placed at the center and on the surface of the large sphere, respectively, again with randomly chosen orientations, and the process is repeated.

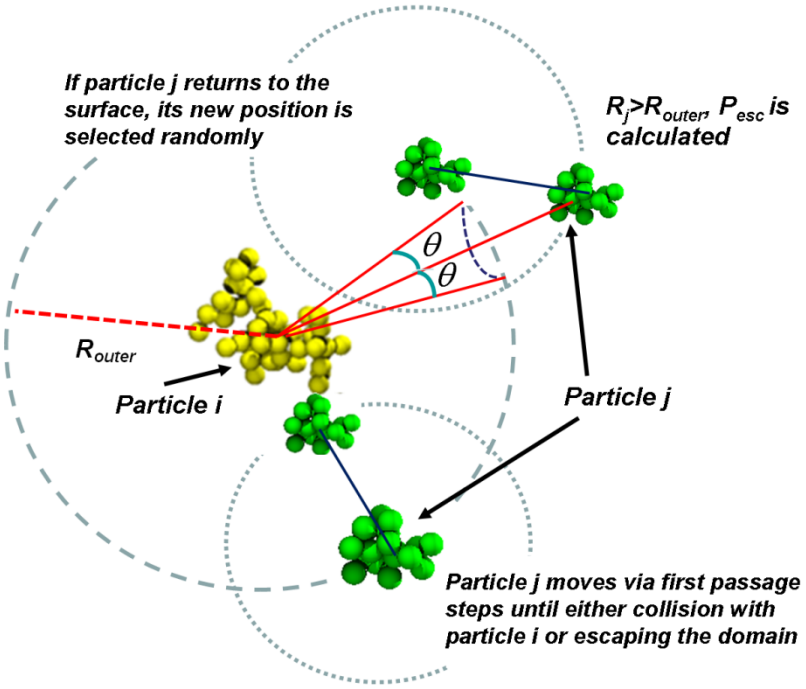

Figure 3.1a. Schematic of the procedure used for Smoluchowski radius calculation for a colliding pair of particles.

However, if, at any time particle j reaches a point at which its center of mass is a distance R_j from the calculation domain center which greater is than R_{outer}, then the probability that particle j will escape the simulation domain entirely rather than return to the outer sphere surface, P_{esc}, is calculated as:

$$P_{esc} = 1 - \frac{R_{outer}}{R_j} \tag{5}$$

A random number is generated from a uniform distribution between 0 and 1; if this number is less than P_{esc} then particle j leaves the calculation domain without colliding with particle i, and calculation procedure is reset and repeated. Finally, if the random

number is greater than P_{esc}, then particle j is returned to the calculation domain with its center of mass placed on R_{outer} with its specific location determined by sampling from the equation (Luty, McCammon et al. 1992):

$$w(\theta) = \frac{2P_{esc} - P_{esc}^2}{4\pi\left[2(1-P_{esc})(1-\cos(\theta)) + P_{esc}^2\right]^{3/2}} \quad (6)$$

where θ is the angle noted in Figure 1a, and w is the probability distribution density for particle j returning to R_{outer} at θ. As all points with a specific θ define a circle on the surface at R_{outer}, to identify the precise point to which particle j returns, a second angle ϕ is sampled randomly from a uniform distribution (once a θ value is identified all points on the circle are equally probable). Particle j again moves via diffusive first passage motion (Kim and Torquato 1991; Luty, McCammon et al. 1992) once returning to R_{outer}. Each portion of this calculation results either in particle j colliding with particle i, or particle j leaving the calculation domain. If N_{col} is the number of collisions between i and j and N_{miss} is the number of instances where particle j leaves the simulation domain, then the combined Smoluchowski radius for i and j can be calculated as:

$$R_{S,ij} = \frac{N_{col}}{N_{col} + N_{miss}} R_{outer} \quad (7)$$

3.2.2. Free Molecular Regime

Following Zurita-Gotor & Rosner (2002), the collision kernel in the mass transfer free molecular regime considering hard sphere interactions between particles i and j can be expressed as:

$$\beta_{ij} = \sqrt{\frac{8kT}{\pi m_{ij}}} PA_{ij} \qquad \text{as } Kn_D \to \infty \quad (8)$$

where m_{ij} is the reduced mass for i and j, i.e. $1/m_{ij} = 1/m_i + 1/m_j$ (m_i = mass of particle i, m_j = mass of particle j), kT is the thermal energy and PA_{ij} is the collisional projected area . Like $R_{S,ij}$, PA_{ij} is a combined geometric parameter for i and j, which can be calculated for particles provided their geometries are appropriately described. Zurita-Gotor & Rosner (2002) describe a procedure to rigorously calculate PA_{ij}, accounting for

the thermal rotation of two particles as they approach each other. As particle rotations are neglected in $R_{S,ij}$ calculations, particle rotation in the simplified PA_{ij} calculation procedure adopted here, is neglected, with the consequences of neglecting particle rotation discussed in subsequent sections. An orthographic projection of particle i is placed with its (three-dimensional) center of mass in the center of a rectangle whose area, A_{rect}, is much larger than the sum of the orientationally averaged projected areas of particle i and particle j. Particle j is then projected onto the rectangle at a random orientation, with its center of mass at a randomly chosen coordinate in the domain. If, in this configuration, the projections of particle i and particle j are in contact, a collision is counted, while if the particles do not contact, a miss is counted. The procedure is continuously repeated for random orientations of particle i and random orientations and positions of particle j, and after a sufficient number of collisions, N_{col}, and misses, N_{miss}, have been monitored, PA_{ij} is determined as:

$$PA_{ij} = \frac{N_{col}}{N_{col}+N_{miss}} A_{rect} \tag{9}$$

As shown in Figure 3.1b, PA_{ij} can be interpreted as the area of the projection bounded within the region where particle j's center of mass must lie in order for the two particles to contact. However, the depiction in the figure is only PA_{ij} for a specific orientation of particle, while the PA_{ij} calculation algorithm determines the orientationally averaged value, i.e. the parameter used in equation (9).

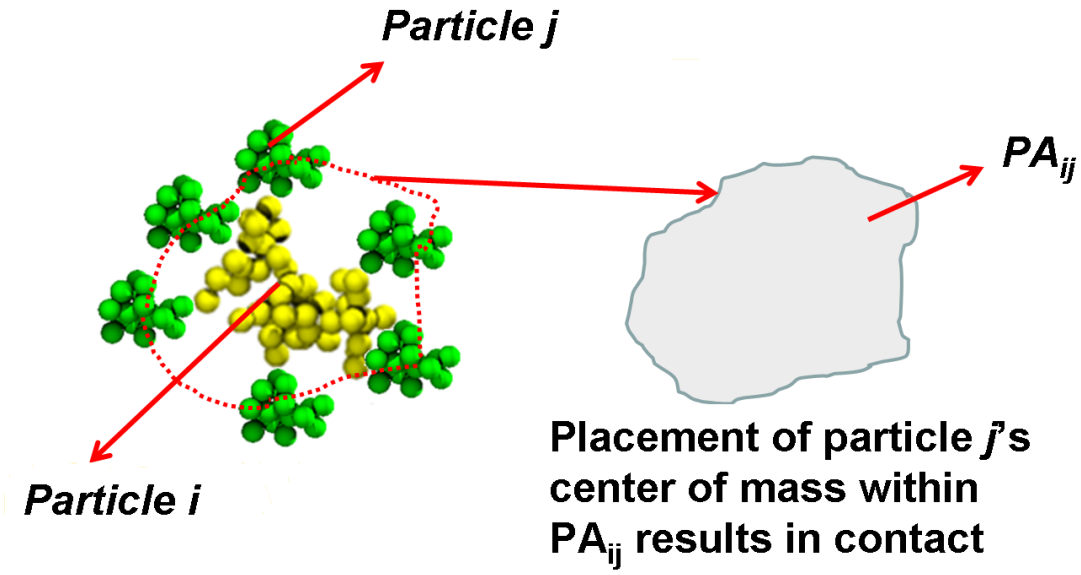

Figure 3.1.b. Schematic of the procedure used for projected area calculation for a colliding pair of particles.

3.2.3. Transition Regime

β_{ij} depends only on the parameters kT, f_{ij}, m_{ij} $R_{S,ij}$, and PA_{ij} in the continuum and free molecular limits. In examining transition regime collisions between a point mass and an arbitrarily shaped particle, Gopalakrishnan et al (2011) found that the interdependencies of a similar set of variables could be described using two dimensionless parameters, H, the non-dimensionalization of β_{ij}, and Kn_D, the non-dimensionalization of kT. Accounting for the aforementioned definitions of $R_{S,ij}$ and PA_{ij} and repeating the dimensional analysis employed in the prior study leads to H defined by the equation:

$$H = \frac{\beta_{ij} m_{ij} \pi^2 R_{S,ij}}{f_{ij} PA_{ij}^2} \tag{10}$$

and Kn_D defined by the equation:

$$Kn_D = \frac{(kT m_{ij})^{1/2} \pi R_{S,ij}}{f_{ij} PA_{ij}} \tag{11}$$

This definition of Kn_D is comparable to the definition of the momentum transfer Knudsen number for non-spherical particles used here and elsewhere (Dahneke 1973; Rogak and Flagan 1992), with the ratio of the size scale describing continuum transport ($R_{S,ij}$) and the size scale describing free molecular transport (PA_{ij}) appearing in the numerator and denominator, respectively. Noting that dimensional equations (2) and (8) must hold valid at $Kn_D \rightarrow 0$ and $Kn_D \rightarrow \infty$, respectively, reveals that:

$$H = 4\pi Kn_D^2 \qquad \text{as } Kn_D \rightarrow 0 \qquad (12a)$$

$$H = \sqrt{8\pi} Kn_D \qquad \text{as } Kn_D \rightarrow \infty \qquad (12b)$$

Further, in investigating sphere-sphere, and non-spherical particle-point mass collisions, prior analysis shows that across the entire Kn_D range, $H(Kn_D)$ can be determined from the expression (Rogak and Flagan 1992):

$$H = \frac{4\pi Kn_D^2 + C_1 Kn_D^3 + \sqrt{8\pi} C_2 Kn_D^4}{1 + C_3 Kn_D + C_4 Kn_D^2 + C_2 Kn_D^3} \qquad (13)$$

where C_1 =25.836, C_2 = 11.211, C_3 = 3.502, and C_4 = 7.211. Alternative collision kernel expressions for particle-vapor molecule collisions (Fuchs 1964; Fuchs and Sutugin 1970; Loyalka 1973), agree well with equation (13) (to within 5% for most Kn_D), as do expressions for high-mass entity collisions proposed elsewhere (Dahneke 1983; Veshchunov 2010; Veshchunov and Azarov 2012), giving high confidence that it is a reasonably accurate expression for $H(Kn_D)$.

The challenge then becomes evaluation of the validity of equation (13) for non-spherical particle collisions with one another, for which mean first passage time simulations (Nowakowski and Sitarski 1981; Narsimhan and Ruckenstein 1985) are used. In these simulations it is assumed that particles are sufficiently dilute such that between collisions, there is ample time for particles to redistribute themselves homogenously within the surrounding background gas, i.e. the characteristic time for collision is >> than the time required for particles to homogenously redistribute themselves in the background gas. Particle motion is subject to inertia (mass x acceleration), drag, and diffusion (Ermak and Buckholz 1980). The equations of motion for two particles, *i* and *j,* subject to these conditions, can be found in

Gopalakrishnan & Hogan (2011). By subtracting the acceleration of particle *i* from that of particle *j* and non-dimensionalizing the resulting equation, one can write the dimensionless difference in acceleration between *i* and *j* as:

$$\frac{d\vec{v}_j^*}{d\tau} - \frac{d\vec{v}_i^*}{d\tau} = \frac{d\left(\vec{v}_j^* - \vec{v}_i^*\right)}{d\tau} = \frac{1-\theta_m}{1-\theta_f}\vec{v}_i^* - \frac{\theta_m}{\theta_f}\vec{v}_j^* + \vec{A}_{ij}^* \tag{14a}$$

where $\vec{v}_j^* = \frac{\pi R_{S,ij} m_{ij} \vec{v}_j^*}{P A_{ij} f_{ij}}$ and $\vec{v}_i^* = \frac{\pi R_{S,ij} m_{ij} \vec{v}_i^*}{P A_{ij} f_{ij}}$ are the dimensionless velocities for particles *i* and *j*, respectively, $\tau = \frac{f_{ij}}{m_{ij}} t$ is the dimensionless time, $\theta_m = \frac{m_i}{m_i + m_j}$, $\theta_f = \frac{f_i}{f_i + f_j}$, and $\vec{A}_{ij}^*$ is a dimensionless vector which is Gaussian distributed in each direction, has zero mean, and variance given by:

$$\langle \vec{A}_{ij}^{*2} \rangle = 6 K n_D^2 \left(\frac{\theta_f^2 - 2\theta_f \theta_m + \theta_m}{\theta_m - \theta_m^2} \right) \tag{14b}$$

It is apparent from equations (14a) and (14b) that unlike the $Kn_D \rightarrow 0$ and $Kn_D \rightarrow \infty$ limits, in the transition regime the parameters θ_m and θ_f influence particle motion. However, it is also clear that under the condition $\theta_m = \theta_f$, θ_m and θ_f dependencies are mitigated. The approximation $\theta_m \approx \theta_f \approx 0.5$ applies for collisions between particles of nearly the same size (friction factor) and mass, and similarly the approximation $\theta_m \approx \theta_f \approx 0.0$ applies for collisions involving particles of highly disparate size and mass (provided that the more massive particle also has the higher friction factor). Because collisions under either of these conditions are quite commonplace, nearly all prior analyses of collisions neglect θ_f and θ_m effects (Dahneke 1983), and as a first approximation we also use the relationship $\theta_m \approx \theta_f$ here, with which equation (14a) becomes similar to a Langevin equation of motion for a single particle. Defining the relative velocity vector $\vec{v}_{ij}^* = \vec{v}_j^* - \vec{v}_i^*$ and the relative position vector $\vec{x}_{ij}^*$:

$$\vec{v}_{ij}^* = \frac{d\vec{x}_{ij}^*}{d\tau}, \qquad \vec{x}_{ij}^* = \frac{\vec{x}_{ij} \pi R_{S,ij}}{P A_{ij}} \tag{14c}$$

the changes in relative velocity and position between particles *i* and *j* as dimensionless time evolves from τ to $\tau + \Delta\tau$ can then be monitored with the equations :

$$\vec{v}_{ij}^{*}(\tau+\Delta\tau)=\vec{v}_{ij}^{*}(\tau)\exp(-\Delta\tau)+\vec{A}_{ij,1} \tag{15a}$$

$$\vec{x}_{ij}^{*}(\tau+\Delta\tau)=\vec{x}_{ij}^{*}(\tau)+\left(\vec{v}_{ij}^{*}(\tau+\Delta\tau)+\vec{v}_{ij}^{*}(\tau)\right)\left(\frac{1-exp\,(-\Delta\tau)}{1+exp\,(-\Delta\tau)}\right)+\vec{A}_{ij,2} \tag{15b}$$

$$\langle\vec{A}_{ij,1}^{2}\rangle=3Kn_{D}^{2}(1-\exp(-2\Delta\tau)) \tag{15c}$$

$$\langle\vec{A}_{ij,2}^{2}\rangle=6Kn_{D}^{2}\left[\Delta\tau-\frac{(1-exp(-\Delta\tau)}{(1+exp(-\Delta\tau)}\right] \tag{15d}$$

Using these equations of relative motion, the average dimensionless collision time (mean first passage time, τ_{mean}) between particles *i* and *j* is determined by placing particle *i* at the center of a cubic simulation domain (with dimensionless side length *s*, represented in Figure 3.2) with a fixed but random orientation, and particle *j* at a random location on the surface of the simulation domain, and also oriented randomly.

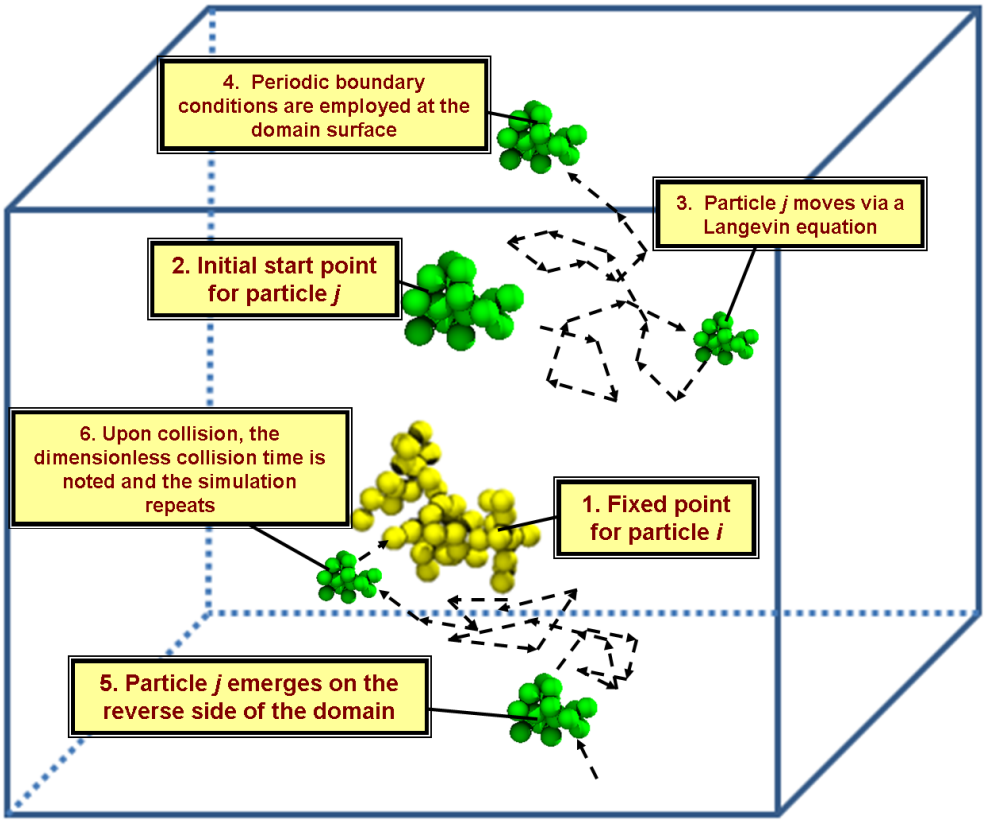

Figure 3.2. Schematic of the mean first passage time calculation procedure.

While particle i remains fixed in the domain center, particle j's initial dimensionless velocity vector is determined from randomly sampling $\vec{A}_{ij,1}$. With a prescribed $\Delta\tau$ and Kn_D, particle j then moves throughout the domain via equations (15a-15d). Periodic boundary conditions are employed on the domain surface, and once the two particles contact one another, the dimensionless time required for collision is recorded, the positions and orientations of the two particles are reset, and the process is repeated. After M collisions have been monitored, τ_{mean} is calculated as:

$$\tau_{mean} = \frac{1}{M}\sum_{i=1}^{M}\tau_i \tag{16a}$$

where τ_l refers to the time necessary for collision in trial l. The dimensionless collision kernel H is subsequently determined from the equation:

$$H = \frac{s^3 PA_{ij}}{\tau_{mean}\pi R_{S,ij}^2} \tag{16b}$$

As with purely continuum and free molecular calculations, in mean first passage time calculations drag is accounted for via orientationally averaged scalar friction factor, entities are moved via translation only, and the hydrodynamic interaction as well as other potential interactions between colliding entities are neglected. It is therefore not a direct test of the validity of these assumptions, and is used simply to examine the functional form $H(Kn_D)$ when these assumptions are in place. Further, calculation results are independent of the functional form of the friction factor employed, as all momentum transfer effects are directly absorbed into the diffusive Knudsen number. To determine a dimensional β_{ij} from the dimensionless $H(Kn_D)$ relationship outside the free molecular regime, however, requires determination of the colliding particle friction factors.

Ten combinations of test particle geometries are used in mean first passage time calculations, from which H is inferred for a specified Kn_D (12 different Kn_D values per aggregate pair). All test particles are quasifractal aggregates composed of 50 or less point contacting spherical subunits (of arbitrary unit radius), which satisfy the fractal law relationship:

$$N_i = k_{f,i}\left[\frac{R_{g,i}}{a_i}\right]^{D_{f,i}} \quad (17)$$

where N_i is the number of primary spheres in aggregate i, $k_{f,i}$ is the pre-exponential factor for aggregate i (set to 1.3 for all cases), a_i is the primary sphere radius, and $D_{f,i}$ is aggregate i's fractal dimension. Each of the test particles is produced by a sequential algorithm (Filippov, Zurita et al. 2000), which generates random aggregates with prescribed N_i, $k_{f,i}$, and $D_{f,i}$. . Table 3.1 displays an image of each test aggregate, and notes the number of primary particles, and fractal dimension. The aforementioned algorithms to compute $R_{S,ij}$ and PA_{ij} are employed on each aggregate pair, as are the algorithms to compute $R_{S,i}$ and PA_i noted in Chapter 2 on each individual aggregate. All computed Smoluchowski radii and orientationally averaged projected areas are also listed in Table 3.1. Sufficiently large simulation domain side lengths (s) and sufficiently small time steps ($\Delta\tau$) must be utilized to mitigate their influence on mean first passage time calculation results. For this purpose domain side lengths of s = 400-800 (units of primary sphere radii) are used, with larger side lengths required for smaller Kn_D and larger aggregates. As in prior work (Dahneke 1983; Gopalakrishnan, Thajudeen et al. 2011; Gopalakrishnan and Hogan 2012), the restriction $\Delta\tau \leq 0.005 Kn_D^2$ sufficiently mitigates timestep influences in these calculation results. Finally, to ensure convergence of τ_{mean} and H, dimensionless collision times are inferred for 5000-15000 collisions and averaged for each reported H value.

Table 3.1. Summary of the properties of the ten test aggregate pairs used in mean first passage time simulations. Reported $R_{S,i}$, $R_{S,j}$, PA_i, PA_j, $R_{S,ij}$, and PA_{ij} are for aggregates with primary particle radii of one (arbitrary units).

	Particle i	Particle j	N_i	N_j	$D_{f,i}$	$D_{f,j}$	$R_{s,i}$	$R_{s,j}$	PA_i	PA_j	$R_{S,ij}$	PA_{ij}
1		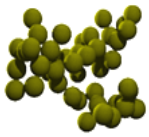	18	48	2.55	2.09	3.36	5.98	35.17	95.55	10.28	341.82
2	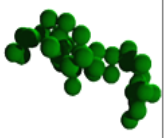	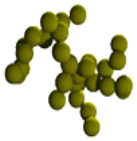	43	32	2.00	2.01	5.77	5.08	87.46	68.16	12.12	482.27
3		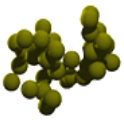	12	40	2.42	2.23	2.93	5.25	26.14	78.31	8.88	257.96
4		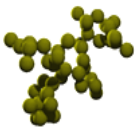	22	46	1.86	1.94	4.40	6.27	49.40	97.09	12.23	476.77
5	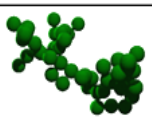	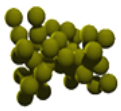	48	44	1.87	2.14	6.42	5.58	100.73	85.16	13.60	600.61
6			6	16	1.66	1.62	2.38	4.07	15.57	39.50	7.29	168.12
7	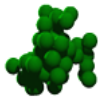		47	17	2.54	2.26	4.96	3.54	76.67	36.48	9.19	274.79
8	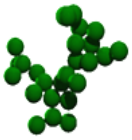		26	6	1.86	2.38	4.79	2.17	58.41	14.33	7.66	190.55
9			24	32	2.32	2.42	4.04	4.43	48.25	59.14	9.19	271.42
10		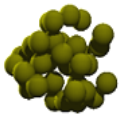	9	35	1.68	2.52	2.93	4.46	22.89	61.05	8.10	211.48

3.3 Results and Discussion

3.3.1. Mean First Passage Time Calculations

$H(Kn_D)$ values for non-spherical particle collisions, as inferred from mean first passage time calculations, are shown in Figure 3.3 (upper panel). For comparison, lines representing the continuum (equation 12a) and free molecular (equation 12b) limiting curves, as well as a curve corresponding to equation (13), are also shown. It is apparent from this curve that as $Kn_D \rightarrow 0$ and $Kn_D \rightarrow \infty$, the calculated values are in excellent agreement with the correct continuum and free molecular expressions, respectively. Also apparent is the good agreement between equation 13 and calculated values in the intermediate Kn_D range. This is further evident in the lower panel of Figure 3.3, where the relative difference, defined as $(H_{MFPT}-H_{eq13})/H_{eq13}$ (where the subscripts MFPT and eq13 denote values determined from mean first passage time calculations and equation 13), respectively, is plotted as a function of Kn_D. All calculated values are within +/- 5% of equation (13) predictions, and the small but apparent oscillation of the relative difference as Kn_D varies is attributable to the fact that equation (13) is a regression equation with a finite number of terms (Gopalakrishnan and Hogan 2012). These results indicate, with little ambiguity, that the $H(Kn_D)$ relationship found for spherical particles can be extended to non-spherical aggregates, and subject to the assumptions of negligible particle rotation and zero particle-particle interaction, it is reasonably valid for collisions between particles of arbitrary shape.

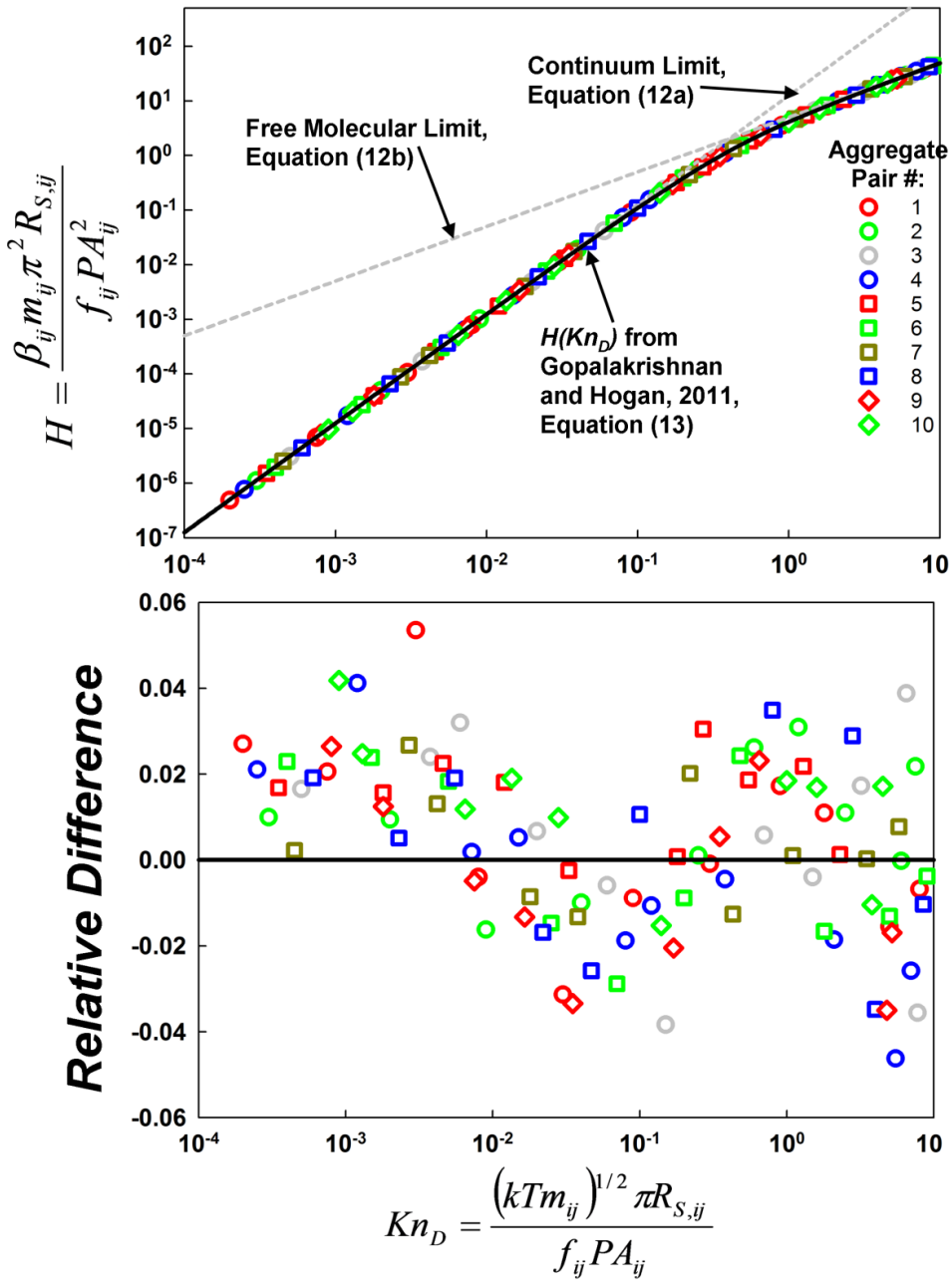

Figure 3.3. (Upper). Summary of the $H(Kn_D)$ results obtained with mean first passage time simulations for 10 test aggregate pairs. For comparison, $H(Kn_D)$ curves corresponding to the continuum limit (12a), free molecular limit (12b), and regression equation from Gopalakrishnan & Hogan (2011, equation (13) in this manuscript) are shown. (Lower) The relative difference between $H(Kn_D)$ inferred from mean first passage time calculations and equation (13) as a function of Kn_D. Relative difference is defined in the text.

With this success in predicting collision rates in the mass transfer transition regime and with the good agreement between measurements, numerical calculations, transition regime momentum transfer rates explained in Chapter 2, one can construct a universal "operating schematic" for aerosol particle collisions in the absence of potential interactions. This schematic is shown in Figure 3.4.

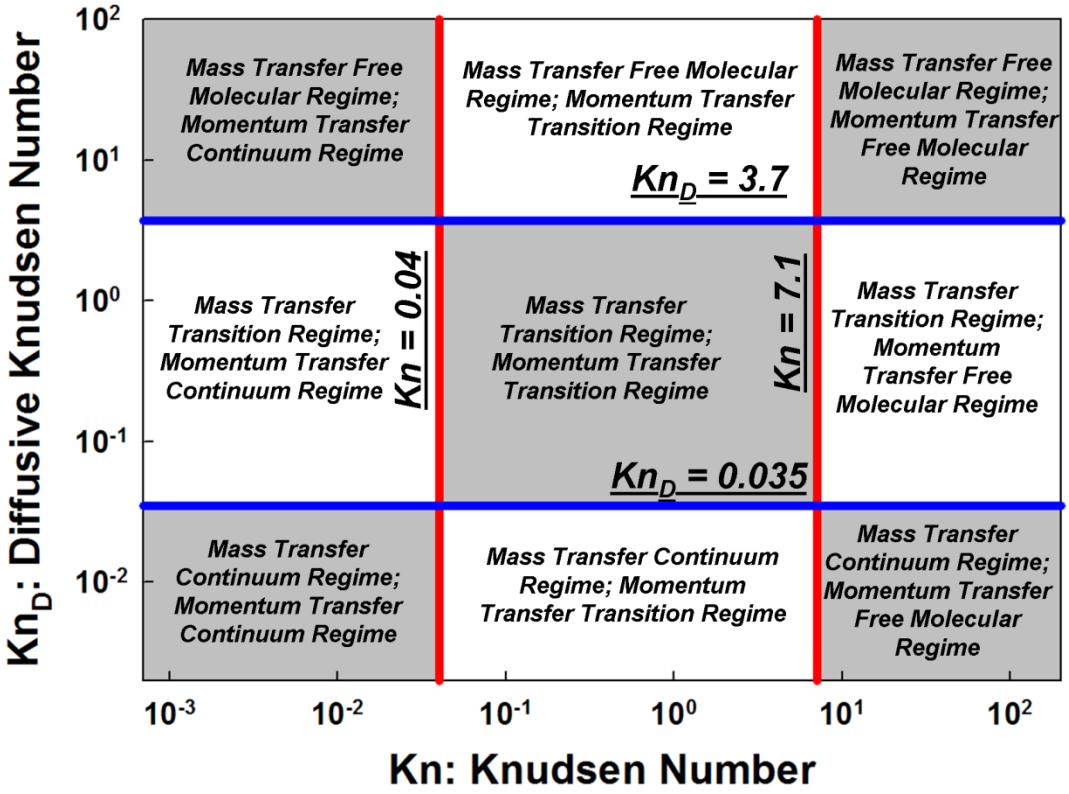

Figure 3.4. Depiction of the phase space noting when gas to particle momentum transfer and particle-particle mass transfer (collisions) lie within the continuum, transition, and free molecular regimes.

The dimensional collision rate between two particles *i* and *j* is dependent upon the Knudsen numbers for *i* and *j* (equation 3b), as well as the diffusive Knudsen number, calculated with the combined particle properties by equation (11). Based upon these numbers, particles may migrate through background gas in the momentum transfer continuum, transition, or free molecular regimes, the boundaries between which are noted in figure 4 by vertical lines at $Kn = 0.04$ (boundary between continuum and transition, below which the friction factor deviates less than 5% of the expected continuum regime value) and $Kn = 7.1$ (boundary between transition and free molecular, above which the friction factor deviates less than 5% from the expected free molecular regime value). Independent of Kn but based on Kn_D, the collision dynamics between two particles may occur in the mass transfer continuum, transition, or free molecular regime, with the bounds between continuum and transition regimes at $Kn_D = 0.035$ and between the transition and free molecular regimes at $Kn_D = 3.7$ (again based upon 5% or less deviation from limiting expressions). While the diffusive Knudsen number is dependent upon the individual Knudsen numbers of both particles through the friction factor and there is some degree of correlation between Kn_D and the Kn of the larger of the two colliding particles, the fact remains that aerosol particle collision dynamics are dependent upon three separate Knudsen numbers, and the dimensional collision kernel is expressed as:

$$\beta_{ij} = \frac{H(Kn_D) f_{ij}(Kn_i, Kn_j) PA_{ij}^2}{m_{ij}\pi^2 R_{S,ij}} \tag{18}$$

3.3.2. Influence of Particle Rotation

While the orientationally averaged friction factor is employed to model the motion of particles in this work, the act of rotation during a collision event is not explicitly considered. The influence of particle rotation on the length scale particle-particle collisions is, however, considered by Zurita-Gotor & Rosner (2002) in the mass transfer free molecular regime. In doing so, they define the ratio φ as:

$$\varphi = \left[\frac{PA_{ij}}{PA_{ij,rot}}\right]^{1/2} \tag{19a}$$

where $PA_{ij,rot}$ is a modified definition of the combined projected area accounting for particle rotation. Should rotations have minimal influence, then φ approaches 1.0, while with significant rotation influence φ <<1. For aggregates obeying equation (17) with a pre-exponential factor of 2.3 and a fractal dimension of 1.8, they find that φ is well-described by the equation:

$$\varphi \approx 0.085\exp(-3.42\sigma^2) + 0.18\exp\left(-0.41N_{min}^{-\frac{1}{3}} - \sigma^{-1}\right) + 0.9054 \qquad (19b)$$

where N_{min} is the smaller of N_i and N_j, N_{max} is the larger of these numbers, and σ is defined as N_{min}/N_{max}. Using equation (19b), φ is plotted as a function of σ for varying N_{min} in figure 3.5.

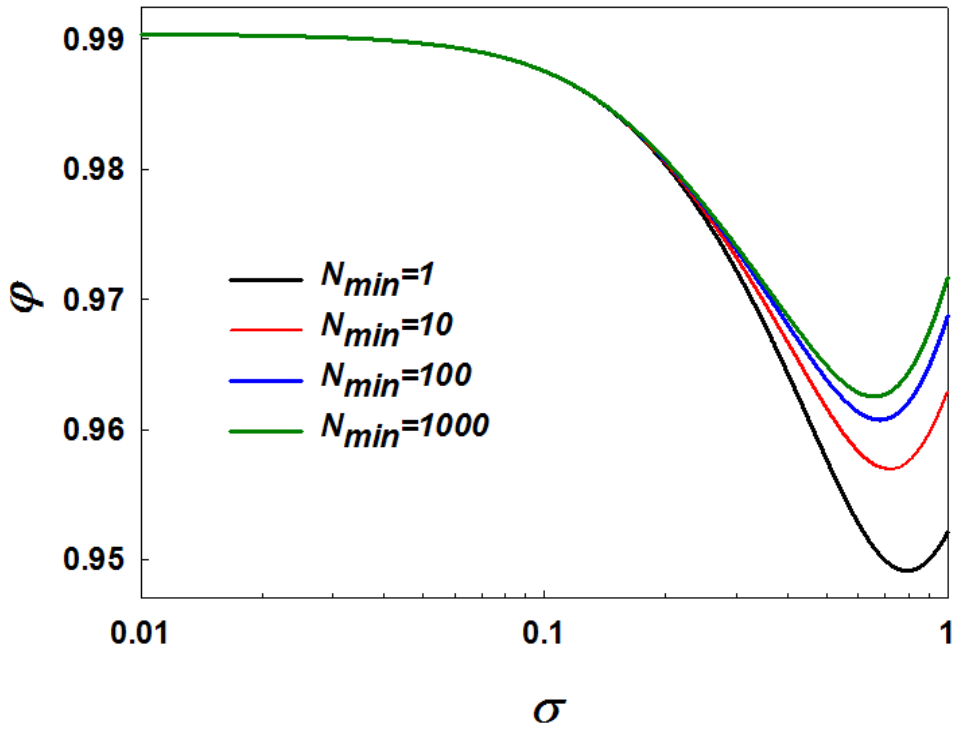

Figure 3.5. Ratio of the square root of the collisional projected area calculated without particle rotations, to the square root of the collisional projected area determined with collisions, as a function of the ration N_{min}/N_{max}.

φ remains greater than 0.95 under all circumstances, and presumably, φ remains even closer to unity for higher fractal dimension aggregates than Zurita-Gotor & Rosner's test aggregates. Further, while their analysis is restricted to free molecular motion, the influence rotational motion continuum regime, which would be quantified by a correction to $R_{S,ij}$ likely also remains in the 0.95-1.0 range. In total this prior work suggests that the influence of rotations on the length scale for particle-particle collision is minimal except in rare circumstances of collisions between extremely low fractal dimension aggregates of near equivalent size.

3.3.3. Comparison to Previously Proposed Expressions

Comparison is made between the $H(Kn_D)$ curve (equation 13) to the expression proposed by (Cho, Chung et al. 2011), as well as to that proposed by(Rogak and Flagan 1992). In many regards these comparisons resemble prior comparison of the $H(Kn_D)$ curve developed through mean first passage time calculations to collision kernels of Fuchs (1964) and Dahneke (1983), which is performed elsewhere (Gopalakrishnan and Hogan 2011). For collisions between spheres, both the Fuchs (1964) and Dahneke (1983) collision kernel expressions differ from equation (13) by only several percent across the entire Kn_D range. In making these comparisons, we further assume that all theories employ the same model for the friction factor of the particles (Zhang, Thajudeen et al. 2012), explained in Chapter 2. Therefore, the comparison is solely limited to the choice of collision length scale employed in substitute of what is employed here, i.e. $(PA_{ij}^2/\pi^2 R_{S,ij})^{1/3}$ for H and $PA_{ij}/\pi R_{S,ij}$ for Kn_D. Firstly, comparison to the equation of Cho et al (2011) is made, which derives from Fuchs (1964). In lieu of $R_{S,ij}$ or PA_{ij} calculation, Cho et al (2011) simply assume that the collision length scale can be calculated as the sum of size scales for the individual particles, i.e. that an appropriate "collision size" can be defined for a particle without consideration of the size and shape of the colliding partner. Specifically, they assume that the radius of gyration for a particle is its contribution to the collision length; hence, rather than make use of $R_{S,ij}$ or $(PA_{ij}/\pi)^{1/2}$ they use $R_{g,i}+R_{g,j}$. With the assumption that the "limiting

sphere" radius in Fuchs's collision kernel model is an amount $(\pi/8(kTm_{ij}/f_{ij})$ larger than the collision length (an assumption which has little effect on the calculation collision kernel (Fuchs 1963; D'yachkov, Khrapak et al. 2007)), the dimensionless version of the collision kernel given by Cho et al (2011), H_{Cho}, is written as:

$$H_{Cho} = 4\pi Kn_D^2 \frac{R_{g,i}+R_{g,j}}{R_{S,ij}} \left[\frac{1}{1+\left(\frac{\pi}{8}\right)^{1/2} Kn_D \frac{PA_{ij}}{\pi R_{S,ij}\left(R_{g,i}+R_{g,j}\right)}} + (2\pi)^{1/2} Kn_D \frac{PA_{ij}}{\pi R_{S,ij}\left(R_{g,i}+R_{g,j}\right)} \right]^{-1} \tag{20a}$$

For four sets of quasifractal aggregate pairs which have properties specified in Table 3.2 (with all pre-exponential factors equal to 1.3), the value $(H_{Cho}-H_{eq13})/H_{eq13}$ is plotted in figure 3.5a as a function of Kn_D. For all test aggregate pairs, deviations are evident with the collision kernel from Cho et al (2011). Specifically, a slight overestimation in the collision kernel is apparent at a fractal dimension 1.6, and underestimation in the collision kernel is found for all other fractal dimensions, increasing in magnitude with increasing fractal dimension and approaching 40% at a fractal dimension of 2.4. The difference between the collision kernel predicted by Cho et al (2011) from that predicted by equation (13) further varies with Kn_D, and as Kn_D is a function of $R_{S,ij}$ and PA_{ij}, without these parameters known a priori it is difficult to quantify the error introduce via the assumption $R_{S,ij} = (PA_{ij}/\pi)^{1/2} = R_{g,i}+R_{g,j}$.

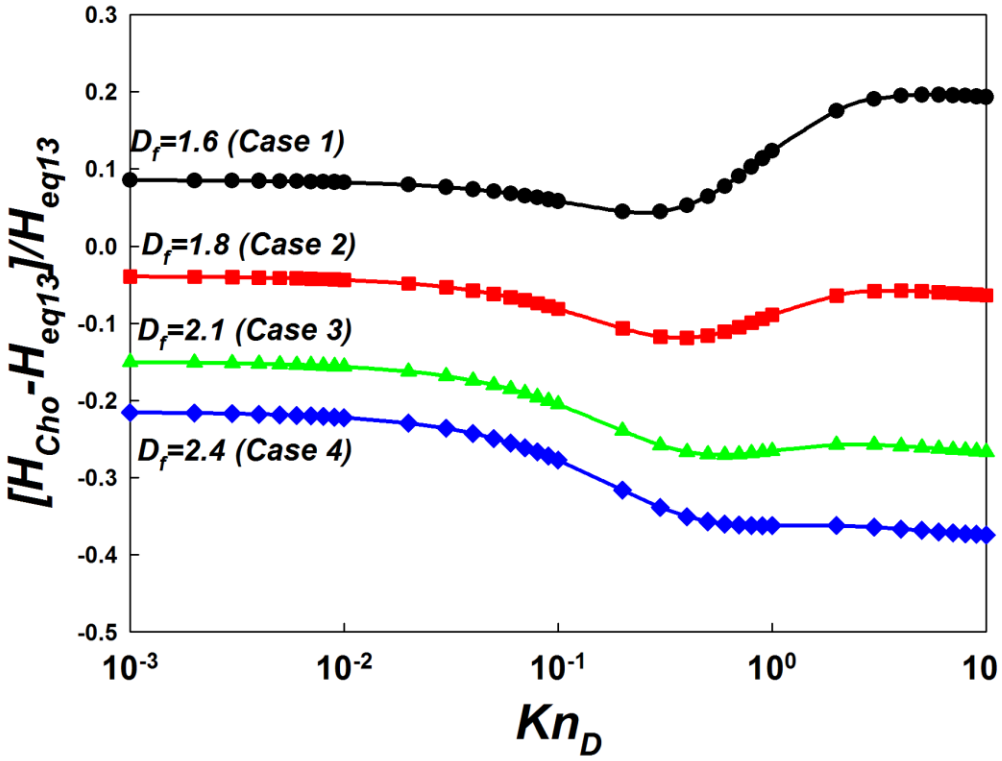

Figure 3.6a. Comparison of the relative difference between H predicted by Cho et al (2011) from H predicted by equation (13), as a function of Kn_D, for 4 test aggregate pairs with properties noted in Table 3.2.

Table 3.2. Summary of the properties of the four test aggregate pairs used for comparison to previously developed aggregate collision kernel models. Reported length scales are for aggregates with primary particle radii of one (arbitrary units).

	Particle i	Particle j	N_i	N_j	$D_{f,i}$	$D_{f,j}$	$R_{s,i}$	$R_{s,j}$	PA_i	PA_j	$R_{s,ij}$	PA_{ij}	$R_{g,i}$	$R_{g,j}$	L_{RF}
1			32	38	1.60	1.60	5.77	6.26	73.73	85.80	14.41	662.05	7.40	8.24	13.47
2			32	47	1.80	1.80	5.47	6.36	71.33	99.05	13.80	615.96	5.93	7.34	11.89
3			44	36	2.10	2.10	5.62	5.17	86.66	73.91	12.01	475.79	5.35	4.86	9.68
4			40	41	2.40	2.40	4.90	4.93	72.22	73.37	10.67	370.26	4.17	4.21	8.36

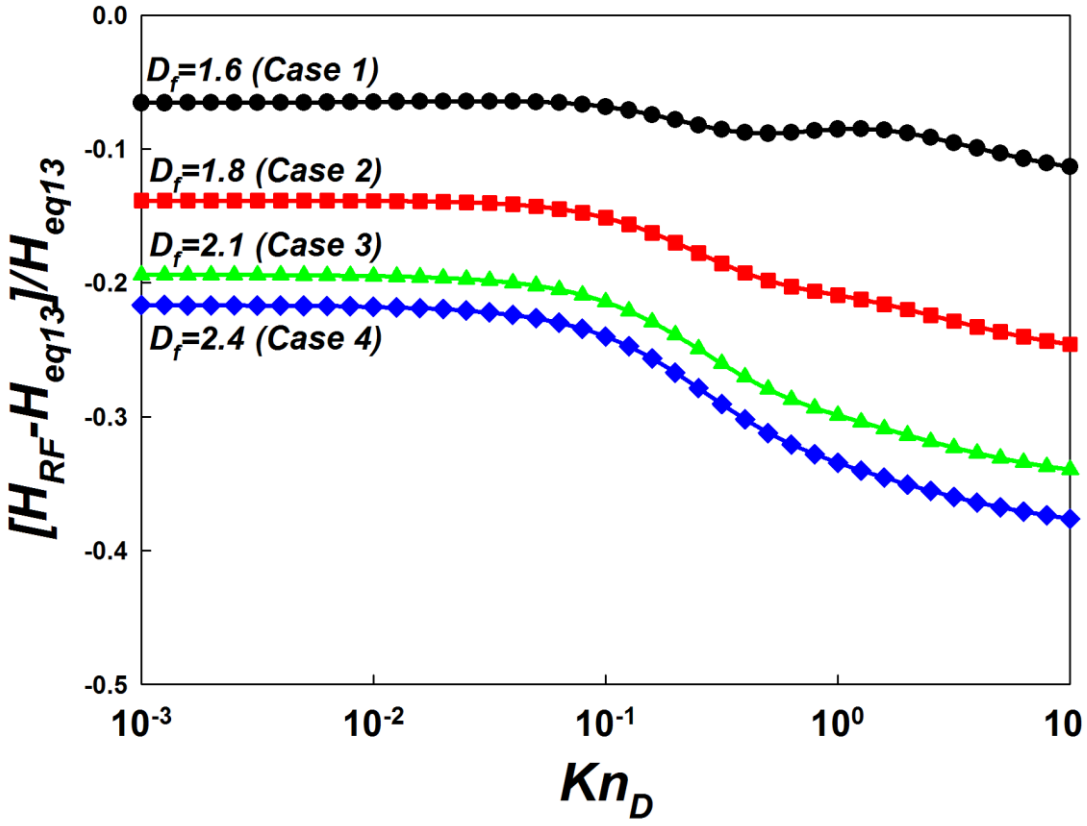

Figure 3.6b. Comparison of the relative difference between H predicted by Rogak & Flagan (1992) from H predicted by equation (13), as a function of Kn_D, for 4 test aggregate pairs with properties noted in Table 3.2.

Unlike Cho et al (2011), Rogak & Flagan (1992) acknowledge the collision length scale (termed the absorbing sphere radius) cannot necessarily be defined as the sum of individual length scales calculated separately for the colliding particles (and is one of the first studies to note this point). Nonetheless, the collision length employed in their work, L_{RF}, is distinct from the collision length scale used in this study. L_{RF} calculation, requires use of 'max' and 'min' functions which contain several theoretical correlations that apply in the low ($D_f = 1.0$) and high ($D_f = 3.0$) fractal dimension limits. Furthermore, L_{RF} is not a pure geometric parameter in all circumstances, but takes a specific value in the continuum limit, $L_{RF,C}$, the free molecular limit, $L_{RF,FM}$, and in the transition regime depends upon Kn_D (aggregate masses, friction factors, and the temperature). For the test aggregates examined, however, $L_{RF} = L_{RF,C}=L_{RF,FM}$ is found,

and is reported in table 3.2. The dimensionless version of the collision kernel used by Rogak & Flagan (1992), H_{RF}, is expressed as:

$$H_{RF} = 4\pi Kn_D^2 \frac{L_{RF,C}}{R_{S,ij}} \frac{\left[1+\left(\frac{\pi}{2}\right)^{1/2} Kn_D \frac{PA_{ij}}{\pi R_{S,ij} L_{RF}}\right]}{1+(2\pi)^{1/2} Kn_D \frac{PA_{ij}}{\pi R_{S,ij} L_{RF}} \left(1+\left(\frac{\pi}{2}\right)^{1/2} Kn_D \frac{PA_{ij}}{\pi R_{S,ij} L_{RF}}\right)} \quad (20b)$$

Figure 3.6b, shows the ratio $(H_{RF}-H_{eq13})/H_{eq13}$ as a function of Kn_D. Equation (20b) consistently underestimates the collision kernel, with the degree of underestimation dependent on Kn_D and increasing with increasing fractal dimension, again approaching 40% underestimation at a fractal dimension of 2.4. Based on comparison to both expressions, it is suggested that whenever possible, in the examination of non-spherical particle collisions/aggregation, the proper values of $R_{S,ij}$ and PA_{ij} be employed, as in many instances, previously utilized collision length scales lead to underestimation of the collision kernel.

3.3.4. Case Study: Relationships for Quasifractal Aggregates

To apply the $H(Kn_D)$ curve to models of collisional growth, or to compare to experimental measurements, it is thus necessary to compute $R_{S,ij}$ and PA_{ij}. Geometric models of the colliding particles are required to calculate these parameters. As such information is not necessarily available, or as often the purpose of the calculation or experiment is indeed to predict particle geometry/morphology, it is necessary to develop relationships between PA_{ij}, $R_{S,ij}$, PA_i, PA_j, $R_{S,i}$, and $R_{S,j}$ for quasifractal aggregates composed of 50 or fewer primary particles of equal sizes with the number of primary particles selected randomly for each aggregate. Similar efforts have been made previously to develop regression expressions relating aggregate geometric descriptors to physical length scales (Naumann 2003). To develop regression expressions for the necessary transport size scales, test aggregates are produced with the sequential algorithm. Although the equations developed are admittedly limited in application to this specific class of particles (i.e. fixed pre-exponential factor, limited number of primary particles, and limited fractal dimension range) and further limited because the sequential algorithm is known to produce unrealistic aggregates with 100 or more

primary particles (Filippov, Zurita et al. 2000), the approach employed in this case study can be used similarly to develop relationships between the size descriptors for collisions involving any type of particle morphology. PA_{ij}, $R_{S,ij}$, PA_i, PA_j, $R_{S,i}$, and $R_{S,j}$ are calculated for 50 aggregate pairs with D_f = 1.50, 1.80, 2.20, and 2.60, as well as with aggregates with randomly selected fractal dimensions in the 1.50-2.60 range (with different fractal dimensions for the two colliding aggregates). For all test aggregates, k_f = 1.30. In the supplemental information Figure 3.7a shows a plot of PA_{ij}/a_i^2 versus $R_{S,ij}/a_i$ for all test pairs, as well as a line denoting $PA_{ij} = \pi R_{S,ij}^2$. It is known that for point mass (i.e. gas or vapor molecule) collisions with a non-spherical particle $PA_{ij} = \pi R_{S,ij}^2$ does not necessarily hold valid, particularly for high aspect ratio particles (Naumann 2003). Conversely, it appears for collisions between particles which are more similar in size, there is a direct relation between the continuum and free molecular size descriptors for collisions; thus only calculation of either $R_{S,ij}$ or PA_{ij} is required. However, it is to be reiterated that this is by no means a universal conclusion, and only applies approximately for the class of aggregates under examination.

Next attempt is to relate $R_{S,ij}$ to $R_{S,i}$ and $R_{S,j}$, the Smoluchowski radii for the individual aggregates. Figure 3.7b shows $R_{S,ij}/a_i$ for all test aggregate pairs as a function of the right hand side of the equation:

$$\frac{R_{S,ij}}{a_i} = \left[1.203 - \frac{0.4315(N_i+N_j)}{(N_i D_{f,i}+N_j D_{f,j})}\right]\left\{\frac{R_{S,i}}{a_i} + \frac{R_{S,j}}{a_i}\right\}^{\left(0.8806+\frac{0.34975(N_i+N_j)}{(N_i D_{f,i}+N_j D_{f,j})}\right)} \quad (21)$$

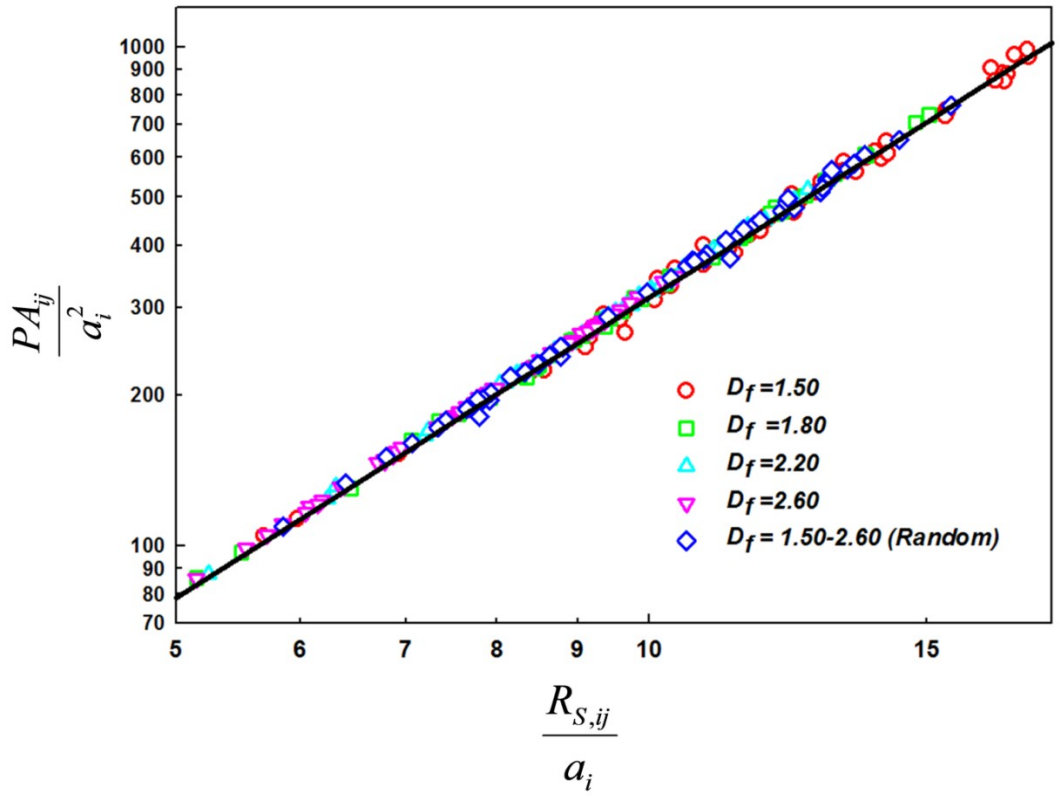

Figure 3.7a. A comparison of PA_{ij} to $R_{S,ij}$ for test aggregate pairs. The black line denotes the curve $PA_{ij} = \pi R_{S,ij}^2$.

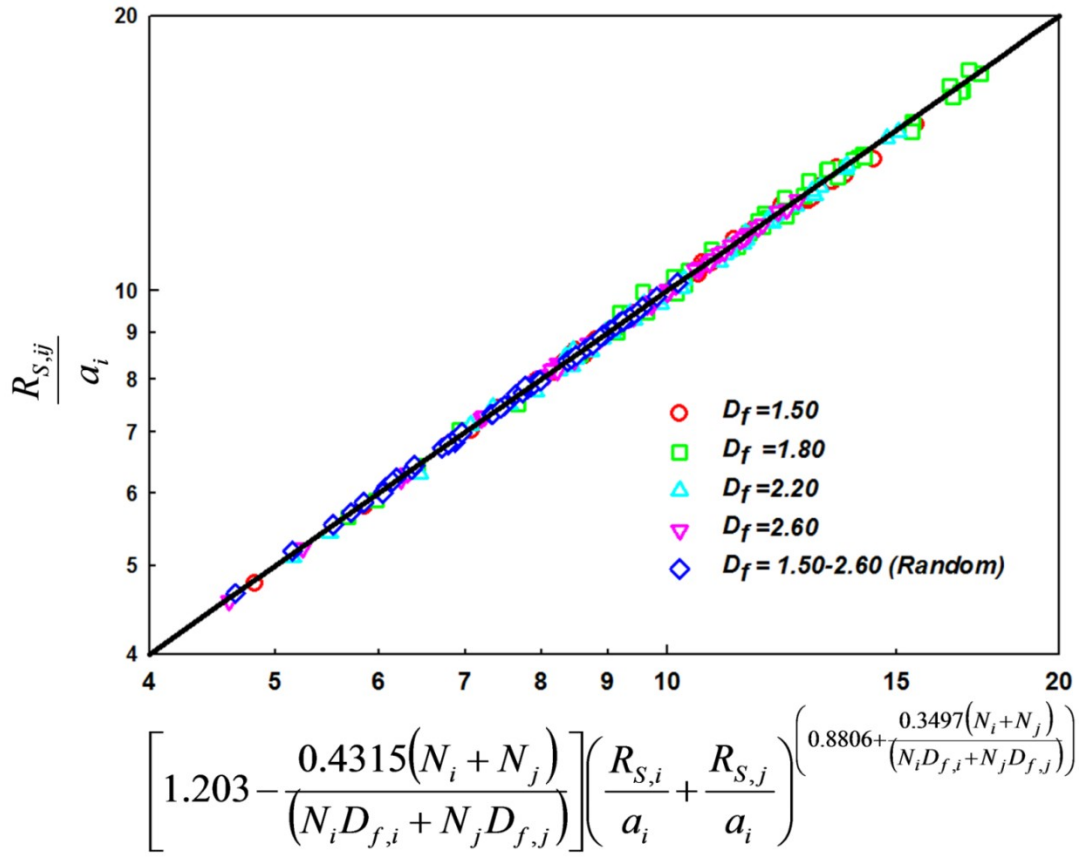

Figure 3.7b. A comparison between calculated $R_{S,ij}$ and a regression equation developed to predict $R_{S,ij}$ from $R_{S,i}$ and $R_{S,j}$.

As is observable in this figure, equation (21), determined via regression with all aggregate test pairs, applies well to this class of aggregates, to within 1% error. What follows is then to relate PA_i and $R_{S,i}$, for aggregates to their fractal descriptors. Considering sequential algorithm generated aggregates composed of 10-100 primary particles, $k_{f,i}$ = 1.30, and $D_{f,i}$ = 1.30-2.60, we find that the following equations predict $R_{S,i}$ to within +/- 3% for the examined range of fractal dimensions:

$$\frac{R_{S,i}}{a_i} = \phi_R \left(\frac{N_i}{k_{f,i}}\right)^{1/D_{f,i}} \tag{22a}$$

$$\phi_R = \frac{1}{\alpha_1 ln[N_i]+\alpha_2} \tag{22b}$$

$$\alpha_1 = 0.253D_{f,i}^2 - 1.209D_{f,i} + 1.433 \quad (22c)$$

$$\alpha_2 = -0.218D_{f,i}^2 + 0.964D_{f,i} - 0.180 \quad (22d)$$

As confirmation of the approximate validity of this regression, figure 8a shows a plot of $R_{S,i}$ as a function of the right side of equation (21). The following equation is similarly found for PA_i:

$$\frac{PA_i}{\pi a_i^2} = \phi_P \left(\frac{N_i}{k_{f,i}}\right)^{2/D_{f,i}} \quad (23a)$$

$$\phi_P = \frac{N_i^{-\alpha_3}}{\alpha_4} \quad (23b)$$

$$\alpha_3 = 0.439D_{f,i}^2 - 2.221D_{f,i} + 2.787 \quad (23c)$$

$$\alpha_4 = -0.232D_{f,i}^3 + 1.273D_{f,i}^2 - 2.183D_{f,i} + 1.906 \quad (23d)$$

which agrees to within 5% of directly calculated PA_i for $D_{f,i} = 1.6\text{-}2.6$. Comparable to figure 8a, a plot of PA_i for test aggregates as a function of the right side of equation (23a) is shown in figure 3.8b.

In total, to employ equation (13) (or equivalently equation (18)) for similarly sized quasifractal aggregates of known fractal properties, $R_{S,i}$ and PA_i can be approximated by equations (22) and (23), which subsequently allows for evaluation of $R_{S,ij}$ (equation 21), PA_{ij} (via $PA_{ij} = \pi R_{S,ij}^2$), f_i (equation (3a)), f_{ij}, and for known gas conditions and aggregate material density, Kn_D. $H(Kn_D)$ can then be calculated and used to infer β_{ij} for type i and type j aggregates.

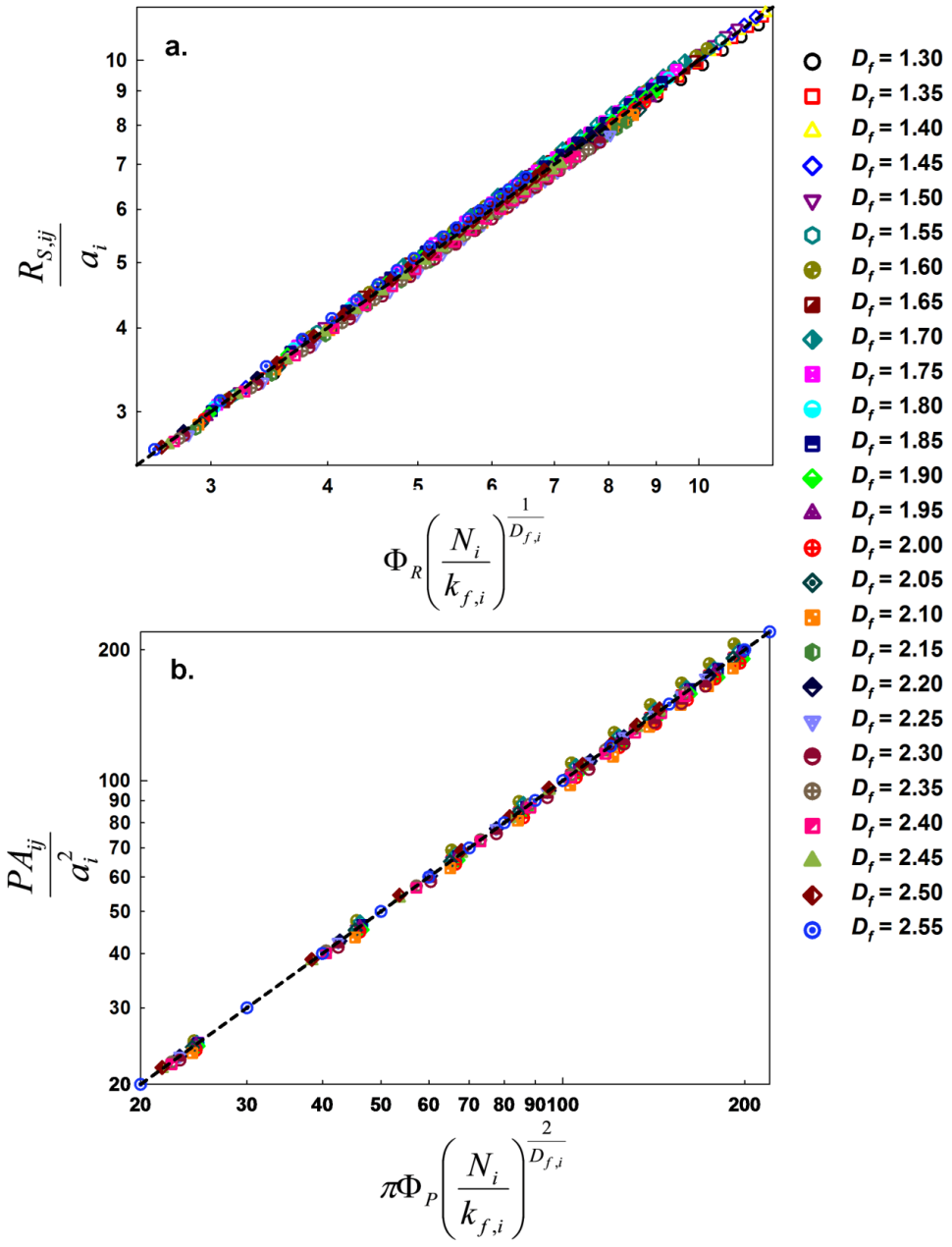

Figure 3.8. (a.) Comparison between calculated $R_{S,i}$ and predictions from a regression equation developed to predict $R_{S,i}$ as a function of aggregate fractal properties. (b.) Comparison between calculated PA_i and predictions from a regression equation developed to predict PA_i as a function of aggregate fractal properties.

Finally, perhaps as important as proper calculation of the collision kernel is correct determination of the properties of the new particle formed from the irreversible

contact-point binding of the two colliding aggregates (assuming little-to-no coalescence). Figure 3.9a and 3.9b show the ratios $R_{S,new}/R_{S,ij}$ and PA_{new}/PA_{ij} and as functions of Kn_D for the 10 test cases shown in Table 3.1, where $R_{S,new}$ and PA_{new} denote the orientationally averaged projected area and Smoluchowski radius of the newly formed aggregate.

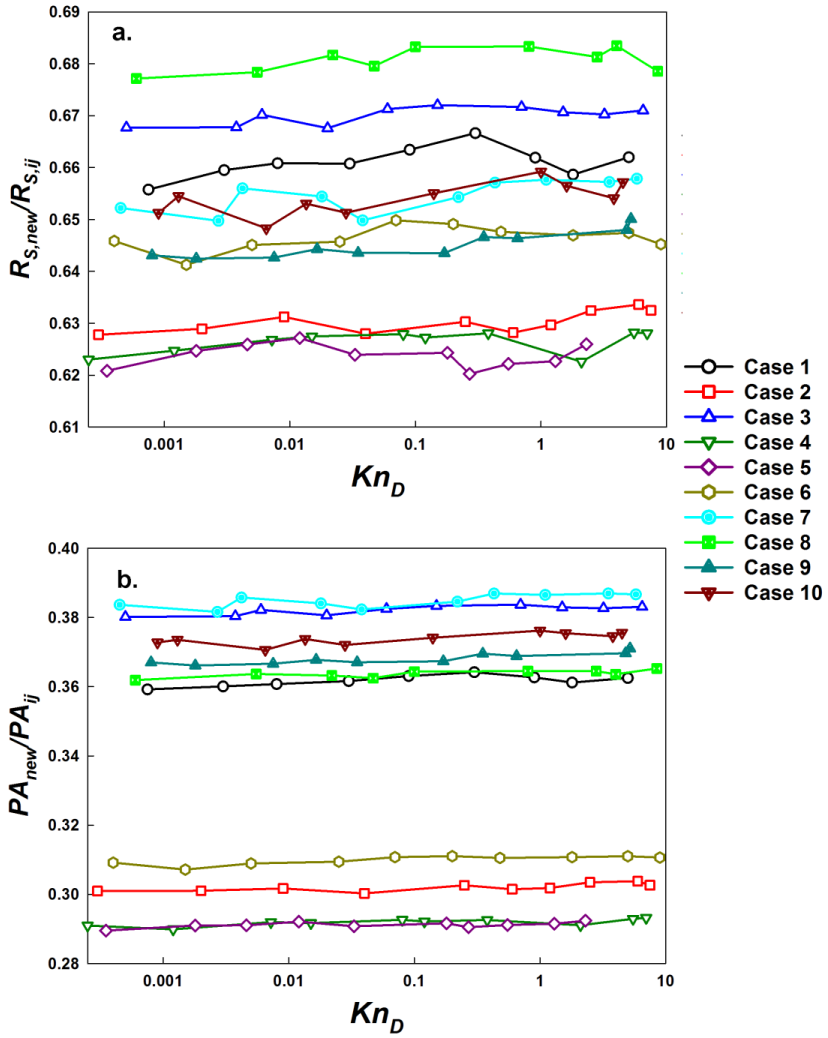

Figure 3.9 (a.) The average Smoluchowski radii and (b.) and orientationally averaged projected area of aggregates formed from the collision of test aggregate pairs, as functions of Kn_D.

Reported ratios are the averages from 50 collisions at the specified Kn_D and in most cases the standard deviation is ~1% of the reported average value. Little-to-no variation with Kn_D is found for both $R_{S,new}/R_{S,ij}$ and PA_{new}/PA_{ij}. Further, all examined $R_{S,new}/R_{S,ij}$ fall within a narrow 0.62-0.68 range, while two similar populations of PA_{new}/PA_{ij} are evident, the first centered of 0.30, and the second on 0.37. Given the low degree of variation from collision to collision, amongst all examined aggregate pairs, and across the entire Kn_D range, these results demonstrate that from R_{Sij} and PA_{ij} (which, can be inferred from $R_{S,i}$ and $R_{S,j}$ for aggregates) it is possible to estimate the properties of the new aggregate formed during a collision.

3.4 Conclusions

The collisions of arbitrarily shaped particles is examined theoretically and numerically in the mass transfer transition regime and based upon results of this examination specific regression equations for quasifractal aggregates composed of 50 or fewer primary particles are developed, which allow for the determination of the transition regime collision rate for aggregates as functions of the fractal descriptors for each aggregate. The main conclusions and the limitations of the undertaken study are as follows:

1. The $H(Kn_D)$ relationship found valid previously for collisions between spheres can be generalized for arbitrarily shaped particles by appropriately redefining H and Kn_D.
2. The universality of the $H(Kn_D)$ relationship in the absence of potential and viscous interaction permits generation of a phase space diagram, defining when collision processes lie within the mass transfer continuum, transition, or free molecular regimes. Significant about this is that the diffusive Knudsen number influence on mass transfer and collision processes in aerosols has been largely ignored in many studies of particle transport. Further, combining the results of this work with the conclusions of the friction factor calculations in Chapter

2, a complete phase space for gas molecule-particle momentum transfer (dependent on Kn) and for particle-particle mass transfer (dependent on Kn_D) can be constructed.

3. For quasifractal aggregates composed of monodisperse primary particles which are similar in size, regression relations can be developed which enable calculation of the collision kernel directly from the quasifractal descriptors. Population balance models (Heine and Pratsinis 2007) of aggregation for aggregates similar to those examined here should gain accuracy through use of the developed equations. For growth of particles of a different morphological class (e.g. fibers), the procedure used here to find relationships approximating $R_{S,ij}$, PA_{ij}, $R_{S,i}$, $R_{S,j}$, PA_i, and PA_j as functions of more direct particle morphological descriptors can be repeated.

4. While based on prior work one can anticipate that the rotation of non-spherical particles during collision minimally alters the collision rate, particle-particle interactions, both viscous and through potential energy (Sceats 1989; Arunachalam, Lucchese et al. 1999; Isella and Drossinos 2010), no doubt influence collision rates. That the $H(Kn_D)$ functional form has been generalized for collisions between spherical particles weakly attracting or repelling one another Coulombically (Gopalakrishnan and Hogan 2012) suggests that such interactions can be accounted for in a realistic manner without major modification to the approach used here.

Chapter 4: Filtration of Non-spherical Particles by Cylindrical Filter Fibers.

Abstract: This study looks at aerosol filtration as quintessentially a collision process. This chapter looks at calculating the collision rate between non-spherical aerosol particles and cylindrical fibers. Attempt is made at developing regression equations to calculate the relevant length scale to predict the non-dimensional collision rate and thereby single fiber efficiency.

4.1 Introduction

Through mean first passage time (MFPT) calculations (Hunt, Thajudeen et al. 2013), it was shown that the dimensionless collision kernel (H) within a Kuwabara (1959) flow cell model, neglecting particle inertia, is described by the equation:

$$H = \frac{2\pi}{\ln\left(V_f^{-1/2}(1+R)^{-1}\right)} Kn_D^2 \left(1 + C_1 \left[\frac{\chi_f^{1/2}}{Kn_D}\right]^{C_2}\right) \tag{1a}$$

$$C_1 = 0.63 - 0.5257\left(\ln\left(\frac{V_f^{-\frac{1}{2}}}{1+R}\right)R\right)^{0.65} + 3.5V_f \tag{1b}$$

$$C_2 = 0.38 - 0.6205\left(\left(\ln\left(\frac{V_f^{-\frac{1}{2}}}{1+R}\right)R\right)^{0.5} + 2V_f\right)^2 - 0.0165\left(\left(\ln\left(\frac{V_f^{-\frac{1}{2}}}{1+R}\right)R\right)^{0.5} + 2V_f\right) \tag{1c}$$

where Kn_D is the diffusive Knudsen number (Dahneke 1983; Gopalakrishnan and Hogan 2011) , R is the particle size to fiber size ratio, and V_f is the filter solid volume fraction. For spherical particles and cylindrical fibers, H, Kn_D, R, and χ_f are defined by the respective equations:

$$H = \frac{\beta m_p}{f(a_f + a_p)^2} \tag{2a}$$

$$Kn_D = \frac{(kTm_p)^{1/2}}{f(a_p+a_f)} \tag{2b}$$

$$R = \frac{a_p}{a_f} \tag{2c}$$

$$\chi_f = \frac{m_p U_0^2}{kT} \tag{2d}$$

where β is the two-dimensional collision rate coefficient/kernel, f is the particle friction factor (Dahneke 1973; Zhang, Thajudeen et al. 2012), m_p is the particle mass, k is the Boltzmann's constant, T is the temperature, U_0 is the fluid flow velocity upstream of the filter, and a_p and a_f are the particle and fiber radii, respectively. Correspondingly, the penetration (P) of spherical particles through a filter of thickness w can be calculated as:

$$P = \exp\left(-\frac{w}{\pi a_f}\frac{V_f(1+R)(1-V_f)}{Kn_D\chi_f^{1/2}}H\right) \tag{3}$$

In a prior study (Hunt, Thajudeen et al. 2013), equation (3) was shown to agree well with the predictions of traditional depth filtration theory considering particle deposition by diffusion and interception (Stechkina and Fuchs 1966; Kirsch, Stechkina et al. 1974; Lee and Liu 1982); hence equation (3) can be used an alternative to prior methods to estimate nanoparticle penetration through fibrous filter media under conditions where $\chi_f^{1/2}/Kn_D < 10^4$, $\chi_f^{1/2}Kn_D < 0.1$, $V_f \leq 0.1$, and $R \leq 0.2$. However, like classical depth filtration theory, equations (1-3) have been developed considering only spherical particles. High temperature synthesis in the gas phase routinely leads to the formation of non-spherical nanoparticles composed of a number of point-contacting primary spheres (aggregates/agglomerates (Schmidt-Ott, Baltensperger et al. 1990; Sorensen 2011), which are collected via filtration for later use. Further non-spherical aggregates are frequently a byproduct of incomplete combustion reactions (Chakrabarty, Moosmuller et al. 2009; Latin, Ferry et al. 2013), and fibrous filtration is a commonly used method to control such particulate combustion emissions. Therefore, calculations of particle penetration applicable to non-spherical particles are of considerable interest.

The purpose of this study is thus to extend the MFPT calculation approach to determine the dimensionless collision rate considering non-spherical particles, while still accounting for particle deposition due to diffusion and interception. Given its importance, this issue has been the focus of both experimental and numerical studies previously. Specifically, Kim et al (2009) examined experimentally the penetration of quasifractal aggregates of varying morphology through fibrous filters. By measuring particle penetration as a function of "mobility diameter" (with a differential mobility analyzer) they were able to compare the penetrations for particles of differing morphology yet with similar diffusion coefficient as one another. At small mobility diameters (higher diffusion coefficients), particle morphology was observed to minimally influence penetration, while at higher mobility diameters (lower diffusion coefficients) it was observed that more "open" chain like aggregates were captured more efficiently. Similar findings have been reported by Seto et al (2010) and later by Wang et al (Kim, Wang et al. 2009; Wang, Kim et al. 2011), who both found that at larger mobility diameters carbon nanotubes and nanotube bundles were collected more efficiently than their spherical counterparts. Balazy & Podgorski (2007) used Brownian Dynamics calculations (a similar framework to the MFPT approach) to examine aggregate deposition onto fibers, also predicting enhanced deposition for aggregates. Collectively, these studies demonstrate that non-spherical particles deposit onto filter fibers more efficiently, while also indicating that further investigation into the filtration of non-spherical particles, both theoretical and experimental, is warranted.

In the subsequent sections, the modifications needed to the MFPT calculation results required to determine the dimensionless collision kernel, and hence the penetration, for non-spherical particles with cylindrical fibers are explained. Analysis is performed for quasifractal aggregates composed of point-contacting, monodisperse, primary spheres, as well as cylindrical particles. It is shown that for these non-spherical particles, equations (1a-c) remain valid; it is only the definitions provided in equations (2a-c) which need to be modified slightly.

4.2 Theoretical Methods

4.2.1 Collision Length Scale Calculations for Non-spherical Particles

As with condensation, coagulation, and diffusion charging, particle deposition onto filter fibers can be analyzed as a transported limited collision processes. In examining collisions between a point mass and a non-spherical particle (Balazy and Podgorski 2007; Gopalakrishnan, Thajudeen et al. 2011), as well as two non-spherical particles (Thajudeen, Gopalakrishnan et al. 2012)(Chapter 3), it has been found that the dimensionless collision kernel valid for sphere-sphere collisions also applies to collisions involving non-spherical entities, provided that modified collision size scales are incorporated into the dimensionless parameters H and Kn_D. Similarly, collision length scales for non-spherical particles with circular fibers are defined here to modify H, Kn_D, and R, which enables us to test the hypothesis that equations (1a-c) remain valid with appropriately modified definitions of these parameters. It is noted however, that the analysis differs slightly from prior studies of particle-particle collisions; particle-particle collisions occur in a three dimensional environment, for which a collision radius (the Smoluchowski radius) be defined for diffusive collisions (the continuum regime), and a collision projected area (two-dimensional) be defined for ballistic collisions (the free molecular regime). Conversely, particle-filter fiber collisions may be treated as two-dimensional when filter fibers are modeled as infinitely long, which leads to the requirement that only a ballistic collision length scale be defined (i.e. diffusive collision rates are not a function of collision length scale in two-dimensions).

The ballistic collision length for a particle of arbitrary shape with an infinitely long fiber is defined as the orientationally averaged maximum distance of closest approach at which the particle and fiber are in contact. A schematic outlining the calculation procedure for this collision length scale is provided in Figure 4.1, which is the two-dimensional analog to the orientationally averaged collision area calculation approach described by Zurita-Gotor & Rosner (2002) and explained in Chapter 3.

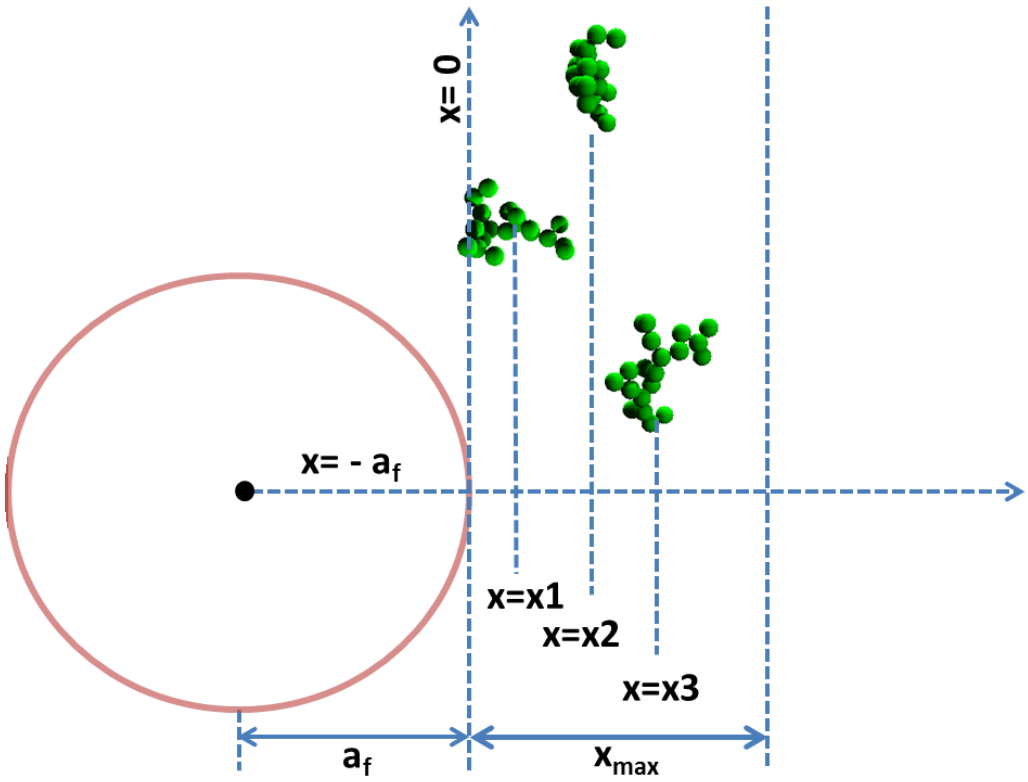

Figure 4.1. Schematic of the procedure used to calculate the collision length scale L for an arbitrary shaped particle with a cylindrical filter fiber of radius a_f.

A non-spherical particle is considered, approaching a cylindrical fiber at a random orientation, along an arbitrary trajectory. At closest approach, its center of mass is a distance $a_f + x$, from the center of the fiber, and hence a distance x from the edge of the fiber. In this position and orientation the particle may or may not be in contact with the fiber, which is readily determined by checking if any portion of the particle crosses the x-axis origin. By selecting random particle orientations and values of x from a uniform distribution between zero and a value x_{max}, where x_{max} is defined as that at location the particle question never collides with the fiber (at any orientation), the collision length between particle any fiber can be defined as a_f+L, where L is calculated as:

$$L = \frac{N_{col}}{N_{tot}} x_{max} \tag{4}$$

where N_{col} is the number of trials resulting in contact, and N_{tot} is the total number of trials. Provided x_{max} is sufficiently large and a sufficient number of trials are performed, such that $N_{col}/N_{tot} < 1$, L is independent of both N_{tot} and x_{max}, and $a_f + L$ is hence the orientationally averaged collision length scale.

With this collision length defined and assuming that equations (1a-c) remain valid, equations (2a-c) can be modified as:

$$H = \frac{\beta m_p}{f(a_f+L)^2} \tag{5a}$$

$$Kn_D = \frac{(kTm_p)^{1/2}}{f(a_f+L)} \tag{5b}$$

$$R = \frac{L}{a_f} \tag{5c}$$

Note that because the definition of χ_f does not involve a description of particle size and shape, it is expected that the definition in equation (2d) remains valid for all particles. From equation (4), it is evident that $L = a_p$ for spherical particles, hence equations (5a-c) are more general versions of equations (2a-c). Here, L is calculated for quasifractal aggregates composed of point contacting, equal radius spheres, which approximately obey the relationship:

$$N_{mon} = k_f \left(\frac{R_g}{a_{mon}}\right)^{D_f} \tag{6}$$

where N_{mon} is the number of monomer spheres per aggregate, k_f is the pre-exponential factor, R_g is the aggregate's radius of gyration, a_{mon} is monomer radius, and D_f is the fractal dimension. In doing so, aggregates are produced which satisfy equation (6) (to within 0.1% error) using a cluster-cluster algorithm described by Fillipov et al (2000) in the range N_{mon} = 20 – 1000, k_f = 1.3 & 1.7, and D_f = 1.5-2.4. This algorithm is selected because it is found to produce aggregates with structure factors (Huang, Oh et al. 1998) similar to those of similar k_f and D_f generated by diffusion limited aggregation algorithms. However, to generate aggregates with D_f = 1.3 & 2.7, the sequential algorithm (Filippov, Zurita et al. 2000; Thajudeen and Hogan 2012) is used, as with the

cluster-cluster algorithm it is difficult to generate such nearly linear (D_f = 1.3) and highly compact (D_f = 2.7) aggregates. Both the cluster-cluster and sequential algorithms are capable of producing random structures, and for each N_{mon}, k_f, and D_f examined 10 aggregates are produced (which are described in calculations by the coordinates of their monomers). Subsequently, L is calculated for each aggregate and also for cylinders of varying radii a_{cyl} and aspect ratios (R_{cyl}, the radius to length ratio). For both aggregates and cylinders, regression equations (for L/a_{mon} for aggregates and for L/a_{cyl} for cylinders, respectively) are developed, enabling direct calculation of L from the structural descriptors of the particle in question.

4.2.2 Fluid Flow in the Cell Model

The two-dimensional Kuwabara (1959) cell model is used to describe the fluid flow around a cylindrical fiber within a staggered array of fibers. A unit cylindrical cell that surrounds each fiber, for which the vorticity is zero on the cell boundary, is defined with dimensionless radius $b^* = b/(L+a_f) = V_f^{-1/2}/(1+R)$, where $R = L/a_f$. The dimensionless stream function is given as::

$$\psi = \frac{1}{2Y}\left(\frac{A}{r(1+R)} + Br(1+R) + Cr(1+R)\ln[r(1+R)] + Dr^3(1+R)^3\right) \qquad (7)$$

where $A = (1-\frac{1}{2}V_f)$, $B = -(1-V_f)$, $C = 2$, $D = -\frac{V_f}{2}$, and $Y = -\frac{1}{2}\ln V_f + \frac{1}{2}V_f - \frac{3}{4} - \frac{V_f^2}{4}$. This can be used to obtain the velocity vector in the cylindrical co ordinate system $U_r^* = -\frac{\partial\psi}{\partial\theta}$ and $U_\theta^* = \frac{1}{r}\frac{\partial\psi}{\partial r}$. The veclocities directly influence the motion of tha particle as explained in the equation 8a-b.

4.2.3 Non-Spherical Particle MFPT Calculations

The validity of equations (1a-c) with equations (5a-c) used to define H, Kn_D, and R is examined via the determination of H from mean first passage time (MFPT) calculations for quasifractal aggregates. The calculation procedure is represented in Figure 4.2. MFPT calculations are performed via monitoring a particle's motion in a Kuwabara flow cell using a dimensionless solution to the Langevin equations.

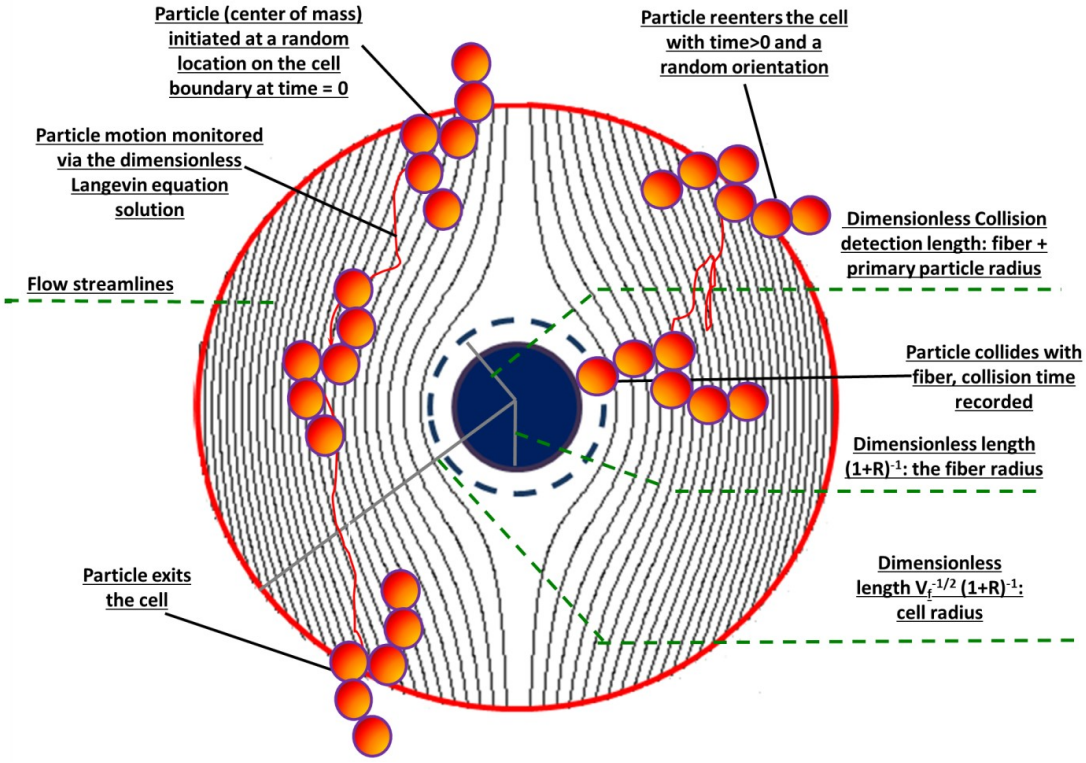

Figure 4.2. Schematic of the mean first passage time calculation approach for aggregates, which may be contrasted which the method of Hunt et al (2013) for spherical particles.

For a non-spherical particle, the dimensionless velocity vector is defined as $\overrightarrow{v_p^*} = \frac{m_p \vec{v}_p}{f(a_f+L)}$ and its dimensionless position as $\overrightarrow{x_p^*} = \frac{\vec{x}_p}{(a_f+L)}$, leaving the solution to the equations of motion as equations:

$$\vec{v}_p^*(\tau+\Delta\tau) = \vec{v}_p^*(\tau)\exp(-\Delta\tau) + \chi_f^{1/2}\, Kn_D\, \vec{U}_{gas}^*[1-\exp(-\Delta\tau)] + \vec{A}_1 \qquad (8a)$$

$$\vec{x}_p^*(\tau+\Delta\tau) = \vec{x}_p^*(\tau) + \left(\vec{v}_p^*(\tau+\Delta\tau) + \vec{v}_p^*(\tau) - 2\chi_F^{\frac{1}{2}}\, Kn_D\, \vec{U}_{gas}^*\right)\left(\frac{1-\exp(-\Delta\tau)}{1+\exp(-\Delta\tau)}\right)$$

$$+\chi_F^{1/2}\, Kn_D\, \vec{U}_{gas}^*\Delta\tau + \vec{A}_2 \qquad (8b)$$

$$\langle \vec{A}_1^2 \rangle = 2Kn_D^2[1 - \exp(-2\Delta\tau)] \quad (8c)$$

$$\langle \vec{A}_2^2 \rangle = 4Kn_D^2 \left[\Delta\tau - 2\left(\frac{1-\exp(-\Delta\tau)}{1+\exp(-\Delta\tau)}\right)\right] \quad (8d)$$

$\vec{U}_{gas}^*$ is the dimensionless gas velocity vector at location $\vec{x}_p^*(\tau)$, with components in polar coordinates of $[U_r^*, U_\theta^*]$. Also in Equations (8a-d), $\vec{A}_1$ and $\vec{A}_2$ are Gaussian distributed random vectors with mean values of zero and the noted variances (in two dimensions). χ_f is as defined in equation 2d and is an important input along with Kn_D, R and V_f.

4.2.4 Simulation Procedure

With the input dimensionless parameters, the cell is defined and the particle motion is tracked using equations 8a-d.Initially, the particle centre of mass is placed at a random location on the cell boundary with a random orientation of the particle. As the particle moves, it can eventually either exit the cell boundary (i.e. the particle center of mass can exit the cell boundary) or collide with the fiber. In the case of particle leaving the cell boundary, the particle is reintroduced at a random location on the cell surface with a random orientation, as it is considered to have entered a new cell, and the dimensionless time continues to increase.

Simulations are therefore performed to determine H as a function of input Kn_D, R (which scales the dimensionless radii of primary particles), χ_f, and V_f. Simulations are restricted to situations to the conditions $\chi_f^{1/2}/Kn_D < 10^4$, $\chi_f^{1/2}Kn_D < 0.1$, $V_f \leq 0.1$, and $R \leq 0.2$. The rotational motion of aggregates during their migration through the Kuwabara cell is neglected, and based upon the calculations of Zurita-Gotor & Rosner (2002), rotations are not expected to substantially alter the particle-fiber collision rate. The only differences between the MFPT calculation approach for non-spherical particles and spherical particles arise when (1) checking if the particle collided with the central fiber, and (2) re-introducing the particle into the Kuwabara cell in instances where it leaves the cell prior to collision. In the case of aggregates, each portion of the aggregate must to examined to determine whether it is in contact with the central fiber.

For example, for aggregates with a dimensionless primary particle radius $a_{mon}^{*} = \frac{a_{mon}}{a_f + L}$, if any primary sphere center is a distance $a_{mon}^{*} + a_f^{*} = \frac{a_{mon} + a_f}{a_f + L}$ or less from the center of the Kuwabara cell, collision has occurred. In (2), each time an aggregate is introduced into the Kuwabara cell, either to commence a calculation or because it left the cell without collision, it is oriented randomly (about its center of mass) via the selection of three Euler angles. MFPT calculations are performed for the eight noted aggregates in Table 4.1, for which *L* is calculated independently. While *L* is used in the non-dimensionalization of the equations of motion for aggregates, this choice is arbitrary; any length scale can be used to normalize dimensions. However, if another length scale is selected computational results must be rescaled to infer the input Kn_D and *R,* and the output *H* (Gopalakrishnan, Thajudeen et al. 2011).

Table 4.1. A summary of the quasifractal aggregates used in mean first passage time calculations.

Aggregate #	Image	D_f	N_{mon}	L/a_{mon}
1		1.8	10	3.73
2	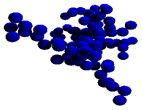	1.8	100	13.22
3	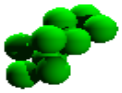	2.3	10	3.11
4	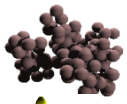	2.3	100	8.79
5	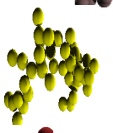	1.78	50	9.07
6		2.4	100	8.27
7		1.78	200	19.17
8	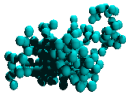	2	200	15.38

4.3 Results and Discussion

4.3.1 Non-spherical Particle Collision Length Scale & Comparison to MFPT Calculations

Plots of L/a_{mon} as a function of R_g/a_{mon} for aggregates (averaged over 10 aggregates) and L/a_{cyl} as a function of $1/R_{cyl}$ are shown in Figures 4.3a and 4.3b, respectively. Interestingly, for aggregates, results collapse to curves independent of k_f; L/a_{mon} versus R_g/a_{mon} is nearly linear ($R^2 > 0.999$), with slope dependent on D_f in all

instances. The linear slope ($1/\alpha$) linking L/a_{mon} to R_g/a_{mon}, as determined from calculations, is summarized in Table 4.2. Additionally, combining all results leads to the regression equation:

$$\frac{L}{a_{mon}} = \frac{1}{\alpha}\frac{R_g}{a_{mon}} \tag{9a}$$

$$\alpha \approx 0.3\left(\frac{3}{D_f} - 1\right)^2 - 0.12\left(\frac{3}{D_f} - 1\right) + 0.774;\ 1.3 \leq D_f \leq 2.7;\ R^2 > 0.98 \tag{9b}$$

Results for cylinders lead to the regression equation:

$$\frac{L}{a_{cyl}} = 0.3183\frac{1}{R_{cyl}} + 0.6332\ ; \qquad R_{cyl} \leq 1.0;\ \ R^2 > 0.99 \tag{9c}$$

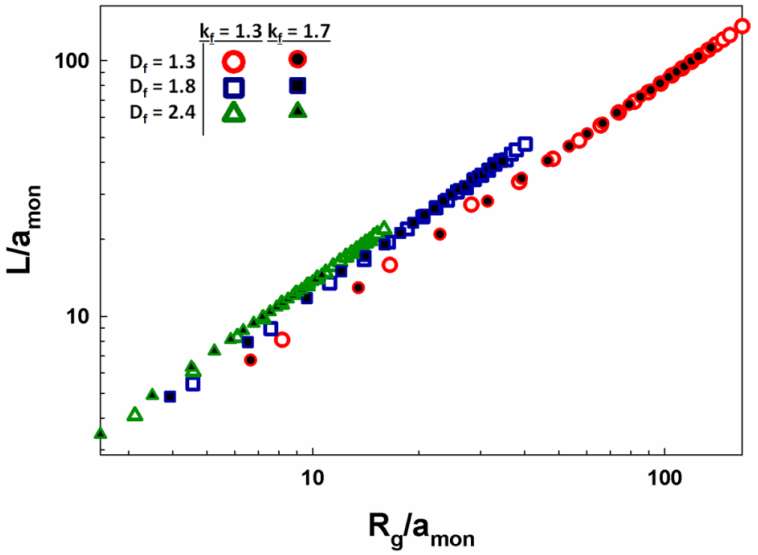

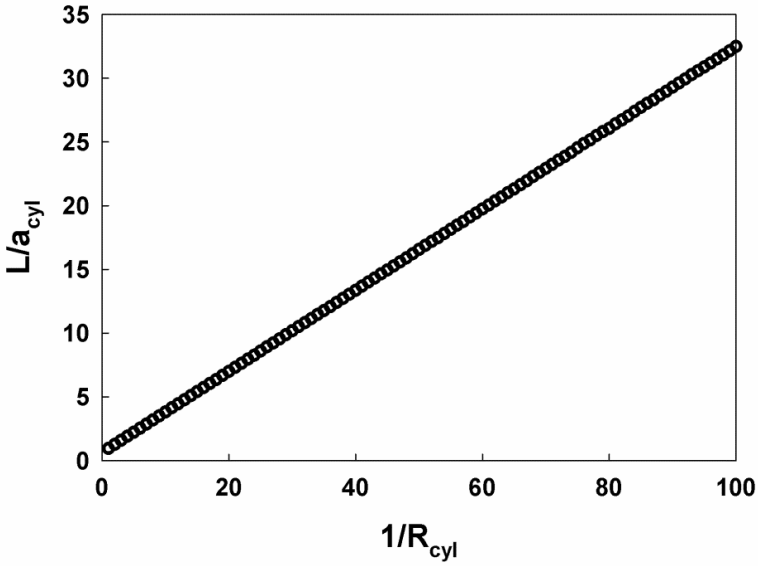

Figure 4.3. Plots of the collision length scale to radius ratio as a function of R_g/a_{mon} for aggregates (a) and $1/R_{cyl}$ for cylinders (b).

Table 4.2. A summary of the slopes ($1/\alpha$) linking L/a_{mon} to R_g/a_{mon} for quasifractal aggregates.

D_f	$1/\alpha$
1.3	0.89
1.5	1.03
1.8	1.19
2.0	1.27
2.2	1.33
2.4	1.37
2.7	1.37

The regression equations for L of aggregates and cylinders gives distinctly different results from the approach of Balazy & Podgorski (2007), who assumed that $L = [(2+D_f)/D_f]^{1/2} R_g$, i.e. that L is equal to the approximate outer radius of an aggregate. The outer radius and the values of L calculated here only agree well with one another as $D_f \rightarrow 3$, and can differ by a factor of up to 2 at lower fractal dimensions. Substantial disagreement between L and the outer radius is also found for cylinders, as the outer radius would be defined as half the cylinder length. Therefore, for large values of $R = L/a_f$ (examined in subsequently in comparison to experiments), the calculations here are in disagreement with the calculations of Balazy & Podgorski (2007).

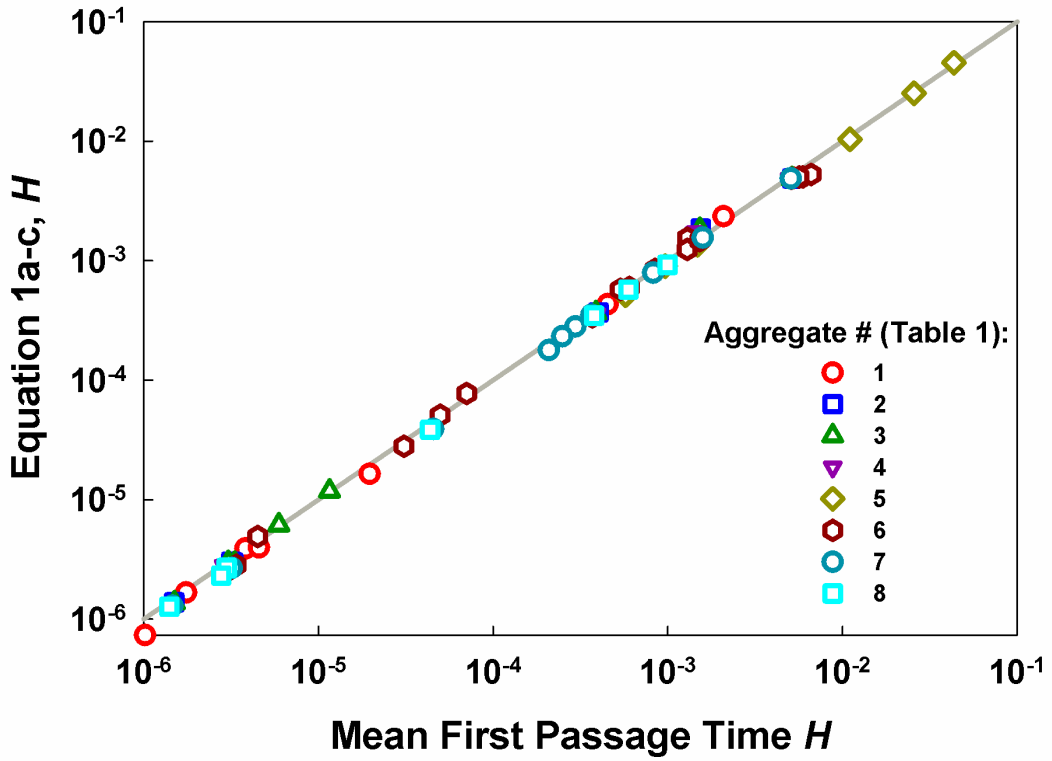

Figure 4.4. A comparison of H inferred from mean first passage time calculations to the values of H calculated with equations (1a-c) for quasifractal aggregates, with properties specified in Table 4.1.

The predictions of equations (1a-c), using the definitions in equation (5a-c) and MFPT calculation results for quasifractal aggregates are plotted against one another in Figure 4.4. For guidance, a 1:1 line is additionally displayed. Across ~5 orders of magnitude in H, independent of aggregate shape, equation predictions and MFPT calculation results are typically agree to within 10% of one another, which is similar to the agreement found between equation (1a-c) predictions and MFPT calculations with spheres. Therefore, it can be safely assumed equation (1a-c) can be used with confidence to predict the dimensionless collision rate, and subsequently the single fiber efficiency, for non-spherical particles.

4.3.2 Comparison to Experimental Measurements

MFPT simulations and equation (1a-c) predictions are made with input values of Kn_D, χ_f, V_f, and R. We now use these equations in comparison to experimental measurements of the penetration of multiwalled carbon nanotubes through fibrous filters reported by Seto et al (2010), who performed such experiments for multiwalled nanotubes with three different radii and aspect ratios (characterized by electron microscopy). A summary of this comparison is provided in Table 4.3, where calculations of the parameters χ_f, Kn_D, H, and the single fiber efficiency are based on the reported particle penetrations, face velocities the filter volume fraction (0.049), and average filter fiber radius (1.4 μm). To define Kn_D, it is necessary to calculate the mass (though in the absence of inertia, the mass does not influence results) as well as the friction factor of the particles under examination. Modeling nanotubes as straight cylinders, the mass can be calculated knowledge of the nanotube material density, radius, and aspect ratio. Particle friction factors can be inferred through use of a differential mobility analyzer; however, while Seto et al (2010) used a DMA upstream of their filtration system to classify particles based on their electrical mobilities (charge to friction factor ratios), many particles transmitted through the DMA may have been multiply charged (Gopalakrishnan, Meredith et al. 2013) and for nanotubes with supermicrometer lengths, particle may have aligned during migration in an electrostatic field (Balazy and Podgorski 2007). With the assumption that the nanotube does not align preferentially in any direction as it migrates through the filter medium, its friction factor (and similarly the friction factor of any particle) can be calculated considering non-continuum drag effects as given in Chapter 2 (Dahneke 1973; Zhang, Thajudeen et al. 2012):

$$f = \frac{6\pi\mu R_S}{1+\frac{\lambda\pi R_S}{PA}\left(1.257+0.4exp\left[\frac{-1.1PA}{\lambda\pi R_S}\right]\right)} \tag{10a}$$

where μ is background gas dynamic viscosity, λ is the gas molecule hard sphere mean free path, PA is the particle's orientationally averaged projected area, and R_S is the

particle's Smoluchowski radius (Gopalakrishnan, Thajudeen et al. 2011), equated with its hydrodynamic radius via the Hubbard-Douglas approximation (Douglas, Zhou et al. 1994). Shown previously (Hansen 2004), for cylinders R_S and PA are given by the equations:

$$R_s = \left(\frac{3a_{cyl}^3}{4R_{cyl}}\right)^{\frac{1}{3}} \left(\begin{array}{c} 1.0304 + 0.0193ln\left[\frac{1}{2R_{cyl}}\right] + 0.0623ln^2\left[\frac{1}{2R_{cyl}}\right] + 0.00476ln^3\left[\frac{1}{2R_{cyl}}\right] + \\ 0.00166ln^4\left[\frac{1}{2R_{cyl}}\right] + 2.66x10^{-7}ln^7\left[\frac{1}{2R_{cyl}}\right] \end{array} \right) \quad (10b)$$

$$PA = \frac{\pi a^2}{2R_{cyl}} \quad (10c)$$

Therefore, for all cylinders under investigation, L, R_s, and PA, and hence Kn_D, R, and χ_f (length scale independent) are calculable, as is H. The single fiber efficiency, E_f is related to H via the equation:

$$E_f = \frac{(1+R)(1-V_f)^2}{2Kn_D\chi_f^{1/2}} H \quad (11)$$

Values of E_f inferred from the measurements of Seto et al (2010) and calculated are displayed in Table 4.3. In addition, for each of the three mobility classified nanotubes examined, these values are plotted as a function of $\chi_f^{1/2}/Kn_D$ in Figure 4.5, with equation (10) predictions shown for R = 0.26, 0.31, & 0.49 (the inferred values for the provided nanotube and filter fiber dimensions), respectively. These predictions, with a specified value of R and V_f are solely a function of $\chi_f^{1/2}/Kn_D$, shown previously to be proportional to the Peclet number (Hunt et al., 2013). Despite needing extrapolate equations (1a-c) beyond their range of validity in R, the agreement between measured and predicted single fiber efficiencies, the agreement is good, with most values within 20% of one another.

Table 4.3. A comparison of parameters used in comparison equation (10) predictions to the measurements of Seto et al (2010). The length and a_{cyl} corresponding to the lengths and radii of the nanotubes studied, *R, KnD*, and χ_f is the calculated value based upon the reported nanotubes and filter fiber dimensions, as well as the reported filter face velocity (*U*). E_f (exp.) refers to experimentally measured values, while E_f (pred.) refers to equation (10) predictions. The percentage different (% Diff.) is normalized by experimental single fiber efficiencies.

Length (nm)	***a_{cyl}***	***R***	***$Kn_D x10^3$***	***U (m/s)***	***X_f***	***$Hx10^4$***	***E_f (exp.)***	***E_f (pred.)***	***% Diff.***
1100	27	0.26	2.49	0.05	2.662244	6.25	0.109	0.088	19.3
1100	27	0.26	2.49	0.1	10.64897	9.64	0.090	0.068	24.5
1100	27	0.26	2.49	0.15	23.96019	12.47	0.078	0.058	25.0
1100	27	0.26	2.49	0.3	95.84077	19.43	0.062	0.045	26.8
1100	27	0.26	2.49	0.5	266.2244	27.00	0.059	0.038	36.0
1300	28.5	0.31	2.30	0.05	3.505586	7.19	0.092	0.099	-6.9
1300	28.5	0.31	2.30	0.1	14.02235	11.41	0.078	0.078	-0.5
1300	28.5	0.31	2.30	0.15	31.55028	14.98	0.073	0.068	6.7
1300	28.5	0.31	2.30	0.3	126.2011	23.95	0.061	0.055	10.5
1300	28.5	0.31	2.30	0.5	350.5586	33.90	0.054	0.046	13.4
2100	28.5	0.49	1.70	0.05	5.66287	10.15	0.143	0.169	-18.0
2100	28.5	0.49	1.70	0.1	22.65148	17.53	0.125	0.146	-17.1
2100	28.5	0.49	1.70	0.15	50.96583	24.18	0.118	0.134	-13.7
2100	28.5	0.49	1.70	0.3	203.8633	41.96	0.100	0.116	-16.1
2100	28.5	0.49	1.70	0.5	566.287	63.03	0.087	0.105	-20.2

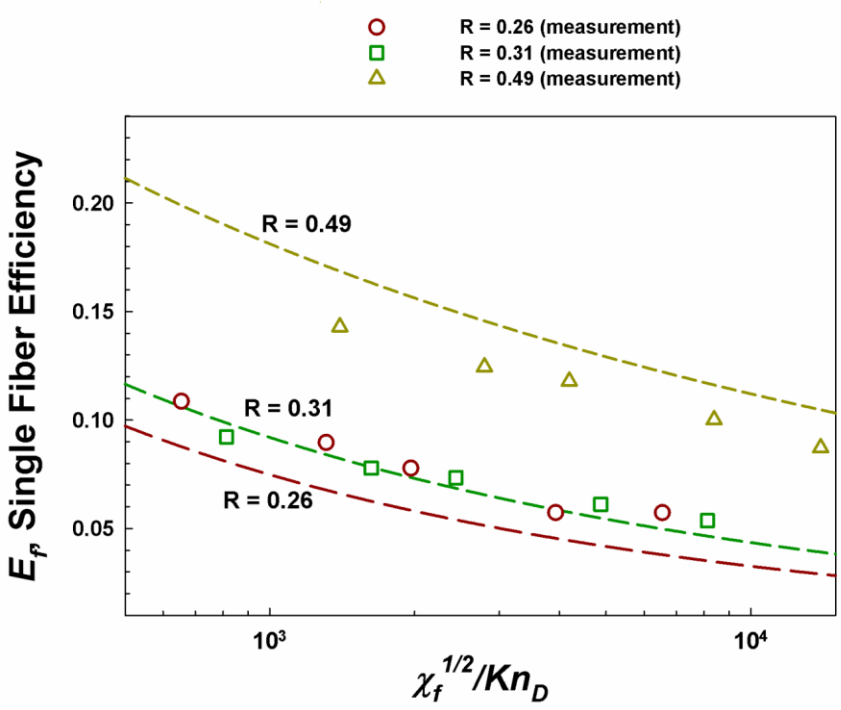

Figure 4.5. A comparison of predicted (dashed line) and measured single fiber efficiencies as a function of $c_f^{1/2}/Kn_D$ for multiwalled carbon nanotube deposition on a fibrous filter. Experimental results are taken from Seto et al (2010).

4.4 Conclusions

Following a procedure as described in Chapter 3 to calculate the collision rate between non-spherical particles, it is shown how to apply the MFPT inferred particle-fiber dimensionless collision kernel expression to particles of arbitrary shape, and provide algebraic equations specifically for calculations with quasifractal aggregates and cylinders. The resulting collision rate calculations are directly linked to the single fiber efficiency. Predicted single fiber efficiencies are in good agreement with those measured for well-characterized carbon nanotubes. The equations developed here should aid in analyzing measurements of non-spherical particle penetration through fibrous filters. Future applications of the MFPT approach should additionally enable determination of the collision rate between particles and non-spherical filter fibers, or with non-fibrous media (e.g. sintered metal spheres).

Chapter 5: Aggregation in the Transition Regime

Abstract: This study looks at the aggregate particle growth and its evolution from the ballistic regime to transition in both momentum and mass transfer. As particles collides forming aggregates, the relevant size descriptors are calculated which are important in accurately modeling the motion of the particles/aggregates.

5.1 Introduction

The aggregation of non-coalescing particles in gas phase environments is challenging to analyze; not only do the aggregates formed have complex, non-spherical structures (Huang, Oh et al. 1998; Filippov, Zurita et al. 2000), but they also have characteristic sizes similar to (1) the hard sphere mean free path of the surrounding gas molecules (Cunningham 1910) and (2) their own persistence distances (Fuchs 1964). The effect of the sizes are morphology have been explained with in the previous chapters, however aggregate growth, which depends on both the mass transfer and momentum transfer effects have not been dealt with. Because of (1), the scalar friction factors and diffusion coefficients for aggregates can be calculated with neither continuum (Lattuada, Wu et al. 2003) nor free molecular (Cai and Sorensen 1994) momentum transfer relationships in all circumstances, and are dependent on momentum transfer Knudsen numbers (*Kn*) (Wang and Sorensen 1999; Zhang, Thajudeen et al. 2012):

$$Kn_i = \frac{\pi\lambda R_{H,i}}{PA_i} \tag{1a}$$

where λ is the gas mean free path, R_H is the aggregate hydrodynamic radius, and PA is the aggregate orientationally averaged projected area. As $Kn \rightarrow 0$, continuum momentum transfer relationships can describe aggregate friction factors, while free molecular relationships apply in the $Kn \rightarrow \infty$ limit. Similarly, because of (2), the collision rates between entities in the gas phase can be determined with neither diffusive (Ziff, McGrady et al. 1985) nor ballistic (Zurita-Gotor and Rosner 2002) mass transfer

approaches, and are dependent upon diffusive Knudsen numbers (Kn_D) (Thajudeen, Gopalakrishnan et al. 2012):

$$Kn_{D,ij} = \frac{(m_{ij}kT)^{1/2}\pi R_{s,ij}}{f_{ij}PA_{ij}} \quad (1b)$$

where kT is the thermal energy, m_{ij} and f_{ij} are the reduced masses and friction factors (which are functions of Kn_i and Kn_j) for colliding entities i and j, $R_{S,ij}$ is the combined Smoluchowski radius for entities i and j, and PA_{ij} is their combined projected area. Additionally, in equation (1b) the term $\frac{(m_{ij}kT)^{1/2}}{f_{ij}}$ is directly proportional to the combined persistence distance for two entities, i.e. the distance over which their relative motion can be described as ballistic. Therefore, as $Kn_D \rightarrow 0$, diffusive mass transfer relationships can describe collision rates and rate coefficients coefficients (collision kernels), while ballistic relationships apply in the $Kn_D \rightarrow \infty$ limit.

Though related, Kn and Kn_D are distinct from one another; the mass transfer regime in which a collision occurs between two entities is not defined by either entity's Knudsen number. To address Kn and Kn_D influences on aggregate motion in the gas phase, our group has recently used direct simulation Monte Carlo (Zhang, Thajudeen et al. 2012) and differential mobility analysis (Gopalakrishnan, McMurry et al. 2013; Thajudeen, Jeon et al. 2013) to examine the friction factors of non-spherical particles in the Kn dependent regime, and a series of Langevin simulations (Gopalakrishnan and Hogan 2011; Gopalakrishnan, Thajudeen et al. 2011; Ouyang, Gopalakrishnan et al. 2012; Thajudeen, Gopalakrishnan et al. 2012) with accompanying experiments (Ouyang, Thajudeen et al. 2013) (with coalescing particles) to examine coagulation in the Kn_D dependent regime. While these studies have led to the development of approaches for friction factor and collision rate calculation for arbitrary shaped entities in the gas phase, they do not completely describe the evolution of the aggregate structures formed by a population of colliding particles. Such structural evolution must be coupled to the evolution of the Kn and Kn_D distributions for a population. For example, monodisperse spherical particles for which $Kn \rightarrow \infty$ and $Kn_D \rightarrow \infty$, may collide with one another and bind (aggregate) upon collision. If such aggregation proceeds

under isothermal, isobaric conditions, the gas mean free path remains constant, but the aggregate projected areas increase proportionally more than the aggregate hydrodynamic radii, thereby decreasing Kn. Eventually, the $Kn \rightarrow \infty$ approximation will no longer hold valid, and Kn influences on friction factors must be considered. Similarly, PA_{ij} for all aggregate pairs increases faster than does $R_{S,ij}$ (coupled with changes to the aggregate persistence distances), leading to a decrease in Kn_D. Therefore, although a system of particles may initially be undergoing ballistic ($Kn_D \rightarrow \infty$) aggregation, eventually all systems have a distribution of finite Kn_D's, and this distribution affects collision rates as well as the structures of the aggregates formed.

Kn and Kn_D evolution for aggregating (non-coalescing) particle populations and the influence this evolution has on aggregate structure have not been examined previously; most studies of aggregation contain implicit assumptions of either fixed Kn or fixed Kn_D for all entities examined, which is never rigorously valid albeit computationally less intensive. Diffusion limited aggregation (DLA) (Witten and Sander 1981) and diffusion limited cluster aggregation (DLCA) (Meakin 1983; Meakin 1984; Meakin, Majid et al. 1984) algorithms, used extensively to model the growth of aggregates, apply specifically in the $Kn_D = 0$ limit, and are often coupled with the assumption of $Kn = 0$, $Kn = \infty$ (Pierce, Sorensen et al. 2006), or with simple yet physically invalid relationships for aggregate diffusion coefficients (Meakin, Vicsek et al. 1985). Conversely, ballistic limited aggregation (BLCA) algorithms mimic aggregation only when $Kn_D = \infty$ (Meakin and Jullien 1988; Mulholland, Samson et al. 1988; Pierce, Sorensen et al. 2006) and remains fixed at this value. As alternative to invoking DLCA or BLCA algorithms, Mountain et al (Mountain, Mulholland et al. 1986) used the dimensional Langevin equation to model aggregation, which enables consideration of changes in Kn_D as aggregation proceeds. However, in their simulations assumptions of either $Kn = 0$ or $Kn = \infty$ were invoked, without considering Kn evolution.

The purpose of this work is to therefore develop and examine the results of a collision limited aggregation algorithm designed to appropriately model the diffusion of

aggregates and their collisions in the transition regime, i.e. for populations where Kn and Kn_D for all aggregates and aggregate pairs, respectively, take on finite, evolving values. In the sections that follow, this algorithm is described. It is based on a dimensionless solution to the Langevin equation and appropriately describes how aggregates growing in a BLCA-like manner to a DLCA-like manner. When applied to initially monodisperse populations of spheres, simulations suggest that the entire system evolution is predicated upon the initial Knudsen number Kn_0, initial diffusive Knudsen number $Kn_{D,0}$. Simulations are used to examine aggregation with different sets of initial Kn_0 and $Kn_{D,0}$ values, with results compared to those obtained for spheres in the transition regime. We also remark on the homogeneity of collision kernels of aggregate populations in the transition regime. Finally, we compute the hydrodynamic radii, projected areas, and radii of gyration for aggregates formed with different initial conditions, and present regression equations to compute these parameters for transition regime aggregates.

5.2 Theory and Numerical Methods

5.2.1 Simulation Overview

Simulations are performed to monitor the size distribution functions of aggregates, which are evolving via thermally driven collisions. We additionally monitor the distributions of Kn and Kn_D for the aggregate population. In all situations, a prescribed number of spherical monomers (n_{tot}) is considered, of prescribed radius a_0, mass m_0, and friction factor f_0, contained in a cubical domain whose dimensionless length ($l^* = l/a_0$) is based on a prescribed solid volume faction:

$$l^* = \sqrt[3]{\frac{4\pi n_{tot}}{3\alpha}} \tag{2}$$

Initially, particles are placed at random locations within the simulation domain, with the condition of no overlap or point contact between monomers. Based on prescribed background gas conditions and the monomer radius, Kn_0 and $Kn_{D,0}$ are defined for this system via equations (1a) and (1b). The monomers move about the simulation domain,

which has periodic boundary conditions on its surface, via the equations of motion noted subsequently. Upon collision, the monomers in question are placed in point contact with one another, and the formed aggregate then moves as a unit. All formed aggregates may subsequently collide with other monomers as well as other aggregates, and in this manner the population of aggregates evolves. For any aggregate and any aggregate pair at any instant in the simulation, Kn_{i} and $Kn_{\mathrm{D,ij}}$ are calculated based upon equations (1a) and (1b), respectively:

$$Kn_i = \left(\frac{Kn_0 \pi R_{H,i}}{PA_i}\right) a_0 \tag{3a}$$

$$Kn_{D,ij} = Kn_{D,0}\sqrt{\frac{N_i N_j}{N_i + N_i}}\left(\frac{\phi_i + \phi_j}{\phi_i \phi_j}\right)\frac{\pi R_{s,ij} a_0}{PA_{ij}} \tag{3b}$$

where N_i is the number of spherical monomers in aggregate i ($N_i = 1$ for a monomer, $\mathrm{N_i} > 1$ for an aggregate), ϕ_i is the ratio of the friction factor of the entity i to the friction factor of a monomer, defined subsequently, and the noted size scales are calculated using the methods described in the *Aggregate Property Calculations* section. Correspondingly, the average Knudsen number, Kn_{ave}, and average diffusive Knudsen number, $Kn_{\mathrm{D,ave}}$ are calculated at any instant with the equations:

$$Kn_{ave} = \frac{\sum_{i=1}^{n_e} Kn_i}{n_e} \tag{3c}$$

$$Kn_{D,ave} = \frac{\sum_{i=1}^{n_e}\sum_{j=i+1}^{n_e} Kn_{D,ij}}{n_e(n_e - 1)} \tag{3d}$$

where n_e is the number of entities, i.e. monomers and aggregates, in the simulation domain.

5.2.2 Equations of Motion

The evolution of the dimensionless velocity and dimensionless position vectors of the center of mass any entity (which all particles within the entity remain fixed with respect to) is determined via a solution to the Langevin equations non-dimensionalized from the equations provided by Ermak and Buckholtz (Ermak and Buckholz 1980). Only the translational motion of entities is considered, and both potential and viscous interactions between monomers and aggregates are neglected (though they can be

considered by modifying the equations of motion). Further, via use of a Langevin equation solution to model motion, entities are moved istropically throughout the domain, i.e. the influence of an aggregate's orientation on its motion is neglected. In these equations the dimensionless forms of the position vector and velocity vector for an entity, as well as the simulation time are given by the relationships: $\vec{\ }_i \quad a_0$,

$\vec{\ }_i \quad a_0 f_0 \vec{\ }_i$ and $\tau = \frac{f_0}{m_0} t$, respectively. The dimensionless recurrence relation for the velocity vector ($\vec{v}_i^*$) of entity *i* at time $\tau + \Delta\tau$, given its velocity vector at dimensionless time τ, is:

$$\vec{v}_i^*(\tau + \Delta\tau) = \vec{v}_i^*(\tau) \exp\left(-\frac{\phi_i}{N_i}\Delta\tau\right) + \vec{A}_{1,i} \tag{4a}$$

$$\langle \vec{A}_{1,i}^2 \rangle = 6\frac{Kn_{D,0}^2}{N_i}\left[1 - exp\left(-2\frac{\phi_i}{N_i}\Delta\tau\right)\right] \tag{4b}$$

where $\Delta\tau$ is the dimensionless timestep, and $\vec{\ }_{1,i}$ is Gaussian distributed random vector with zero mean and a variance defined by equations (4b). Similarly, the dimensionless position vector of entity *i* at time $\tau + \Delta\tau$ is determined with the recurrence relation:

$$\vec{x}_i^*(\tau + \Delta\tau) = \vec{x}_i^*(\tau) + \frac{N_i}{\phi_i}\left(\vec{v}_i^*(\tau + \Delta\tau) + \vec{v}_i^*(\tau)\right)\left[\frac{1-exp\left(\frac{\phi_i}{N_i}\Delta\tau\right)}{1+exp\left(\frac{\phi_i}{N_i}\Delta\tau\right)}\right] + \vec{A}_{2,i} \tag{4c}$$

$$\langle \vec{A}_{2,i}^2 \rangle = 12Kn_{D,0}^2\frac{N_i}{\phi_i^2}\left[\frac{\phi_i}{N_i}\Delta\tau - 2\left[\frac{1-exp\left(\frac{\phi_i}{N_i}\Delta\tau\right)}{1+exp\left(\frac{\phi_i}{N_i}\Delta\tau\right)}\right]\right] \tag{4d}$$

$\vec{\ }_{2,i}$ is additionally a Gaussian distributed random vector with mean zero and variance (4d). Equations (4a-d) consider the influences of inertia, drag, and diffusion on entity motion. Apparent in these equations, entity motion depends upon $Kn_{D,0}$, the initial diffusive Knudsen number for monomer (an input to simulations), as well as N_i and ϕ_i. The distribution of the latter two parameters is dependent on the simulation itself, hence (4a-d) suggest that the evolution of a population of monomers is solely dependent on $Kn_{D,0}$ (as well as α, which is also an input). However, through examination of the

equations defining ϕ_i, it is evident that system evolution is also dependent on Kn_0, the initial monomer Knudsen number. The friction for a monomer is defined as (Davies 1945):

$$f_0 = \frac{6\pi\mu a_0}{1+Kn_0\left(1.257+0.4exp\left(\frac{-1.1}{Kn_0}\right)\right)} \tag{5a}$$

where μ is the background gas dynamic viscosity. Following Dahneke (Dahneke 1973), it has been recently shown numerically (Zhang, Thajudeen et al. 2012) and experimentally (Gopalakrishnan, McMurry et al. 2013; Thajudeen, Jeon et al. 2013) that the orientationally averaged friction factor for an aggregate is well described by the relationship (explained in Chapter 2) :

$$f_i = \frac{6\pi\mu R_{H,i}}{1+Kn_i\left(1.257+0.4exp\left(\frac{-1.1}{Kn_i}\right)\right)} \tag{5b}$$

Noting $\phi_i = f_i/f_0$, leads to:

$$\phi_i = \frac{R_{H,i}}{a_0}\frac{\left(1+Kn_0\left(1.257+0.4exp\left(-1.1/Kn_0\right)\right)\right)}{\left(1+Kn_i\left(1.257+0.4exp\left(-1.1/Kn_i\right)\right)\right)} \tag{5c}$$

5.2.3 Aggregate Property Calculations

To solve the equations of motion for aggregates, as well as to track the evolution of Kn_{ave} and $Kn_{D,ave}$ as functions of τ, it is necessary to calculate several size descriptors for aggregates and aggregates pairs upon aggregate formation: $R_{H,i}$ and PA_i for each aggregate, and $R_{S,ij}$ and PA_{ij} for aggregate pairs and aggregate-monomer pairs. As in prior studies, for each aggregate, the orientationally averaged hydrodynamic radius is equated with the Smoluchowski radius for the aggregate with a point mass, as per the Hubbard-Douglas approximation (Hubbard and Douglas 1993; Douglas, Zhou et al. 1994; Given, Hubbard et al. 1997), and is calculated using the Brownian Dynamics algorithm described in the supplemental information of Gopalakrishnan et al (Gopalakrishnan, Thajudeen et al. 2011) and in Chapter 2 in this thesis. Similarly,

orientationally averaged projected areas are calculated with previously described algorithms (Larriba and Hogan 2013), and determine of these two parameters for all aggregates enables determine of Kn_{ave} (equation 3d). $R_{S,ij}$ and PA_{ij} calculations are performed at all times in simulations for 200 randomly selected entity pairs using the algorithms described by in Chapter 3. (Thajudeen, Gopalakrishnan et al. 2012). Calculations are limited to 200 entity pairs due to computational constraints, and determine $Kn_{D,ave}$ at each time using $R_{H,i}$, $R_{H,j}$, PA_i, PA_j, $R_{S,ij}$, and PA_{ij} to calculate $Kn_{D,ij}$ for these pairs only. Additionally, for aggregate-aggregate pairs (non-monomer), we utilize the approximation $\pi R^2_{S,ij} \approx PA_{ij}$ found reasonably valid previously for similarly sized aggregates (Thajudeen, Gopalakrishnan et al. 2012).

While the aforementioned length scales are evaluated specifically because they influence particle transport, the radii of gyration ($R_{g,i}$) for aggregates are also of interest, as prior numerical studies of aggregation (in which a specific constant diffusive Knudsen number is assumed (Meakin 1984; Pierce, Sorensen et al. 2006)) find that the number of monomers per aggregate scales with the aggregate radius of gyration via the relationship

$$N_i = k_{f,i}\left(\frac{R_{g,i}}{a_0}\right)^{D_{f,i}} \tag{6a}$$

where $k_{f,i}$ is the pre exponential factor and $D_{f,i}$ is the Hausdorff fractal dimension. For each aggregate, $R_{g,i}/a_0$ is calculated as:

$$R_{g,i} = \sqrt{\frac{\sum_{j=1}^{N_i}(\vec{x}_j^* - \vec{x}_{cm}^*)^2 + 0.6a_0^2}{N_i}} \tag{6b}$$

where $\vec{x}_j^*$ is the coordinate of the center of j^{th} monomer in an aggregate with N_i monomers and $\vec{x}_{cm}^*$ is the coordinate of the center of mass of the aggregate.

5.2.4 Simulation Parameters

In total, as inputs, simulations require a value of n_{tot}, $\Delta\tau$, α, Kn_0, and $Kn_{D,0}$. As noted previously, such simulations are computationally intense; each time an aggregate forms it is necessary to calculate is hydrodynamic radius and projected area, as well as

the combined Smoluchowski radii and collision areas. Simulations are restricted to several cases, summarized Table 5.1, and chosen to monitor the evolution of a population of particles from the free molecular/ballistic regimes to the continuum/diffusive regimes of momentum and mass transfer. Simulations are ceased prior to the formation of aggregates with more than 300 primary particles. While the stopping simulations at this point limits this study to smaller aggregations than are examined in many prior aggregation simulations (Meakin, Majid et al. 1984; Meakin, Vicsek et al. 1985; Wang and Sorensen 2001; Pierce, Sorensen et al. 2006), aggregates composed of 10^1-10^2 primary particles are frequently observed in scalable flame synthesis systems (Scheckman, McMurry et al. 2009; Eggersdorfer, Grohn et al. 2012; Thajudeen, Jeon et al. 2013), hence our results have direct implications for particle growth in high temperature gas phase reactors. For all reported results n_{tot} = 10,000 (though results are found insensitive to n_{tot} through simulations which both larger and smaller values) and we vary α from 0.005 to 0.20 to examine the influence of the solid volume fraction. While such α values are extremely high for aerosols, we show that the evolution of Kn_{ave} and $Kn_{\mathrm{D,ave}}$ is minimally influenced by α over the simulation times examined, during which the aerosol remains in the dilute limit (Sorensen and Chakrabarti 2011). Finally, based on prior simulations (Gopalakrishnan and Hogan 2011), the function $\Delta\tau=0.005/Kn_{D,0}^2$ is used.

5.3 Results and Discussion

5.3.1 Simulation Validation & Depiction

To examine the validity of the presented algorithm, we compare Kn_{ave} and $Kn_{\mathrm{D,ave}}$ resulting from simulations of completely coalescing spheres (i.e. not aggregates) to those resulting from constant number Monte Carlo simulations (Smith and Matsoukas 1998; Lin, Lee et al. 2002) as performed by Ouyang et al (Ouyang, Thajudeen et al. 2013) for hard sphere potentials, in which the collision rate of particles is described by the regression equation provided by Gopalakrishnan and Hogan (Gopalakrishnan and Hogan 2011). This collision rate expression has been developed

for particles whose motion is described by a Langevin equation, agrees well with many expressions describing collisions between spherical particles throughout the entire Kn_D range (Fuchs 1964; Dahneke 1983; Veshchunov 2010), and is further supported by experimental measurements (Wagner and Kerker 1977; Chan and Mozurkewich 2001). Therefore, modification of the noted simulation approach to have particles coalesce upon collision, such that each collision creates a spherical particle whose volume and mass are taken as the sum of the colliding particles volumes and masses respectively, should lead to good agreement with the results of such constant number Monte Carlo simulations. With $\alpha = 0.005$, coalescing particle simulation and constant number Monte Carlo simulation results are shown in Figure 5.1 for three different Kn_0, $Kn_{D,0}$ pairs. As time evolves in both simulations, both Kn_{ave} and $Kn_{D,ave}$ decrease, hence all plots begin in the upper right and cease in the lower left regions of plots. This additionally leads to a change in the manner in which both momentum and mass transfer occur throughout simulations; with the exception of results for $Kn_{D,0} = 3$ (which are initially the transition regime for mass transfer), initially, all simulations begin with collisions occurring ballistically.

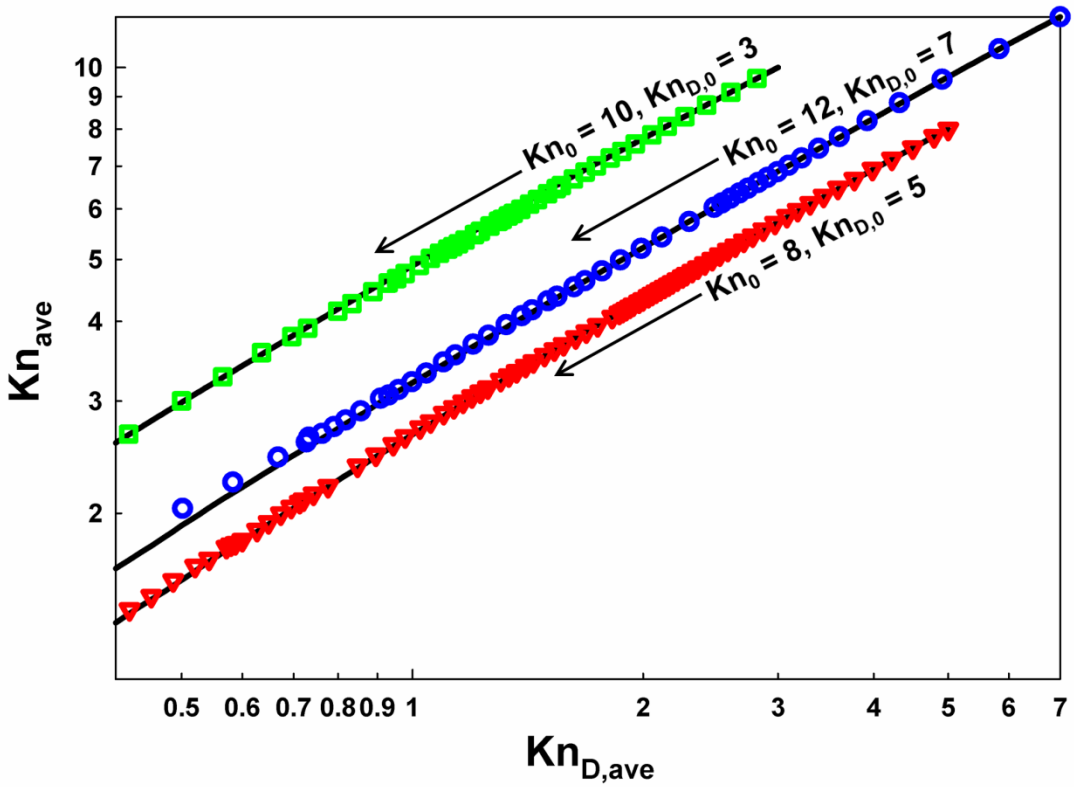

Figure 5.1. Plots of the evolution of the average Knudsen number and diffusive *Kn*udsen number for coalescing particles with initially monodisperse particles at a solid volume fraction of 0.005. The initial Knudsen numbers and diffusive Knudsen numbers, as well as the direction of evolution, are labelled on the plot. Symbols represent results from Langevin dynamics simulations, while lines represent results from constant number Monte Carlo simulations.

As collision proceed and particles grow in size, $Kn_{D,ave}$ decreases, and below $Kn_D \approx 3.7$ the collision kernel for two entities differs begins to differ noticeably from ballistic collision kernel (Thajudeen, Gopalakrishnan et al. 2012), as explained in Chapter 3. Similarly, as *Kn* drops below approximately 7.1, the friction factor for an entity begins to differ appreciably from the friction factor expected in the free molecular regime, and depends upon viscous influences (gas molecule-gas molecule momentum exchange). Therefore, as noted in the introduction section, collision based growth leads to a change in the manner in which entities move between collisions as well as the manner in which gas molecules transfer momentum to entities, with further Kn_D and *Kn* decreases leading to wholly diffusive motion between collision and wholly continuum

(viscous) momentum transfer. In modeling this evolution both simulation types are in excellent agreement with one another, and as evidenced in Ouyang et al (Ouyang, Thajudeen et al. 2013), for coalescing particles such results are supported by experimental measurements. It can therefore be concluded that the presented algorithm is able to reproduce expected results for Langevin simulations, and enables us to monitor the evolution of both Knudsen numbers while appropriately modeling entity motion through the entire Kn and Kn_D ranges.

Analogous to Figure 4 of Pierce et al (Pierce, Sorensen et al. 2006), the formation of aggregates in simulations with non-coalescing particles is depicted in Figure 5.2a for $\alpha = 0.001$ and $n_{tot} = 2000$ (used to avoid visual crowding in the figure), which is depicts all primary particles in the simulate initially, and after 95,000 timesteps at constant $\Delta\tau = 5.55 \times 10^{-4}$, with $Kn_0 = 10$ and $Kn_{D,0} = 3$. Clearly evident are both isolated spheres and multiple primary particle-containing aggregating after 95,000 timesteps are completed. Also with non-coalescing particles and this initial Knudsen number-diffusive Knudsen number pair (with $n_{tot} = 10{,}000$), Figure 5.2b displays the evolution of Kn_{ave} and $Kn_{\mathrm{D,ave}}$ for a range of solid volume fractions, from $\alpha = 0.01$ to $\alpha = 0.20$. As with coalescing particles, Kn_{ave} and $Kn_{\mathrm{D,ave}}$ progressively decrease as simulations proceed. However, somewhat surprisingly, Kn_{ave} and $Kn_{\mathrm{D,ave}}$ evolution is found to be insensitive to solid volume fraction (though both Knudsen numbers decrease more rapidly at higher solid volume fractions). In accordance with the findings of Sorensen & Chakrabarti (Sorensen and Chakrabarti 2011), as simulations proceed, one might expect the average nearest neighbor distance between aggregates to decrease, with larger solid volume fractions leading to progressively smaller nearest neighbor distances. As the nearest neighbor distance begins to approach the persistence distance, aggregate motion between collisions is expected to be constrained to the ballistic regime (i.e. aggregates do not have sufficient time to behave diffusively, as they might in a particle dilute system), in contrast to the ballistic to diffusive motion transition examined here. Such nearest neighbor influences would presumably influence Kn_{ave} and $Kn_{D,ave}$ evolution. However, in our simulations suggest that this is

not the case, that Knudsen number evolution is not strongly influenced by solid volume fraction, at least for the simulation times examined (note all simulations are ceased well prior to gelation).

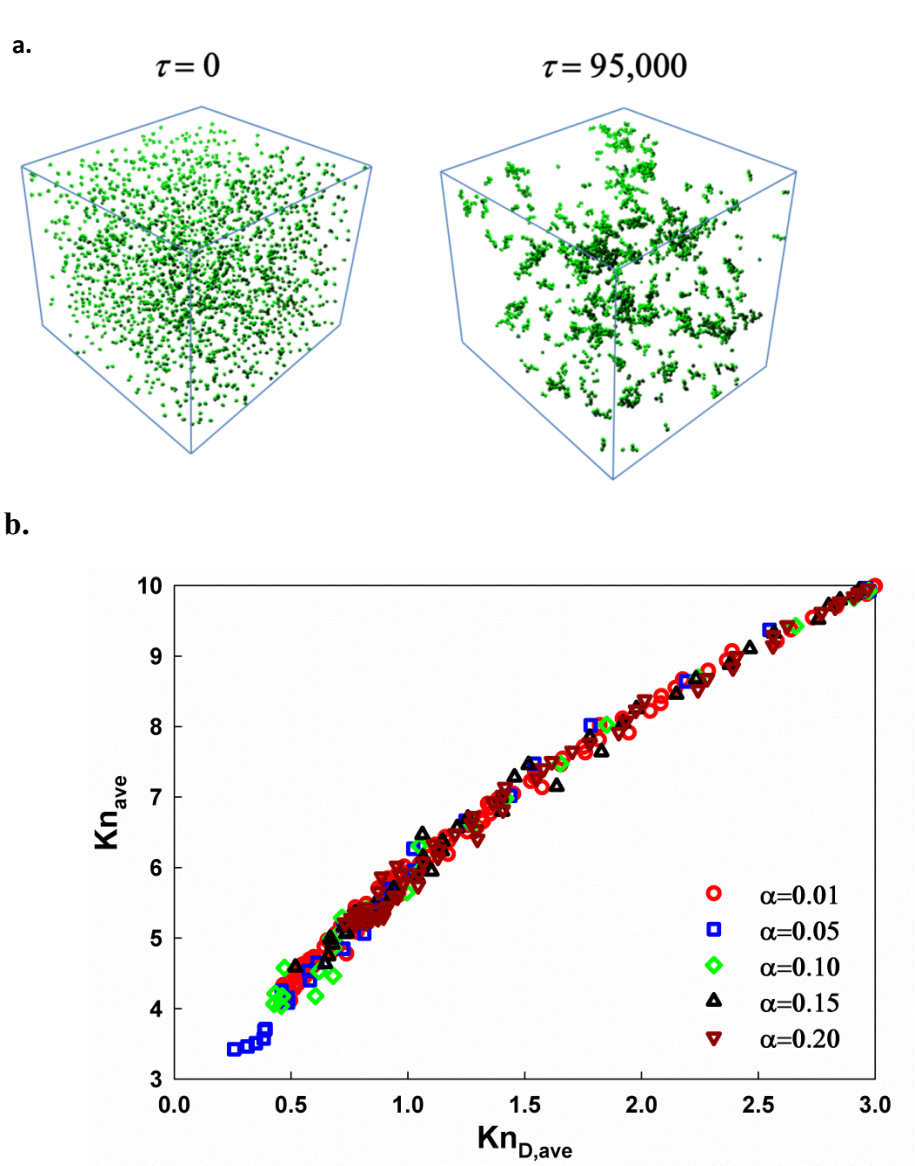

Figure 5.2 (a.) Depiction of Langevin simulations initially and after 95,000 dimensionless time steps. (b.) The evolution of Kn_{ave} and $Kn_{D,ave}$ for $Kn_0 = 10$, $Kn_{D,0} = 3$, with various monomer solid volume fractions.

5.3.2 Knudsen Number and Diffusion Knudsen Number Evolution for Non-Coalescing Particles

As already noted, Ouyang et al (Ouyang, Thajudeen et al. 2013) show through simulations and experiments that the evolution of the two average Knudsen numbers for coalescing particles can be described clearly, and the algorithm presented here is able to reproduce their results. The Knudsen number evolution of non-coalescing particles is compared to coalescing systems with the same initial monodisperse Kn_0 and $Kn_{D,0}$. It is reiterated that for both systems Kn and Kn_D are defined for any entity and pair of entities by equations (1a) and (1b), respectively. Figure 3a displays plots of Kn_{ave} as a function of $Kn_{D,ave}$ for coalescing spheres with Kn_0 = 12, $Kn_{D,0}$ = 7, non-coalescing spheres with Kn_0 = 12, $Kn_{D,0}$ = 7, Kn_0 = 9.55, $Kn_{D,0}$ = 4.90, and Kn_0 = 7.75, $Kn_{D,0}$ = 3.58, all with α = 0.005. The latter two initial conditions are Knudsen number-Diffusive Knudsen number pairs which arise during simulations with coalescing spheres with Kn_0 = 12, $Kn_{D,0}$ = 7 as initial conditions. They are examined here because with monomodal coalescing spheres, it has been found that Kn_{ave}-$Kn_{D,ave}$ curves for isothermal, isobaric collisional growth are not strongly influenced by the polydispersity of the distribution. Also marked on the curve is a vertical line corresponding to $Kn_{D,ave}$ = 3.7, the approximate barrier between the ballistic regime and the transition regime for mass transfer (Thajudeen, Gopalakrishnan et al. 2012). Clearly evident is the differing Kn_{ave}-$Kn_{D,ave}$ evolution for non-coalescing particles. In all displayed circumstances, aggregate formation leads to a more rapid decrease in $Kn_{D,ave}$ relative to the decrease observed in coalescing systems. Therefore, aggregate collisional growth is more likely to be described by transition or diffusive kinetics than ballistic, when compared to spheres of the same for a given Kn_{ave}.

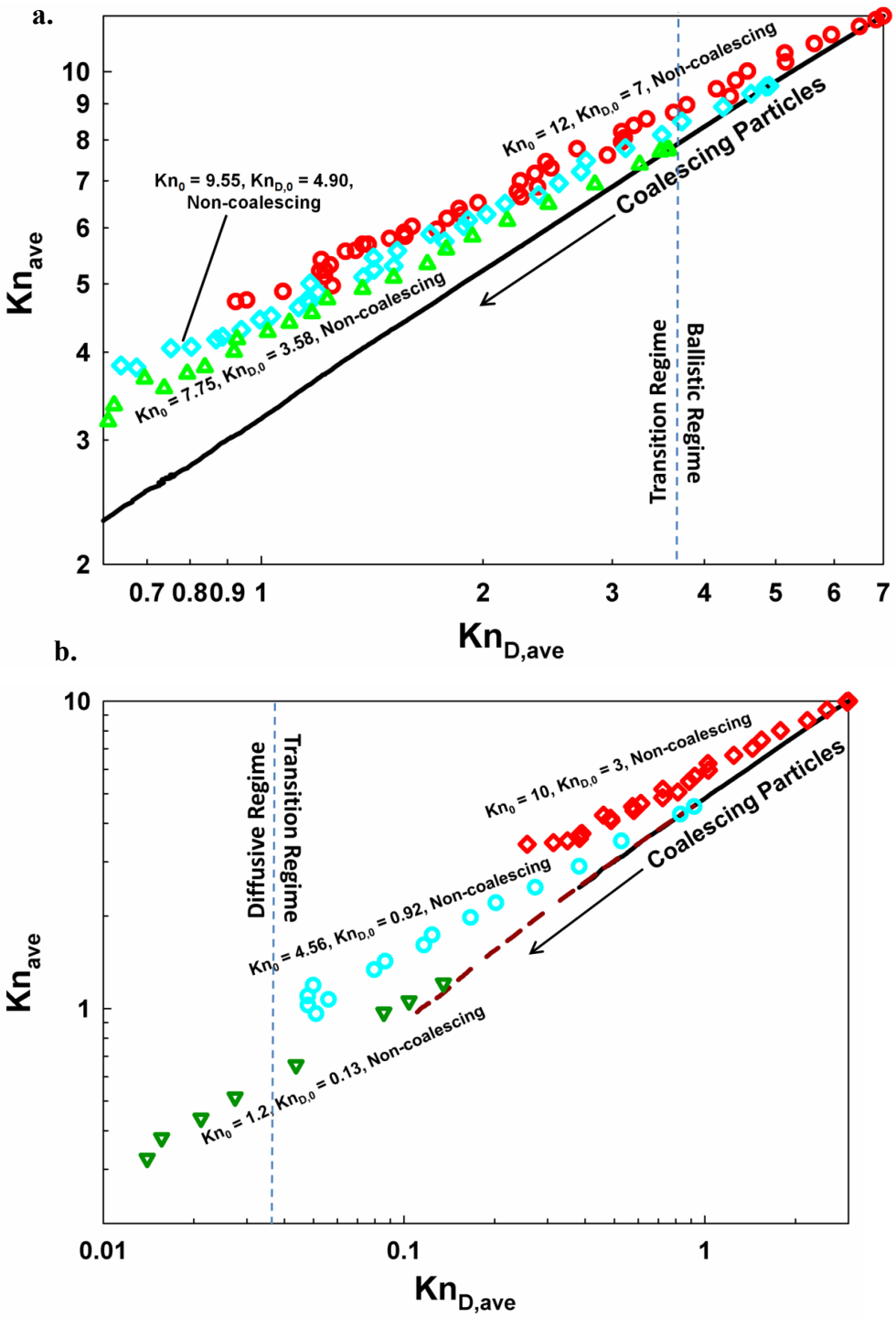

Figure 5.3: The evolution of Kn_{ave} and $Kn_{D,ave}$ for non-coalescing (symbols) and coalescing (lines) particles undergoing collisions. Displayed results have Kn_0, Kn_{D0} values which derive from coalescing particle simulations with (a.) $Kn_0 = 12$, $Kn_{D,0} = 7$ and (b.) $Kn_0 = 10$, $Kn_{D,0} = 3$.

This result is not unique to the conditions shown in Figure 5.3a; Figure 5.3b is a similar plot of Kn_{ave}-$Kn_{D,ave}$ evolution for coalescing spheres of Kn_0 = 10, $Kn_{D,0}$ =3 and Kn_0 = 4.54, $Kn_{D,0}$ = 0.92 (which fall on the same Kn_{ave}-$Kn_{D,ave}$ curve), as well as non-coalescing spheres of varying Kn_0, $Kn_{D,0}$ pairs. In all circumstances, $Kn_{D,ave}$ for aggregates increases more rapidly. These results show clearly that the regime in which collisions occur cannot be defined simply from knowledge on the Kn distribution for a system, as is often done (Vemury and Pratsinis 1995). Rather, collisions are governed by the evolving Kn_D distribution, which differs significantly for non-coalescing particles (and presumably for partially coalescing particles). Further, results suggest that aggregating aerosol systems (near atmospheric pressure) initially in the ballistic collision regime very quickly leave this regime, limiting the appropriateness of BLCA-type simulations (Mulholland, Samson et al. 1988) to only systems of exceedingly low pressure or to very limited extents of particle growth.

The rapid evolution of $Kn_{D,ave}$ and the Kn_D distribution for aggregating systems additionally draws into questions the definition of a collision kernel homogeneity factor in this instance. In the dilute limit, the number of collisions between two entities of type i and j per unit volume per unit time (the collision rate, R_{ij}) is defined as:

$$R_{ij} = \beta_{ij} n_i n_j \tag{7a}$$

where n_i and n_j are the number concentrations of entities i and j, respectively, and β_{ij} is the collision rate coefficient/collision kernel. A commonly invoked assumptions is that the collision kernel is a homogenous function, such that for aggregates with number of monomers N_i and N_j:

$$\beta_{ij}(CN_i, CN_j) = C^{\gamma}\beta_{ij}(N_i, N_j) \tag{7b}$$

where C is a positive real number, and γ is the kernel homogeneity factor. With a homogenous kernel function, a plot of $1/n(\tau) - 1/n(0)$ (where n is the total number concentration of all entitites present) versus dimensionless time yields a power law relationship with scaling $z = (1-\gamma)^{-1}$ (z is commonly referred to as the kinetic exponent). However, Langevin simulations with aggregates give rise to a collision kernel function of the form as given in Chapter 3

$$\beta_{ij} = \frac{f_{ij}}{m_p}\frac{{PA_{ij}}^2}{\pi^2 R_{S,ij}} H\left(Kn_{\mathrm{D,ij}}\right) \tag{7c}$$

where $H(Kn_{\mathrm{D,ij}})$ is defined as:

$$H = \frac{12.566Kn_{D,ij}^2+25.836Kn_{D,ij}^3+56.204Kn_{D,ij}^4}{1+3.502Kn_{D,ij}+7.211Kn_{D,ij}^2+11.211Kn_{D,ij}^3} \tag{7d}$$

This functional form suggests that collision kernel homogeneity would only be found in particular circumstances, i.e. for particular aggregate geometries where $R_{S,ij}$, PA_{ij}, $R_{S,i}$, $R_{S,j}$, PA_i, and PA_j all scale with N_i and N_j in an appropriate fashion.

For $Kn_0 = 8$, $Kn_{\mathrm{D},0} = 5$, $Kn_0 = 4.54$, $Kn_{\mathrm{D},0} = 0.92$, and $Kn_0 = 0.01$, $Kn_{\mathrm{D},0} = 0.01$, Figure 5.4 shows plots of the number of entities present in simulations as functions of dimensionless simulation time.

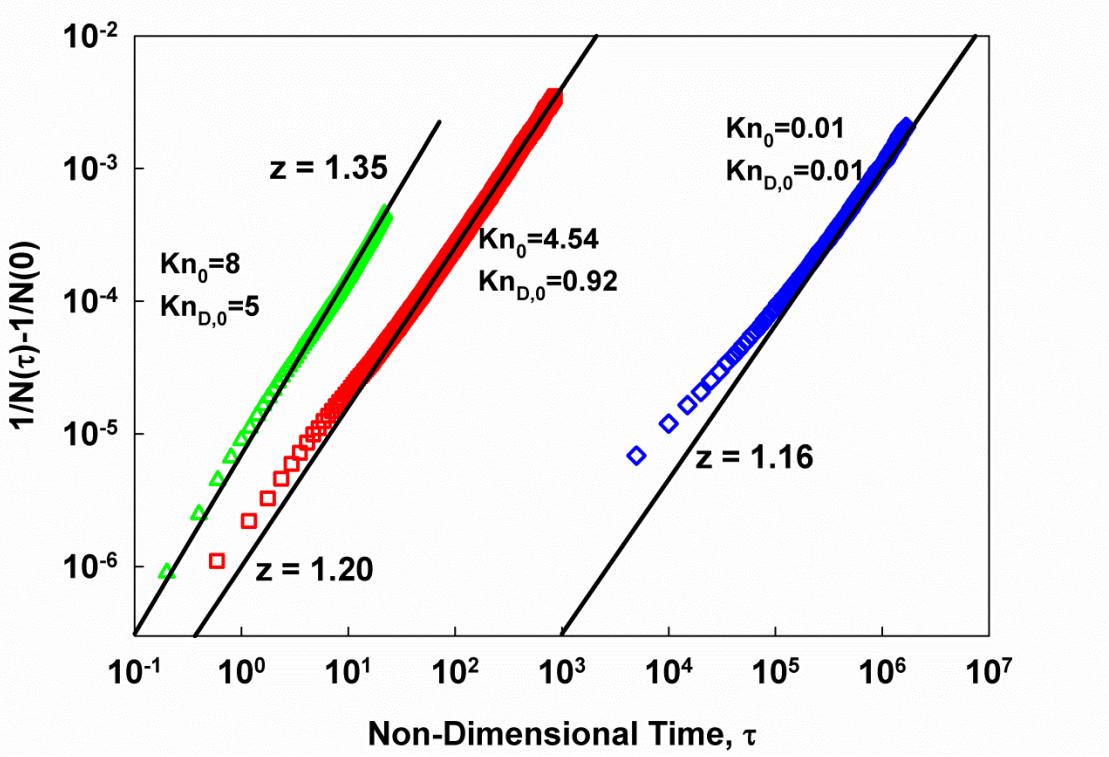

Figure 5.4: Plots of $1/n_e(\tau) - 1/n_e(0)$ as functions of τ deriving from Langevin simulations with a = 0.005. $\alpha = 0.005$ for all displayed results.

All simulations were initiated with 10,000 monomers and a solid volume fraction of 0.005. The first two initial Knudsen number-diffusive Knudsen number pairings lead to simulations in which mass and momentum transfer do not occur

initially in the diffusive and continuum regimes respectively, while $Kn_0 = Kn_{D,0} = 0.01$ is close to these limits. In related simulations which apply in the $Kn = \infty$, $Kn_D = 0$ regime (constant), Pierce et al (Pierce, Sorensen et al. 2006) found that such plots show an initial region in which $z = 1$, and a later time region in which $z < 1$. A non-constant value of z is also observed here, with regression lines displayed based upon inferred values of z at later simulations times. These kinetic exponent values are all found to be greater than one, and are in reasonable agreement with experimentally inferred kinetic exponents and kernel homogeneities (Wang and Sorensen 2001). However, the inferred kinetic exponents are found to be dependent upon the initial Knudsen number and diffusive Knudsen number conditions and unlike the suggestions of Pierce et al, not predictable *a priori*. Further, the early time regions of all plots do not all have kinetic exponents of $z = 1$. Based on these results, we caution against the assumption of a homogenous collision kernel function of constant homogeneity for aggregating systems in the transition regime, and remark that further detailed study, probing the influences of Kn_0, $Kn_{D,0}$, and α will be necessary to determine under what conditions the collision kernel can be approximated as homogenous.

5.3.3 Aggregate Hydrodynamic Radii and Projected Areas

Figure 5.5a is a plot of the number of primary particle in aggregates as a function of the normalized radius of gyration for aggregates from all simulations at varying simulation times. The legend for all figure 5.5 plots is provided in table 5.1. Despite the varying initial conditions and solid volume fractions, and simulation times, all simulations lead to aggregates which lie in similar regions of $[N_i, (R_g/a_0)]$ space. However, this region is sufficiently broad to suggest that equation (6a) is only approximately valid for aggregates in the transition regime, or, as has been proposed by Heinson and coworkers (Heinson, Sorensen et al. 2010; Heinson, Sorensen et al. 2012), there are multiple "families" of quasifractal aggregates with a distribution in pre-exponential factor (as proposed by Heinson et al) and/or a distribution in fractal dimension. Perhaps more important to understanding aggregate behavior than the

relation between N_i and R_g, however, is the scaling of $R_{H,i}$ and PA_i with N_i for aggregates formed under different conditions, as it these parameters which define aggregate friction/mobility (Melas, Isella et al.), and hence aggregate transport both in the environment and in mobility based measurement devices. With the aforementioned procedures to infer R_H and PA for aggregates in simulations, figures 5.5b & 5.5c are plots of R_H/a_0 versus N_i and PA/a_0^2 versus N_i for the same aggregates plotted in figure 5.5a. Somewhat remarkably, for all simulated conditions and simulation times, these plots both collapse to near power-law relationships, with both R_H/a_0 and PA/a_0^2 revealing a much clearer relationship with N_i than does R_g/a_0.

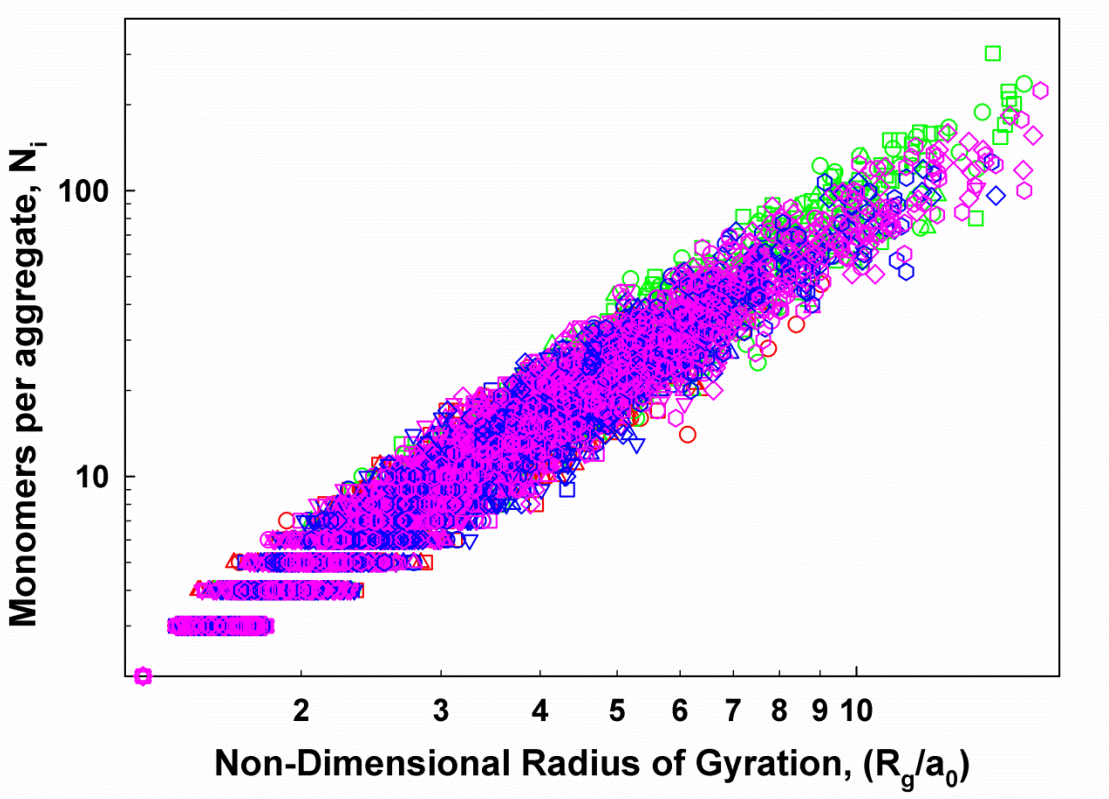

Figure 5.5a: Number of monomers per aggregate plotted against the aggregate radius of Gyration for different initial conditions. The conditions for each symbol are displayed in Table 5.1.

This observation is in line with a number of experimental studies (Scheckman, McMurry et al. 2009; Eggersdorfer, Grohn et al. 2012; Shapiro, Vainshtein et al. 2012) in which the equivalent mobility size of aggregates is found to scale with the aggregate

mass under nearly all conditions, including recent work from our group (Thajudeen, Jeon et al. 2013), in which the mobility equivalent size was found to scale with the aggregate mass in spite of aggregates of disparate morphologies observed (though in these experiments, aggregate sintering and restructuring may have occurred).

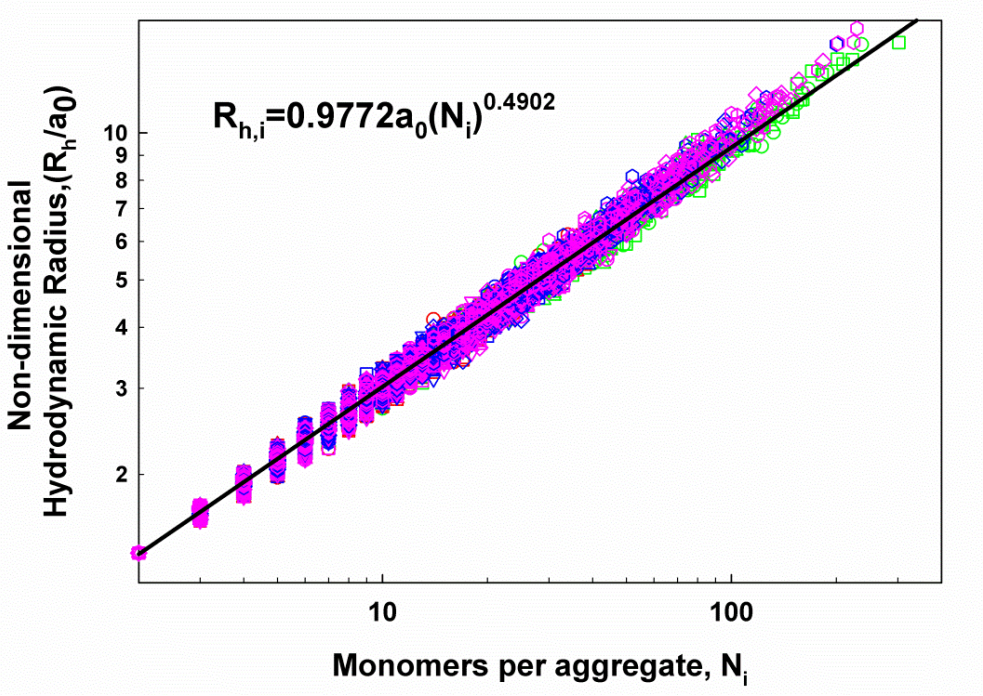

Figure 5.5b: Non-dimensional Hydrodynamic radius plotted against the number of monomers in an aggregate. The conditions for each symbol are displayed in Table 5.1.

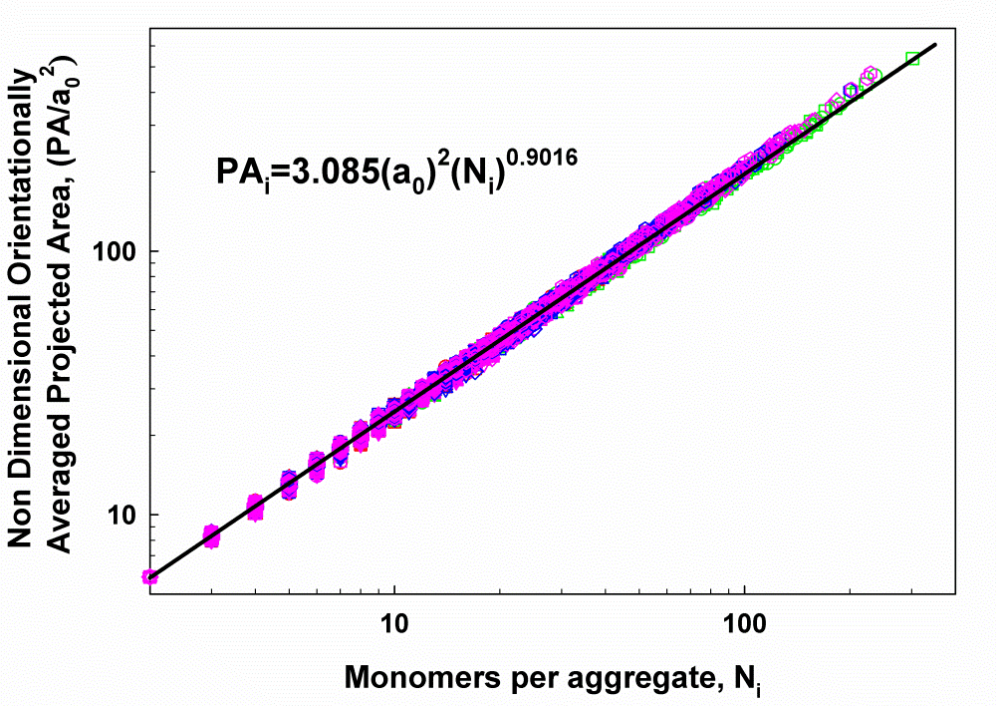

Figure 5.5c: Non-dimensional Orientationally Averaged projected Area plotted against the number of monomers in an aggregate. The conditions for each symbol are displayed in Table 5.1.

This scaling enables the development of regression equations for the hydrodynamic radius and projected area:

$$R_{H,i} = 0.9772 a_0 N_i^{0.4902} \quad (8a)$$

$$PA_i = 3.085 a_0^2 N_i^{0.9016} \quad (8b)$$

These equations can be used, in conjunction with the equations provided by Zhang et al (Zhang, Thajudeen et al. 2012) and also utilized here, to determine the scalar friction factors, diffusion coefficients, and electrical mobilities of aggregates formed in the transition regime. However, in instances when significant aggregate sintering or restricting occur (Schmid, Tejwani et al. 2004), these equations will likely not be valid. Further, the results displayed in Figure 5.3, focusing on the evolution of Kn_{ave} and $Kn_{D,ave}$ would strongly influence by aggregate restructuring and sintering, with the results presented here serving as the limiting curves for Kn_{ave}-$Kn_{D,ave}$ with zero coalescence and complete coalescence respectively.

Table 5.1. List of the solid volume fractions, initial Knudsen numbers, and diffusive Knudsen numbers used in Langevin simulations, as well as the average Knudsen numbers and diffusive Knudsen numbers at the time simulations were ceased. The "Symbols" column display the symbol used for simulation results in Figures 5.5a-c.

α	Kn_0	$Kn_{D,0}$	Kn_{ave}	$Kn_{D,ave}$	Symbols
0.01	10	3	6.76	1.35	
0.01	10	3	4.04	0.46	
0.01	12	7	9.03	3.81	
0.01	12	7	6.56	1.25	
0.01	8	5	5.43	2.33	
0.01	8	5	3.64	1.08	
0.005	10	3	5.69	0.9	
0.005	10	3	4.96	0.65	
0.005	12	7	8.94	3.75	
0.005	12	7	8.07	3.11	
0.005	8	5	5.54	2.31	
0.005	8	5	5.08	1.82	
0.005	9.55	4.9	6.45	2.1	
0.005	9.55	4.9	5.77	1.75	
0.005	4.54	0.92	1.78	0.13	
0.005	4.54	0.92	1.39	0.08	
0.005	0.01	0.01	0.0043	0.0028	
0.005	0.01	0.01	0.0038	0.0023	

Finally, equations (8a) and (8b) can be compared to both previously proposed equations for the hydrodynamic radii and projected areas of aggregates, as well as experimental measurements. Figures 5.6a and 5.6b are plots of R_H/a_0 and PA/a_0^2 as functions of N_i from equations (8a) & (8b), the values for the "average aggregates" inferred from images of mobility classified aggregates whose properties are given in Table A.2 in Appendix section and regression equations proposed by Sorensen (Sorensen 2011), which for R_H are given as:

$$R_{H,i} = a_0 N_i^{0.46} \qquad N_i < 100 \qquad (9a)$$

$$R_{H,i} = 0.65 a_0 N_i^{0.56} \qquad N_i > 100 \qquad (9b)$$

and for PA:

$$PA_i = 3.1415 a_0^2 N_i^{0.92} \qquad (9c)$$

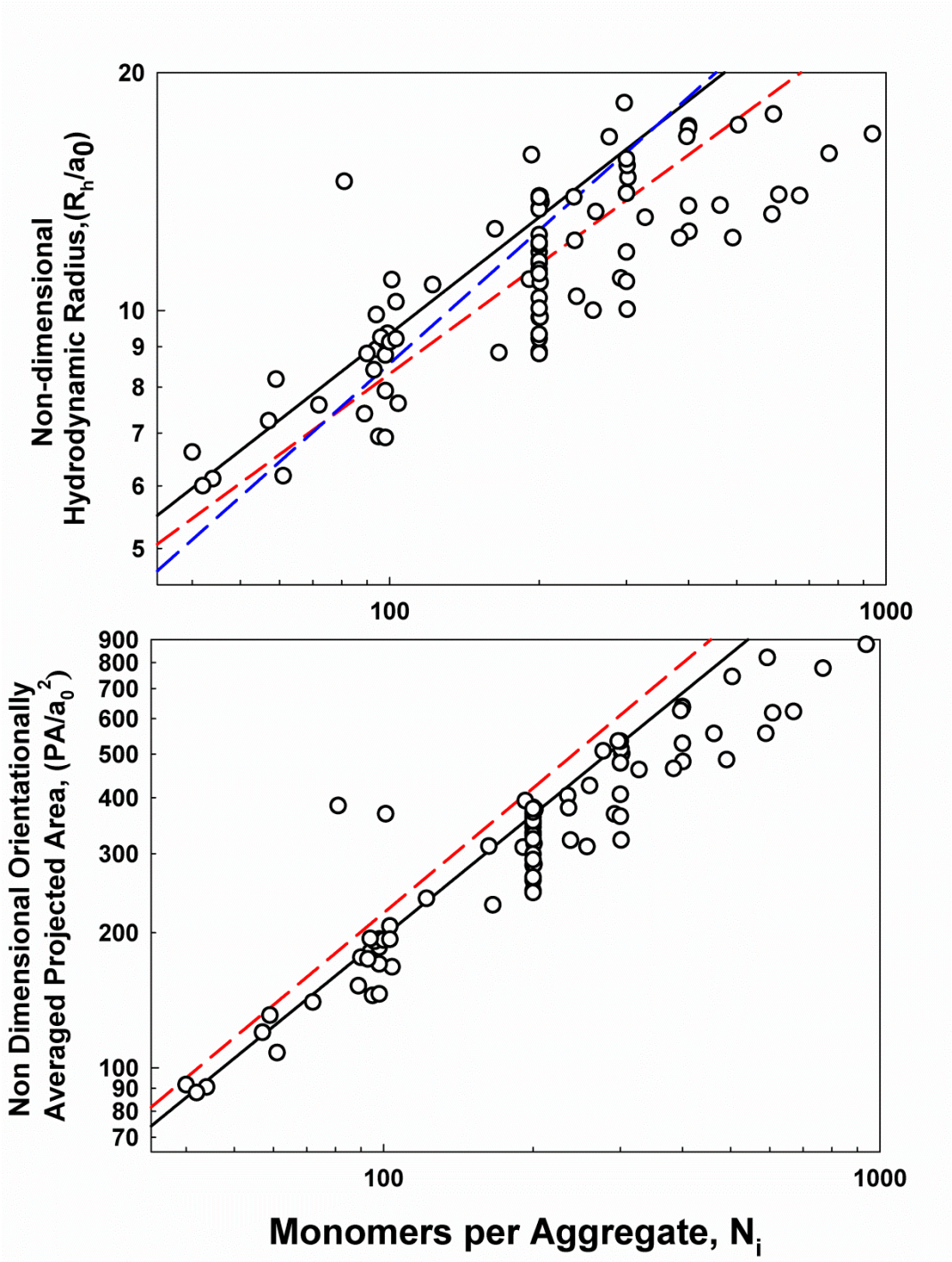

Figure 5.6. (a.) Plots of equations (8a) (solid black), (9a) (dashed red), and (9b) (dashed blue) as well as the hydrodynamic radii of the "average aggregates" provided by Table A.1 in Appendix. (b.) Plots of equations (8b) (solid black) and (9c) (dashed red) as well as the projected areas of the "average aggregates"

From direct inspection, it is clear that equations (8a) and (8b) will lead to reasonable agreement with equations (9a-c); although (9a-c) were developed without consideration of mass and momentum transfer transition regime aspects of aggregation, these features appear to minimally influence the scaling between aggregate size descriptors and N_i. Reasonable agreement is also found with experimental observations and is particularly good for $N_i < 300$, the region of validity for the developed expressions, supporting their use. The slightly lower values of R_H and PA at larger N_i attained for experimentally imaged aggregates can be attributed to aggregate restructuring and sintering, which, as already noted, are not considered in simulations here.

5.4 Conclusions

Aggregation of non-coalescing particles is examined here, monitoring the evolution of the momentum and diffusive Knudsen numbers and transport properties of the formed aggregates. The Langevin simulations used in this work take initial values of the Knudsen numbers and the solid volume fraction of the monomers as inputs, hence results are solely dependent on these dimensionless parameters. The evolution of the Knudsen numbers due to aggregation appears to be independent of the solid volume fraction. The Knudsen number-diffusive Knudsen number evolution differs noticeably from the evolution observed for a system of completely coalescing spherical monomers; there is a more rapid decrease diffusive Knudsen numbers for non-coalescing systems. Inference of system average Knudsen numbers over time can therefore serve as an indicator of the degree of coalescence in a system growing via collisions. Simulation results suggest that collision kernel homogeneities are not fixed values, but rather depend upon the Knudsen number distributions in the transition regime. Further, plots of the number of monomers per aggregate as functions of aggregate radius of gyration show only weak scaling between these parameters, and suggest that there are multiple families of quasifractal aggregates produced in system with evolving Kn and Kn_D distributions. Clearer scaling between the hydrodynamic

radius and the orientationally averaged projected area of the aggregates with the number of monomers per aggregate is observed, enabling the development regression equations to calculate these parameters. There is reasonable agreement with experimental observations for flame synthesized titanium dioxide aggregates for these parameters, in the region where the regression equations are valid. Future studies of aggregation in aerosols will be aided by both the use of the presented algorithm, and the regression equations developed to determine aggregate transport properties.

Chapter 6: Calculation of the Effective Conductivity of Aggregate-laden Suspensions and Composites using First Passage Simulations

Abstract: This work investigates the effect of aggregate morphology on the effective conductivity of aggregate-lade suspensions using first passage time simulations. Quasifractal aggregates are computationally generated using Sequential Algorithm, with prescribed morphological parameters. The effective conductivity is then calculated for different volume fractions and different degree of coalescence between primary particles.

6.1. Introduction

Numerous studies show that the rate of conductive transport in suspensions and composite materials, in which solid particles are embedded within a host medium, can be substantially different from the rate of conductive transport in the host medium alone (Torquato 1985; Torquato and Stell 1985; Beasley and Torquato 1986; Torquato and Lado 1991; Kim and Torquato 1992; Kim and Torquato 1993; Torquato, Kim et al. 1999). For example, the thermal conductivities (Wang, Xu et al. 1999; Eastman, Choi et al. 2001; Xie, Wang et al. 2002; Yu, France et al. 2008), electrical conductivities (Jäger and McQueen 2001; Schürmann, Takele et al. 2006; Ganguly, Sikdar et al. 2009), and dielectric constants (Qi, Lee et al. 2005; Mukherjee, Chen et al. 2010; Kofod, Risse et al. 2011) of particle laden suspensions and composites are noticeably enhanced (often increased by 10-25%) (Das, Putra et al. 2003) even with low volume fractions (1-4%) of embedded particles. In light of these results, in the past decade, there has been a significant effort to examine the transport properties of particle suspensions, e.g. nanofluids (nanoparticle suspensions) (Eastman, Phillpot et al. 2004; Das, Choi et al. 2006; Krishnamurthy, Lhattacharya et al. 2006; Yu, France et al. 2008; Choi 2009; Ganguly, Sikdar et al. 2009), and a better understanding of the conductivity enhancement in suspensions and composites is of considerable interest. When particles are well-dispersed (isolated from one another) at low volume fractions, the

enhancement in conductivity in these multiphase systems is expected, and is theoretically predicted using the effective medium approximation (EMA). EMA predictions are generally in good agreement with experimental measurements of conductive transport properties in well-dispersed systems. For example, a recent collaborative examination (Buongiorno, Venerus et al. 2009) of well-dispersed suspensions, in which thermal conductivities were measured by a number of laboratories using a variety of techniques, shows clearly that the EMA predicts well the conductivity enhancement under these conditions.

However, without considerable effort towards dispersing particles, aggregation within host media is prevalent (Schwarzer and Peukert 2002; Peukert, Schwarzer et al. 2005; Schwarzer and Peukert 2005; Stenger, Mende et al. 2005; Inkyo, Tahara et al. 2006; Sommer, Stenger et al. 2006; Hwang, Lee et al. 2008; Inkyo, Tokunaga et al. 2008; Kim, Lee et al. 2010). Particle synthesis processes at high temperature additionally lead to the formation of partially coalesced, aggregated particles, which will remain as aggregates when incorporated into host media (Grass, Tsantilis et al. 2006). For these reasons, aggregated particles are more commonly encountered than are isolated, spherical particles, and particle laden-systems typically are not considered well-dispersed. The morphology of aggregates, i.e. interconnected networks of primary spherical particles, is considered quasifractal (Oh and Sorensen 1997; Havlin and Ben-Avraham 2002; Lattuada, Wu et al. 2003; Schmid, Al-Zaitone et al. 2006), and can thus be described in terms of the number of primary particles per aggregate, the aggregate fractal dimension (Hausdorff dimension, varying from 1.0 for completely linear aggregates, and increasing up to 3.0 for dense aggregates), the pre-exponential factor, as well as the degree of coalesce of the primary particles (Schmid, Tejwani et al. 2004) (in addition to the particle volume fraction in the suspension/composite). The enhancement in the conductivity (either thermal or electrical, or the dielectric constant) of suspensions and composites containing such morphologically complex aggregates should not necessarily agree with EMA predictions, and should depend upon these morphological descriptors (Prasher, Evans et al. 2006; Prasher, Phelan et al. 2006;

Evans, Prasher et al. 2008). Unlike the examination of well-dispersed particle-laden systems (Buongiorno, Venerus et al. 2009), most experimental investigations in multiphase systems do in fact reveal conductivity enhancements beyond that predicted by the EMA (Wang, Xu et al. 1999; Eastman, Choi et al. 2001; Jäger and McQueen 2001; Xie, Wang et al. 2002; Schürmann, Takele et al. 2006; Yu, France et al. 2008; Ganguly, Sikdar et al. 2009). Despite numerous investigations into possible conductivity enhancement brought about by particle diffusion (Bhattacharya, Saha et al. 2004; Prasher, Bhattacharya et al. 2005; Evans, Fish et al. 2006; Prasher, Bhattacharya et al. 2006; He and Qiao 2008; Nie, Marlow et al. 2008), the aggregation of particles into quasifractal networks appears to be the main cause for larger conductivity enhancements than is predicted by the EMA (Keblinski, Phillpot et al. 2002; Evans, Fish et al. 2006; Prasher, Evans et al. 2006; Timofeeva, Gavrilov et al. 2007; Gharagozloo, Eaton et al. 2008; Karthikeyan, Philip et al. 2008; Keblinski, Prasher et al. 2008; Nie, Marlow et al. 2008; Gao, Zheng et al. 2009; Timofeeva, Routbort et al. 2009; Fan and Wang 2011; Sharma, Baek et al. 2011).

Attempts have been made to address the influence of aggregation on conductivity enhancement (Nan, Birringer et al. 1997; Wang, Zhou et al. 2003; Prasher, Evans et al. 2006; Prasher, Phelan et al. 2006; Eapen, Li et al. 2007; Evans, Prasher et al. 2008), primarily via modifications to the EMA. However, the extent to which quasifractal formation can enhance conductivity still remains poorly understood. Along these lines, the purpose of this study is to utilize a first passage simulation technique developed by Kim and Torquato (Kim and Torquato 1990; Kim and Torquato 1990; Kim and Torquato 1991; Kim and Torquato 1991; Kim and Torquato 1992; Kim and Torquato 1992; Kim and Torquato 1993) to computationally examine the effect of the morphology of quasifractal networks on the conductivity of particle-laden systems. We combine first passage simulations with a modified sequential aggregate generation algorithm (Filippov, Zurita et al. 2000), which allows for generation of a random quasifractal aggregate of prescribed morphological properties. In subsequent sections, the algorithm for generating quasifractals is first described, followed by a brief

description of the first passage technique, and finally the results of first passage calculations are discussed.

6.2. Theoretical Methods

6.2.1 Generation of Random Quasifractal Aggregates

A two-step approach is employed to randomly generate quasifractal aggregates with a prescribed number of primary particles per aggregate (N_p), fractal dimension (D_f), pre-exponential factor (k_f), and degree of coalescence between primary particles (δ). We first utilize the sequential algorithm (SA), described in detail by Filippov et al (Filippov, Zurita et al. 2000), which allows for generation of a random aggregate of prescribed N_p, k_f, and D_f, with point contacts between primary particles. Other algorithms are available for quasifractal generation (Lattuada, Wu et al. 2004; Schmid, Tejwani et al. 2004; Pierce, Sorensen et al. 2006; Schmid, Al-Zaitone et al. 2006; Soos, Ehrl et al. 2009; Eggersdorfer, Kadau et al. 2011), many of which attempt to mimic the physics of aggregate formation either in host media or during particle synthesis. However, these algorithms do not afford the degree of control over aggregate properties that is provided by the SA algorithm, and they are often limited in the diversity of aggregate morphologies that can be produced. Further, at this juncture, the underlying physical and chemical processes controlling simultaneous aggregate growth and coalescence are not fully understood (Hawa and Zachariah 2006; Hawa and Zachariah 2007; Eggersdorfer, Kadau et al. 2011); hence, aggregates of known properties are tailor generated in an effort to understand how these properties influence conductive transport through aggregate-laden media.

In the SA, primary particles are added to a pre-existing aggregate one at a time, and at each point in the generation process the scaling relation is satisfied:

$$N_{p,SA} = k_{f,SA}\left(\frac{R_{g,SA}}{a_{p,SA}}\right)^{D_{f,SA}} \tag{1a}$$

where the subscript SA denotes the input values into the SA, and R_g is the radius of gyration as defined by Filippov et al(Filippov, Zurita et al. 2000):

$$R_{g,SA}^2 = \frac{1}{N_{p,SA}}\sum_{i=1}^{N_{p,SA}}(\vec{r}_i - \vec{r}_{cm})^2 + a_{p,SA}^2 \tag{1b}$$

$\vec{r}_{cm}$ is the center of mass of the aggregate and $\vec{r}_i$ is the coordinate vector of the center of primary particle *i*. Note that with this definition of the radius of gyration, $R_g = a_{p,SA}$ for a single spherical particle. This differs slightly from the traditional definition, wherein $0.6a^2_{p,SA}$ is added rather than $a^2_{p,SA}$. The effect is minimal as $N_{p,SA} > 10$. The fractal dimension inferred from structure factor calculations on individual aggregates is not always the same as the prescribed $D_{f,SA}$ (Huang, Oh et al. 1998; Oh and Sorensen 1998; Filippov, Zurita et al. 2000). However, here, for reasons listed in the results and discussion section, we limit quasifractal generation to $N_p \leq 50$, for which the SA can successfully generate random aggregates of prescribed properties. After generation of an aggregate via the SA, the second step in random quasifractal generation is to introduce a degree of coalescence between primary particles. This is accomplished by defining the overlap parameter, δ, as:

$$\delta = \frac{d}{2a_p} \tag{2}$$

where d is the minimum distance between the centers of two primary particles in contact with one another after increasing the radius of the primary particles from $a_{p,SA}$ to a_p. Following the introduction of non-point contacts between primary particles, each primary particle must have its center a distance d from at least one other primary particle (though it may be in contact with others with a lesser degree of overlap). A δ value of 1.0 denotes point contacts between primary particles, as generated by the SA, and lesser values denote a larger degree of overlap between primary particles.

The introduction of overlap induces other changes in the morphology of the quasifractal aggregates such that $D_f \neq D_{f,SA}$ and $k_f \neq k_{f,SA}$. To quantify the morphology of overlapped primary particles, we adopt the approach of Schmid et al (Schmid, Tejwani et al. 2004; Schmid, Al-Zaitone et al. 2006), wherein quasifractal aggregates with partially coalesced primary particles are described by the equation:

$$N_{eff} = \frac{3V_{agg}}{4\pi a_p^3} = k_f \left(\frac{R_g}{a_p}\right)^{D_f} \quad (3)$$

N_{eff} is the effective (non-integer) number of primary particles in the aggregate and V_{agg} is the volume occupied by the aggregate. To determine k_f and D_f after introducing overlap, a number of aggregates of prescribed $k_{f,SA}$ and $D_{f,SA}$ with varying $N_{p,SA}$ are generated. Overlap is next introduced between primary particles to a prescribed δ value for all aggregates. A plot of $\ln[N_{eff}]$ as a function of $\ln[R_g/a_p]$ then yields D_f and $\ln(k_f)$. With this procedure, specific "recipes" can be developed to randomly generate quasifractal aggregates of prescribed D_f, k_f, and δ.

The resulting aggregates have four morphological descriptors (N_{eff}, D_f, k_f, and δ), which, when combined with the effect of the aggregate conductivity relative to the conductivity of the host medium, complicates complete analysis of all morphological influences on composite/suspension conductivity. As an alternative to examination of all D_f, k_f, and δ combinations, we examine conductivity enhancement for four different classes of aggregates, which vary drastically in quasifractal descriptors, and represent appropriate limiting cases (upper and lower limits in D_f and k_f) for aggregates observed in suspensions and composites: (I) chain like aggregates (D_f = 1.5, k_f = 1.3) with near point contacts (δ = 0.95), (II) chain like aggregates (D_f = 1.5, k_f = 1.3) with substantial primary particle coalescence (δ = 0.65), (III) dense aggregates (D_f = 2.6, k_f = 1.8) with near point contacts (δ = 0.95), and (IV) dense aggregates (D_f = 2.6, k_f = 1.8) with substantial primary particle coalescence (δ = 0.65). Table 6.1 summarizes the properties of these 4 classes, and images of these aggregates after generation by the SA

and after introducing primary particle overlap are shown in Figures 6.1 and 6.2 respectively.

Table 6.1: Morphological parameters of the four different types of fractals used

Type	D_f	k_f	δ
1	1.50	1.30	0.95
2	1.50	1.30	0.65
3	2.60	1.80	0.95
4	2.60	1.80	0.65

Qualitatively, these four aggregate types indeed resemble the most linear (Types I and II) and most compact (Types III and IV) aggregates observed in experiments (Scheckman, McMurry et al. 2009; Soos, Harshe et al. 2011), though we note that the observation of highly linear, yet highly coalesced type II aggregates is quite rare.

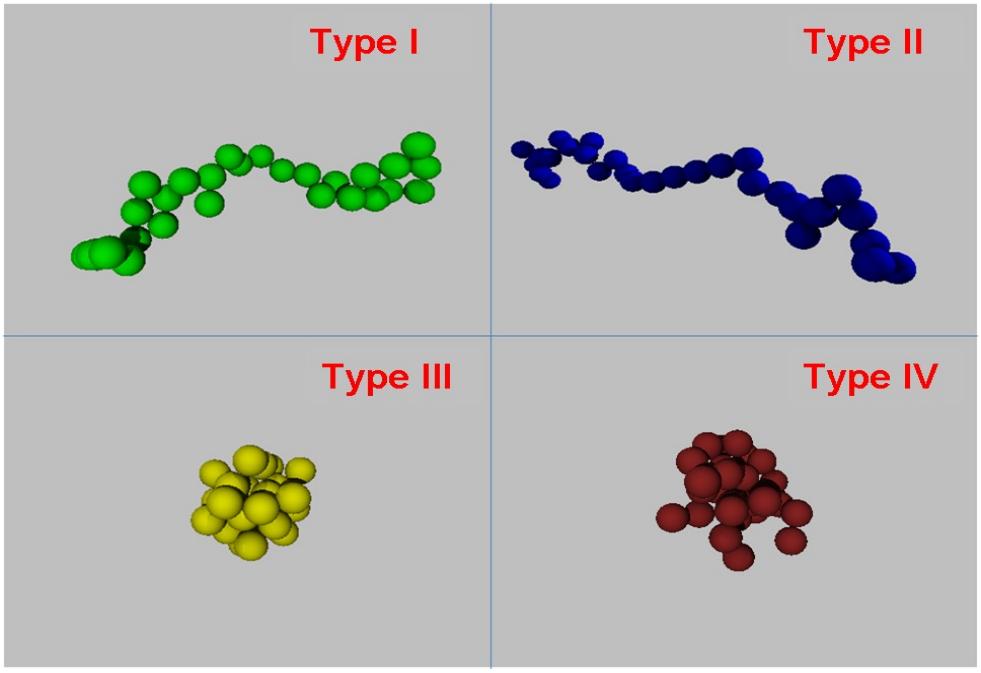

Figure 6.1. Sample images of types I-IV aggegrates generated via the sequential algorithm, prior to the introduction of overlap.

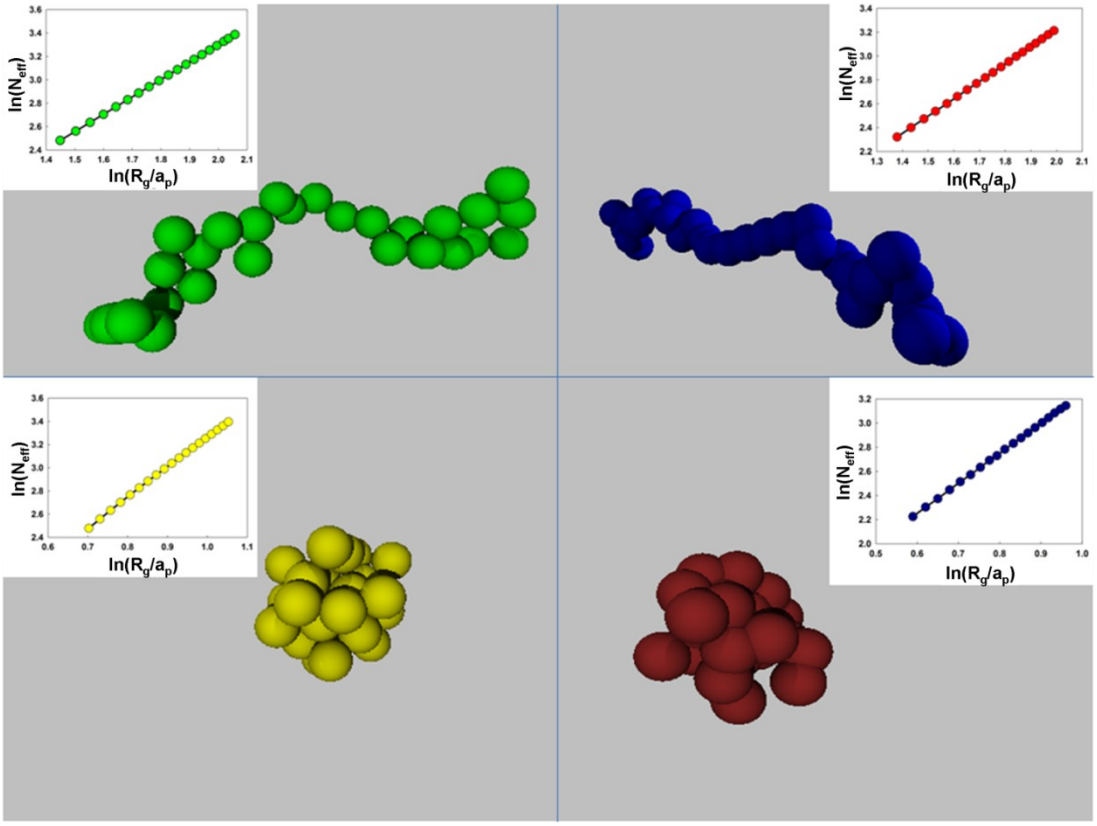

Figure 6.2. Sample images of types I-IV aggegrates generated via the sequential algorithm, after the introduction of overlap. Inset plots show ln[N_{eff}] vs. ln(R_g/a_p), used to determine D_f and k_f for each type of aggregate.

6.2.2 First Passage Simulations

A first passage simulation technique developed by Kim and Torquato (Kim and Torquato 1991; Kim and Torquato 1992) is applied to subsequently determine the effective conductivity of a suspension/composite composed of known volume fraction (V_f) of quasifractal aggregates (Type I, II, III, or IV) of conductivity σ_p within a host medium of conductivity σ_h. In first passage simulations, the motion of a random Brownian walker through a composite of well-described microstructure is monitored, and from this motion the effective conductivity of the composite is inferred. This approach may be used to evaluate the effective transport properties for any process for which transport obeys a Poisson equation; hence, the results of our calculations apply to

systems in the continuum limit. Details on the first passage approach are given in prior work (Kim and Torquato 1990; Kim and Torquato 1990; Kim and Torquato 1991; Kim and Torquato 1991; Kim and Torquato 1992; Kim and Torquato 1992; Kim and Torquato 1993), with a brief description also given here.

A schematic representation of the first passage simulation is shown in Figure 6.3. First, a single, randomly generated quasifractal aggregate is enclosed within a rectangular box, with the box dimensions determined by specifying the volume fraction of the quasifractal aggregates within the composite. Periodic boundary conditions are used on the domain surface. A Brownian walker is placed randomly within the simulation domain; thus it originally lies either inside the aggregate, or within the host medium. The longest distance which the walker can move within a single phase, R, is then determined. The average time required to travel this distance, τ, is given as:

$$\tau = \frac{R^2}{6\sigma_{p,h}} \tag{4}$$

As motion in all directions is equally probable, the walker is given a random direction, moved a distance, R, and the average time necessary for this motion, τ, is recorded. Subsequently, a new distance, R, is calculated based on the walker's new location, and this process is repeated. Eventually, the walker will reach a distance which is less than a critically small distance Δ (0.01% of the primary particle radius in coalesced aggregates) from the interface between the aggregate and host medium. At this point, there is a chance that in traveling a distance l (1% of the primary particle radius), the walker will cross the interface, entering into a different phase of different conductivity.

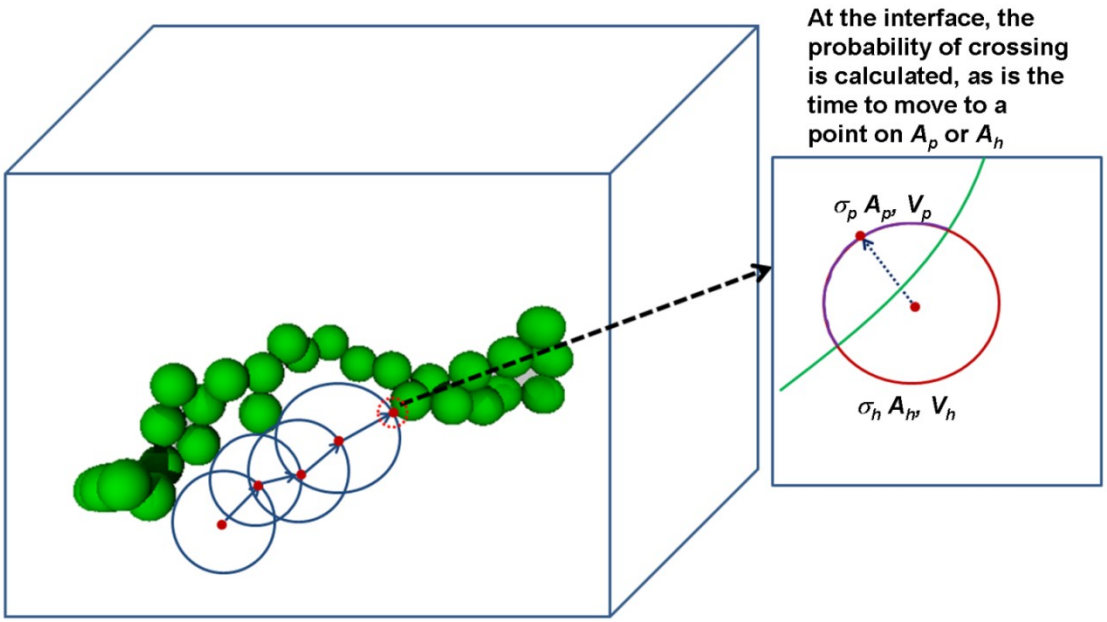

Figure 6.3. Schematic of the first passage simulation approach wherein the motion of a random Brownian walker is used to determine the effective conductivity of a particle laden suspension/composite. Each time the walker approaches the interface between the host and aggregate particle network, the probability that the walker will cross the interface is determined.

From Kim and Torquato (Kim and Torquato 1990) the probability that the walker, originally within the particle aggregate, crosses the interface into the host medium, $p_{cross,\ p->h}$, is given as:

$$p_{cross,p->h} = \frac{A_h}{A_h + \left(\sigma_p/\sigma_h\right)A_p}\left[1 - \sum_{m=0}^{\infty} B_{2m+1}\varepsilon^{2m+1}\right] \tag{5a}$$

Conversely, the probability that the walker, originally within the host medium, crosses the interface into the aggregate, $p_{cross,\ h->p}$, is given as:

$$p_{cross,h->p} = \frac{\left(\sigma_p/\sigma_h\right)A_h}{A_h + \left(\sigma_p/\sigma_h\right)A_p}\left[1 - \left(\sigma_p/\sigma_h\right)\sum_{m=0}^{\infty} B_{2m+1}\varepsilon^{2m+1}\right] \tag{5b}$$

where:

$$B_{2m+1} = \frac{(-1)^m (2m)!(4m+3)}{2^{2m+1}(m!)^2(m+1)} \tag{5c}$$

In equations 5a and 5b, ε is the shortest distance from the walker to the host medium-aggregate interface, A_h is the surface area of a sphere of radius l centered on the nearest interfacial point to the walker and exposed to the host medium, and A_p is the remaining surface area of the same sphere, which is exposed to the aggregate. To determine if the walker will cross the interface, a uniformly distributed random number between 0 and 1 is calculated. If the walker is within the aggregate and this number is less than $p_{cross,\ p->h}$, the walker is placed at a random location on A_h. Similarly, if the walker is within the host medium and the random number is less than $p_{cross,h->p}$, the walker is placed at a random location on A_p. In both cases, if the random number is greater than the required crossing probability, the walker is placed at a random location on the surface of the sphere exposed to the region the walker is currently within. Irrespective of whether the walker crosses the interface, the time required for the walker to move from its current location to either A_h or A_p is calculated as (Kim and Torquato 1990):

$$\tau_p = \frac{l^2}{6\sigma_h} \frac{V_h+V_p}{V_h+\left(\sigma_p/\sigma_h\right)V_p} \left[1 + \frac{\left(\sigma_p/\sigma_h\right)-3}{2\left(\sigma_p/\sigma_h\right)}\varepsilon^2 - \frac{\left(\sigma_p/\sigma_h\right)-1}{2\left(\sigma_p/\sigma_h\right)} \sum_{m=0}^{\infty} C_{2m+1}\varepsilon^{2m+1}\right] \tag{6a}$$

if the walker is originally within the aggregate, and as:

$$\tau_h = \frac{l^2}{6\sigma_h} \frac{V_h+V_p}{V_h+\left(\sigma_p/\sigma_h\right)V_p} \left[1 + \frac{3\left(\sigma_p/\sigma_h\right)-1}{2}\varepsilon^2 - \frac{\left(\sigma_p/\sigma_h\right)-1}{2} \sum_{m=0}^{\infty} C_{2m+1}\varepsilon^{2m+1}\right] \tag{6b}$$

if the walker is originally within the host medium, where:

$$C_{2m+1} = \frac{(-1)^{m+1}(2m)!(4m+3)^3}{2^{2m+1}(m!)^2(2m-1)(m+1)(m+2)} \tag{6c}$$

In equations 6a and 6b, V_h is the volume bounded by A_h and the interface, and V_p is the volume bounded by A_p and the interface. After crossing the interface or moving away from it, the walker again moves via first passage steps until it again reaches a distance less than Δ from an aggregate-host medium interface. The walker will occasionally reach a point which is within close proximity to a complex interface (i.e. where two primary particles intersect one another). The probability of crossing the interface at these points and the corresponding time necessary to cross this type of interface are determined with the procedure described by Kim and Torquato (Kim and Torquato 1992), as equations (5-6) apply for an interface of unambiguous radius of curvature.

Over time, the walker takes a number of simulation steps in which it has either moved within the host medium, moved within the aggregate, or crossed the interface. It then lies a distance X_i from its original starting point, and has taken a total time τ_i to arrive at this point. Special care is taken to determine X_i because of the periodic boundary conditions used on the simulation domain. To infer the effective conductivity of a composite/suspension with a prescribed σ_p/σ_h, prescribed volume fraction, V_f, and prescribed aggregate morphology, the motion of multiple walkers through a number of different aggregates must be monitored. For each conductivity calculation performed here, 150 Brownian walkers are used for a single quasifractal aggregate at specified V_f, and 25-50 different randomly generated aggregates of specified morphology are used (3750-7500 Brownian walkers per calculation). Equivalently, a single large simulation domain containing 25-50 different quasifractal aggregates at the desired volume fraction could be examined to determine the effective conductivity. Separate simulations on single aggregates are utilized here as this approach simplifies construction of the simulation domain, particularly at higher volume fractions where percolation is a possibility. As discussed by Kim and Torquato (Kim and Torquato 1992), for

simulation convergence, each Brownian walker must be monitored for a sufficiently long time, which depends upon the aggregate volume fraction and σ_p/σ_h. Summing over all examined Brownian walkers and all examined aggregates under specified conditions, the effective conductivity, σ_e of the composite/suspension is calculated as:

$$\sigma_e = \frac{1}{6nq_{qa}} \sum_{j=1}^{n_{qa}} \frac{\sum_{i=1}^{n_{bw}} X_{ij}^2}{\sum_{i=1}^{n_{bw}} \tau_{ij}} \tag{7}$$

where n_{qa} denotes the number of quasifractal aggregates examined (25-50) and n_{bw} (150) denotes the number of Brownian walkers per aggregate.

6.3. Results and Discussion

6.3.1. First Passage Calculation Validation

The accuracy of the first passage approach is examined by computing the effective conductivity of a composite with perfectly spherical particle inclusions, with the ratio of particle to host conductivity σ_p/σ_h = 10 and particle volume fractions ranging from 0.1 to 0.5. Results are shown in Figure 6.4 (open circles connected by solid black lines). Also shown are expected results from the EMA (Maxwell-Garnet model, dashed gray line), which is given by the equation:

$$\frac{\sigma_e}{\sigma_h} = \frac{\left(\frac{\sigma_p}{\sigma_h}\right)(1+2V_f)-2V_f+2}{\left(\frac{\sigma_p}{\sigma_h}\right)(1-V_f)+V_f+2} \tag{8}$$

Lastly, the exact values for σ_e/σ_h taken from Kim and Torquato (Kim and Torquato 1991) are also shown in Figure 6.4 (black triangles).

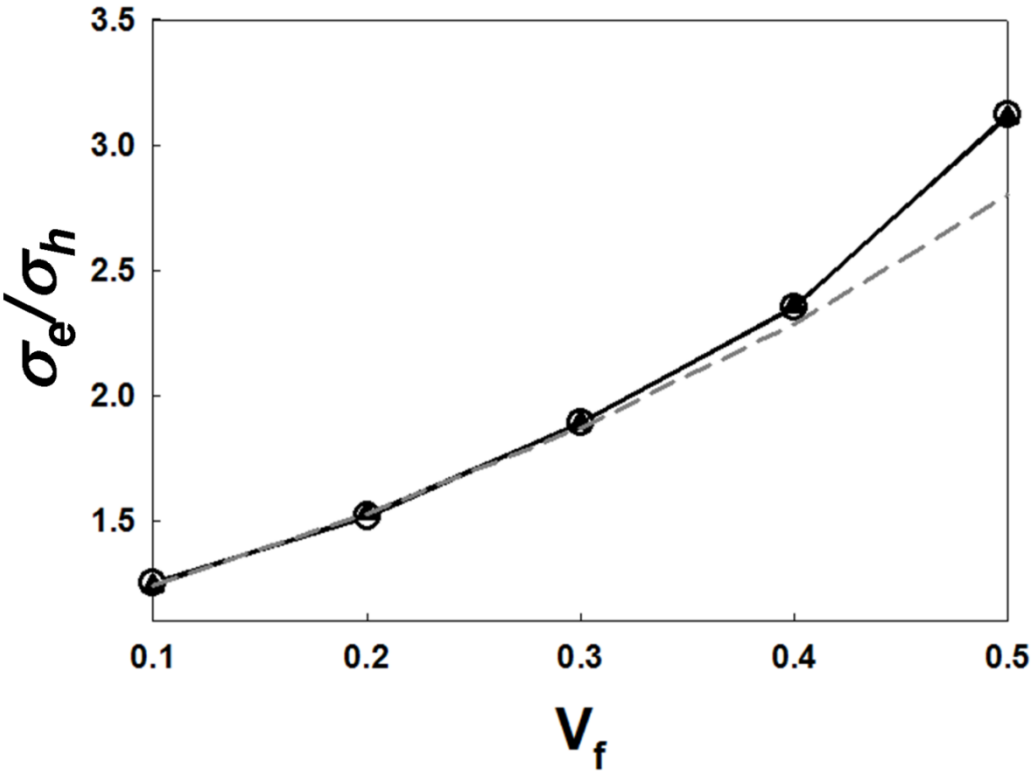

Figure 6.4. The effective conductivity to host medium conductivity for a particle to host medium conductivity ratio of 10 and well-dispersed, spherical particles as a function of particle volume fraction. Open cirles with black lines- from first passage calculations. Gray dashed line- the Maxwell-Garnet model. Black Triangles- the exact solution.

Immediately apparent is the excellent agreement between the exact solution and first passage results, indicating that correct values are obtained from first passage calculations. At low volume fractions, EMA predictions and first passage simulations are also in excellent agreement, with deviations apparent only at volume fractions greater than ~0.3. This too, is expected, as the EMA only applies at low volume fractions, and we may conclude that the first passage technique correctly predicts the effective conductivity of composite media.

6.3.2. Influence of the Number of Primary Particles

While the introduction of four classes of aggregates reduces the number of parameters to examine, the ratio σ_e/σ_h for each aggregate type still depends upon V_f, N_{eff}, and the ratio σ_p/σ_h. We first specifically examine the influence of N_{eff}, the number of primary particles per aggregate. Figure 5 shows σ_e/σ_h as a function of V_f for type IV aggregates with σ_p/σ_h= 10. Results are shown for aggregates composed of 20 (Circles), 30 (squares), and 50 (triangles) original primary particles (N in the SA algorithm, as opposed to N_{eff}).

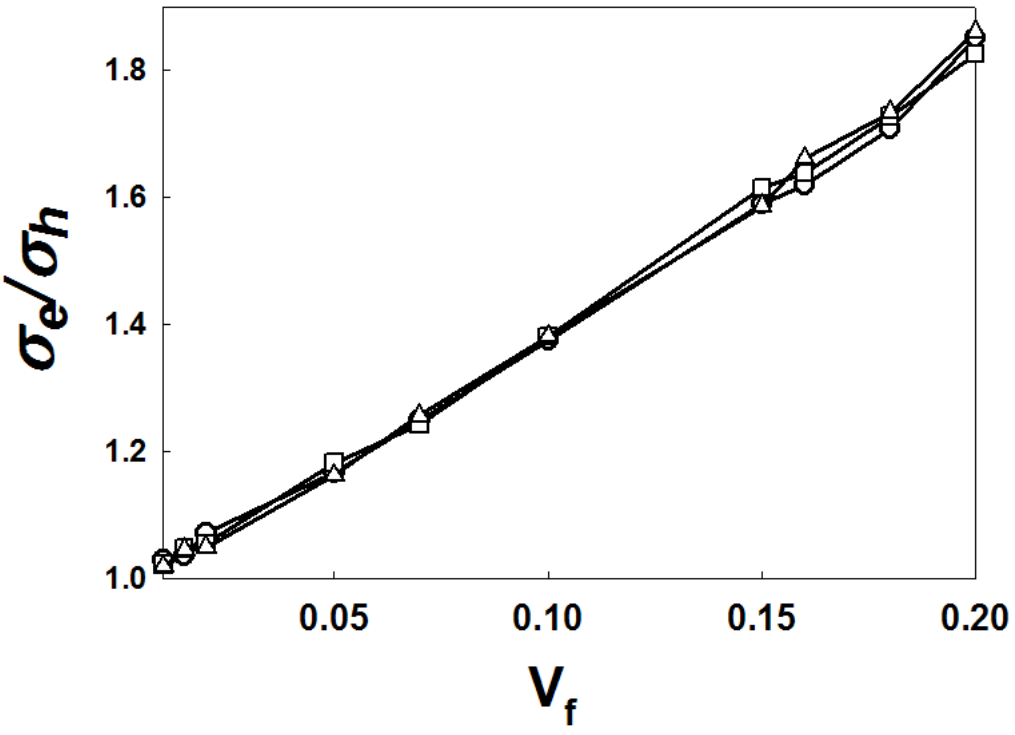

Figure 6.5. σ_e/σ_h for type IV aggregates with σ_p/σ_h = 10 as a function of volume fraction. Circles- 20 primary particles per aggregate, squares- 30 primary particles per aggregate, triangles- 50 primary particles per aggegrate.

Somewhat surprisingly, there is little-to-no change in effective conductivity with increasing N for aggregates of composed of ~20 primary particles or more. This result is not unique; for all examined aggregate types at both $\sigma_p/\sigma_h = 10$ and $\sigma_p/\sigma_h = 100$, the effective conductivity is found to be insensitive to the number of primary particles in each aggregate (results not shown for brevity). This indicates that with a sufficient number of primary particles, the morphology of the fractal aggregates, which are scaling invariant objects (Oh and Sorensen 1998), is well defined and insensitive to the further addition of primary particles. This, in turn, leads to the insensitivity of the effective conductivity to the number of primary particles per aggregate.

6.3.3 Influence of Aggregate Morphology

The number of primary particles is henceforth fixed at 30 to examine the influence of morphology on suspension/composite conductivity. The effective conductivities of suspensions/composites with types I-IV aggregates as inclusions are shown as a function of volume fraction for $\sigma_p/\sigma_h = 10$ (low conductivity particles) and $\sigma_p/\sigma_h = 100$ (high conductivity particles) in Figures 6.6 and 6.7, respectively. At the maximum examined volume fraction for each aggregate type, suspensions/composites contain unpercolated aggregates, as is expected in a stable suspension and in most composites (Hamming, Qiao et al. 2009; Qiao, Deng et al. 2011). Insets in Figures 6.6 and 6.7 show results for volume fractions of 0.02 and less, as is frequently utilized in nanofluids (Eastman, Phillpot et al. 2004). Also shown in all graphs are predicted conductivities from the EMA, and first passage results for dimers for $\delta = 0.95$.

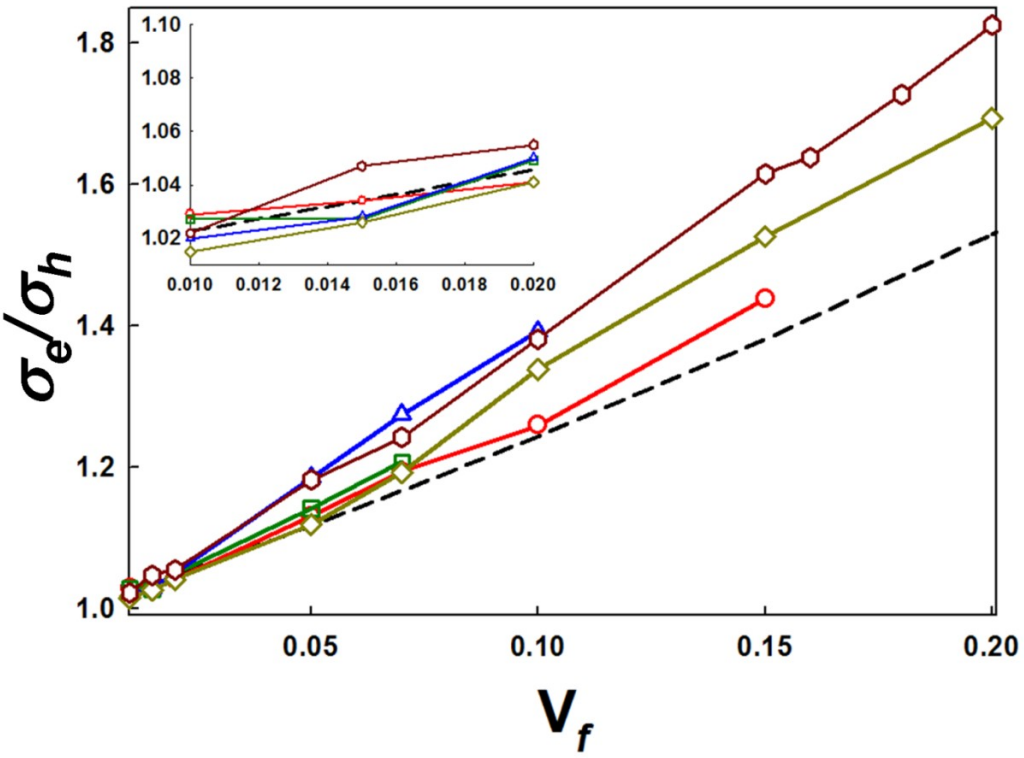

Figure 6.6. σ_e/σ_h for σ_p/σ_h = 10 as a function of volume fraction. Dashed black line- Maxwell-Garnet predictions. Red circles- dimers. Green squares- Type I aggregates. Blue triangles- Type II aggregates. Gold diamonds- Type III aggregates. Purple hexagons- Type IV aggregates. All aggregates contained 30 primary particles. Inset- results in the V_f = 0.01-0.02 range.

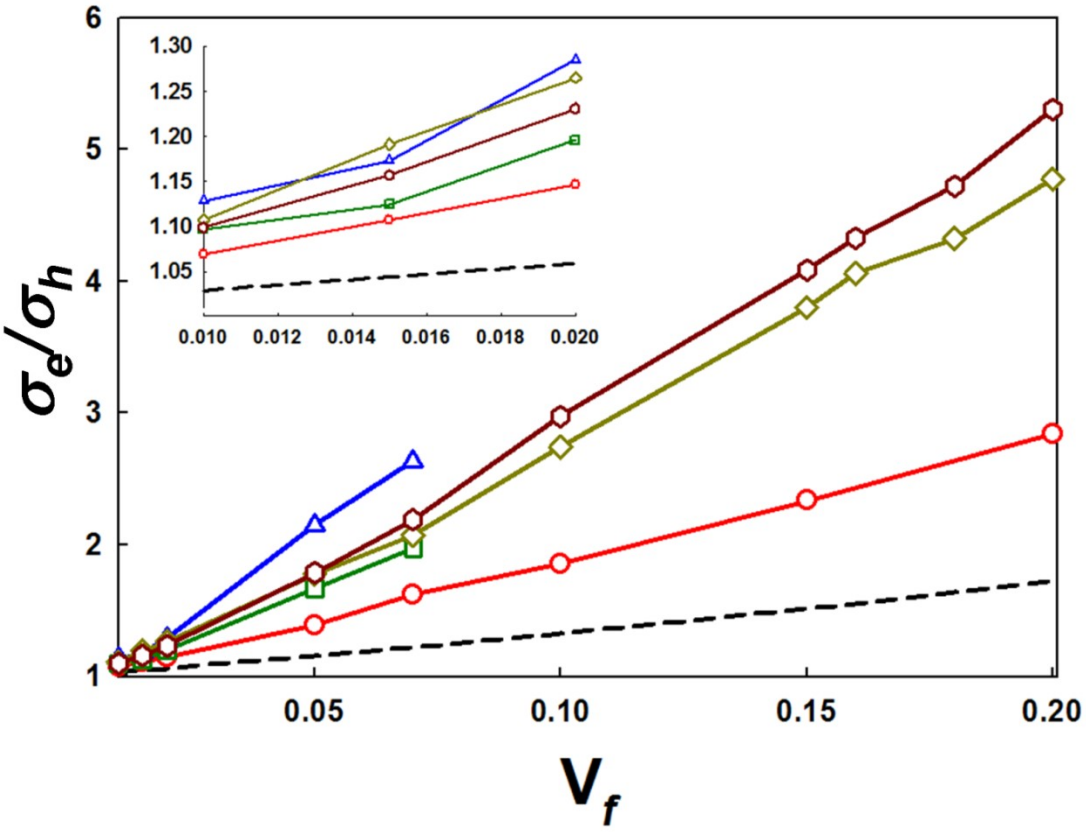

Figure 6.7. σ_e/σ_h for σ_p/σ_h = 100 as a function of volume fraction. Dashed black line- Maxwell-Garnet predictions. Red circles- dimers. Green squares- Type I aggregates. Blue triangles- Type II aggregates. Gold diamonds- Type III aggregates. Purple hexagons- Type IV aggregates. All aggregates contained 30 primary particles. Inset- results in the V_f = 0.01-0.02 range.

For σ_p/σ_h= 10 and V_f > 0.05, all aggregate types give rise to higher conductivity enhancements than do dimers, which in turn, give rise to higher conductivity enhancement than predicted by the EMA. The enhancement beyond the EMA increases with increasing volume fraction, reaching a maximum value 20% higher than the EMA prediction at V_f = 0.2 for type IV aggregates. The conductivity enhancement is near-identical for types I and II aggregates as well as for types III and IV aggregates. It appears that in this instance the fractal dimension and pre-exponential factor (as well as the number of primary particles) has little influence on conductivity enhancement, and the conductivity enhancement is most strongly influenced by the degree of overlap (δ) between primary particles. That δ = 0.65 gives rise to a larger conductivity

enhancement than does $\delta = 0.95$ further implies that with low conductivity particles, there is an optimum amount of overlap to promote conductivity enhancement, as $\delta = 0.0$ leads to a single sphere and hence a lower degree of enhancement. In light of the low overall conductivity enhancements brought about with $\sigma_p/\sigma_h = 10$ (within 20% of the EMA for all examined volume fractions), however, this effect is not examined further here. Moreover, at volume fractions equal to or less than 0.02, all examined aggregates give rise to conductivity enhancements in line EMA predictions. This finding is in good agreement with the recent work of Wu et al (Wu, Cho et al. 2010), wherein it was found that the aggregation of low thermal conductivity silica suspensions had no influence on suspension conductivity. Moreover, combined with the agreement between measured thermal conductivities and EMA predictions found by Buongiorno et al (Buongiorno, Venerus et al. 2009), both experiments and model calculations suggest that low thermal conductivity particles incorporated into a host matrix at low volume fraction do not give rise to increases in conductivity beyond EMA predictions, regardless of the morphology of the included particles.

Similar to calculation results with $\sigma_p/\sigma_h = 10$, for $\sigma_p/\sigma_h = 100$ the effective conductivities of suspensions/composites composed of aggregates are beyond that of both dimers and EMA predictions. However, the magnitude of the increase beyond the EMA is substantially higher. For example, for $\sigma_p/\sigma_h = 100$ for type IV aggregates at $V_f = 0.2$, a ~300% greater enhancement beyond the EMA prediction is found, as compared to the 20% greater enhancement found for $\sigma_p/\sigma_h = 10$. While again aggregates with $\delta = 0.65$ lead to greater enhancement than do those with $\delta = 0.95$, an influence of morphology beyond the overlap parameter is also apparent with $\sigma_p/\sigma_h = 100$. For $\delta = 0.95$, dense aggregates produce a greater conductivity enhancement than do linear aggregates, as evidenced by type III aggregates leading to greater enhancements than type I aggregates. Conversely, for $\delta = 0.65$, conductivity enhancement is greater with linear type II aggregates than it is with dense type IV aggregates.

Overall, it is clear from first passage calculations that at high σ_p/σ_h, aggregation and aggregate morphology drastically influence the conductivity of suspensions and composites. Under these circumstances, calculation results suggest the enhancement in conductivity brought about by aggregation can account completely for the "anomalous" enhancement found in particle-laden composites, in particular, the aforementioned studies of nanofluids (Eastman, Choi et al. 2001; Eastman, Phillpot et al. 2004; Das, Choi et al. 2006; Choi 2009). This is further made clear in the inset of Figure 6.7, where substantial enhancement in conductivity with aggregates is observed beyond EMA predictions at volume fractions typically found in nanofluids. The degree of enhancement beyond EMA predictions can be further demonstrated by determining a Maxwell-Garnet "effective volume fraction," $V_{f,eff}$, for each aggregate, i.e. the volume fraction required to give rise to the first passage calculated conductivity enhancement calculated using the EMA (equation 8). The ratio $V_{f,eff}/V_f$ is shown as a function of V_f in Figure 6.8. Gray dashed lines denote the mean value of $V_{f,eff}/V_f$ in each graph.

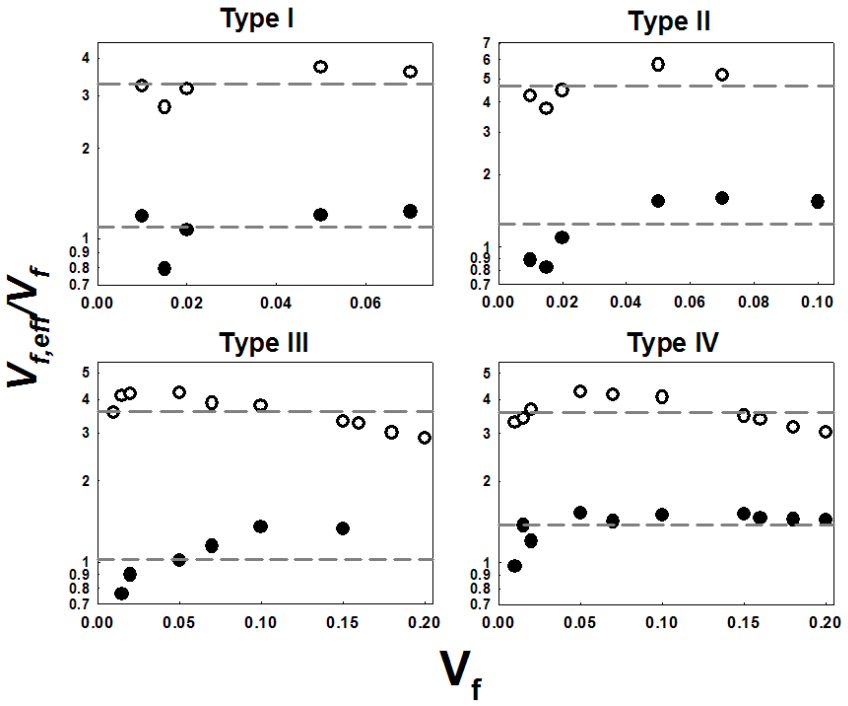

Figure 6.8. The ratio of the effective volume fraction for each aggregate type to the true volume faction, as a function of the true volume fraction. Closed symbols- σ_p/σ_h = 10. Open symbols- σ_p/σ_h = 100. Gray dashed lines denote the average value for all examined volume fractions.

As mentioned above, for σ_p/σ_h = 10, little enhancement beyond the EMA is observed, and the ratio $V_{f,eff}/V_f$ is bound close to one at low volume fractions, increasing slightly at higher volume fractions for all aggregate types. For σ_p/σ_h = 100, the $V_{f,eff}/V_f$ ratio initially increases with increasing V_f until a volume fraction of ~0.05, then slowly decreases with further increase in particle volume fraction. Across all examined volume fractions and for all aggregate types, $V_{f,eff}/V_f$ stays bound within the 3-5 range. Although this leads to considerable variation in suspension/composite conductivity between aggregate types, it demonstrates an enormous increase in effective conductivity due to aggregation; the formation of high conductivity particle aggregates, at any volume fraction, has a similar effect to increasing the volume fraction of well-dispersed particles of the same conductivity by a factor of 3-5.

6.3.4. Limitations, Controlled Morphology Aggregates, and Controlled Conductivities

It is clear from first passage calculation that aggregate formation can substantially enhance the conductivity of suspensions and composites beyond traditional EMA predictions. However, these enhancements can only be realized for either very high particle volume fractions, or high conductivity particles. The former is often mitigated by the inability to disperse particles (even partially) in liquid and solid matrices with particle volume fractions greater than 0.10 (Inkyo, Tahara et al. 2006; Inkyo, Tokunaga et al. 2008). Therefore, to realize high conductivity enhancements at achievable particle volume fractions, high conductivity particles are needed. Neglected in the calculations performed here is any interfacial resistance (Nan, Birringer et al. 1997) to conductive transport, which is often non-negligible for nano- and nanostructured particles. In many circumstances, interfacial resistance likely reduces the conductivity of suspensions and composites an appreciable amount; thus we suggest that if the bulk conductivity is used in first passage calculations to predict the conductivity of a suspension/composite, then the calculation result is an upper limit to what is achievable in the actual material.

With high conductivity particles, first passage calculations predict that it should be possible to produce high conductivity suspensions and composites through the aggregation of particles, and that by controlling to what degree aggregation occurs, suspensions and composites of tailored conductivity could be produced. We note, however, that first passage results show that the production of increasingly aggregated particles (higher N) does not influence the resulting conductivity of a composite; rather, calculations suggest it is necessary to restructure the aggregates in order to change the conductivity. Simplified models of quasifractal aggregate laden suspension conductivity also show insensitivity to the number of primary particles per aggregate (Prasher, Evans et al. 2006; Evans, Prasher et al. 2008). Furthermore, that the thermal conductivity of particle suspensions is highly sensitive to temperature (Das, Putra et al.

2003) and pH (Prasher, Phelan et al. 2006) suggests that aggregate restructuring, which would occur with temperature and pH changes for weakly bonded primary particles (high δ), has a major influence on conductivity.

The production of controlled property aggregates is a relatively new area of research, with most prior efforts in aggregates focused on the dispersion of aggregates into primary particles in host media. While recent work shows that D_f and k_f can be controlled in suspensions by controlling solvent properties(Kim, Lee et al. 2010), controlled property aggregates would be more easily produced via gas-phase synthesis(Schmid, Tejwani et al. 2004; Tsantilis and Pratsinis 2004; Grass, Tsantilis et al. 2006; Schmid, Al-Zaitone et al. 2006; Scheckman, McMurry et al. 2009; Eggersdorfer, Kadau et al. 2011), in which a degree of overlap between primary particles could be produced. Related to the issue of controlled property aggregates, it seems that much of the controversy regarding conduction in particle-laden suspensions and composites arises due to a lack of techniques to fully characterize particle and aggregate morphology in suspensions and solid matrices when the particles are in the nanometer size range, as is often the case in current suspension and composite research. Attempts to measure D_f, k_f, and δ, all of which appear to influence conductivity, are rarely made (though structure factor measurements can often reliably determine D_f for sufficiently large aggregates (Lattuada, Wu et al. 2004; Wu, Xie et al. 2005; Ibaseta and Biscans 2010)), and methods to determine these parameters in aggregate laden materials will be necessary to improve both understanding of the behavior of aggregate-laden systems and the ability to tailor make aggegrate-laden suspensions and composites of controlled conductivity. Until such methods are in place, comparisons between model calculations and experimental measurements will be qualitative (as is performed here).

6.4 Conclusions

First passage calculations based upon the methods of Kim and Torquato (Kim and Torquato 1990; Kim and Torquato 1991) are used in this work to examine the conductivity of aggregate laden-composites and suspensions. Aggregates with

controlled D_f, k_f, and degree of overlap are produced using a sequential algorithm, allowing for the influence of these parameters on conductivity to be examined. Based upon this work, we draw the following conclusions:

1. Aggregation leads to enhancements in material conductivity beyond what is expected from the effective medium approximation. The enhancements driven by aggregate formation are only observed at high aggregate volume fraction, or with high conductivity aggregates. For high conductivity aggregates, aggregate morphology (fractal dimension and pre-exponential factor) can strongly influence the conductivity of a suspension or composite. For lower conductivity aggregates, suspension and composite conductivity is only weakly influenced by aggregate structure, with the degree of overlap (coalescence) between primary particles composing the aggregate having the most significant effect.

2. For aggregates with a sufficient number of primary particles to be described as a quasifractal, the resulting conductivity of a material incorporating aggregates is insensitive to the number of primary particle in each aggregate. Therefore, a change in the conductivity of a suspension or composite containing aggregates cannot be driven by further aggregation; rather, restructuring of the aggregates is necessary.

3. The first passage calculation approach applies only in the continuum limit, and omits any influence that particle size dependent conductivity or interfacial resistance to conduction may have on the resulting suspension/composite conductivity. Nonetheless, our calculations suggest that aggregate formation can fully account for any and all observed enhancements in conductivity beyond what is expected from the EMA in the case of either high particle volume fractions or high conductivity particles. With aggregates formed, the suspension/composite conductivity is a complex function of aggregate morphology.

Chapter 7: Convection Heat Transfer in Aggregate-laden Nanofluids

Abstract: This study looks at the effect of particle morphology in altering the viscosity and thermal conductivity of particle-laden nanofluids and thereby the effect on convective heat transfer coefficient. Two specific cases are studied here, Dittus Boelter ocrrelation for forced convection and Globe –Dropkin correlation for natural Convection.

7.1 Introduction

Heat transfer in particle suspensions is of considerable importance, as suspensions can be applied in a number of engineered heating and cooling systems, and are also encountered ubiquitously in the environment. In particular, suspensions containing nanoparticles, i.e. nanofluids (Keblinski, Phillpot et al. 2002; Eastman, Phillpot et al. 2004; Choi 2009), receive a great deal of attention due to their anomalously high thermal conductivities, beyond what is predicted by effective medium approximations (Eastman, Choi et al. 2001). Most evidence suggests that these enhancements arise due to the aggregation of particles (Prasher, Evans et al. 2006; Prasher, Phelan et al. 2006; Evans, Prasher et al. 2008; Keblinski, Prasher et al. 2008; Wensel, Wright et al. 2008; Gao, Zheng et al. 2009), either during particle synthesis processes (Schmid, Tejwani et al. 2004; Tsantilis and Pratsinis 2004; Schmid, Al-Zaitone et al. 2006; Eggersdorfer, Kadau et al. 2011) or within nanofluids themselves (Kim, Lee et al. 2010). Aggregation leads to a morphologically complex, chain-like unpercolated network composed of connecting primary particles in suspension (Huang, Oh et al. 1998; Oh and Sorensen 1998; Cerda, Sintes et al. 2004), and conduction through such a morphologically complex system can occur much more rapidly than through a system of well-dispersed particles (Kim and Torquato 1991; Kim and Torquato 1992; Havlin and Ben-Avraham 2002).

Similarly, the study of both forced and natural convection in nanofluids is of interest (Pak and Cho 1998; Xuan and Li 2003; Wen and Ding 2004; Buongiorno 2006;

Heris, Etemad et al. 2006; Wang and Mujumdar 2007; Tzou 2008; Kakac and Pramuanjaroenkij 2009; Corcione 2011), as there is the possibility that nanofluids may be applicable in convective heat transfer systems, and the presence of particles in natural environments may influence environmental convective heat transfer. While in the past decade conduction in nanofluids has indeed been well studied both experimentally and theoretically, studies of convection in nanofluids are comparatively rare. The prior experimental examinations of nanofluid convection that have been carried out show inconsistent results; in some cases the presence of nanoparticles increases the heat transfer coefficient (Anoop, Sundararajan et al. 2009), and in others the influence of nanoparticles on heat transfer is deleterious (Putra, Roetzel et al. 2003). Likewise, depending upon the models used for nanofluid thermal conductivity and viscosity, theoretical examination of convection in nanofluids can predict an enhancement or a reduction in the heat transfer coefficient (Khanafer, Vafai et al. 2003; Ho, Chen et al. 2008; Bachok, Ishak et al. 2011). To better understand convection in nanofluids, it is thus clear that more detailed models of how nanoparticles influence the bulk properties of suspensions are necessary. In most prior experimental and theoretical studies of convection in nanofluids, the focus has been on a single or several specific types of nanoparticles (of known thermal conductivity), the assumption has been made that the particles are morphologically simple (e.g. are spherical, rod-like, or are oblate or prolate spheroids), and differences in heat transfer found with different nanoparticles have primarily been attributed to the differing material properties of the nanoparticles (Pak and Cho 1998). This approach, however, neglects what appears to be a key factor controlling nanofluid thermal conductivity and likely convection in nanofluids, namely, the aggregation state and morphological complexity of the suspended nanoparticles. While the simplifications in particle morphology made in prior nanofluid studies stem from the fact that nanoparticle morphology in suspension is at present, not easily quantifiable (Keblinski, Prasher et al. 2008), it is nonetheless critical to examine how aggregation and aggregate morphology in nanofluids can alter nanofluid convection characteristics. Along these lines, the purpose of this work is to make initial predictions

of the convective heat transfer coefficients of nanofluids, accounting for the morphological complexity of suspended particles and the subsequent influence that particle morphology has on nanofluid dynamic viscosity and thermal conductivity (which both determine the heat transfer coefficient). In subsequent sections, the Monte Carlo based analysis approach employed is laid out in detail, including discussion of the assumptions made, the model of nanoparticle aggregates, the influence of aggregate morphology on the nanofluid dynamic viscosity and thermal conductivity, and, using well-studied convective heat transfer correlations, the influence of aggregated particles on the heat transfer coefficient in both forced and natural convection. Overall, this study can serve as a baseline for future experimental and theoretical examinations of convection in nanofluids, wherein particle morphology must be accounted for in greater detail.

7.2 Theoretical Approach

7.2.1 Heat Transfer in Nanofluids

In developing predictive models of forced and natural convective heat transfer coefficients for aggregate-laden nanofluids, the definition of a nanofluid, and correspondingly the assumptions involved in analysis must first be made clear. Building upon the arguments presented by Buongiorno (2006), nanoparticle suspensions can be analyzed with the following restrictions:

1. The suspended nanoparticles and their aggregates are sufficiently small such that they are in thermal equilibrium with their surrounding fluid under all circumstances.
2. For any practical application of nanofluids, stable suspensions are indeed necessary, and colloidal chemistry techniques may be used to create such stable dispersions (Jiang, Oberdorster et al. 2009; Kim, Lee et al. 2010). Cases wherein the aggregated particles are well dispersed in a stable suspension are examined, such that further aggregation does not occur via aggregate-aggregate collisions.

3. Particle inertia is negligible (i.e. particles Stokes number ≈ 0) (Friedlander 2000), enabling the motion of particles in suspension to be monitored via a convective-diffusion equation. This assumption holds valid for nearly all particles suspended in liquids, with perhaps the exception of high density supermicrometer particles traveling at high velocity.
4. Temperature gradients in nanofluids may certainly promote the development of nanoparticle concentration gradients via thermophoresis, and there is some evidence that during convective transport, thermophoresis may influence the resulting heat transfer coefficient (Buongiorno 2006; Oueslati and Bennacer 2011). However, for the initial examination presented here, the influence of thermophoresis is neglected and analysis is restricted to situations wherein the distribution of aggregates/nanoparticles in suspension is initially spatially homogenous and remains so as the nanofluid flows.
5. Heat transfer via conduction through a nanofluid occurs in the continuum limit, and the Brownian motion of particles has a negligible influence on the nanofluid's conductivity (Nie, Marlow et al. 2008). Therefore, the conductivity enhancement in nanofluids arises primarily from particle aggregate formation (Evans, Prasher et al. 2008; Thajudeen and Hogan 2011).
6. The volume fraction of particles in suspension is relatively low (≤0.05), such that the influence of nanoparticles on the dynamic viscosity can be described via the intrinsic viscosity relationship (Mansfield, Douglas et al. 2001). The change in viscosity resulting from the addition of nanoparticles to a suspension therefore depends only upon the particle volume fraction and the morphology dependent intrinsic viscosity.

With these assumptions, this model of heat transfer in an aggregate-laden nanofluid is similar to convective heat transfer in a single-phase fluid containing a known volume fraction of spatially homogenous solute molecules. Traditional Nusselt number correlations can therefore be used to determine the heat transfer coefficient in forced and natural convection with aggregate-laden nanofluids. For simplicity, in

forced convection the influence of aggregate morphology is examined using the well-known Dittus-Boelter correlation (Incropera, Dewitt et al. 2007) for the cooling of a cylindrical pipe by a fluid flowing through it under turbulent conditions, for which the heat transfer coefficient, h_0, is given as:

$$h_0 = 0.023 \frac{k_0}{D} \left(\frac{\rho_0 U_0 D}{\mu_0}\right)^{0.8} \left(\frac{c_{p,0}\mu_0}{k_0}\right)^{0.4} \quad (1a)$$

where k_0 is the thermal conductivity of the fluid, D is the pipe diameter, ρ_0 is the fluid density, U_0 is the average axial velocity through the pipe, μ_0 is the fluid dynamic viscosity, and $c_{p,0}$ is the fluid specific heat. The Dittus-Boelter correlation agrees reasonably well with experimental measurements for smooth pipes with 10,000 < Re < 20,000 (Re = $\rho_0 U_0 D/ \mu_0$, Reynolds Number) and 0.7 < Pr < 120 (Pr = $c_{p,0}\mu_0/k_0$, Prandtl Number). A given system employing nanofluids would have dimensional requirements (e.g. a specific flowrate and specific pipe diameter). For this reason the change in heat transfer coefficient due to the addition of particles of a given morphology (described subsequently) and volume fraction (V_f) to a system of fixed pipe diameter and fixed average axial velocity is examined here. With these conditions, the Dittus-Boelter heat transfer coefficient of the nanofluid relative to the base fluid is given as:

$$\frac{h}{h_0} = \left(\frac{c_{p,nf}}{c_{p,0}}\right)^{0.4} \left(\frac{\mu_0}{\mu_{nf}}\right)^{0.4} \left(\frac{k_{nf}}{k_0}\right)^{0.6} \left(\frac{\rho_{nf}}{\rho_0}\right)^{0.8} \quad (1b)$$

where the subscript "*nf*" denotes the effective property of the nanofluids and "*0*" denotes the base fluid properties.

To investigate natural convection with nanofluids, well-studied Globe-Dropkin expression (Globe and Dropkin 1959; Incropera, Dewitt et al. 2007) for the heat transfer within a fluid held between two horizontal parallel plates is studied, wherein the lower plate is fixed at a higher temperature than is the upper plate, which is given as:

$$h_0 = 0.069 \frac{k_0}{L} \left[\frac{g\beta_0 \rho_0^2 L^3}{\mu} (T_l - T_u)\right]^{0.333} \left(\frac{c_{p,0}\mu_0}{k_0}\right)^{0.407} \quad (2a)$$

where L is the distance between the plates, g as the acceleration due to gravity, β_0 is the fluid thermal expansion coefficient, T_l is the temperature of the lower plate, and T_u is the temperature of the upper plate. The Globe-Dropkin expression applies for 3 x 10^5 <

Ra < 7 x 10^9 (Ra = $g\beta_0\rho_0^2L^3c_{p,0}\ (T_l\text{-}T_u)/(\mu_0k_0)$, Rayleigh Number). Similar to forced convection, the change in heat transfer coefficient in natural convection due to the addition of nanoparticles of a given morphology and volume fraction is examined here, where the plates are the same distance from one another and the same temperature difference is maintained. The Globe-Dropkin expression gives the heat transfer coefficient of the nanofluid relative to the base fluid as:

$$\frac{h}{h_0} = \left(\frac{c_{p,nf}}{c_{p,0}}\right)^{0.407}\left(\frac{\mu_0}{\mu_{nf}}\right)^{0.260}\left(\frac{k_{nf}}{k_0}\right)^{0.593}\left(\frac{\rho_{nf}}{\rho_0}\right)^{0.666}\left(\frac{\beta_{nf}}{\beta_0}\right)^{0.333} \tag{2b}$$

While the choice to examine convection via the Dittus-Boelter and Globe-Dropkin expressions is somewhat arbitrary, nearly all heat transfer coefficient correlation expressions which derive from dimensional analysis will involve the Reynolds number and Prandtl number in forced convection, and similarly the Rayleigh number/Grashof number (Ra/Pr) and Prandtl number in natural convection. This further applies to recently derived heat transfer correlations for convection in nanofluids, in which the influence of thermophoresis is considered (Buongiorno 2006). Therefore, examination of almost all available heat transfer correlation expressions will lead to comparable results to that of our analysis. Because of the dependence upon these dimensionless numbers, the change in heat transfer coefficient brought about by the addition of nanoparticles in both forced and natural convection is a function of the ratios μ_{nf}/μ_0, k_{nf}/k_0, ρ_{nf}/ρ_0, $c_{p,nf}/c_p$, and β_{nf}/β_0. The ratios ρ_{nf}/ρ_0, $c_{p,nf}/c_p$, and β_{nf}/β_0 are not influenced by the morphology of the nanoparticles, and can be determined from the equations:

$$\frac{\rho_{nf}}{\rho_0} = 1 + V_f\left(\frac{\rho_p}{\rho_0} - 1\right) \tag{3}$$

$$\frac{C_{p,nf}}{C_{p,0}} = \frac{1+V_f\left(\frac{\rho_p c_{p,p}}{\rho_0 c_{p,0}}-1\right)}{1+V_f\left(\frac{\rho_p}{\rho_0}-1\right)} \tag{4}$$

$$\frac{\beta_{nf}}{\beta_0} = 1 + V_f\left(\frac{\beta_p}{\beta_0} - 1\right) \tag{5}$$

where the subscript "p" denotes a property of the nanoparticles in suspension. Conversely, the ratios μ_{nf}/μ_0 and kn_f/k_0 are indeed dependent upon the morphology of

the suspended particles, thus realistic models of particle structure in suspension are necessary and must be used in conjunction with appropriate computation procedures to predict μ_{nf}/μ_0 and k_{nf}/k_0.

7.2.2 Particle Morphology

As noted in the introduction section, at high production rates, inorganic nanoparticles, synthesized via nucleation-condensation reactions in either the gas or liquid phase, eventually reach a number concentration at which particle-particle collisions are prevalent, and under most circumstances nearly all collisions result in particles sticking to one another (Swihart 2003; Tsantilis and Pratsinis 2004; Schwarzer and Peukert 2005). Further, depending on the temperature during which such collisions occur, colliding particles may partially coalesce. The net result of this process is that nanoparticles exist as quasifractal aggregates in suspension (Sorensen 2011; Sorensen and Chakrabarti 2011) unless specific measures are taken to avoid aggregation (Peukert, Schwarzer et al. 2005) or breakup aggregates (Stenger, Mende et al. 2005; Inkyo, Tahara et al. 2006). The morphology of a quasifractal aggregate (statistical fractal) can be described by the aggregate's volume, V_{agg}, the radii of the primary particles in the aggregate a_{pp}, the fractal (Hausdorff) dimension of the aggregate, D_f, , and the aggregate pre-exponential factor, K_f). These four morphological descriptors for aggregates within the same population can be related to one another via the equation (Schmidt-Ott 1988; Schmid, Tejwani et al. 2004; Schmid, Al-Zaitone et al. 2006) and similarly explained in Chapter 6:

$$\frac{3V_{agg}}{4\pi a_{pp}^3} = k_f \left(\frac{R_g}{a_{pp}}\right)^{D_f} \tag{6}$$

where R_g is the radius of gyration of an aggregate. With the coalescence of particles leading to non-point contacts between primary particles, a fifth morphological descriptor must be introduced. To describe overlap between primary particles, we define the minimum distance between the centers of primary particles within an aggregate as d, with which we can define the overlap parameter δ, as (explained in Chapter 6):

$$\delta = \frac{d}{2a_{pp}} \tag{7}$$

To theoretically examine convection in aggregate-laden nanofluids, it is therefore necessary to computationally generate aggregates of a prescribed V_{agg} (or in-lieu of V_{agg}, the number of primary particles in the aggregate), a_{pp}, K_f, D_f, and δ. This is accomplished here following the procedure described in detail in Chapter 6. As an alternative to examination of all D_f, K_f, and δ combinations, this study examines differences in the heat transfer coefficient brought about by four different classes of aggregates, which vary drastically in quasifractal parameters and whose conductivity enhancement is studied and explained in Chapter 6, and represent appropriate limiting cases for aggregates observed in nanofluids: (I) chain like aggregates (D_f = 1.5, K_f = 1.3) with near point contacts (δ = 0.95), (II) chain like aggregates (D_f = 1.5, K_f = 1.3) with substantial primary particle coalescence (δ = 0.65), (III) dense aggregates (D_f = 2.6, K_f = 1.8) with near point contacts (δ = 0.95), and (IV) dense aggregates (D_f = 2.6, K_f = 1.8) with substantial primary particle coalescence (δ = 0.65). Sample images of types (I-IV) aggregates composed of 20, 50, and 100 primary particles are shown in Figure 7.1, displaying the diversity in morphology which is achieved via particle aggregation.

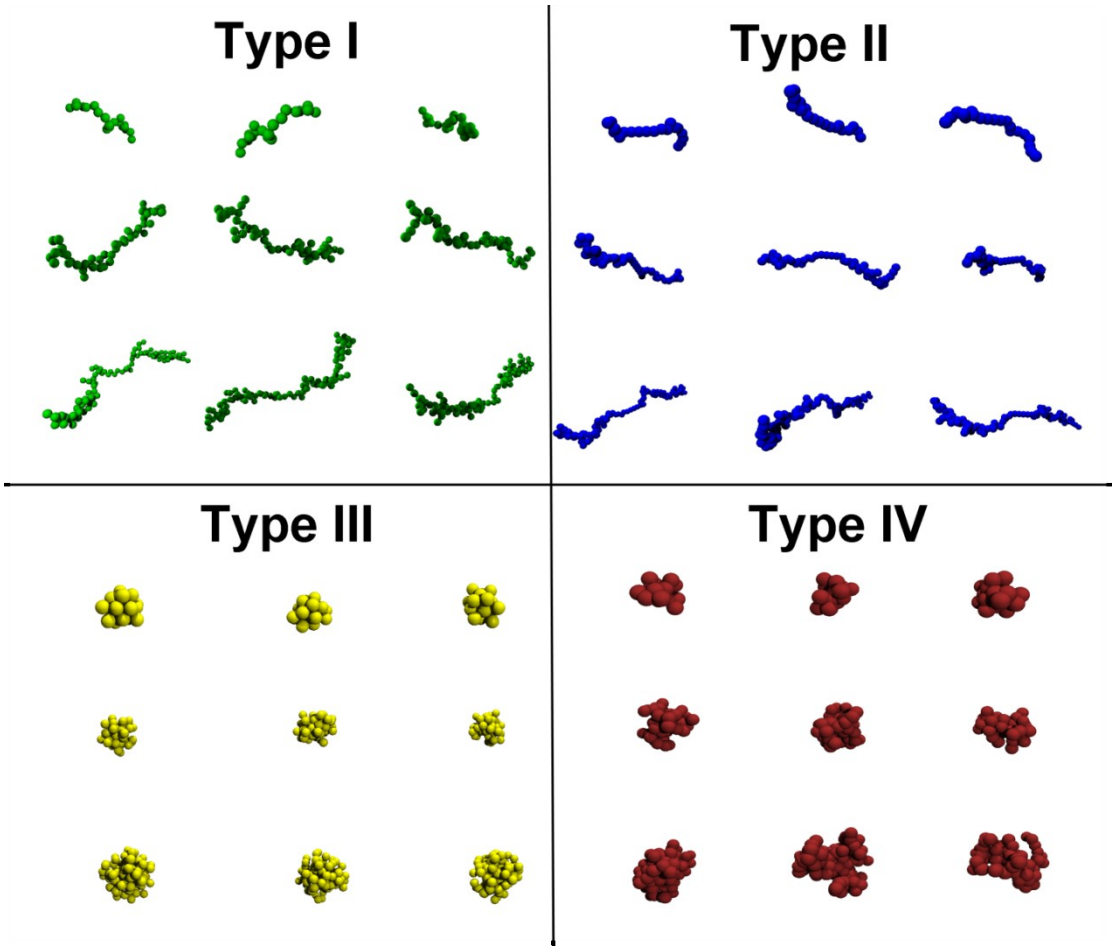

Figure 7.1. Selected images of randomly generated Types I-IV aggregates.

7.2.3 Dynamic Viscosity

For low nanoparticle volume fractions, the viscosity of a nanofluid as compared to the viscosity of the base fluid can be described by the equation (Mansfield, Douglas et al. 2001):

$$\frac{\mu_{nf}}{\mu_0} = 1 + [\eta_{agg}]V_f \tag{8}$$

where $[\eta_{agg}]$ is the intrinsic viscosity of the particles (known to be 2.5 for perfectly spherical particles). While intrinsic viscosity calculations are commonplace in the

examination of protein and polymer solutions (Kang, Mansfield et al. 2004; Mansfield, Douglas et al. 2007; Mansfield and Douglas 2008; Mansfield and Douglas 2008; Mansfield and Douglas 2010), the examination of aggregate nanoparticle intrinsic viscosities is rarely undertaken. As the ratio μ_{nf}/μ_0 plays a role in determining nanofluid heat transfer coefficients, we evaluate the intrinsic viscosities of types I-IV aggregates composed of 10-100 primary particles, using the path-integration technique described in detail by Mansfield et al (2001). In truth, the path-integration technique does not lead to explicit calculation of the intrinsic viscosity, but rather leads to calculation of the intrinsic conductivity $[\sigma_\infty]$ of a conducting, arbitrarily shaped object. Justification for the use of this approach in intrinsic viscosity calculation is discussed in great detail in several studies by Mansfield, Douglas, and coworkers (Mansfield, Douglas et al. 2001; Mansfield, Douglas et al. 2007; Mansfield and Douglas 2008; Mansfield and Douglas 2008; Mansfield and Douglas 2008; Mansfield and Douglas 2010; Mansfield and Douglas 2010). We refer readers to these works for further information on the path integration technique. The intrinsic viscosity of an object is related to the intrinsic conductivity through the relationship:

$$[\eta_{agg}] \approx \varphi[\sigma_\infty] \tag{9}$$

Comparisons of exact solutions for the intrinsic viscosity and intrinsic conductivity show that across several orders magnitude in $[\sigma_\infty]$, φ ranges from 0.75-0.83, with the lower end of the range more applicable to slender bodies and the upper end conversely more applicable to denser structures (Mansfield, Douglas et al. 2001). $\varphi = 0.83$ is used here for all calculations, as the intrinsic conductivity of a sphere is 3.0; thus, with this φ, calculation of the intrinsic conductivity yields the correct intrinsic viscosity for spheres. A schematic of the path integration technique is shown in Figure 7.2.

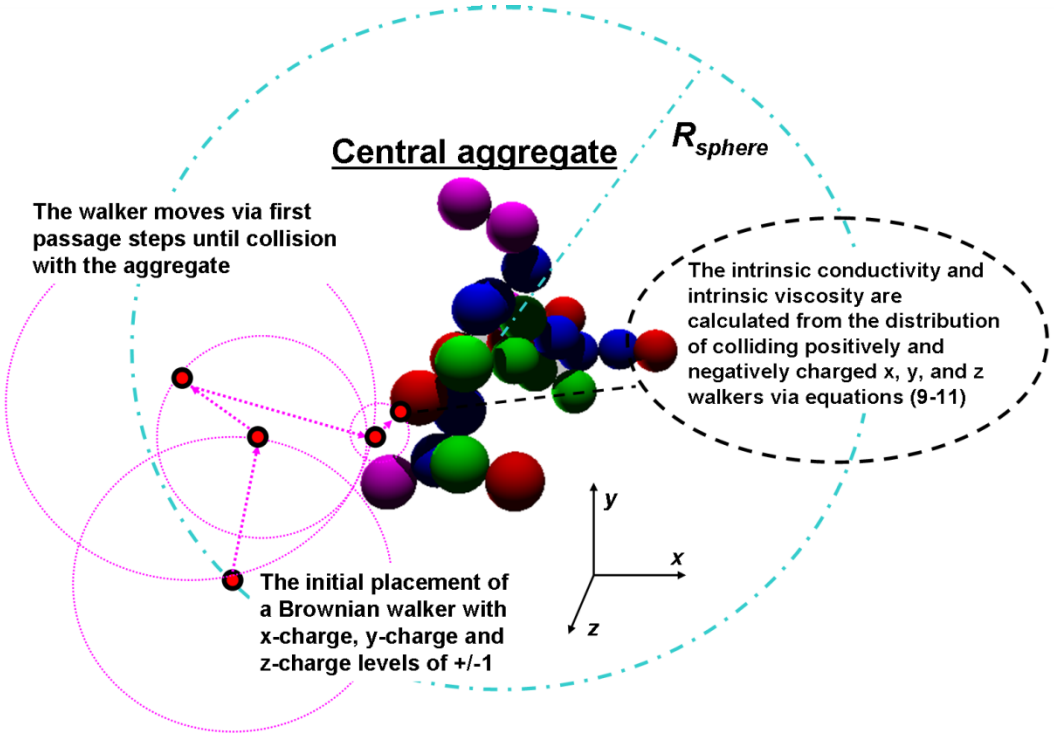

Figure 7.2. Graphic representation of the stochastic path integration technique used in intrinsic viscosity determination for Types I-IV aggregates.

An aggregate, produced via the previously described algorithm, is centered at the origin in a spherical domain where the sphere (with radius, R_{sphere}) must completely enclose the aggregate but otherwise is arbitrarily large. A number, N, ($\sim 10^6$) of Brownian walkers are randomly placed on the surface of the outer sphere. Based on a walker's initial (x,y,z) coordinates on the sphere's surface, it is assigned three "charge" numbers, one for each principle direction. A walker's x-charge level is assigned as +1 with probability $(1+x/R_{sphere})/2$; otherwise it is assigned a negative charge. Similarly, the walker's y-charge level and z-charge level are assigned as +1 with probabilities $(1+y/R_{sphere})/2$ and $(1+y/R_{sphere})/2$, respectively (otherwise, these charge levels are designated as -1). After charge assignment, each Brownian walker moves in a random direction via the first passage algorithm described by Kim and Torquato (Kim and

Torquato 1991; Kim and Torquato 1992). If the walker moves farther away from the origin than distance R_{sphere}, the probability that the walker continues an infinite distance from the aggregate is calculated as $1-R_{sphere}/b$, where b is the radial coordinate of the walker. If, through random number calculation, it is determined that the walker remains in the domain, it is placed on the surface of the sphere with its angular coordinates determined as described in Chapter 2. Otherwise, a new Brownian walker is placed at a random location at radial distance R_{sphere} and again assigned x, y, and z charge levels. Brownian walkers which remain in the domain continue to take successive first passage steps in random directions until they reach a small distance (< 0.1% of the primary particle radius in the aggregate) from the surface of the aggregate. Upon reaching this point, a given Brownian walker's coordinates are recorded as (x_f, y_f, z_f), and for each principle direction j, the number of walkers with a positive charge A_j^+ and the number of walkers with a negative charge A_j^- are calculated. V_{ij}^+ and V_{ij}^- are then defined as the sums of the ith components of the displacement vectors (i.e. x_f, y_f, and z_f) at which the direction j positively charged walkers absorb and direction j negatively charged walkers absorb, respectively, and finally t is defined as the ratio $(A_x^+ + A_x^-)/N$. With these values the following parameters are calculated:

$$u_j = \frac{\left(A_j^+ - A_j^-\right)}{N} \tag{10a}$$

$$v_{ij} = \frac{\left(V_{ij}^+ + V_{ij}^-\right)}{N} \tag{10b}$$

$$w_{ij} = \frac{\left(V_{ij}^+ - V_{ij}^-\right)}{N} \tag{10c}$$

Subsequently, with these calculations the components of the polarizability tensor for the aggregate are determined as:

$$\sigma_\infty = 12\pi R_{sphere}^2 \left(w_{ij} - \frac{u_j}{t} v_{ij}\right) \tag{11}$$

The intrinsic conductivity [σ_∞] is calculated as the trace of the polarizability tensor, and with equation (9) the intrinsic viscosity [η_{agg}] of the aggregate of interest is thus inferred.

The path integration technique is verified by using it to compute the intrinsic conductivity of a sphere, which it does with an error less than 0.1%. The intrinsic viscosities of type I-IV aggregates are plotted in Figure 7.3 for 10-100 primary particles (integer values) averaged over 50 aggregates.

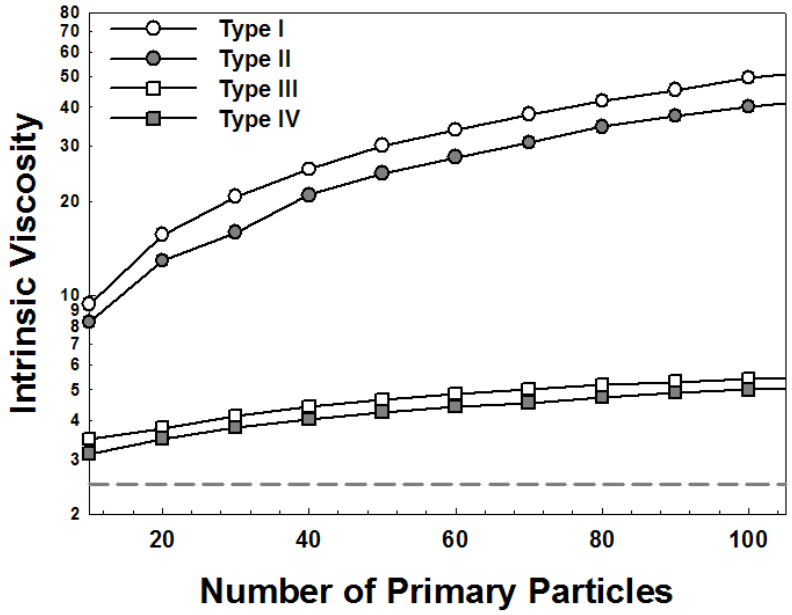

Figure 7.3. Intrinsic viscosities of Types I-IV aggregates as functions of the number of primary particles per aggregate. Dashed gray line denotes the intrinsic viscosity of isolated spherical particles.

For each aggregate type, the intrinsic viscosity increases monotonically with the number of primary particles, and, not surprisingly, the lower fractal dimension aggregates (Types I-II) with a greater extent of branching have larger intrinsic viscosities than do higher fractal dimension, denser aggregates (Types III-IV). For the former, the calculated intrinsic viscosity is sufficiently high to suggest that at particle volume fractions as low as 0.03, the nanofluid will have a dynamic viscosity 150% greater than the base fluid dynamic viscosity.

7.2.4 Thermal Conductivity

As explained in Chapter 6, along the lines of approach of Kim & Torquato (1991; 1992) to determine the effective conductivities of suspensions and composites containing types I-IV aggregates with particle volume fractions up to 0.20, a first passage time simulation was employed to arrive at the effective thermal conductivity. These simulations revealed that, unlike aggregate intrinsic viscosities, the number of primary particles per aggregate has little-to-no influence on the thermal conductivity of a nanofluid at any volume fraction. Further, for aggregates where the ratio of the nanoparticle thermal conductivity, k_p, to base fluid thermal conductivity, k_0, is 10 and the volume fraction of particles is ≤0.05, irrespective of aggregate morphology, the nanofluid thermal conductivity can be reliably calculated from the Maxwell-Garnet effective medium approximation, which is given as (Buongiorno, Venerus et al. 2009):

$$\frac{k_{nf}}{k_0} = \frac{\left(\frac{k_p}{k_0}\right)(1+2V_f)-2V_f+2}{\left(\frac{k_p}{k_0}\right)(1-V_f)+V_f+2} \tag{12a}$$

Conversely, it was found that aggregation does indeed promote greater enhancement in thermal conductivity when the ratio k_p/k_0 = 100, and the degree of enhancement is largely dependent upon the aggregate morphology. For particle volume fractions ≤0.05, an effective volume fraction $V_{f,eff}$ can be defined, such that:

$$\frac{k_{nf}}{k_0} = \frac{\left(\frac{k_p}{k_0}\right)(1+2V_{f,eff})-2V_{f,eff}+2}{\left(\frac{k_p}{k_0}\right)(1-V_{f,eff})+V_{f,eff}+2} \tag{12b}$$

where:

$$V_{f,eff} = \theta_e V_f \frac{k_{nf}}{k_0} \tag{12c}$$

and θ_e is the enhancement factor in nanoparticle volume fraction brought about by aggregation. For particle volume fractions ≤0.05, enhancement factors for types I-IV aggregates with k_p/k_0 = 100, as determined from first passage simulations, are 3.217 (type I), 4.54 (type II), 4.027 (type III), and 3.667 (type IV). For convection analysis, we examine particles at both k_p/k_0 = 10 and k_p/k_0 = 100, using equation (12a) when k_p/k_0 = 10 and equations (12b-c) when k_p/k_0 = 100, respectively.

7.3 Results and Discussion

7.3.1 Examined Aggregate Material Properties

Combining equations (1b) and (2b) with equations (3-5), (8), and (12a-c), the ratio h/h_0 can be calculated from the equation

$$\frac{h}{h_0} = \left(\frac{1+V_f\left(\frac{\rho_p C_{p,p}}{\rho_0 C_{p,0}}-1\right)}{1+V_f\left(\frac{\rho_p}{\rho_0}-1\right)}\right)^{0.4}\left(\frac{1}{1+[\eta_{agg}]V_f}\right)^{0.4}\left(\frac{\left(\frac{k_p}{k_0}\right)(1+2V_{f,eff})-2V_{f,eff}+2}{\left(\frac{k_p}{k_0}\right)(1-V_{f,eff})+V_{f,eff}+2}\right)^{0.6}\left(1+V_f\left(\frac{\rho_p}{\rho_0}-1\right)\right)^{0.8} \quad (13a)$$

for Dittus-Boelter forced convection and:

$$\frac{h}{h_0} = \left(\frac{1+V_f\left(\frac{\rho_p}{\rho_0}\frac{C_{p,p}}{C_{p,0}}-1\right)}{1+V_f\left(\frac{\rho_p}{\rho_0}-1\right)}\right)^{0.407}\left(\frac{1}{1+[\eta_{agg}]V_f}\right)^{0.260}\left(1+V_f\left(\frac{\rho_p}{\rho_0}-1\right)\right)^{0.666}\left(\frac{\left(\frac{k_p}{k_0}\right)(1+2V_{f,eff})-2V_{f,eff}+2}{\left(\frac{k_p}{k_0}\right)(1-V_{f,eff})+V_{f,eff}+2}\right)^{0.593}\left(1+V_f\left(\frac{\beta_p}{\beta_0}-1\right)\right)^{0.333} \quad (13b)$$

for Globe-Dropkin natural convection. In addition to the nanoparticle volume fraction, these expressions are influenced by the particle material-dependent ratios ρ_p/ρ_0, $c_{p,p}/c_{p,0}$, β_p/β_0, and k_p/k_0. Here, two sets of ratios are used: the first based on characteristic values for a metal oxide nanoparticle-water suspension (MO) and the second based on characteristic values for a metal nanoparticle-water suspension (M). The equations (13a) and (13b) required ratios are given in Table 7.1 for these two theoretical nanoparticle types.

Table 7.1. Summary of the test properties used for nanofluids containing representative metal oxide and metal nanoparticles.

	Model Values	
	Metal Oxide	Metal
ρ_p/ρ_0	4	10
$c_{p,p}/c_{p,0}$	0.125	0.125
β_p/β_0	0.1	0.1
k_p/k_0	10	100

7.3.2 Aggregate Nanofluid Prandtl Numbers and Heat Transfer Coefficients

As the Prandtl number influences both forced and natural convection and unlike most dimensionless ratios, is a property of a fluid, the ratio of the Prandtl number of an aggregate laden nanofluid, Pr, relative to the Prandtl number of the base liquid, Pr_0 is of interest. With the assumptions made in this work it can be calculated from the equation:

$$\frac{Pr}{Pr_0} = \left(1 + [\eta_{agg}]V_f\right)\left(\frac{1 + V_f\left(\frac{\rho_p}{\rho_0}\frac{C_{p,p}}{C_{p,0}} - 1\right)}{1 + V_f\left(\frac{\rho_p}{\rho_0} - 1\right)}\right)\left(\frac{\left(\frac{k_p}{k_0}\right)\left(1 + 2V_{f,eff}\right) - 2V_{f,eff} + 2}{\left(\frac{k_p}{k_0}\right)\left(1 - V_{f,eff}\right) + V_{f,eff} + 2}\right)^{-1} \quad (14)$$

Figure 7.4 shows the ratio Pr/Pr_0 as a function of particle volume fraction for nanofluids containing MO and M nanoparticles, with types I-IV morphologies and 10-100 primary particles per aggregate. For reference, the ratio expected for isolated, spherical particles is also shown. Similarly, the equation 13a and 13b determined changes in heat transfer coefficient brought about by the presence of aggregates are shown in Figures 7.5 and 7.6, respectively. The particle volume fraction is restricted to the range 0.001-0.05, for which the model of intrinsic viscosity holds reasonably valid and which would most likely be used in an experimental setting. Each of these three

figures reveals similar phenomena about the influence of aggregation on convective heat transfer; thus, the figures are discussed here collectively, as opposed to separately.

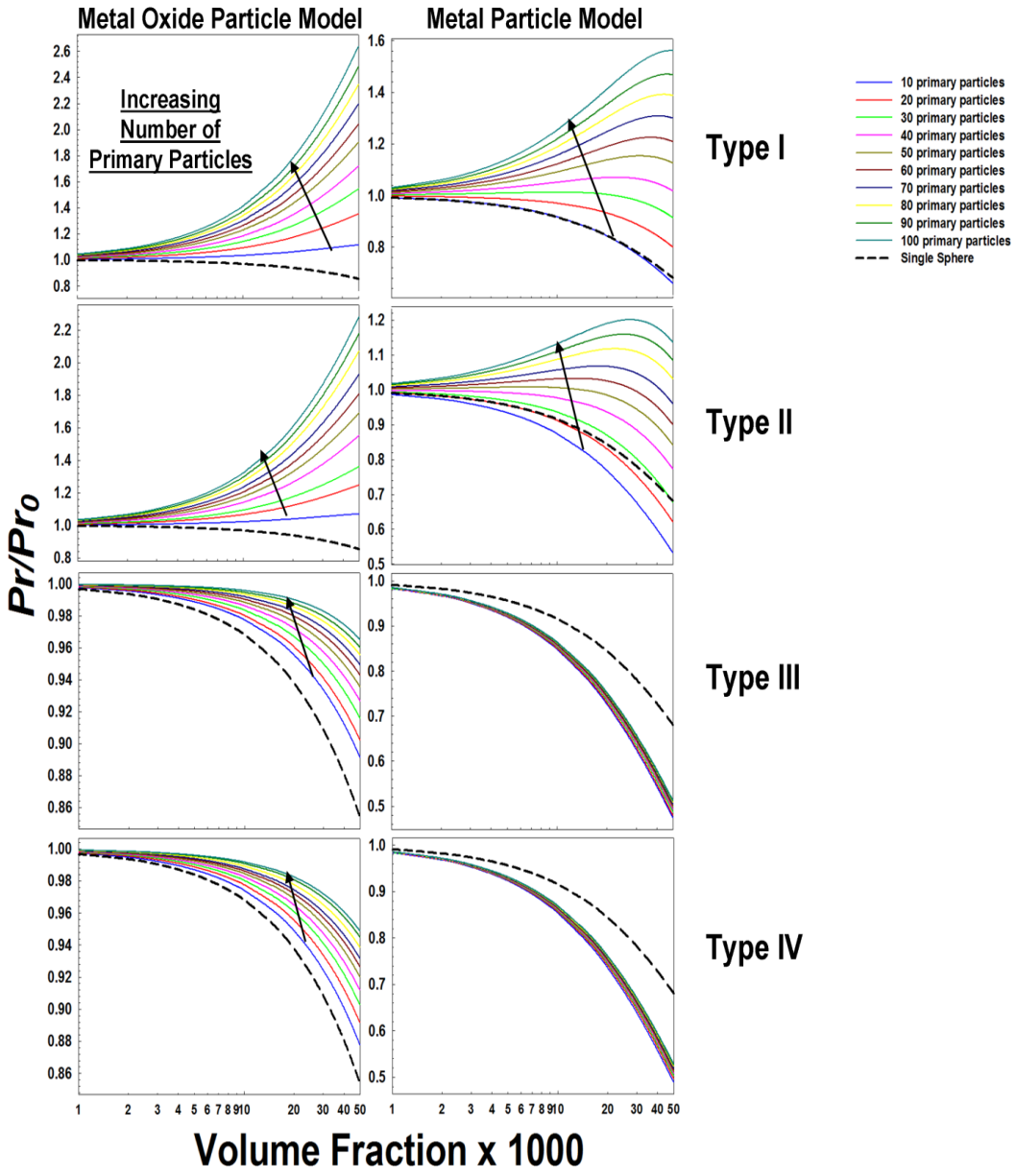

Figure 7.4. The Prandtl number (Pr) of nanofluids containing types I-IV aggregates relative to the Prandtl number of the base liquid. Arrows point in the direction of increasing number of primary particles per aggregate to aid in distinguishing curves from one another.

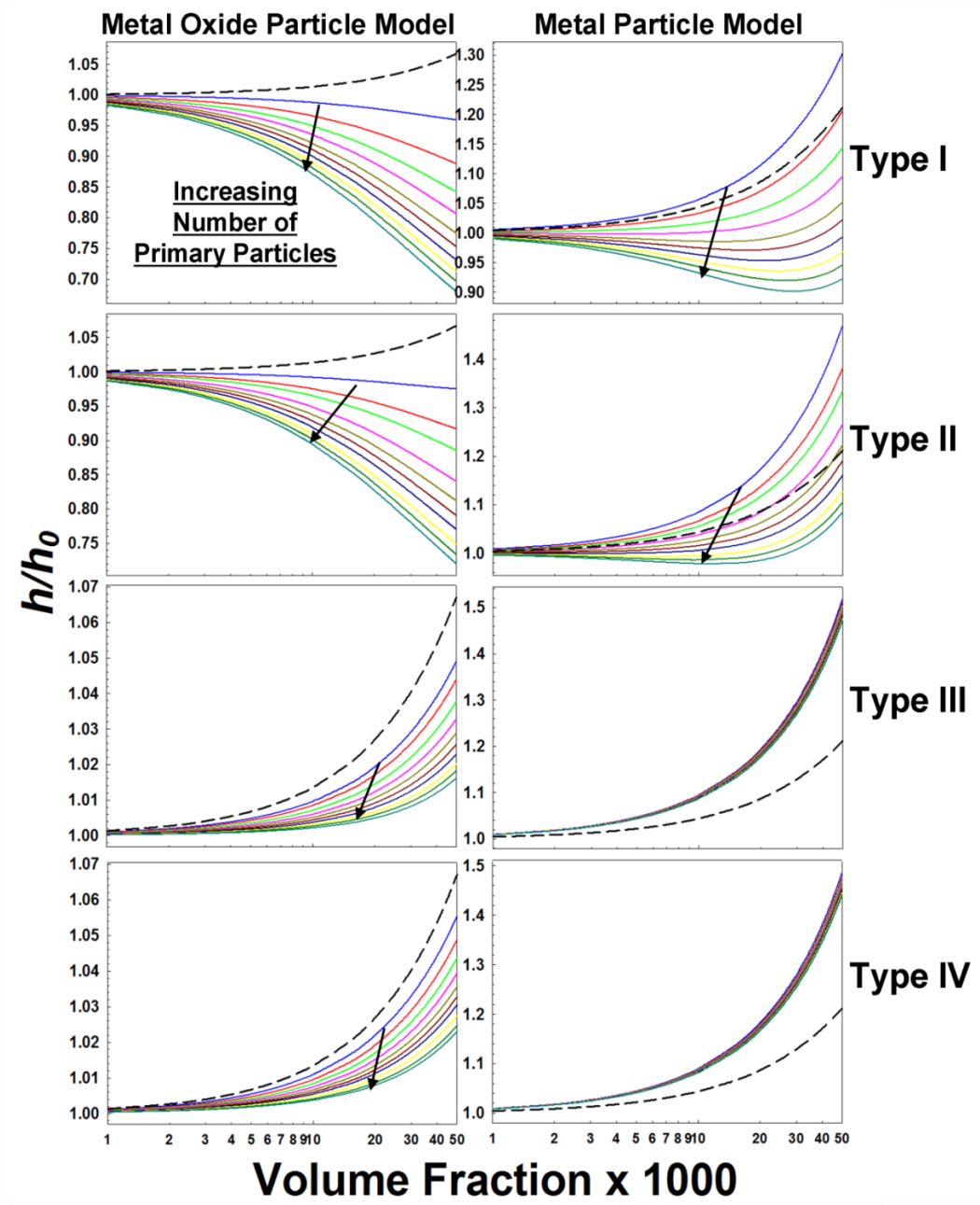

Figure 7.5. The heat transfer coefficient (h) of the nanofluid relative to the base fluid for forced convection in accordance with the Dittus-Boelter correlation. The color of each curve corresponds to the number of primary particles per aggregate as noted in the legend of Figure 7.4 Arrows point in the direction of increasing number of primary particles per aggregate to aid in distinguishing curves from one another.

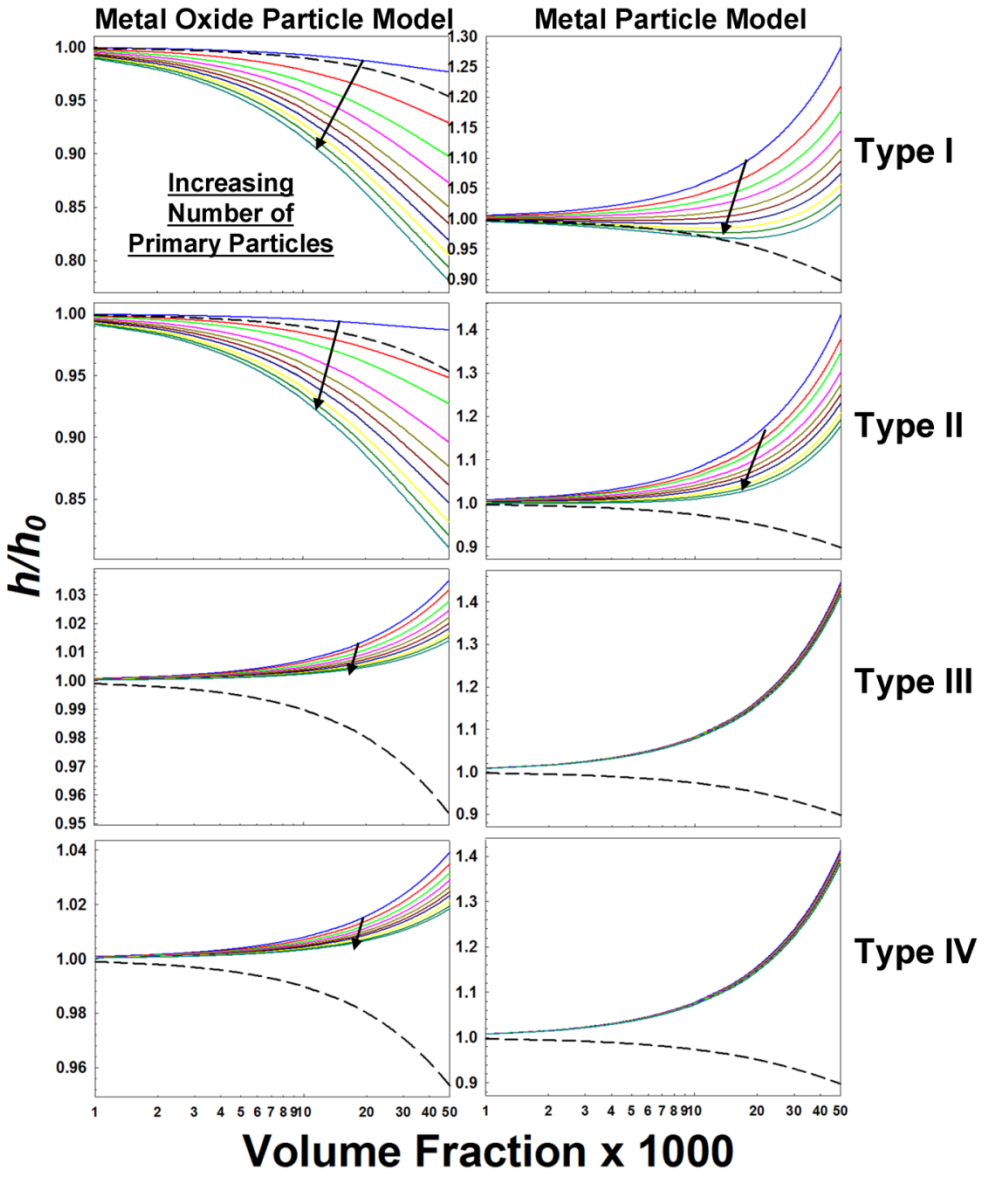

Figure 7.6. The heat transfer coefficient (h) of the nanofluid relative to the base fluid for natural convection in accordance with the Globe-Dropkin correlation. The color of each curve corresponds to the number of primary particles per aggregate as noted in the legend of Figure 7.4. Arrows point in the direction of increasing number of primary particles per aggregate to aid in distinguishing curves from one another.

It is immediately clear from figures 7.4-7.6 that both the material properties of the nanoparticles as well as the morphology of aggregates influence the change in heat

transfer coefficient for nanofluids as compared to the base fluid in a complex manner. A 51% increase (Type IV-M aggregates composed of 10 primary particles at 5% volume fraction, forced convection) and a 32% decrease (Type I-MO aggregates composed of 100 primary particles at 5% volume fraction, forced convection) in the heat transfer coefficient achievable for the cases examined. Table 7.2 briefly summarizes the qualitative influence of aggregation in each type of nanofluid. From these results, we can find that:

1. Depending on the aggregate morphology and material, the addition of particles to suspensions can cause an increase or a decrease in heat transfer coefficient with increasing particle volume fraction, and in some cases leads to a critical particle volume fraction at which the heat transfer coefficient is a maximum or a minimum. This widely varying behavior indeed suggests that the disparate results found in experimental studies (Pak and Cho 1998; Putra, Roetzel et al. 2003; Xuan and Li 2003; Anoop, Sundararajan et al. 2009) of nanofluid convection and in numerical studies (which are dependent upon the thermal conductivity and intrinsic viscosity models used) are attributable to differing particle morphologies and the extent of aggregation in suspension.
2. The addition of compact MO aggregates (type III or type IV) to suspensions has a negligibly small predicted influence on the heat transfer coefficient in both forced and natural convection. In this case, the slight increase in thermal conductivity by the particles is counteracted by the increase in dynamic viscosity. Conversely, highly linear, low conductivity MO aggregates lead to a proportionally larger increase in dynamic viscosity than in thermal conductivity, and have a deleterious influence on heat transfer coefficients. Overall, low conductivity nanoparticles, such as most metal oxides, appear unable to enhance convective heat transfer in suspensions.
3. The addition of high conductivity M nanoparticles to a suspension, under most circumstances, enhances the heat transfer coefficient. In this case, the enhancement in thermal conductivity brought about by aggregation (Thajudeen

and Hogan 2011) outweighs the increase in viscosity. This is particularly evident for compact, high fractal dimension aggregates, where aggregation does not substantially increase the intrinsic viscosity beyond the value for spheres.

4. As compared to spherical particles, the formation of aggregates and further aggregation of MO nanoparticles always reduces the heat transfer coefficient in forced convection. With the exception of types III and IV aggregates, where little-to-no-change is observed with nanoparticles, the aggregation of MO nanoparticles also reduces the heat transfer coefficient in natural convection. Conversely, with M nanoparticles, the formation of aggregates quite often enhances heat transfer as compared to spheres, particularly for compact type III and type IV aggregates. While the formation of aggregates can clearly enhance heat transfer, once an aggregate of a given morphology (D_f, K_f, and δ) is formed, further aggregation, which increases the number of primary particles per aggregate, can only lead to deleterious effects on convective heat transfer, as further aggregation only serves to increase the aggregate intrinsic viscosity.

Overall, calculation results suggest that to enhance convective heat transfer coefficients in suspensions, high thermal conductivity nanoparticles must be used. Of equal, importance, however, is the need to produce compact aggregates of these particles which have intrinsic viscosities close to that of spheres, yet enhanced thermal conductivities over their spherical counterparts.

Table 7.2. Summary of the qualitative influence of the addition of aggregate nanoparticles to suspensions on the suspension Prandtl number, forced convection heat transfer coefficient, and natural convection heat transfer coefficient.

		Change in Prandtl Number	Change in Forced Convection Heat Transfer Coefficient	Change in Natural Convection Heat Transfer Coefficient
Type I	**Metal Oxide**	Aggregates greatly increase Prandtl Number*	Aggregates decrease the heat transfer coefficient*	Aggregates decrease the heat transfer coefficient
	Metal	Prandtl number has a maximum	Aggregates both increase and decrease the heat transfer coefficient*	Aggregates both increase and decrease the heat transfer coefficient*
Type II	**Metal Oxide**	Aggregates greatly increase Prandtl Number*	Aggregates decrease the heat transfer coefficient*	Aggregates decrease the heat transfer coefficient
	Metal	Prandtl number has a maximum	Aggregates increase the heat transfer coefficient	Aggregates increase the heat transfer coefficient*
Type III	**Metal Oxide**	Aggregates slightly decrease Prandtl Number	Aggregates slightly increase the heat transfer coefficient	Aggregates slightly increase the heat transfer coefficient*
	Metal	Aggregates greatly decrease Prandtl Number	Aggregates greatly increase the heat transfer coefficient	Aggregates greatly increase the heat transfer coefficient*
Type IV	**Metal Oxide**	Aggregates slightly decrease Prandtl Number	Aggregates slightly increase the heat transfer coefficient	Aggregates slightly increase the heat transfer coefficient*
	Metal	Aggregates greatly decrease Prandtl Number	Aggregates greatly increase the heat transfer coefficient	Aggregates greatly increase the heat transfer coefficient*

*The change in Prandtl number / heat transfer coefficient brought about by aggregates which is qualitatively different from that brought about by isolated spheres

7.4 Conclusions

The change in heat transfer coefficient in forced and natural convection brought about by the addition of morphologically complex aggregates to suspensions was studied theoretically using detailed, Monte Carlo based models to predict the dynamic viscosity and thermal conductivity of aggregate-laden suspensions. Heat transfer coefficients for aggregate suspensions were predicted using the well-known Dittus-Boelter correlation for turbulent heat transfer in a pipe and the Globe-Dropkin expression for natural convection between two plates. Results of these calculations show that aggregation can bring about either an increase or decrease in heat transfer coefficient, and that to enhance heat transfer coefficients it is equally important to suspend high conductivity aggregates of particles as well as to produce compact, high fractal dimension aggregates which enhance thermal conductivity and minimize the increase in suspension viscosity. This study can serve as a baseline for future experimental and numerical investigations of convection in nanofluids. In future experimental studies, we suggest that greater emphasis be made to assess the morphology of nanoparticles in nanofluids, and building upon this study, in future theoretical studies the influence of thermophoresis on heat transfer correlations, which is not considered here, should be accounted for in convection.

Chapter 8: Summary and Future Work

8.1 Summary

This dissertation has theoretical, numerical and experimental aspects dealing with the effect of particle morphology in various mass, momentum and energy transfer processes involving aggregates. Collision processes which are most often the driving mechanisms in gas phase synthesis system is dealt with in detail, specifically in mass and momentum transfer transition regimes.

Electrical mobility measurements are one of the most commonly used techniques to size classify aerosol particles, where friction factor is an important parameter in evaluating the particle mobility. The typical size ranges of aerosol particles necessitate the need to calculate the friction factor at intermediate momentum transfer Knudsen number regime, where neither continuum theory nor kinetic theory can be applied. Through this work, an expression is proposed, with the calculation of two geometric size descriptors that can calculate the friction factor of a non-spherical entity in all momentum transfer regimes. This is validated with an experimental study by collecting flame synthesized Titania particles that are collected based on electrical mobilities and then analyzed to compare the mobilities predicted by the expression.

An equation for determination of collision rate of non-spherical entities under all regimes of mass transfer is also given which requires the knowledge of the friction factors and geometries of the colliding entities. This study proves that the binary collision rate can be determined with the accurate knowledge of the Diffusive Knudsen number that defines the regime in which mass transfer processes happen.

With the information on the two Knudsen numbers, a code was developed, which to date is physically the most accurate to study aggregation kinetics and growth of aerosol nanoparticles via collision and subsequent binding. Particle growth in the system is monitored via the evolution of the two Knudsen numbers and also different size descriptors that sheds light on the morphological aspects of the particles in the

system as well. This study proves the importance of both the momentum and Diffusive Knudsen numbers in shaping aerosol growth processes.

The case of anomalous increase in thermal conductivity of nanofluids and composites is dealt with in detail here, looking at the effect of particle shape and coalescence between monomers in an aggregate and explains the importance of particle morphology and coalescence in altering the effective conductivity of the system. The increase in conductivity is offset by the increase in the effective viscosity of nanofluids and Brownian Dynamics simulations are employed to study the effective increase in the viscosities as well. The effect of the particle morphology and degree of coalescence between primary particles in altering the heat transfer coefficients is looked into, specifically one case each of forced and natural convection heat transfer.

8.2 Recommendations for Future Work

An exhaustive list of the possible extensions to this study is hard to enlist. However, there are a few suggestions which definitely look promising and can be useful extensions to this study.

Chapter 2: A recent investigation from our group has proved the validity of the expression for calculating the drag on nanotubes as well. Hence, the expression is found to be accurate for the most common type of non-spherical entities found in aerosol science and can be safely extended to all non-spherical entities. There is definitely room for improvement in the optimization and prediction of three dimensional morphological parameters from two dimensional images. The database is close to exhaustive considering most commonly found aerosol particles, but can work better with more data points or interpolated values can be used for the inversion technique utilizing more powerful optimization tools.

Chapter 3: The algorithm for calculating the combined Smoluchowski radius and the combined projected area can be used to get the values for particles other than ensemble of spheres as well. This can be extended for other pairs of non-spherical particles like

nanotubes. It is also assumed in the study that the ratio of the masses and the friction factors of the colliding entities are roughly the same. This could be invalid in the cases of colliding entities with very different mass densities. The effect of the assumption in the calculation of $H(Kn_D)$ could be interesting.

The collision kernel determination technique is an important tool with immense scope to be used in practical applications. The developed non-dimensional collision kernel has been found to be accurate in the calculation of collision rates in many different cases, even in the presence of potential interaction between particles, numerically. Experimental validation of the collision kernel will be a very important advancement in this field and prove to be a very useful tool for aerosol engineering toolboxes.

Chapter 4: This study looks at fibrous filtration as an aerosol collision process with the assumption that all particles get filtered on colliding with the fibers. The underlying assumption of sticking probability of 1 could be revisited, especially with a lot of particle deposits on the fibers. A possible step would be to look at bouncing off the particles from the filter surface and also taking into account the particles that are already attached to the filters.

Polydispersity effects and non-homogeneous fibrous filters need to be taken into account to make direct comparisons with experimental data. This could be studied by slight modifications in the mean first passage simulations by sampling different sizes for the particles as well as the fibers.

Chapter 5: This study is a baseline with scope for a number of modifications to investigate the effect of various parameters. As a first step, the effect of shear on the particles and also the effect of particle rotation could be considered. The growth kinetics can also be studied in the case of a reaction limited system where particles need not bind together on undergoing a collision.

The results also suggest the difference in the evolution pattern of the Knudsen numbers between a completely coalescing system and one with point contact between collided entities. Partially coalescing particles could be a more physically accurate method of modeling medium high temperature synthesis systems and the evolution pattern of the Knudsen numbers could be used as an indicator of the degree of coalescence between the primary particles in the system,

The current study has only looked at the case of monodisperse particles to start with. This can be modified to start with a known size distribution of particles and a direct measurement can be done experimentally with an aggregating system before and after coagulation.

Chapters 6&7: Experimental measurements can throw more insight into the effect of particle morphology in altering the bulk properties of the medium. The intrinsic viscosity of nanofluids could be used as a parameter in predicting the morphological properties of the dispersed particles. The results from the simulations could be used as a guideline in synthesizing particles used to enhance bulk properties of a system.

Bibliography

Alam, M. K. (1987). "The Effect of van der Waals and Viscous Forces on Aerosol Coagulation." Aerosol Science and Technology **6**: 41-52.

Anoop, K. B., T. Sundararajan and S. K. Das (2009). "Effect of particle size on the convective heat transfer in nanofluid in the developing region." International Journal of Heat and Mass Transfer **52**(9-10): 2189-2195.

Arunachalam, V., R. R. Lucchese and W. H. Marlow (1999). "Simulations of aerosol aggregation including long-range interactions." Physical Review E **60**(2): 2051-2064.

Bachok, N., A. Ishak and I. Pop (2011). "Flow and heat transfer over a rotating porous disk in a nanofluid." Physica B-Condensed Matter **406**(9): 1767-1772.

Balazy, A. and A. Podgorski (2007). "Deposition efficiency of fractal-like aggregates in fibrous filters calculated using Brownian dynamics method." Journal of Colloid and Interface Science **311**(2): 323-337.

Ball, R., M. Nauenberg and T. A. Witten (1984). "Diffusion-Controlled Aggregation in the Continuum Approximation." Physical Review A **29**(4): 2017-2020.

Beasley, J. D. and S. Torquato (1986). "Bounds on the Conductivity of a Suspension of Random Impenetrable Spheres." Journal of Applied Physics **60**(10): 3576-3581.

Bhattacharya, P., S. K. Saha, A. Yadav, P. E. Phelan and R. S. Prasher (2004). "Brownian dynamics simulation to determine the effective thermal conductivity of nanofluids." Journal of Applied Physics **95**(11): 6492-6494.

Brasil, A. M., T. L. Farias and M. G. Carvalho (1999). "A recipe for image characterization of fractal-like aggregates." Journal of Aerosol Science **30**(10): 1379-1389.

Buongiorno, J. (2006). "Convective transport in nanofluids." Journal of Heat Transfer-Transactions of the Asme **128**(3): 240-250.

Buongiorno, J., D. C. Venerus, N. Prabhat, T. McKrell, J. Townsend, R. Christianson, Y. V. Tolmachev, P. Keblinski, L. W. Hu, J. L. Alvarado, I. C. Bang, S. W. Bishnoi, M. Bonetti, F. Botz, A. Cecere, Y. Chang, G. Chen, H. S. Chen, S. J. Chung, M. K. Chyu, S. K. Das, R. Di Paola, Y. L. Ding, F. Dubois, G. Dzido, J. Eapen, W. Escher, D. Funfschilling, Q. Galand, J. W. Gao, P. E. Gharagozloo, K. E. Goodson, J. G. Gutierrez, H. P. Hong, M. Horton, K. S. Hwang, C. S. Iorio, S. P. Jang, A. B. Jarzebski, Y. R. Jiang, L. W. Jin, S. Kabelac, A. Kamath, M. A. Kedzierski, L. G. Kieng, C. Kim, J. H. Kim, S. Kim, S. H. Lee, K. C. Leong, I. Manna, B. Michel, R. Ni, H. E. Patel, J. Philip, D. Poulikakos, C. Reynaud, R. Savino, P. K. Singh, P. X. Song, T. Sundararajan, E. Timofeeva, T. Tritcak, A. N. Turanov, S. Van Vaerenbergh, D. S. Wen, S. Witharana, C. Yang, W. H. Yeh, X. Z. Zhao and S. Q. Zhou (2009). "A benchmark study on the thermal conductivity of nanofluids." Journal of Applied Physics **106**(9).

Cai, J., N. L. Lu and C. M. Sorensen (1995). "Analysis of Fractal Cluster Morphology Parameters - Structural Coefficient and Density Autocorrelation Function Cutoff." Journal of Colloid and Interface Science **171**(2): 470-473.

Cai, J. and C. M. Sorensen (1994). "Diffusion of Fractal Aggregates in the Free Molecular Regime." Physical Review E **50**(5): 3397-3400.

Carpineti, M. and M. Giglio (1993). "Aggregation Phenomena." Advances in Colloid and Interface Science **46**: 73-90.

Cerda, J. J., T. Sintes, C. M. Sorensen and A. Chakrabarti (2004). "Structure factor scaling in colloidal phase separation." Physical Review E **70**(5): 051405.

Chakrabarty, R. K., M. A. Garro, B. A. Garro, S. Chancellor, H. Moosmuller and C. M. Herald (2011). "Simulation of Aggregates with Point-Contacting Monomers in the Cluster-Dilute Regime. Part 1: Determining the Most Reliable Technique for Obtaining Three-Dimensional Fractal Dimension from Two-Dimensional Images." Aerosol Science and Technology **45**(1): 75-80.

Chakrabarty, R. K., H. Moosmuller, W. P. Arnott, M. A. Garro, G. X. Tian, J. G. Slowik, E. S. Cross, J. H. Han, P. Davidovits, T. B. Onasch and D. R. Worsnop (2009). "Low Fractal Dimension Cluster-Dilute Soot Aggregates from a Premixed Flame." Physical Review Letters **102**(23).

Chan, P. and B. Dahneke (1981). "Free-molecule drag on straight chains of uniform spheres." Journal of Applied Physics **52**(5): 3106-3110.

Chan, T. W. and M. Mozurkewich (2001). "Measurement of the coagulation rate constant for sulfuric acid particles as a function of particle size using tandem differential mobility analysis." Journal of Aerosol Science **32**: 321-339.

Chen, D. R., D. Y. H. Pui, D. Hummes, H. Fissan, F. R. Quant and G. J. Sem (1998). "Design and evaluation of a nanometer aerosol differential mobility analyzer (Nano-DMA)." Journal of Aerosol Science **29**(5-6): 497-509.

Chen, Z. Y., J. M. Deutch and P. Meakin (1984). "Translational Friction Coefficient of Diffusion Limited Aggregates." Journal of Chemical Physics **80**(6): 2982-2983.

Chen, Z. Y., P. C. Weakliem and P. Meakin (1988). "Hydrodynamic Radii of Diffusion-Limited Aggregates and Bond-Percolation Clusters." Journal of Chemical Physics **89**(9): 5887-5889.

Cheng, Y. S., M. D. Allen, D. P. Gallegos, H. C. Yeh and K. Peterson (1988). "Drag force and slip correction of aggregate aerosols." Aerosol Science and Technology **8**(3): 199-214.

Cho, K., K. S. Chung and P. Biswas (2011). "Coagulation Coefficient of Agglomerates with Different Fractal Dimensions." Aerosol Science and Technology **45**(6): 740-743.

Cho, K., C. J. Hogan and P. Biswas (2007). "Study of the mobility, surface area, and sintering behavior of agglomerates in the transition regime by tandem differential mobility analysis." Journal of Nanoparticle Research **9**: 1003-1012.

Choi, S. U. S. (2009). "Nanofluids: From Vision to Reality Through Research." Journal of Heat Transfer-Transactions of the Asme **131**(3): 033106.

Chun, J. and D. L. Koch (2006). "The effects of non-continuum hydrodynamics on the Brownian coagulation of aerosol particles." Journal of Aerosol Science **37**(4): 471-482.

Corcione, M. (2011). "Rayleigh-Benard convection heat transfer in nanoparticle suspensions." International Journal of Heat and Fluid Flow **32**: 65-77.

Cunningham, E. (1910). "On the Velocity of Steady Fall of Spherical Particles through Fluid Medium." Proceedings of the Royal Society of London. Series A. **83**(563): 357-365.

D'yachkov, L. G., A. G. Khrapak, S. A. Khrapak and G. E. Morfill (2007). "Model of grain charging in collisional plasmas accounting for collisionless layer." Physics of Plasmas **14**(4): 042102.

Dahneke, B. E. (1973). "Slip Correction Factors for Nonspherical Bodies- III The Form of the General Law." Journal of Aerosol Science **4**: 163-170.

Dahneke, B. E. (1983). Simple Kinetic Theory of Brownian Diffusion in Vapors and Aerosols. Theory of Dispersed Multiphase Flow. R. E. Meyer. New York, Academic Press.

Das, S. K., S. U. S. Choi and H. E. Patel (2006). "Heat transfer in Nanofluids - A review." Heat Transfer Engineering **27**(10): 3-19.

Das, S. K., N. Putra, P. Thiesen and W. Roetzel (2003). "Temperature dependence of thermal conductivity enhancement for nanofluids." Journal of Heat Transfer-Transactions of the Asme **125**(4): 567-574.

Davies, C. N. (1945). "Definitive Equations for the Fluid Resistance of Spheres." Proc. Phys. Soc. **57**: 259-270.

Douglas, J. F., H. X. Zhou and J. B. Hubbard (1994). "Hydrodynamic Friction and the Capacitance of Arbitrarily-Shaped Objects." Physical Review E **49**(6): 5319-5337.

Eapen, J., J. Li and S. Yip (2007). "Beyond the Maxwell limit: Thermal conduction in nanofluids with percolating fluid structures." Physical Review E **76**(6).

Eastman, J. A., S. U. S. Choi, S. Li, W. Yu and L. J. Thompson (2001). "Anomalously increased effective thermal conductivities of ethylene glycol-based nanofluids containing copper nanoparticles." Applied Physics Letters **78**(6): 718-720.

Eastman, J. A., S. R. Phillpot, S. U. S. Choi and P. Keblinski (2004). "Thermal transport in nanofluids." Annual Review of Materials Research **34**: 219-246.

Eggersdorfer, M. L., A. J. Grohn, C. M. Sorensen, P. H. McMurry and S. E. Pratsinis (2012). "Mass-mobility characterization of flame-made ZrO2 aerosols: Primary particle diameter and extent of aggregation." Journal of Colloid and Interface Science **387**: 12-23.

Eggersdorfer, M. L., D. Kadau, H. J. Herrmann and S. E. Pratsinis (2011). "Multiparticle Sintering Dynamics: From Fractal-Like Aggregates to Compact Structures." Langmuir **27**(10): 6358-6367.

Eglin, J. M. (1923). "The Coefficients of Viscosity and Slip of Carbon Dioxide by the Oil Drop Method and the Law of Motion of an Oil Drop in Carbon Dioxide,Oxygen and Helium,at Low Pressures." Physical Review(22): 161-170.

Epstein, P. S. (1924). "On the Resistance Experienced by Spheres in their Motion through Gases." Physical review **23**: 710-733.

Ermak, D. L. and H. Buckholz (1980). "Numerical-Integration of the Langevin Equation - Monte-Carlo Simulation." Journal of Computational Physics **35**(2): 169-182.

Evans, W., J. Fish and P. Keblinski (2006). "Role of Brownian motion hydrodynamics on nanofluid thermal conductivity." Applied Physics Letters **88**(9): -.

Evans, W., R. Prasher, J. Fish, P. Meakin, P. Phelan and P. Keblinski (2008). "Effect of aggregation and interfacial thermal resistance on thermal conductivity of nanocomposites and colloidal nanofluids." International Journal of Heat and Mass Transfer **51**(5-6): 1431-1438.

Fan, J. and L. Q. Wang (2011). "Review of Heat Conduction in Nanofluids." Journal of Heat Transfer-Transactions of the Asme **133**(4).

Feldermann, C., H. Jander and H. G. Wagner (1994). "Soot Particle Coagulation in Premixed Ethylene Air Flames at 10-Bar." Zeitschrift Fur Physikalische Chemie-International Journal of Research in Physical Chemistry & Chemical Physics **186**: 127-140.

Filippov, A. V., M. Zurita and D. E. Rosner (2000). "Fractal-like aggregates: Relation between morphology and physical properties." Journal of Colloid and Interface Science **229**(1): 261-273.

Friedlander, S. K. (2000). Smoke, Dust, and Haze. New York, Oxford University Press.

Fuchs, N. A. (1963). "On the Stationary Charge Distribution on Aerosol Particles in a Bipolar Ionic Atmosphere." Geofis. Pura Appl. **51**: 185-193.

Fuchs, N. A. (1964). The mechanics of aerosols. New York,, Macmillan.

Fuchs, N. A. and A. G. Sutugin (1970). Highly dispersed aerosols. Ann Arbor,, Ann Arbor Science Publishers.

Ganguly, S., S. Sikdar and S. Basu (2009). "Experimental investigation of the effective electrical conductivity of aluminum oxide nanofluids." Powder Technology **196**(3): 326-330.

Gao, J. W., R. T. Zheng, H. Ohtani, D. S. Zhu and G. Chen (2009). "Experimental Investigation of Heat Conduction Mechanisms in Nanofluids. Clue on Clustering." Nano Letters **9**: 4128-4132.

Gharagozloo, P. E., J. K. Eaton and K. E. Goodson (2008). "Diffusion, aggregation, and the thermal conductivity of nanofluids." Applied Physics Letters **93**(10).

Given, J. A., J. B. Hubbard and J. F. Douglas (1997). "A first-passage algorithm for the hydrodynamic friction and diffusion-limited reaction rate of macromolecules." Journal of Chemical Physics **106**(9): 3761-3771.

Given, J. A. and B. B. Mandelbrot (1984). "Comment on Transport Processes on Fractal Structures." Journal of Physics a-Mathematical and General **17**(9): 1937-1939.

Globe, S. and D. Dropkin (1959). "Natural convection heat transfer in liquids confined by two horizontal plates and heated from below." Journal of Heat Transfer **81**: 24-28.

Gopalakrishnan, R. and C. J. Hogan (2011). "Determination of the Transition Regime Collision Kernel from Mean First Passage Times." Aerosol Science and Technology **45**(12): 1499-1509.

Gopalakrishnan, R. and C. J. Hogan (2012). "Coulomb-Influenced Collisions in Aerosols and Dusty Plasmas." Physical Review E **85**: 026410.

Gopalakrishnan, R., P. H. McMurry and C. J. Hogan (2013). "The Electrical Mobility of Modest to High Aspect Ratio Particles in the Transition Regime." Journal of Aerosol Science **In Review**.

Gopalakrishnan, R., M. J. Meredith, C. Larriba-Andaluz and C. J. Hogan (2013). "Brownian dynamics determination of the bipolar steady state charge distribution on spheres and non-spheres in the transition regime." Journal of Aerosol Science **63**(0): 126-145.

Gopalakrishnan, R., M. R. Meredith, C. Larriba-Andaluz and C. J. Hogan (2013). "Brownian Dynamics Determination of the Bipolar Steady State Charge Distribution on Spheres and Non-spheres in the Transition Regime." Journal of Aerosol Science **63**: 126-145.

Gopalakrishnan, R., T. Thajudeen and C. J. Hogan (2011). "Collision limited reaction rates for arbitrarily shaped particles across the entire diffusive Knudsen number range." Journal of Chemical Physics **135**(5).

Gopinath, A. and D. L. Koch (1999). "Hydrodynamic interactions between two equal spheres in a highly rarefied gas." Physics of Fluids **11**(9): 2772-2787.

Grass, R. N., S. Tsantilis and S. E. Pratsinis (2006). "Design of high-temperature, gas-phase synthesis of hard or soft TiO2 agglomerates." Aiche Journal **52**(4): 1318-1325.

Gutsch, A., S. E. Pratsinis and F. Loffler (1995). "Agglomerate Structure and Growth-Rate by Trajectory Calculations of Monomer-Cluster Collisions." Journal of Aerosol Science **26**(2): 187-199.

Hamming, L. M., R. Qiao, P. B. Messersmith and L. C. Brinson (2009). "Effects of dispersion and interfacial modification on the macroscale properties of TiO2 polymer-matrix nanocomposites." Composites Science and Technology **69**(11-12): 1880-1886.

Hansen, S. (2004). "Translational friction coefficients for cylinders of arbitrary axial ratios estimated by Monte Carlo simulation." Journal of Chemical Physics **121**(18): 9111-9115.

Havlin, S. and D. Benavraham (1987). "Diffusion in disordered media." Advances in Physics **36**(6): 695-798.

Hawa, T. and M. R. Zachariah (2006). "Coalescence kinetics of unequal sized nanoparticles." Journal of Aerosol Science **37**(1): 1-15.

Hawa, T. and M. R. Zachariah (2007). "Development of a phenomenological scaling law for fractal aggregate sintering from molecular dynamics simulation." Journal of Aerosol Science **38**(8): 793-806.

He, P. and R. Qiao (2008). "Self-consistent fluctuating hydrodynamics simulations of thermal transport in nanoparticle suspensions." Journal of Applied Physics **103**: 094305.

Heine, M. C. and S. E. Pratsinis (2007). "Polydispersity of primary particles in agglomerates made by coagulation and sintering." Journal of Aerosol Science **38**(1): 17-38.

Heinson, W. R., C. M. Sorensen and A. Chakrabarti (2010). "Does Shape Anisotropy Control the Fractal Dimension in Diffusion-Limited Cluster-Cluster Aggregation?" Aerosol Science and Technology **44**(12): I-IV.

Heinson, W. R., C. M. Sorensen and A. Chakrabarti (2012). "A three parameter description of the structure of diffusion limited cluster fractal aggregates." Journal of Colloid and Interface Science **375**: 65-69.

Heris, S. Z., G. Etemad and M. N. Esfahany (2006). "Experimental investigation of oxide nanofluids laminar flow convection heat transfer." International Communications in Heat and Mass Transfer **33**: 529-535.

Hinds, W. C. (1999). Aerosol Technology, John Wiley & Sons.

Ho, C. J., M. W. Chen and Z. W. Li (2008). "Numerical simulation of natural convection of nanofluid in a square enclosure: Effects due to uncertainties of viscosity and thermal conductivity." International Journal of Heat and Mass Transfer **51**(17-18): 4506-4516.

Hogan, C. J. and J. F. de la Mora (2011). "Ion Mobility Measurements of Nondenatured 12-150 kDa Proteins and Protein Multimers by Tandem Differential Mobility Analysis-Mass Spectrometry (DMA-MS)." Journal of the American Society for Mass Spectrometry **22**(1): 158-172.

Huang, H., C. Oh and C. M. Sorensen (1998). "Structure factor scaling in aggregating systems." Physical Review E **57**(1): 875-880.

Hubbard, J. B. and J. F. Douglas (1993). "Hydrodynamic Friction of Arbitrarily Shaped Brownian Particles." Physical Review E **47**(5): R2983-R2986.

Hunt, B., T. Thajudeen and C. J. Hogan (2013). "The Single Fiber Collision Rate & Filtration Efficiency for Nanoparticles I. The First Passage Time Calculation Approach." Aerosol Science and Technology **Submitted**.

Hwang, Y., J. K. Lee, Y. M. Jeong, S. I. Cheong, Y. C. Ahn and S. H. Kim (2008). "Production and dispersion stability of nanoparticles in nanofluids." Powder Technology **186**(2): 145-153.

Ibaseta, N. and B. Biscans (2010). "Fractal dimension of fumed silica: Comparison of light scattering and electron microscope methods." Powder Technology **203**(2): 206-210.

Incropera, F. P., D. P. Dewitt, T. L. Bergman and A. S. Lavine (2007). Fundamentals of Heat and Mass Transfer. Hoboken, New Jersey.

Inkyo, M., T. Tahara, T. Iwaki, F. Iskandar, C. J. Hogan and K. Okuyama (2006). "Experimental Investigation of Nanoparticle Dispersion by Beads Milling with Centrifugal Bead Separation." Journal of Colloid and Interface Science **304**: 535-540.

Inkyo, M., Y. Tokunaga, T. Tahara, T. Iwaki, F. Iskandar, C. J. Hogan and K. Okuyama (2008). "Beads mill-assisted synthesis of poly methyl methacrylate (PMMA)-TiO2 nanoparticle composites." Industrial & Engineering Chemistry Research **47**(8): 2597-2604.

Isella, L. and Y. Drossinos (2010). "Langevin agglomeration of nanoparticles interacting via a central potential." Physical Review E **82**: 011404.

Isella, L. and Y. Drossinos (2011). "On the friction coefficient of straight-chain aggregates." Journal of Colloid and Interface Science **356**(2): 505-512.

Jäger, K.-M. and D. H. McQueen (2001). "Fractal agglomerates and electrical conductivity in carbon black polymer composites." Polymer **42**(23): 9575-9581.

Jiang, J., D. R. Chen and P. Biswas (2007). "Synthesis of nanoparticles in a flame aerosol reactor with independent and strict control of their size, crystal phase and morphology." Nanotechnology **18**: 285603.

Jiang, J. K., G. Oberdorster and P. Biswas (2009). "Characterization of size, surface charge, and agglomeration state of nanoparticle dispersions for toxicological studies." Journal of Nanoparticle Research **11**(1): 77-89.

Jullien, R. (1986). "A new model of cluster aggregation." Journal of Physics a-Mathematical and General **19**(11): 2129-2136.

Jullien, R., R. Botet and P. M. Mors (1987). "Computer-Simulations of cluster cluster aggregation." Faraday Discussions **83**: 125-+.

Kakac, S. and A. Pramuanjaroenkij (2009). "Review of convective heat transfer enhancement with nanofluids." International Journal of Heat and Mass Transfer **52**: 3187-3196.

Kang, E. H., M. L. Mansfield and J. F. Douglas (2004). "Numerical path integration technique for the calculation of transport properties of proteins." Physical Review E **69**(3): 031918.

Karthikeyan, N. R., J. Philip and B. Raj (2008). "Effect of clustering on the thermal conductivity of nanofluids." Materials Chemistry and Physics **109**(1): 50-55.

Kasper, G. (1982). "Dynamics and Measurement of Smokes. II The Aerodynamic Diameter of Chain Aggregates in the Transition Regime." Aerosol Science and Technology **1**(2): 201-215.

Kasper, G. and D. T. Shaw (1982). "Comparative Size Distribution Measurements on Chain Aggregates." Aerosol Science and Technology **2**(3): 369-381.

Keblinski, P., A. Maritan, F. Toigo and J. R. Banavar (1994). "Continuum approach to diffusion-limited-aggregation type of growth." Physical Review E **49**(6): R4795-R4798.

Keblinski, P., S. R. Phillpot, S. U. S. Choi and J. A. Eastman (2002). "Mechanisms of heat flow in suspensions of nano-sized particles (nanofluids)." International Journal of Heat and Mass Transfer **45**(4): 855-863.

Keblinski, P., R. Prasher and J. Eapen (2008). "Thermal conductance of nanofluids: is the controversy over?" Journal of Nanoparticle Research **10**(7): 1089-1097.

Khanafer, K., K. Vafai and M. Lightstone (2003). "Buoyancy-driven heat transfer enhancement in a two-dimensional enclosure utilizing nanofluids." International Journal of Heat and Mass Transfer **46**(19): 3639-3653.

Kim, I. C. and S. Torquato (1990). "Determination of the Effective Conductivity of Heterogeneous Media by Brownian-Motion Simulation." Journal of Applied Physics **68**(8): 3892-3903.

Kim, I. C. and S. Torquato (1990). "Monte-Carlo Calculations of Connectedness and Mean Cluster Size for Bidispersions of Overlapping Spheres." Journal of Chemical Physics **93**(8): 5998-6002.

Kim, I. C. and S. Torquato (1991). "1st-Passage-Time Calculation of the Conductivity of Continuum Models of Multiphase Composites." Physical Review A **43**(6): 3198-3201.

Kim, I. C. and S. Torquato (1991). "Effective Conductivity of Suspensions of Hard-Spheres by Brownian-Motion Simulation." Journal of Applied Physics **69**(4): 2280-2289.

Kim, I. C. and S. Torquato (1992). "Diffusion of Finite-Sized Brownian Particles in Porous-Media." Journal of Chemical Physics **96**(2): 1498-1503.

Kim, I. C. and S. Torquato (1992). "Effective conductivity of suspensions of overlapping spheres." Journal of Applied Physics **71**(6): 2727-2735.

Kim, I. C. and S. Torquato (1992). "Effective Conductivity of Suspensions of Overlapping Spheres." Journal of Applied Physics **71**(6): 2727-2735.

Kim, I. C. and S. Torquato (1993). "Effective conductivity of composites containing spheroidal inclusions - comparison of simulation with theory." Journal of Applied Physics **74**(3): 1844-1854.

Kim, I. C. and S. Torquato (1993). "Effective Conductivity of Composites Containing Spheroidal Inclusions - Comparison of Simulations with Theory." Journal of Applied Physics **74**(3): 1844-1854.

Kim, S., K.-S. Lee, M. R. Zachariah and D. Lee (2010). "Three-dimensional off-lattice Monte Carlo simulations on a direct relation between experimental process parameters and fractal dimension of colloidal aggregates." Journal of Colloid and Interface Science **344**(2): 353-361.

Kim, S. C., J. Wang, M. S. Emery, W. G. Shin, G. W. Mulholland and D. Y. H. Pui (2009). "Structural Property Effect of Nanoparticle Agglomerates on Particle Penetration through Fibrous Filter." Aerosol Science and Technology **43**(4): 344-355.

Kirkwood, J. G. and J. Riseman (1948). "The Intrinsic Viscosities and Diffusion Constants of Flexible Macromolecules in Solution." Journal of Chemical Physics **16**: 565-573.

Kirsch, A. A., I. B. Stechkina and N. A. Fuchs (1974). "Gas flow in aerosol filters made of polydisperse ultrafine fibres." Journal of Aerosol Science **5**(1): 39-45.

Knutson, E. O. and K. T. Whitby (1975). "Aerosol classification by electric mobility: apparatus, theory, and applications." Journal of Aerosol Science **6**(6): 443-451.

Kofod, G., S. Risse, H. Stoyanov, D. N. McCarthy, S. Sokolov and R. Kraehnert (2011). "Broad-Spectrum Enhancement of Polymer Composite Dielectric Constant at Ultralow Volume Fractions of Silica-Supported Copper Nanoparticles." ACS Nano **5**(3): 1623-1629.

Koylu, U. O., Y. C. Xing and D. E. Rosner (1995). "Fractal morphology analysis of combustion-generated aggregates using angular light scattering and electron microscope images." Langmuir **11**(12): 4848-4854.

Krishnamurthy, S., P. Lhattacharya, P. E. Phelan and R. S. Prasher (2006). "Enhanced mass transport in nanofluids." Nano Letters **6**(3): 419-423.

Kuwabara, S. (1959). "The Forces Experienced by Randomly Distributed Parallel Circular Cylinders or Spheres in a Viscous Flow at Small Reynolds Numbers." Journal of the Physical Society of Japan **14**: 527-532.

Lall, A. A. and S. K. Friedlander (2006). "On-line measurement of ultrafine aggregate surface area and volume distributions by electrical mobility analysis: I. Theoretical analysis." Journal of Aerosol Science **37**(3): 260-271.

Larriba, C. and C. J. Hogan (2013). "Free Molecular Collision Cross Section Calculation Methods for Nanoparticles and Complex Ions with Energy Accommodation." Journal of Computational Physics **251**: 344–363.

Latin, D., D. Ferry, J. M. Gay, D. Delhaye and F. X. Ouf (2013). "On methods determining the fractal dimension of combustion aerosols and particle clusters." Journal of Aerosol Science **58**: 41-49.

Lattuada, M., H. Wu and M. Morbidelli (2003). "Hydrodynamic radius of fractal clusters." Journal of Colloid and Interface Science **268**(1): 96-105.

Lattuada, M., H. Wu and M. Morbidelli (2004). "Experimental investigation of colloidal gel structures." Langmuir **20**(11): 4355-4362.

Lee, K. W. and B. Y. H. Liu (1982). "Theoretical-Study of Aerosol Filtration by Fibrous Filters." Aerosol Science and Technology **1**(2): 147-161.

Li, Z. and H. Wang (2003). "Drag force, diffusion coefficient, and electric mobility of small particles. I. Theory applicable to the free-molecule regime." Physical Review E **68**: 061206.

Lin, Y. L., K. Lee and T. Matsoukas (2002). "Solution of the population balance equation using constant-number Monte Carlo." Chemical Engineering Science **57**(12): 2241-2252.

Liu, Z., S. C. Kim, J. Wang, W. G. Shin, H. Fissan and D. Y. H. Pui (2012). "Measurement of Metal Nanoparticle Agglomerates Generated by Spark Discharge Using the Universal Nanoparticle Analyzer (UNPA)." Aerosol Science and Technology **46**(3): 333-346.

López-Yglesias, X. and R. C. Flagan (2013). "Ion–Aerosol Flux Coefficients and the Steady-State Charge Distribution of Aerosols in a Bipolar Ion Environment." Aerosol Science and Technology **47**(6): 688-704.

Loyalka, S. K. (1973). "Condensation on a spherical droplet." J Chem. Physics **58**(1).

Luty, B. A., J. A. McCammon and H. X. Zhou (1992). "Diffusive Reaction Rates from Brownian Dynamics Simulations - Replacing the Outer Cutoff Surface by an Analytical Treatment." Journal of Chemical Physics **97**(8): 5682-5686.

Mansfield, M. L. and J. F. Douglas (2008). "Improved path integration method for estimating the intrinsic viscosity of arbitrarily shaped particles." Physical Review E **78**(4).

Mansfield, M. L. and J. F. Douglas (2008). "Improved path integration method for estimating the intrinsic viscosity of arbitrarily shaped particles." Physical Review E **78**(4): 046712.

Mansfield, M. L. and J. F. Douglas (2008). "Transport properties of rodlike particles." Macromolecules **41**(14): 5422-5432.

Mansfield, M. L. and J. F. Douglas (2008). "Transport properties of wormlike chains with applications to double helical DNA and carbon nanotubes." Macromolecules **41**(14): 5412-5421.

Mansfield, M. L. and J. F. Douglas (2010). "Influence of variable hydrodynamic interaction strength on the transport properties of coiled polymers." Physical Review E **81**(2): 021803.

Mansfield, M. L. and J. F. Douglas (2010). "Properties of Knotted ring polymers. II. Transport properties." Journal of Chemical Physics **133**(4): 044904.

Mansfield, M. L., J. F. Douglas and E. J. Garboczi (2001). "Intrinsic viscosity and the electrical polarizability of arbitrarily shaped objects." Physical Review E **64**(6).

Mansfield, M. L., J. F. Douglas, S. Irfan and E. H. Kang (2007). "Comparison of approximate methods for calculating the friction coefficient and intrinsic viscosity of nanoparticles and macromolecules." Macromolecules **40**(7): 2575-2589.

Maricq, M. M. (2007). "Coagulation dynamics of fractal-like soot aggregates." Journal of Aerosol Science **38**(2): 141-156.

Mason, E. A. and E. W. McDaniel (1988). Transport Properties of Ions in Gases. New York, Wiley.

Meakin, P. (1983). "Formation of Fractal Clusters and Network by Irreversible Diffusion-Limited Aggregation." Physical Review Letters **51**(13): 1119-1122.

Meakin, P. (1984). "Diffusion-Controlled Aggregation onTwo-Dimensional Square Lattices - Results from a New Cluster-Cluster Aggregation Model." Physical Review B **29**(6): 2930-2942.

Meakin, P. (1984). "Diffusion-Limited Aggregation in 3 Dimensions - Results From a New Cluster Aggregation Model." Journal of Colloid and Interface Science **102**(2): 491-504.

Meakin, P. and R. Jullien (1988). "The Effects of Restructuring on the Geometry of Clusters Formed by Diffusion-Limited, Ballistic, and Reaction-Limited Cluster Cluster Aggregation." Journal of Chemical Physics **89**(1): 246-250.

Meakin, P., I. Majid, S. Havlin and H. E. Stanley (1984). "Topological Properties of Diffusion Limited Aggregation and Cluster Cluster Aggregation." Journal of Physics a-Mathematical and General **17**(18): L975-L981.

Meakin, P., T. Vicsek and F. Family (1985). "Dynamic Cluster-Size Distribution in Cluster-Cluster Aggregation - Effects of Cluster Diffusivity." Physical Review B **31**(1): 564-569.

Melas, A. D., L. Isella, A. G. Konstandopoulos and Y. Drossinos "Morphology and mobility of synthetic colloidal aggregates." Journal of Colloid and Interface Science(0).

Millikan, R. A. (1923). "The General Law of Fall of a Small Spherical Body through a Gas, and its Bearing upon the Nature of Molecular Reflection from Surfaces." Physical Review **22**: 1-23.

Mountain, R. D., G. W. Mulholland and H. Baum (1986). "Simulation of aerosol agglomeration in the free molecular and continuum flow regimes " Journal of Colloid and Interface Science **114**(1): 67-81.

Mukherjee, S., C. H. Chen, C. C. Chou, K. F. Tseng, B. K. Chaudhuri and H. D. Yang (2010). "Colossal dielectric and magnetodielectric effect in Er2O3 nanoparticles embedded in a SiO2 glass matrix." Physical Review B **82**(10).

Mulholland, G. W., R. J. Samson, R. D. Mountain and M. H. Ernst (1988). "Cluster Size Distribution for Free Molecular Agglomeration." Energy & Fuels **2**(4): 481-486.

Nan, C. W., R. Birringer, D. R. Clarke and H. Gleiter (1997). "Effective thermal conductivity of particulate composites with interfacial thermal resistance." Journal of Applied Physics **81**(10): 6692-6699.

Narsimhan, G. and E. Ruckenstein (1985). "Monte-Carlo Simulation of Brownian Coagulation over the Entire Range of Particle Sizes from near Molecular to Colloidal - Connection between Collision Efficiency and Interparticle Forces." Journal of Colloid and Interface Science **107**(1): 174-193.

Naumann, K.-H. (2003). "COSIMA- a computer program simulating the dynamics of fractal aerosols." Journal of Aerosol Science **34**: 1371-1397.

Nie, C., W. H. Marlow and Y. A. Hassan (2008). "Discussion of proposed mechanisms of thermal conductivity enhancement in nanofluids." International Journal of Heat and Mass Transfer **51**(5-6): 1342-1348.

Northrup, S. H., S. A. Allison and J. A. McCammon (1984). "Brownian Dynamics Simulation of Diffusion-Influenced Bimolecular Reactions." Journal of Chemical Physics **80**(4): 1517-1526.

Nowakowski, B. and M. Sitarski (1981). "Brownian coagulation of aerosol particles by Monte Carlo simulation." Journal of Colloid and Interface Science **83**: 614-622.

Oh, C. and C. M. Sorensen (1997). "The effect of overlap between monomers on the determination of fractal cluster morphology." Journal of Colloid and Interface Science **193**(1): 17-25.

Oh, C. and C. M. Sorensen (1997). "Light scattering study of fractal cluster aggregation near the free molecular regime." Journal of Aerosol Science **28**(6): 937-957.

Oh, C. and C. M. Sorensen (1998). "Structure factor of diffusion-limited aggregation clusters: Local structure and non-self-similarity." Physical Review E **57**(1): 784-790.

Oueslati, F. S. and R. Bennacer (2011). "Heterogeneous nanofluids: natural convection heat transfer enhancement." Nanoscale Research Letters **6**: 222.

Ouyang, H., R. Gopalakrishnan and C. J. Hogan (2012). "Nanoparticle collisions in the gas phase in the presence of singular contact potentials." The Journal of Chemical Physics **137**(6): 064316.

Ouyang, H., T. Thajudeen and C. J. Hogan (2013). "Experimental and Theoretical Examination of Coagulation in the Mass and Momentum Transfer Transition Regimes." Journal of Colloid and Interface Science **Submitted**.

Pak, B. C. and Y. Cho (1998). "Hydrodynamic and Heat Transfer Study of Dispersed Fluids with Submicron Metallic Oxide Particles." Experimental Heat Transfer **11**: 151-170.

Peukert, W., H. C. Schwarzer and F. Stenger (2005). "Control of aggregation in production and handling of nanoparticles." Chemical Engineering and Processing **44**(2): 245-252.

Pierce, F., C. M. Sorensen and A. Chakrabarti (2006). "Computer simulation of diffusion-limited cluster-cluster aggregation with an Epstein drag force." Physical Review E **74**(2): 021411.

Prasher, R., P. Bhattacharya and P. E. Phelan (2005). "Thermal conductivity of nanoscale colloidal solutions (nanofluids)." Physical Review Letters **94**(2).

Prasher, R., P. Bhattacharya and P. E. Phelan (2006). "Brownian-motion-based convective-conductive model for the effective thermal conductivity of nanofluids." Journal of Heat Transfer-Transactions of the Asme **128**(6): 588-595.

Prasher, R., W. Evans, P. Meakin, J. Fish, P. Phelan and P. Keblinski (2006). "Effect of aggregation on thermal conduction in colloidal nanofluids." Applied Physics Letters **89**(14): 143119.

Prasher, R., P. E. Phelan and P. Bhattacharya (2006). "Effect of aggregation kinetics on the thermal conductivity of nanoscale colloidal solutions (nanofluid)." Nano Letters **6**(7): 1529-1534.

Puri, R., T. F. Richardson, R. J. Santoro and R. A. Dobbins (1993). "Aerosol Dynamic Processes of Soot Aggregates in a Laminar Ethene Diffusion Flame." Combustion and Flame **92**(3): 320-333.

Putnam, S. A., D. G. Cahill, P. V. Braun, Z. B. Ge and R. G. Shimmin (2006). "Thermal conductivity of nanoparticle suspensions." Journal of Applied Physics **99**(8).

Putra, N., W. Roetzel and S. K. Das (2003). "Natural convection of nano-fluids." Heat and Mass Transfer **39**(8-9): 775-784.

Qi, L., B. I. Lee, S. Chen, W. D. Samuels and G. J. Exarhos (2005). "High-Dielectric-Constant Silver–Epoxy Composites as Embedded Dielectrics." Advanced Materials **17**(14): 1777-1781.

Qiao, R., H. Deng, K. W. Putz and L. C. Brinson (2011). "Effect of Particle Agglomeration and Interphase on the Glass Transition Temperature of Polymer Nanocomposites." Journal of Polymer Science Part B-Polymer Physics **49**(10): 740-748.

Rader, D. J. (1985). "Application of the Tandem Differential Mobility Analyzer to Studies of Droplet Evaporation and Growth ".
Rader, D. J. (1990). "Momentum Slip Correction Factor for Small Particles in Nine Common Gases." Journal of Aerosol Science **21**: 161-168.
Rogak, S. N. and R. C. Flagan (1992). "Coagulation of Aerosol Agglomerates in the Transition Regime." Journal of Colloid and Interface Science **151**(1): 203-224.
Rogak, S. N., R. C. Flagan and H. V. Nguyen (1993). "The mobility and structure of aerosol agglomerates." Aerosol Science and Technology **18**(1): 25-47.
Sceats, M. G. (1989). "Brownian Coagulation in Aerosols- The Role of Long Range Forces." Journal of Colloid and Interface Science **129**: 105-112.
Scheckman, J. H., P. H. McMurry and S. E. Pratsinis (2009). "Rapid Characterization of Agglomerate Aerosols by In Situ Mass-Mobility Measurements." Langmuir **25**(14): 8248-8254.
Schmid, H. J., B. Al-Zaitone, C. Artelt and W. Peukert (2006). "Evolution of the fractal dimension for simultaneous coagulation and sintering." Chemical Engineering Science **61**(1): 293-305.
Schmid, H. J., S. Tejwani, C. Artelt and W. Peukert (2004). "Monte Carlo simulation of aggregate morphology for simultaneous coagulation and sintering." Journal of Nanoparticle Research **6**(6): 613-626.
Schmidt-Ott, A. (1988). "In situ measurement of the fractal dimensionality of ultrafine aerosol particles." Applied Physics Letters **52**: 954-956.
Schmidt-Ott, A., U. Baltensperger, H. W. Gaggeler and D. T. Jost (1990). "Scaling behaviour of physical parameters describing agglomerates." Journal of Aerosol Science **21**: 711-717.
Schürmann, U., H. Takele, V. Zaporojtchenko and F. Faupel (2006). "Optical and electrical properties of polymer metal nanocomposites prepared by magnetron co-sputtering." Thin Solid Films **515**(2): 801-804.
Schwarzer, H. C. and W. Peukert (2002). "Experimental investigation into the influence of mixing on nanoparticle precipitation." Chemical Engineering & Technology **25**(6): 657-661.
Schwarzer, H. C. and W. Peukert (2005). "Prediction of aggregation kinetics based on surface properties of nanoparticles." Chemical Engineering Science **60**(1): 11-25.
Seto, T., T. Furukawa, Y. Otani, K. Uchida and S. Endo (2010). "Filtration of Multi-Walled Carbon Nanotube Aerosol by Fibrous Filters." Aerosol Science and Technology **44**(9): 734-740.
Shapiro, M., P. Vainshtein, D. Dutcher, M. Emery, M. Stolzenburg, D. B. Kittelson and P. H. McMurry (2012). "Characterization of agglomerates by simultaneous measurement of mobility, vacuum aerodynamic diameter and mass." Journal of Aerosol Science **44**: 24-45.
Sharma, P., I. H. Baek, T. Cho, S. Park and K. B. Lee (2011). "Enhancement of thermal conductivity of ethylene glycol based silver nanofluids." Powder Technology **208**(1): 7-19.

Smith, M. and T. Matsoukas (1998). "Constant-number Monte Carlo simulation of population balances." Chemical Engineering Science **53**(9): 1777-1786.
Sommer, M., F. Stenger, W. Peukert and N. J. Wagner (2006). "Agglomeration and breakage of nanoparticles in stirred media mills - a comparison of different methods and models." Chemical Engineering Science **61**(1): 135-148.
Soos, M., L. Ehrl and M. Lattuada (2009). "Generation and Geometrical Analysis of Dense Clusters with Variable Fractal Dimension." Journal of Physical Chemistry B **113**(31): 10587-10599.
Soos, M., Y. M. Harshe and M. Lattuada (2011). "Experimental and Modeling Study of Breakage and Restructuring of Open and Dense Colloidal Aggregates." Langmuir **27**(10): 5739-5752.
Sorensen, C. M. (2001). "Light scattering by fractal aggregates: A review." Aerosol Science and Technology **35**(2): 648-687.
Sorensen, C. M. (2011). "The Mobility of Fractal Aggregates: A Review." Aerosol Science and Technology **45**(7): 765-779.
Sorensen, C. M. and A. Chakrabarti (2011). "The sol to gel transition in irreversible particulate systems." Soft Matter **7**(6): 2284-2296.
Sorensen, C. M. and G. D. Feke (1996). "The morphology of macroscopic soot." Aerosol Science and Technology **25**(3): 328-337.
Sorensen, C. M. and G. C. Roberts (1997). "The prefactor of fractal aggregates." Journal of Colloid and Interface Science **186**(2): 447-452.
Stechkina, I. B. and N. A. Fuchs (1966). "Studies on Fibrous Aerosol Filters—I. Calculation of Diffusional Deposition of Aerosols in Fibrous Filters." Annals of Occupational Hygiene **9**(2): 59-64.
Stenger, F., S. Mende, J. Schwedes and W. Peukert (2005). "Nanomilling in stirred media mills." Chemical Engineering Science **60**(16): 4557-4565.
Stolzenburg, M. R. and P. H. Mcmurry (1991). "An Ultrafine Aerosol Condensation Nucleus Counter." Aerosol Science and Technology **14**(1): 48-65.
Swihart, M. T. (2003). "Vapor-phase synthesis of nanoparticles." Current Opinion in Colloid & Interface Science **8**(1): 127-133.
Tammet, H. (1995). "Size and Mobility of Nanometer Particles, Clusters and Ions." Journal of Aerosol Science **26**(3): 459-475.
Thajudeen, T., R. Gopalakrishnan and C. J. Hogan (2012). "The Collision Rate of Non-spherical Particles and Aggregates for all Diffusive Knudsen Numbers." Aerosol Science and Technology **46**(11): 1174-1186.
Thajudeen, T. and C. J. Hogan (2012). "First Passage Calculation of the Conductivity of Particle Aggregate-Laden Suspensions and Composites " Powder Technology **218**: 31-39.
Thajudeen, T., S. Jeon and C. J. Hogan (2013). "The Mobility of Flame Synthesized Aggregates/Agglomerates in the Transition Regime." Langmuir **Submitted**.
Timofeeva, E. V., A. N. Gavrilov, J. M. McCloskey, Y. V. Tolmachev, S. Sprunt, L. M. Lopatina and J. V. Selinger (2007). "Thermal conductivity and particle

agglomeration in alumina nanofluids: Experiment and theory." Physical Review E **76**(6).
Timofeeva, E. V., J. L. Routbort and D. Singh (2009). "Particle shape effects on thermophysical properties of alumina nanofluids." Journal of Applied Physics **106**(1).
Torquato, S. (1985). "Effective Electrical-Conductivity of 2-Phase Disordered Composite Media." Journal of Applied Physics **58**(10): 3790-3797.
Torquato, S., I. C. Kim and D. Cule (1999). "Effective conductivity, dielectric constant, and diffusion coefficient of digitized composite media via first-passage-time equations." Journal of Applied Physics **85**(3): 1560-1571.
Torquato, S. and F. Lado (1991). "Trapping Constant, Thermal-Conductivity, and the Microstructure of Suspensions of Oriented Spheroids." Journal of Chemical Physics **94**(6): 4453-4462.
Torquato, S. and G. Stell (1985). "Bounds on the Effective Thermal-Conductivity of a Dispersion of Fully Penetrable Spheres." International Journal of Engineering Science **23**(3): 375-383.
Tsantilis, S. and S. E. Pratsinis (2004). "Soft- and hard-agglomerate aerosols made at high temperatures." Langmuir **20**(14): 5933-5939.
Tzou, D. Y. (2008). "Thermal instability of nanofluids in natural convection." International Journal of Heat and Mass Transfer **51**(11-12): 2967-2979.
Vemury, S. and S. E. Pratsinis (1995). "Self-Preserving Size Distributions of Agglomerates." Journal of Aerosol Science **26**(2): 175-185.
Veshchunov, M. S. (2010). "A new approach to the Brownian coagulation theory." Journal of Aerosol Science **41**(10): 895-910.
Veshchunov, M. S. and I. B. Azarov (2012). "Next approximation of the random walk theory for Brownian coagulation." Journal of Aerosol Science **47**: 70-77.
Wagner, P. E. and M. Kerker (1977). "Brownian coagulation of aerosols in rarified gases." Journal of Chemical Physics **66**: 638-646.
Wang, B.-X., L.-P. Zhou and X.-F. Peng (2003). "A fractal model for predicting the effective thermal conductivity of liquid with suspension of nanoparticles." International Journal of Heat and Mass Transfer **46**: 2665-2672.
Wang, G. M. and C. M. Sorensen (1999). "Diffusive mobility of fractal aggregates over the entire Knudsen number range." Physical Review E **60**(3): 3036-3044.
Wang, G. M. and C. M. Sorensen (2001). "Aggregation kernel homogeneity for fractal aggregate aerosols in the slip regime." Aerosol Science and Technology **34**(3): 297-306.
Wang, G. M. and C. M. Sorensen (2002). "Experimental test of the Rayleigh-Debye-Gans theory for light scattering by fractal aggregates." Applied Optics **41**(22): 4645-4651.
Wang, J., S. C. Kim and D. Y. H. Pui (2011). "Carbon Nanotube Penetration through a Screen Filter: Numerical Modeling and Comparison with Experiments." Aerosol Science and Technology **45**(3): 443-452.

Wang, J., W. G. Shin, M. Mertler, B. Sachweh, H. Fissan and D. Y. H. Pui (2010). "Measurement of Nanoparticle Agglomerates by Combined Measurement of Electrical Mobility and Unipolar Charging Properties." Aerosol Science and Technology **44**(2): 97-108.

Wang, S. C. and R. C. Flagan (1990). "Scanning Electrical Mobility Spectrometer." Aerosol Science and Technology **13**(2): 230-240.

Wang, X. Q. and A. S. Mujumdar (2007). "Heat transfer characteristics of nanofluids: a review." International Journal of Thermal Sciences **46**(1): 1-19.

Wang, X. W., X. F. Xu and S. U. S. Choi (1999). "Thermal conductivity of nanoparticle-fluid mixture." Journal of Thermophysics and Heat Transfer **13**(4): 474-480.

Weber, A. P., U. Baltensperger, H. W. Gaggeler and A. Schmidt-Ott (1996). "In situ characterization and structure modification of agglomerated aerosol particles." Journal of Aerosol Science **27**(6): 915-929.

Wen, D. and Y. Ding (2004). "Experimental investigation into convective heat transfer of nanofluids at the entrance region under laminar flow conditions." International Journal of Heat and Mass Transfer **47**: 5181-5188.

Wensel, J., B. Wright, D. Thomas, W. Douglas, B. Mannhalter, W. Cross, H. P. Hong, J. Kellar, P. Smith and W. Roy (2008). "Enhanced thermal conductivity by aggregation in heat transfer nanofluids containing metal oxide nanoparticles and carbon nanotubes." Applied Physics Letters **92**(2): 023110.

Wiedensohler, A. (1988). "An Approximation of the Bipolar Charge-Distribution for Particles in the Sub-Micron Size Range." Journal of Aerosol Science **19**(3): 387-389.

Witten, T. A. and L. M. Sander (1981). "Diffusion-Limited Aggregation, a Kinetic Critical Phenomenon." Physical Review Letters **47**(19): 1400-1403.

Wu, C. W., T. J. Cho, J. J. Xu, D. Lee, B. Yang and M. R. Zachariah (2010). "Effect of nanoparticle clustering on the effective thermal conductivity of concentrated silica colloids." Physical Review E **81**(1): 011406.

Wu, H., J. J. Xie, M. Lattuada and M. Morbidelli (2005). "Scattering structure factor of colloidal gels characterized by static light scattering, small-angle light scattering, and small-angle neutron scattering measurements." Langmuir **21**(8): 3291-3295.

Xie, H. Q., J. C. Wang, T. G. Xi, Y. Liu, F. Ai and Q. R. Wu (2002). "Thermal conductivity enhancement of suspensions containing nanosized alumina particles." Journal of Applied Physics **91**(7): 4568-4572.

Xuan, Y. and Q. Li (2003). "Investigation on Convective Heat Transfer and Flow Features of Nanofluids." Journal of Heat Transfer **125**: 151-155.

Yu, W. H., D. M. France, J. L. Routbort and S. U. S. Choi (2008). "Review and comparison of nanofluid thermal conductivity and heat transfer enhancements." Heat Transfer Engineering **29**(5): 432-460.

Zhang, C., T. Thajudeen, C. Larriba, T. E. Schwartzentruber and C. J. Hogan (2012). "Determination of the Scalar Friction Factor for Non-spherical Particles and

Aggregates Across the Entire Knudsen Number Range by Direct Simulation Monte Carlo (DSMC)." Aerosol Science and Technology **46**: 1065-1078.

Zhou, H. X., A. Szabo, J. F. Douglas and J. B. Hubbard (1994). "A Brownian Dynamics Algorithm for Calculating the Hydrodynamic Friction and the Electrostatic Capacitance of an Arbitrarily-Shaped Object." Journal of Chemical Physics **100**(5): 3821-3826.

Ziff, R. M., E. D. McGrady and P. Meakin (1985). "On the validity of Smoluchowski's equation for cluster-cluster aggregation kinetics." Journal of Chemical Physics **82**: 5269-5274.

Zimmer, A. T. and P. Biswas (2001). "Characterization of the aerosols resulting from arc welding processes." Journal of Aerosol Science **32**(8): 993-1008.

Zurita-Gotor, M. and D. E. Rosner (2002). "Effective diameters for collisions of fractal-like aggregates: Recommendations for improved aerosol coagulation frequency predictions." Journal of Colloid and Interface Science **255**(1): 10-26.

Appendix

Table A.1. A summary of the properties of the most probable aggregates, i.e. those with minimum E_k, found via calculations with TEM images. The noted parameters are defined in the main text in Chapter 2.

Most Probable Aggregates

DMA Mobility Diameter (nm)	$a_{p,mean}$ (nm)	N_p	D_f	k_f	R_s(nm)	PA(nm^2)	Kn	TEM Image Inferred Mobility Dia.(nm)	z	A_{vis}(nm^2)
45	3.51	700	2.5	1.5	49.25	7775.93	1.32	46.09	4	7181.00
45	2.70	400	2.3	1.7	33.63	3444.38	2.04	45.55	2	3211.11
45	2.94	300	2.1	2.0	34.87	3514.63	2.07	46.12	2	2886.36
45	2.32	900	2.5	1.2	39.09	4747.96	1.72	53.14	2	3832.94
45	2.60	800	2.5	1.2	41.14	5346.61	1.61	45.18	3	4174.39
45	2.95	60	1.8	1.5	21.30	1082.65	4.11	37.39	1	968.93
45	2.75	100	1.8	2.0	23.32	1374.65	3.54	42.10	1	1235.96
45	2.53	100	1.9	1.2	23.46	1287.70	3.81	40.82	1	1156.89
45	3.73	40	1.6	1.3	24.21	1269.65	3.98	40.61	1	1280.97
45	3.76	40	2.0	1.5	19.85	1113.43	3.72	37.76	1	1105.00
45	2.69	100	1.7	2.0	24.36	1361.47	3.74	42.01	1	1438.89
45	3.95	100	1.7	2.0	35.78	2935.61	2.55	42.66	2	2422.47
45	3.10	70	1.8	2.0	21.74	1245.87	3.65	40.03	1	1206.88
45	3.54	60	2.1	1.7	21.55	1318.68	3.41	41.10	1	1294.01
45	2.86	100	2.0	2.0	21.76	1321.85	3.44	41.17	1	1128.38
50	3.04	100	1.9	1.5	27.40	1836.94	3.12	48.78	1	1670.28
50	3.04	100	2.1	1.7	23.06	1519.65	3.17	44.13	1	1696.22
50	3.05	100	1.9	2.0	24.08	1590.56	3.16	45.20	1	1399.11
50	3.65	200	1.9	2.0	41.11	4395.07	1.95	51.69	2	3424.89
50	3.41	300	2.5	1.2	36.66	4169.42	1.84	49.91	2	3692.81
50	3.68	200	2.5	1.2	33.68	3509.78	2.00	45.93	2	3075.78
50	3.45	90	2.0	1.5	27.80	1958.22	2.97	50.32	1	1643.72
50	3.63	200	1.5	1.7	55.40	5159.65	2.24	45.92	3	3357.28
50	3.00	100	1.7	2.0	27.94	1731.61	3.37	47.49	1	1470.83
50	3.88	200	2.2	1.2	41.50	4708.05	1.84	53.31	2	3499.56
50	4.04	90	2.4	1.3	26.87	2225.85	2.52	53.28	1	2280.72
50	3.96	60	1.6	1.3	33.33	2101.17	3.31	52.64	1	2097.47

50	3.96	200	2.0	1.5	45.31	5201.07	1.82	56.19	2	3673.59
50	3.32	90	2.0	1.5	26.79	1818.69	3.08	48.48	1	1774.45
50	4.03	40	2.0	1.3	21.04	1260.35	3.49	40.18	1	1326.61
50	3.89	200	1.9	2.0	44.11	4901.95	1.88	54.61	2	4916.23
60	3.94	400	2.3	1.7	48.87	7377.03	1.38	65.66	2	6503.59
60	3.66	300	1.9	2.0	51.46	6406.37	1.68	62.36	2	4912.97
60	3.64	200	1.8	2.0	42.71	4464.46	2.00	52.25	2	3918.37
60	4.00	300	1.6	2.0	69.43	8758.94	1.66	59.18	3	6757.34
60	3.89	300	1.9	2.0	54.69	7236.85	1.58	66.17	2	5454.65
60	3.45	600	2.2	1.3	59.93	9869.08	1.27	60.85	3	8222.11
60	3.17	200	1.6	2.0	44.22	3815.43	2.42	71.33	1	2837.48
60	3.02	200	2.3	1.3	30.20	2671.85	2.36	58.51	1	2615.94
60	3.44	300	1.9	1.5	51.63	6033.72	1.79	60.80	2	5452.43
60	4.06	300	2.6	1.3	40.64	5243.72	1.62	55.66	2	5003.22
60	3.44	500	2.0	1.7	59.19	8828.94	1.40	58.12	3	7232.30
60	3.39	500	2.4	1.7	42.82	5810.50	1.54	58.47	2	5511.88
60	3.49	300	1.8	1.7	55.25	6493.56	1.78	63.25	2	5687.84
60	2.97	200	1.9	2.0	33.44	2910.00	2.40	61.39	1	2352.28
60	2.98	200	1.6	2.0	41.56	3371.09	2.58	66.94	1	2823.44
60	3.27	400	1.8	2.0	55.96	6806.86	1.72	64.65	2	4716.12
70	3.84	100	1.4	2.0	41.87	3129.47	2.79	64.66	1	3120.56
70	3.57	200	2.5	1.3	31.85	3193.16	2.08	63.76	1	2698.95
70	3.04	400	1.8	2.0	52.11	5893.77	1.85	60.25	2	4583.07
70	3.36	200	2.0	1.2	40.25	4017.03	2.09	72.42	1	2385.04
70	3.23	300	2.3	1.7	35.82	3839.04	1.95	70.10	1	3189.73
70	3.38	300	2.5	1.2	36.54	4156.51	1.84	72.78	1	3838.22
70	3.38	200	1.8	2.0	40.97	3923.22	2.18	71.76	1	3373.50
70	3.57	200	1.6	2.0	49.80	4840.77	2.15	80.61	1	3757.59
70	4.27	200	2.5	1.3	38.00	4545.99	1.75	76.07	1	3582.53
70	3.59	200	1.9	1.5	44.09	4530.33	2.03	77.23	1	3325.88
70	3.31	300	2.5	1.3	34.89	3789.60	1.92	69.50	1	3223.79
70	3.91	200	1.5	1.7	59.59	5971.03	2.08	90.54	1	3643.31
70	4.07	100	1.9	1.5	35.93	3096.57	2.42	63.57	1	3705.69
70	2.77	300	2.0	2.0	36.15	3404.37	2.22	66.44	1	3181.98
70	3.45	200	2.0	2.0	36.09	3603.54	2.09	68.18	1	3754.28
75	3.32	400	1.9	2.0	53.33	6706.59	1.66	94.27	1	5908.74
75	3.11	400	2.1	2.0	42.20	5114.36	1.72	81.15	1	4218.41
75	3.29	200	1.4	2.0	53.24	4396.67	2.53	77.50	1	3278.42
75	3.37	200	1.6	2.0	45.38	4167.99	2.27	74.52	1	4022.69
75	3.24	200	1.9	1.5	41.37	3871.92	2.23	71.39	1	3296.54

75	3.29	300	2.5	1.2	35.60	3889.87	1.91	70.47	1	3407.93
75	3.70	200	1.9	2.0	41.67	4516.31	1.93	76.66	1	3593.26
75	3.47	200	2.0	2.0	37.19	3706.58	2.10	69.26	1	3160.44
75	3.17	200	1.6	2.0	42.13	3617.67	2.43	69.28	1	3467.89
75	3.26	200	1.9	1.5	41.18	3893.71	2.21	71.55	1	3007.58
75	3.23	200	2.0	1.7	36.91	3488.34	2.21	67.32	1	3659.40
75	4.34	100	1.6	2.0	40.55	3588.89	2.36	68.80	1	3625.91
75	4.28	200	1.5	1.7	65.25	7156.15	1.90	99.52	1	4259.18
75	3.11	400	2.1	2.0	42.13	5097.92	1.73	81.02	1	4176.65
75	3.95	200	2.2	2.0	36.36	4060.05	1.87	71.99	1	3806.48
80	3.43	300	2.0	1.3	44.14	5174.47	1.78	82.02	1	5721.20
80	2.85	500	2.5	1.2	43.98	4286.95	2.14	75.27	1	4213.67
80	3.41	300	1.9	2.0	47.87	5544.78	1.80	85.42	1	4503.33
80	4.31	200	1.9	1.5	54.52	6826.78	1.67	95.29	1	4971.43
80	4.23	200	1.8	1.7	56.39	6662.83	1.77	94.65	1	4934.07
80	3.20	600	2.5	1.5	42.45	5716.70	1.55	85.26	1	4828.26
80	4.36	200	2.1	2.0	43.39	5392.31	1.68	83.35	1	4614.98
80	4.01	200	2.1	2.0	39.57	4572.57	1.81	76.64	1	3776.88
80	3.04	400	1.8	2.0	52.02	5874.40	1.85	88.53	1	4328.84
80	3.95	300	1.8	2.0	56.13	7499.56	1.56	99.74	1	5473.27
80	3.91	100	1.7	2.0	33.23	2722.03	2.55	59.48	1	3300.46
80	4.15	200	2.2	2.0	38.64	4535.17	1.78	76.14	1	3716.03
80	2.91	600	2.5	1.2	41.50	5400.47	1.61	82.93	1	4929.71
80	3.68	300	1.3	2.0	83.90	8358.55	2.10	74.05	2	4655.54
80	3.52	200	1.8	1.7	45.97	4546.90	2.11	77.68	1	3826.03

Table A.2. A summary of the properties of the average aggregates, i.e. those with the weighted average quasifractal and transport properties. The noted parameters are defined in the main text in Chapter 2.

Average Aggregates

DMA Mobility Diameter (nm)	$a_{p,mean}$ (nm)	N_p	D_f	k_f	R_s (nm)	PA (nm^2)	Kn	TEM Image Inferred Mobility Dia.(nm)
45	3.51	670	2.48	1.54	48.99	7645.79	1.34	45.75
45	2.70	401	2.34	1.52	33.97	3501.39	2.03	45.92
45	2.94	300	2.10	2.00	34.86	3515.99	2.07	46.12
45	2.32	939	2.45	1.47	38.81	4729.15	1.71	53.00
45	2.60	768	2.43	1.39	41.02	5233.32	1.64	44.77
45	2.95	57	1.71	1.62	21.40	1044.47	4.28	36.76
45	2.75	94	1.78	1.70	24.56	1369.20	3.75	42.14
45	2.53	98	1.82	1.53	23.11	1233.93	3.91	39.97
45	3.73	40	1.57	1.50	24.70	1276.38	4.04	40.76
45	3.76	44	1.83	1.57	23.04	1281.45	3.76	40.69
45	2.69	90	1.74	1.73	23.73	1275.43	3.89	40.66
45	3.95	99	1.72	1.76	36.95	3007.56	2.57	43.24
45	3.10	72	1.83	1.65	23.51	1342.99	3.66	41.66
45	3.54	61	2.14	1.52	21.84	1351.27	3.38	41.61
45	2.86	95	2.27	1.60	19.81	1185.89	3.49	38.90
50	3.04	98	1.82	1.70	26.71	1715.78	3.25	47.15
50	3.04	104	2.13	1.67	23.17	1546.22	3.13	44.50
50	3.05	98	1.90	1.96	24.11	1579.54	3.19	45.06
50	3.65	200	1.89	1.94	41.90	4461.01	1.96	52.13
50	3.41	101	2.40	1.42	37.26	4268.67	1.82	50.51
50	3.68	200	2.44	1.49	32.62	3352.61	2.03	44.88
50	3.45	89	2.07	1.66	25.50	1808.48	2.95	48.19
50	3.63	81	1.60	1.66	52.88	5061.30	2.18	45.34
50	3.00	96	1.76	1.74	27.74	1722.32	3.37	47.34
50	3.88	200	2.26	1.51	38.04	4256.93	1.87	50.56
50	4.04	98	2.31	1.57	27.87	2379.02	2.45	55.10
50	3.96	59	1.58	1.48	32.38	2049.43	3.30	51.93
50	3.96	191	2.04	1.52	43.33	4852.18	1.87	54.26
50	3.32	93	1.91	1.57	27.93	1926.99	3.03	49.96

50	4.03	42	1.81	1.51	24.19	1430.64	3.53	43.00
50	3.89	235	1.79	1.96	54.10	6105.56	1.85	61.44
60	3.94	384	2.34	1.50	48.64	7195.42	1.41	64.96
60	3.66	300	1.90	2.00	51.50	6404.55	1.68	62.36
60	3.64	200	1.93	1.78	42.06	4421.58	1.99	51.95
60	4.00	277	1.60	1.99	66.25	8117.70	1.70	56.98
60	3.89	300	1.89	2.00	54.80	7229.58	1.58	66.16
60	3.45	593	2.10	1.64	61.15	9769.24	1.31	60.80
60	3.17	200	1.60	2.00	44.18	3812.57	2.42	71.30
60	3.02	201	2.24	1.61	29.62	2590.96	2.39	57.59
60	3.44	302	1.91	1.67	50.67	5934.06	1.78	60.23
60	4.06	301	2.55	1.43	40.75	5303.32	1.61	55.94
60	3.44	504	2.01	1.71	58.99	8786.00	1.40	57.98
60	3.39	491	2.48	1.57	41.91	5587.52	1.57	57.37
60	3.49	301	1.85	1.68	53.25	6259.25	1.78	61.99
60	2.97	200	1.90	2.00	33.45	2910.05	2.40	61.39
60	2.98	202	1.61	2.00	40.84	3331.30	2.56	66.48
60	3.27	400	1.80	2.00	55.91	6798.45	1.72	64.61
70	3.84	103	1.54	1.89	39.40	3053.62	2.70	63.62
70	3.57	200	2.39	1.46	32.95	3345.80	2.06	65.33
70	3.04	400	1.81	1.99	51.67	5864.24	1.84	60.06
70	3.36	200	2.02	1.21	39.82	3968.45	2.10	71.94
70	3.23	238	2.25	1.62	33.66	3354.71	2.10	65.55
70	3.38	292	2.35	1.52	37.16	4202.70	1.85	73.28
70	3.38	200	1.82	1.93	40.93	3928.34	2.18	71.80
70	3.57	200	1.60	2.00	49.43	4804.82	2.15	80.27
70	4.27	166	2.28	1.44	37.74	4196.98	1.88	73.37
70	3.59	200	1.99	1.55	41.46	4290.22	2.02	74.85
70	3.31	257	2.42	1.45	33.13	3409.44	2.03	65.93
70	3.91	163	1.60	1.77	49.53	4754.58	2.18	79.89
70	4.07	100	1.83	1.56	37.10	3182.95	2.44	64.56
70	2.77	327	2.06	1.88	36.34	3544.63	2.14	67.71
70	3.45	201	2.03	1.76	37.45	3761.16	2.08	69.77
75	3.32	400	1.86	1.87	56.42	6988.74	1.69	96.72
75	3.11	400	2.10	2.00	42.19	5112.68	1.72	81.14
75	3.29	193	1.44	1.88	51.79	4263.82	2.54	76.19
75	3.37	201	1.60	1.87	47.00	4284.54	2.29	75.73
75	3.24	200	1.91	1.60	39.50	3674.33	2.25	69.38
75	3.29	300	2.45	1.31	35.75	3921.53	1.90	70.75
75	3.70	200	1.90	2.00	41.66	4515.19	1.93	76.64

75	3.47	200	2.00	1.73	38.60	3881.68	2.08	71.00
75	3.17	200	1.69	1.80	42.69	3686.85	2.42	69.98
75	3.26	200	1.90	1.57	40.60	3832.42	2.21	70.93
75	3.23	236	1.99	1.66	39.62	3961.82	2.09	71.85
75	4.34	94	1.62	1.63	42.83	3647.81	2.45	69.65
75	4.28	122	1.63	1.75	46.09	4360.40	2.21	76.21
75	3.11	400	2.10	2.00	42.15	5093.07	1.73	80.99
75	3.95	200	2.42	1.58	34.85	3836.14	1.90	69.87
80	3.43	300	1.99	1.28	53.35	6287.18	1.77	91.57
80	2.85	463	2.31	1.55	38.74	4514.57	1.79	76.01
80	3.41	300	1.90	2.00	47.92	5545.13	1.81	85.43
80	4.31	200	1.90	1.67	52.53	6590.72	1.67	93.35
80	4.23	200	1.74	1.78	56.82	6645.81	1.79	94.63
80	3.20	589	2.49	1.51	42.32	5681.20	1.56	84.99
80	4.36	200	2.14	1.65	45.20	5681.85	1.66	85.74
80	4.01	200	2.09	1.92	40.40	4685.30	1.80	77.65
80	3.04	397	1.89	1.80	50.40	5760.14	1.83	87.42
80	3.95	260	1.85	1.91	52.69	6642.08	1.66	93.71
80	3.91	103	1.69	1.93	35.97	2949.65	2.55	62.15
80	4.15	200	2.36	1.50	38.73	4580.95	1.77	76.50
80	2.91	608	2.45	1.44	40.80	5234.48	1.63	81.63
80	3.68	297	1.64	1.92	67.30	7219.22	1.95	67.74
80	3.52	200	1.70	1.67	48.97	4681.41	2.19	79.23